# Microstructural coarsening of multicomponent multiphase polycrystalline materials

Zur Erlangung des akademischen Grades
**Doktor der Ingenieurwissenschaften**
von der KIT-Fakultät für Maschinenbau des
Karlsruher Instituts für Technologie (KIT)

genehmigte
**Dissertation**
von

**M.Tech. Ramanathan Perumal**

# Abstract

Engineering materials such as metals, alloys, and ceramics, generally possess multicomponent, multiphase polycrystalline microstructures. When thermomechanical treatments are employed, the processing parameters can alter the microstructure, thereby controlling their physical and mechanical properties. The microstructural evolution is often governed by grain growth, recrystallization and coarsening phenomenon, reforming the mean grain size of the system. For instance, in a polycrystalline setup, wherein the grains are chemically-identical, grain growth has primarily dictated the migration of the grain boundaries. Whereas, in a multiphase system, the Ostwald ripening accompanies grain growth. During evolution, the microstructures are more complex owing to the characteristic distribution of the phases and chemical components. Limited computational studies exist in these complex alloys which interpreted the results in terms of single-phase like growth power laws. Therefore, the detailed study on microstructural transformations is demanded. The purpose of this dissertation is to investigate the microstructural evolution of single-phase, binary two-phase and ternary two and three-phase polycrystalline systems, with the aid of large scale phase-field simulations.

The first part of the thesis examines grain growth phenomena in pure single-phase materials. The study consists of three sections. Chapter 5 focuses on topological evolution of the grains and its first-neighbors resulting from 2-D and 3-D simulations. The face-loss event affinity decreases with increase in face-class. A face-class switching affinity is proposed, wherein above a face-class 14, the face-gain events are preferred over loss events. Contact affinity exhibit attraction towards major to minor face-classes while avoiding same face-classes. The first-neighbors topological behavior during evolution is quantitatively captured through a statistical tool called heat-maps. The formation of topological clusters which represent the time-invariant behavior of the grains is elucidated. Chapter 6 addresses some of the open issues, concerning the self-similarity and correlation behavior of the 2-D and 3-D microstructures in detail. The self-similar state has been characterized by the short- and long-range geometrical and topological features of the microstructure. The role of the dimensionality effect has been perceived during growth. It is shown that the correlation of the short-range neighbors is much more significant than the long-range interactions. Various initial polycrystalline grain arrangements are studied and revealed that accomplishing quasi-steady state regime is roughly independent of the

initial microstructure. Chapter 7 investigates the deviations from the normal grain growth behavior introduced by the presence of pre-existing large sized ($> 2R_c$) grains. These abnormal grains induce a period of transition that establishes a bimodal distribution, which subsequently evolves into a unimodal time-invariant distribution. Influence of the factors like initial volume-fraction of the abnormal grains $F_o$ and degree of abnormality $U_{max}$ on the duration of the transient period is quantified.

The following part of the thesis is subdivided into three sections and provides an outline of grain coarsening in multicomponent multiphase systems. Chapter 8 examines the influence of relative volume fractions and bulk diffusivity on the concurrent grain growth and coarsening phenomena in binary two-phase systems. The slowest growth kinetics is observed for the equivolume fraction case, irrespective of the bulk diffusivity. The relative growth rates of the individual phases follow the normal grain growth behavior. While considering the concomitant coarsening of the minor phase constituents, it is difficult to reconcile all the observed (grain boundary dragging) behaviors with a universal Zener relation. Chapter 9 looks at the grain coarsening of equivolume fraction duplex materials with a wide range of interfacial energy ratio combinations. The mechanisms of formation of the complex microstructural patterns have been briefly discussed. The two-phase grain size distributions (GSD) are difficult to approximate with available single-phase analytical models. Therefore, statistical parameters have been used to evaluate the obtained GSD. The relative growth rates of the individual phases are nearly identical, without being largely affected by interfacial energy ratios used. For the first time, the parallel coordinates plot is used to represent the multidimensional input/output dataset in duplex materials and can be used to design the microstructures with required features. Microstructural coarsening of the ternary two and three-phase systems with different relative volume fraction is studied in chapter 10. An exceptional grain growth resistance is observed for the ternary $0.33\alpha$-$0.33\beta$-$0.33\gamma$ volume fraction case compared to the ternary $0.5\alpha$-$0.5\gamma$ and the binary $0.5\alpha$-$0.5\gamma$ systems. As the volume fraction decreases for the particular phase, the intergrain distance increases and long-range diffusion slows down the coarsening. The grain growth is suppressed with an increase in the number of phases and components. In addition, the diffusivity of the components dictates the growth kinetics. The maximum attainable grain size to mean size ratio for the individual phases supports the isotropic growth behavior. An empirical Zener type relation, for a three-phase system with a low volume fraction, is proposed. The thesis is concluded by a brief summary of the main findings and possible future extensions in chapter 11.

This research is important since the computational study of the microstructural coarsening of complex microstructures, taking into account the significance of multicomponent multiphase constituents, may attempt to increase our understanding and improve the properties of the materials, thereby ensuring enhanced lifespan and improvement of its services.

# Kurzfassung

Technische Werkstoffe wie Metalle, Legierungen und Keramiken besitzen im Allgemeinen mehrkomponentige, mehrphasige polykristalline Mikrostrukturen. Wenn thermomechanische Behandlungen angewendet werden, können die Verarbeitungsparameter die Mikrostruktur verändern und dadurch ihre physikalischen und mechanischen Eigenschaften steuern. Die Entwicklung der Mikrostruktur wird häufig durch das Kornwachstum, die Rekristallisation und das Vergröberungsphänomen bestimmt, wodurch die mittlere Korngröße des Systems verändert wird. In einem polykristallinen Aufbau beispielsweise, in dem die Körner chemisch identisch sind, hat das Kornwachstum hauptsächlich die Wanderung der Korngrenzen bestimmt, während in einem Mehrphasensystem die Ostwald-Reifung mit dem Kornwachstum einhergeht. Während der Evolution sind die Mikrostrukturen aufgrund der charakteristischen Verteilung der Phasen und chemischen Komponenten komplexer. Für diese komplexen Legierungen existieren begrenzte Berechnungsstudien, die die Ergebnisse in Form von einphasigen Wachstumspotenzgesetzen interpretieren. Daher ist eine detaillierte Untersuchung der Gefügeumwandlungen erforderlich. Der Zweck dieser Dissertation ist es, die mikrostrukturelle Entwicklung von einphasigen, binären zweiphasigen und ternären zwei- und dreiphasigen polykristallinen Systemen mithilfe von großskaligen Phasenfeldsimulationen zu untersuchen.

Der erste Teil der Arbeit untersucht Kornwachstumsphänomene in reinen einphasigen Materialien. Die Untersuchung besteht aus drei Abschnitten. Kapitel 5 befasst sich mit der topologischen Entwicklung der Körner und deren ersten Nachbarn, die sich aus 2D- und 3D-Simulationen ergibt. Mit zunehmender Flächenklasse kommt es seltener vor, dass eine Fläche verloren geht. Deshalb wird ein Wechsel der Flächenklassen vorgeschlagen, bei dem es oberhalb einer Flächenklasse von 14 eher zu Ereignissen der Flächengewinnung als zu Ereignissen des Flächenverlustes kommt. Die Kontaktaffinität zeigt eine Anziehungskraft auf wichtige und unwichtige Flächenklassen, während dieselben Flächenklassen vermieden werden. Das topologische Verhalten der ersten Nachbarn während der Evolution wird mithilfe eines statistischen Tools namens Heat Maps quantitativ erfasst. Die Bildung von „topologischen Clustern“, die das zeitinvariante Verhalten der Körner darstellen, wird erklärt. Außerdem wird die Bildung von „topologischen Clustern“, die das zeitinvariante Verhalten der Körner darstellen, erläutert. In Kapitel 6 werden einige der offenen Fragen in Bezug auf die Selbstähnlichkeit und das Korrelationsver-

halten der zweidimensionalen und dreidimensionalen Mikrostrukturen ausführlich behandelt. Der selbstähnliche Zustand wurde durch die kurz- und langfristigen geometrischen und topologischen Merkmale der Mikrostruktur charakterisiert. Während des Wachstums wurde die Rolle des Dimensionalitätseffekts erkannt. Es wird gezeigt, dass die Korrelation der Nachbarn mit geringer Entfernung viel bedeutsamer ist als die der Nachbarn mit großer Entfernung. Verschiedene anfängliche polykristalline Kornanordnungen werden untersucht und zeigen, dass das Erreichen eines Quasi-Steady-State-Regimes in etwa unabhängig von der anfänglichen Mikrostruktur ist. In Kapitel 7 werden die Abweichungen vom normalen Kornwachstumsverhalten untersucht, die durch die Präsenz von bereits vorhandenen großen Körnern ($> 2R_c$) verursacht werden. Durch diese abnormalen Körner wird eine Übergangsphase eingeleitet, die eine bimodale Verteilung hervorruft, die sich anschließend in eine unimodale, zeitinvariante Verteilung entwickelt. Der Einfluss von Faktoren wie der anfängliche Volumenanteil der abnormalen Körner $F_o$ und der Grad der Abnormalität $U_{max}$ auf die Dauer der Übergangsphase wird quantifiziert.

Der folgende Teil der Arbeit gliedert sich in drei Abschnitte und gibt einen Überblick über die Kornvergröberung in mehrkomponentigen Mehrphasensystemen. Kapitel 8 untersucht den Einfluss von relativen Volumenanteilen und den Einfluss der Bulk-Diffusivität auf das gleichzeitige Kornwachstum und das Vergröberungsphänomen in binären Zweiphasensystemen. Die langsamste Wachstumskinetik wird für den Fall des Äquivolumenanteils beobachtet, die unabhängig von der Bulk-Diffusivität ist. Die relativen Wachstumsraten der einzelnen Phasen folgen dem normalen Kornwachstumsverhalten. Unter Berücksichtigung der gleichzeitigen Vergröberung der Nebenphasenbestandteile ist es schwierig, alle beobachteten Verhaltensweisen (Ziehen der Korngrenzen) mit einer universellen Zener-Beziehung in Einklang zu bringen. Kapitel 9 befasst sich mit der Kornvergröberung von Duplexmaterialien mit einem Äquivolumenanteil und einer Vielzahl von Kombinationen des Energieverhältnisses zwischen den Grenzflächen. Die Mechanismen der Bildung der komplexen Mikrostrukturmuster wurden kurz diskutiert. Mit den verfügbaren einphasigen, analytischen Modellen können die zweiphasigen Korngrößenverteilungen (GSD) nur schwer approximiert werden. Daher wurden statistische Parameter verwendet, um die erhaltene Korngrößenverteilung zu bewerten. Die relativen Wachstumsraten der einzelnen Phasen sind nahezu identisch, ohne stark von den verwendeten Grenzflächen-Energieverhältnissen beeinflusst zu werden. Das Parallelkoordinatendiagramm wird erstmals dazu verwendet, den mehrdimensionalen Eingabe- / Ausgabedatensatz in Duplexmaterialien darzustellen und die Mikrostrukturen mit den erforderlichen Merkmalen zu bilden. Die mikrostrukturelle Vergröberung des ternären Zwei- und Dreiphasensystems mit unterschiedlichem relativen Volumenanteil wird in Kapitel 10 untersucht. Für den Fall des ternären Volumenanteils $0.33\alpha$-$0.33\beta$-$0.33\gamma$ wird im Vergleich zu dem ternären $0.5\alpha$-$0.5\gamma$ und dem binären $0.5\alpha$-$0.5\gamma$ System eine außergewöhnliche Kornwachstumsbeständigkeit beobachtet. Wenn der Volumenanteil für die bestimmte Phase abnimmt, nimmt der Abstand zwischen den Körnern zu und die Diffusion über große Entfernungen verlangsamt die Vergröberung.

Das Kornwachstum wird mit zunehmender Anzahl der Phasen und Komponenten unterdrückt. Darüber hinaus wird die Wachstumskinetik durch die Diffusionsfähigkeit der Komponenten bestimmt. Das maximal erreichbare Verhältnis von Korngröße zu mittlerer Größe für die einzelnen Phasen unterstützt das isotrope Wachstumsverhalten. Für ein Dreiphasensystem mit einem geringen Volumenanteil wird eine empirische Beziehung vom Zener-Typ vorgeschlagen. In Kapitel 11 wird die Arbeit mit einer kurzen Zusammenfassung der wichtigsten Ergebnisse und möglichen zukünftigen Erweiterungen abgeschlossen.

Diese Forschung ist wichtig, da die rechnerische Untersuchung der mikrostrukturellen Vergröberung komplexer Mikrostrukturen unter Berücksichtigung der Bedeutung mehrkomponentiger, mehrphasiger Bestandteile unser Verständnis und die Eigenschaften der Materialien verbessern kann, wodurch eine längere Lebensdauer und eine Verbesserung ihrer Leistung gewährleistet wird.

# Acknowledgments

# Contents

# Part I
# Introduction and Literature review

# Chapter 1

# Introduction : Motivation & Synopsis

Microstructural coarsening generally is observed in engineering materials during thermomechanical processes. The increase in the complexity of the microstructures with increasing the number of components and/or phases. With progressive in-situ experimental tools and a concomitant increase in the computational methods in the microstructural studies, open issues pertaining to self-similarity behavior on geometrical and topological features, concurrent grain growth and coarsening phenomena, the interplay between the components and phases during evolution is attempt in this thesis.

Numerical simulations, such as the phase-field approach can be used to explore the growth and/or coarsening of multi-component multi-phase polycrystalline materials. With the motivation to address the above mentioned phenomenon, the results of the present dissertation can be divided into two parts. In the first part, self-similar behavior on normal grain growth phenomena is elucidated in the form of short- and long-range grain size and topological correlations, effect of initial Voronoi filling in 2-D and 3-D microstructures. Further, the influence of pre-existing abnormal grains on transient grain growth behavior is investigated. The initial volume fraction of abnormal grains, grain size variation, mean distance between the grains are parameterized with more than hundred simulations. In the second part of the thesis, the effect of relative volume fraction, diffusivity and interfacial energy anisotropy in binary two-phase polycrystalline structures is studied. The simulations reveal the lowest growth kinetics for equivolume fraction systems. In addition, the microstructural patterns depending on the energy ratio between grain boundary and inter-phase boundary are demonstrated. Finally, suppressed microstructural coarsening phenomena is obtained for ternary three-phase polycrystalline microstructures. Various local morphological features are reported during the evolution processes. The extended abstract of the each chapter results presented below.

1. **Formation of first-neighbor topological clusters during the isotropic grain growth**

   Grain growth in polycrystalline material is influenced by numerous factors which convolute the understanding of the process. Present work intends to delineate certain aspects of this complexity by quantitatively analyzing the topological evolution of the grains and its first-neighbors resulting from multiphase-field simulations. Upon verifying the consistency of this approach with the existing 2- and 3- dimensional analytical predictions, face-switching events of about 75000 grains in 3-D domain is extensively analyzed. Despite the expected numerical dominance of the face-loss event, we find the affinity of this event to decrease with increase in face-class. A transition in 'switching affinity ' is observed above face-class 14, wherein, the face-gain events are preferred over loss events. The pathway of the topological evolution is comprehensively analyzed to identify its influence on the life-span of the grains. This analysis indicates that the topological evolution around the average face-class, 'dead zone', invariably shortens the life-span of the grains and considerable gain in the face-class is seldom observed. The topological behavior of the first-neighbors during grain growth is quantitatively captured through a well-known statistical tool called heat-maps. And for the first time, the formation of 'topological clusters' which account for the time-invariant behavior of the grains is elucidated. The results presented in the chapter has been published in *Computational Materials Science* [1].

2. **Grain size and topological correlations on normal grain growth**

   Since the analytical grain growth models hold many simplified assumptions, the experiments and simulation results often differ from classical theories. In this chapter, the phase field simulations attempt to elucidate some of the open questions, concerning the self-similarity and correlation behavior of the 2-D and 3-D microstructures. The validity of Hillert's linear growth law assumption, based on mean curvature, is addressed. Furthermore, the role of the dimensionality effect has been observed during growth. The self-similar state has been characterized by the geometrical and topological features of the microstructure. The short- and long-range neighbor grain size and topological correlation behavior in 2-D have been validated and extended to 3-D microstructures. It is found that the correlation of the short-range neighbors is much more significant than the long-range interactions. Accomplishing a quasi-steady state regime in the isotropic growth case is roughly independent of the initial grain arrangements. The results presented in this chapter forms the content of a manuscript which has been submitted for publication.

3. **Transient phenomena induced by 'abnormally' large grains during 2-dimensional isotropic grain growth.**

   'Abnormally' large grains, whose sizes are greater than twice the critical radius
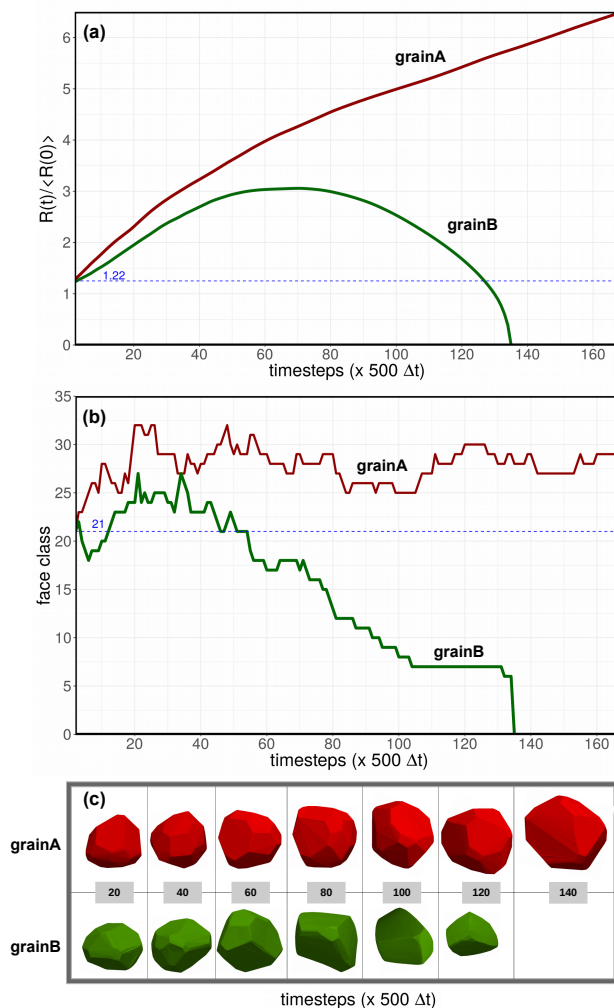
Figure 1.1: (a) Change in the size of the two grains ($R(t)/R(0)$) with identical initial size, $R(0)$ during grain growth. (b) Temporal evolution of the face-class of two topologically similar grains of face-class 21. (c) Visual representation of the topological nature of the identical grains (grainA and grainB) at different time-steps. grainB at time, $t = 140 \times 500\Delta t$ is intentionally left vacant to indicate its disappearance.
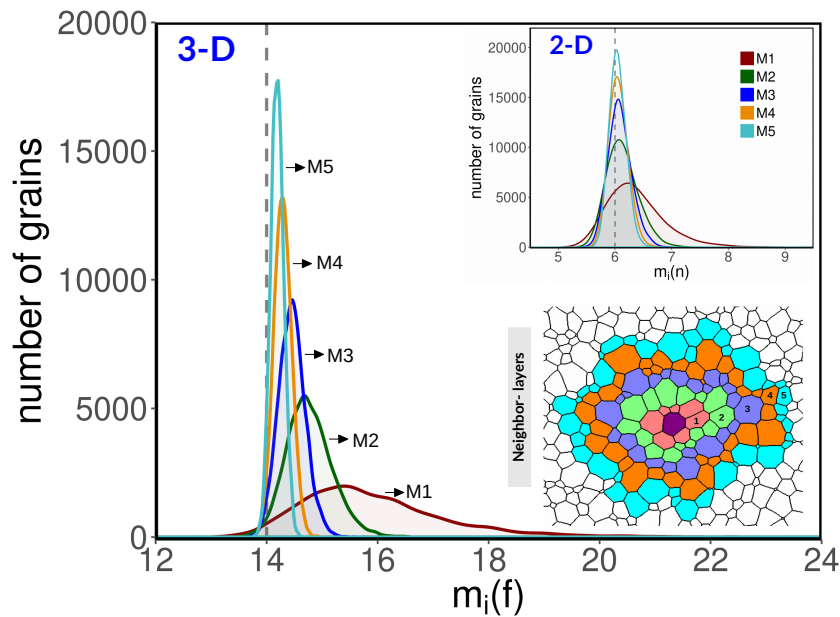
*Figure 1.2:    The short- and long-range topological correlations in 2-D and 3-D. The subplot shows the schematic representation of the neighbor layers. Note that the correlation behavior in the QS state clearly depends on the layer of the cells; the short-range neighbors display a strong correlation, while the long-range grains show a random arrangement*

$(2R_c)$, are known to alter the isotropic grain growth phenomena. In the present work, phase-field simulations of 2-dimensional microstructures are extensively analyzed to elucidate the deviations from the normal grain growth introduced by the presence of abnormal grains. Polycrystalline microstructures that are 'artificially' made to resemble physical structures, by governing the distribution and the sizes of the abnormal grains, is employed to analyse the grain growth in the presence of large grains. This study unravels that the abnormal grains induce a period of transition during which its grain size distribution is shifted and confined within $2R_c$, indicating a complete disappearance of the abnormality in the microstructure. Furthermore, it is identified that this transition period establishes a bimodal distribution, which subsequently evolves into a unimodal time-invariant distribution. This behaviour noticeably reveals the misconception that the disappearance of the abnormality signifies the onset of normal grain growth. Moreover, despite the apparent disappearance of the abnormal grains, a continued increase in the volume-fraction of these 'pre-existing' abnormal grains is recognized, and in the steady-state condition, it is observed that the microstructure predominantly consists of these pre-existing abnormal grains. Influence of the factors like initial volume-fraction of the abnormal grains $F_o$ and degree of abnormality $\overline{U}_{max}$ on the duration of the transient period is quantified by investigating close to hundred microstructures with unique $F_o$ and $\overline{U}_{max}$. The results presented in the chapter has been published in *Computational*
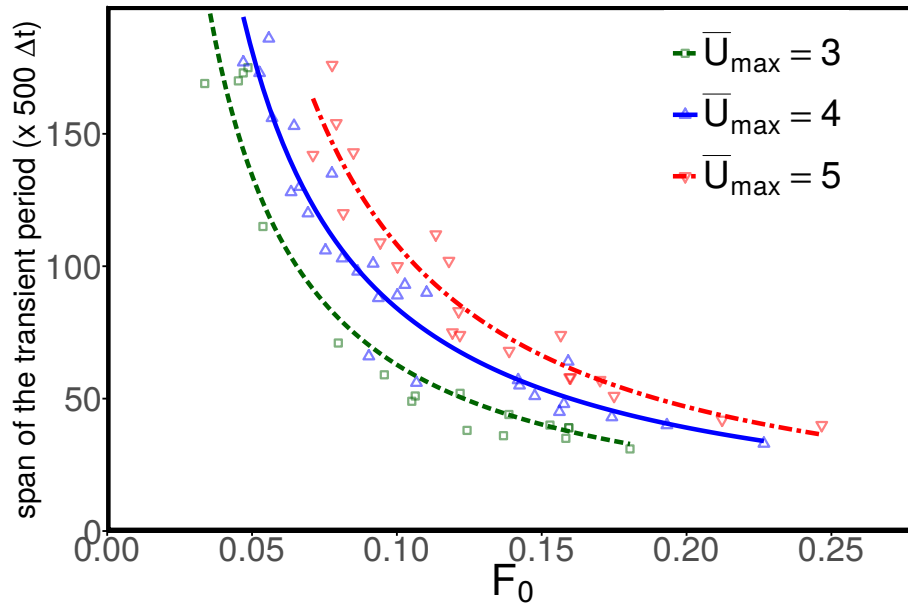
*Figure 1.3: Influence of initial volume-fraction of abnormal grains $F_o$ on time taken for their disappearance $F_{tp}$. Microstructures for this illustration are categorized based on $\overline{U}_{max}$ through color scheme.*

Materials Science [2].

4. **Concurrent grain growth and coarsening of binary two-phase microstructures**

   A phase-field model is exploited to demonstrate the influence of relative volume fractions and bulk diffusivity on the grain growth phenomena in two-phase polycrystalline systems. For very small and high volume fractions, the simulated morphology consists of a dispersion of isolated minor phase grains embedded in the matrix of major phase grains. At intermediate fractions, the obtained microstructure resembles an interpenetrating network-like structure. The performed large-scale 2-D simulations elucidate the governing mechanisms for the concurrent two-phase growth at low and high volume fractions, and the continuous transition between interface-controlled and diffusion-limited regimes. While the slowest kinetics is observed for the $0.5\alpha$-$0.5\beta$ volume fraction case, irrespective of the diffusivity, the fastest kinetics is displayed by the pure systems, with a slight difference, which is due to relative interfacial energies. The relative growth rates of the individual phases and the maximum attainable grain size to mean size ratio are observed to follow the well-known trends for isotropic systems. The obtained results for the concurrent growth of a minor phase with various diffusivities, reveal that it is difficult to reconcile all observed behaviors with a universal Zener relation, in contradiction to the previously made claims in the literature. The results presented in the chapter has been published in *Computational Materials Science* [3].
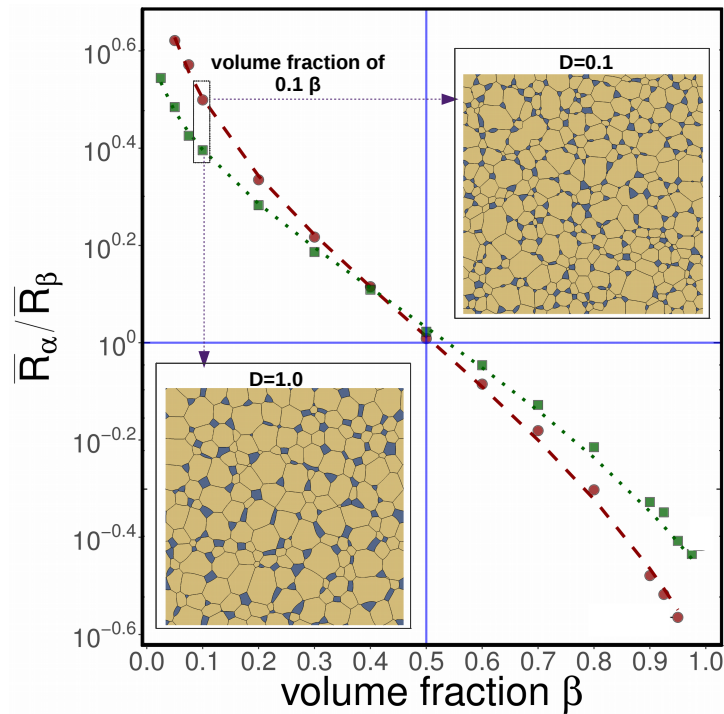
*Figure 1.4:    The influence of diffusivity on the $\bar{R}_\alpha/\bar{R}_\beta$ ratio, as a function of the $\beta$ volume fraction.*

5. **Microstructural coarsening of equivolume fraction duplex materials**

A multi-phase field model is employed to study the microstructural coarsening of $0.5\alpha$-$0.5\beta$ system with wide range of interfacial energy ratio ($ER_\alpha = \frac{\sigma_{\alpha_i\alpha_j}}{\sigma_{\alpha\beta}}$ and $ER_\beta = \frac{\sigma_{\beta_i\beta_j}}{\sigma_{\alpha\beta}}$) combinations. The aim has been to cover the full range of microstructures observed in the nonconserved (NCS) and conserved systems (CS). The mechanisms of formation of the complex microstructures and the characteristic individual phase morphologies have been briefly discussed. Besides, four interface energy regime criteria were proposed to describe the predicted microstructural features. The mean grain size evolution elucidate that the governing mechanisms for NCS and CS are interface-controlled and bulk diffusion-limited coarsening mechanisms respectively. The stable quadruple junctions over the triple junctions can be seen for some higher energy ratio cases. It is difficult to reconcile all observed two-phase GSD with single-phase analytical models. Additionally, statistical parameters have been exploited to evolute the GSD. The relative growth rates of the individual phases are nearly identical, irrespective of the varying interfacial energy ratios used. The parallel-coordinate plot is introduced to consolidate the results and proposed to design the duplex microstructures with the required properties. The results presented in this chapter forms the content of a manuscript which has been submitted for publication.

6. **Microstructural coarsening of ternary two and three-phase polycrystalline**
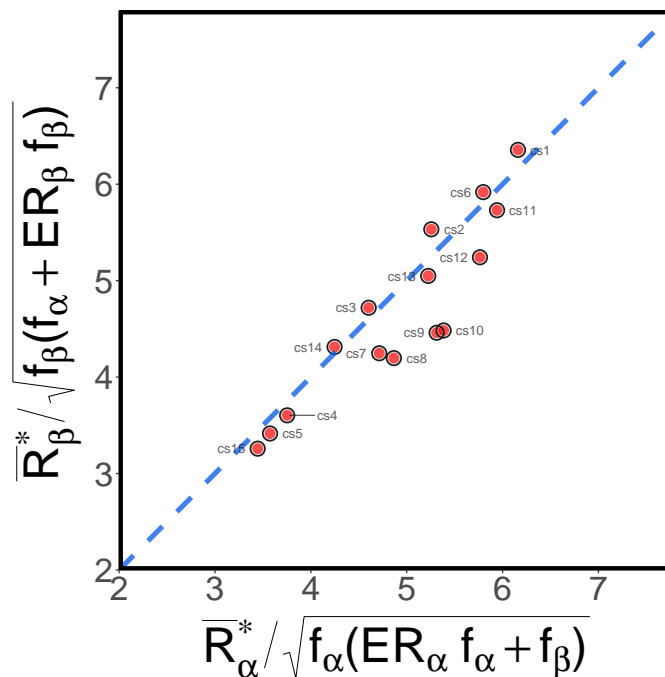
*Figure 1.5: Relation between the mean radii of α and β grains in dual-phase microstructures. The positive correlation can be seen in the figure where as the dotted line is the earlier stainless steel experimental result [4, 5].*

**materials**

A thermodynamically consistent phase-field model is exploited to demonstrate the influence of relative volume fractions on the microstructural coarsening of complex polycrystalline systems. The performed two-dimensional mean grain size data are found to follow the power growth law kinetics with the growth coefficient in the range of $3 < m < 4$ depending on process parameters. While the slowest kinetics is perceived for the $0.33\alpha$-$0.33\beta$-$0.33\gamma$ volume fraction case, the fastest kinetics is exhibited by the pure systems. The transition between interface-controlled and diffusion-limited regimes ascertains the individual phase coarsening. As the volume fraction decreases for the particular phase, the intergrain distance increases and long-range diffusion slows down the coarsening. In the domain, cooperative diffusion of multicomponent elements further suppresses the grain growth. At intermediate volume fractions, the obtained grain size distribution is more closely approximated by the Weibull function than by the Hillert distribution. The relative growth rates of the individual phases and the maximum attainable grain size to mean size ratio follow the isotropic growth behavior. It is difficult to reconcile the concurrent coarsening of minor constituents with a universal Zener relation, provided that an empirical Zener relation, like the formulation for a three-phase system with a low volume fraction, is proposed. The results presented in this chapter forms the content of a manuscript which has been submitted for publication.
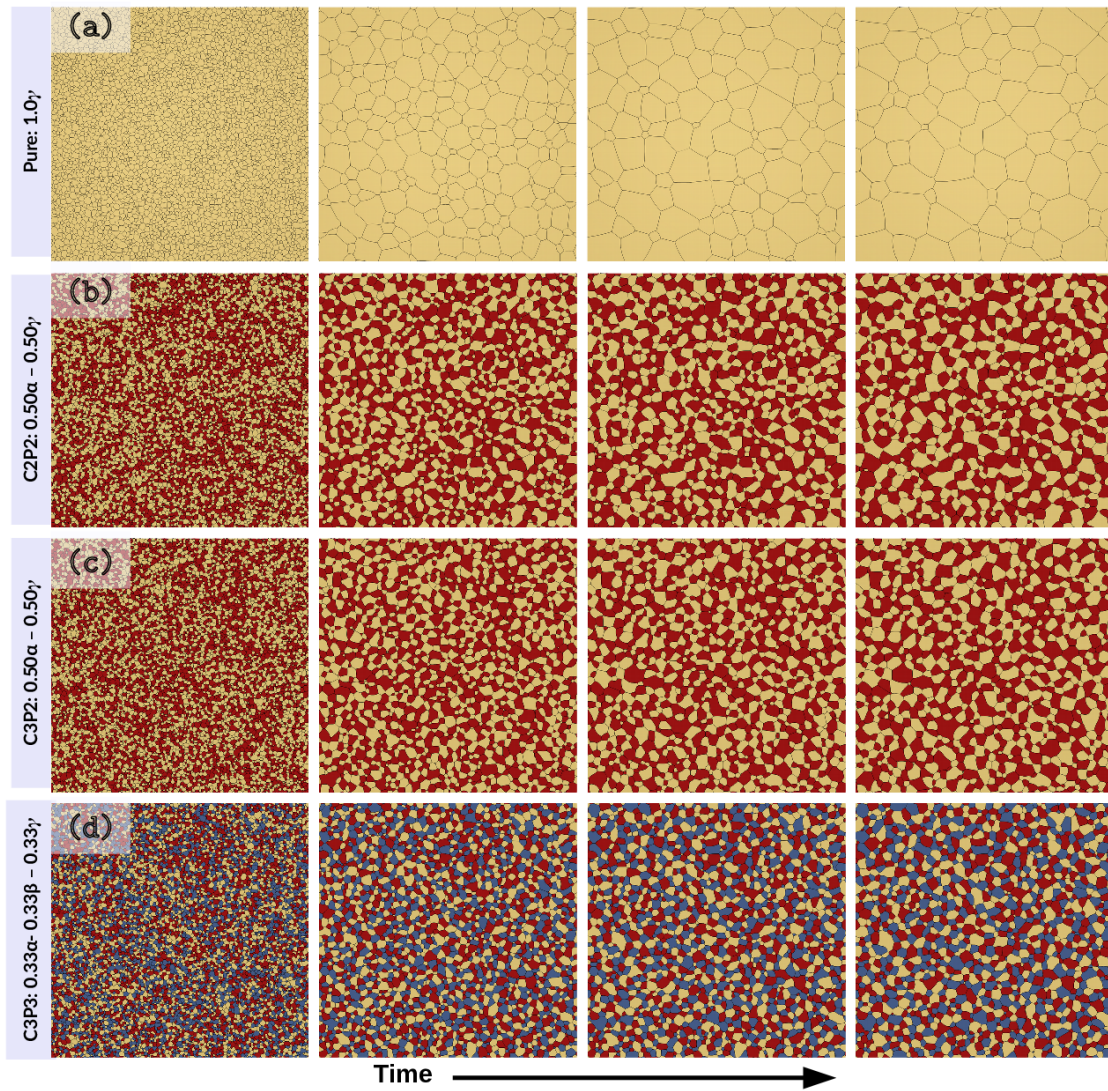
Figure 1.6: Microstructural evolution of (a) pure: $1.0\gamma$, (b) $C2P2$ : $0.5\alpha$-$0.5\gamma$, (c) $C3P2$ : $0.5\alpha$-$0.5\gamma$, and (d) $C3P3$ : $0.33\alpha$-$0.33\beta$-$0.33\gamma$. As can be seen, the mean grain size increases, while decreasing the total number of grains. The addition of the $\alpha$ and $\beta$ phase in the microstructure suppresses the grain growth.

The thesis not only contributes to the advancement of our understanding of microstructural coarsening in bulk polycrystalline structures but provides a general framework in phase-field models, illustrate the applicability to examine other physical phenomenon in materials science such as thin-films, multi-layers etc.

# Chapter 2

# Literature Review

## 2.1 Microstructures in materials

Material properties can be optimized by the appropriate control of the microstructure. A number of technologically important materials exhibits multicomponent, multiphase systems where the physical properties and microstructural changes can be governed by the distribution and shape modification of the constituting phases [6, 7]. In order to enhance the performance, a comprehensive understanding of the underlying microstructural evolution is demanded. Thermomechanical treatment could significantly customize the properties, by the selection of desired microstructures [8]. Microstructural evolution through phase transformation, grain growth, and particle coarsening phenomena has been investigated to a large extent in earlier studies [9, 10, 11]. It has been known that the addition of the secondary phase considerably inhibits the grain boundary movement, and influences the mean grain size of the system [12, 13]. From the high-temperature application standpoint, commonly used super alloys and ceramics undergo complex microstructural evolution [14].

Serial sectioning and diffraction contrast tomography are widely used for microstructural visualization and characterization in 3-D [15, 16] (Fig. 2.1). In situ quantification of the morphological transitions using the present-day experimental setup is a challenging task for the researchers [17, 18, 19]. It is therefore necessary to obtain a reliable physical model which can explain the microstructural evolution and can then be utilized to predict their engineering properties. Although there has been much work concentrated on the grain coarsening behavior of single phase materials, both theoretically and experimentally, little efforts have so far been expended to characterize the multiphase systems [20, 21, 22].
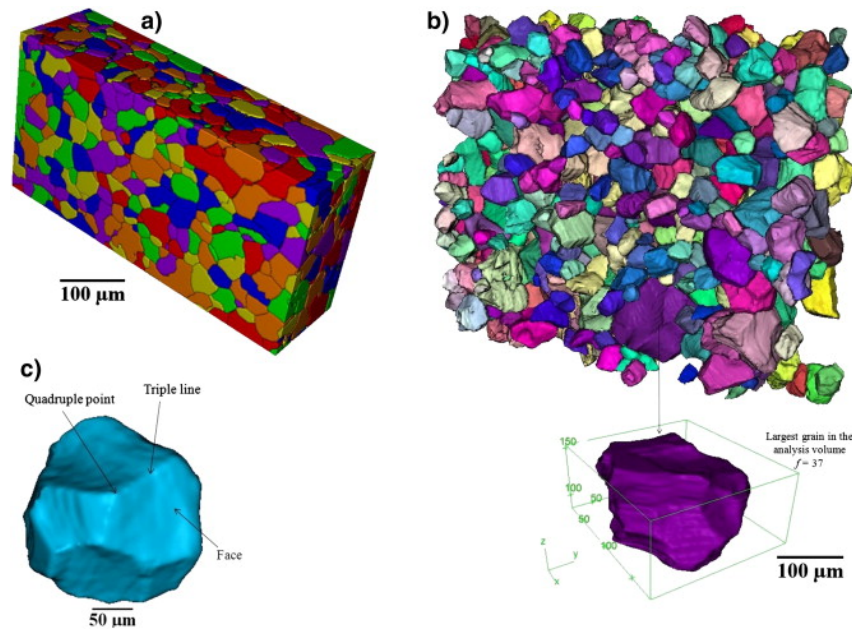
*Figure 2.1:    Quantitative characterization of grains in polycrystalline iron (a) experimental serial sectioned reconstructed microstructure (b) visualization of internal grain structures (border intersecting grains removed); the largest grain in the domain is highlighted. (c) The topological characteristics of extracted 3-D grain is indicated. [15]*

## 2.2    Normal grain growth

Grain growth has been the field of study in materials science and physics for more than six decades [23]. This can be classified as Normal (NGG) and Abnormal (AGG) grain growth processes [20, 24, 25]. In NGG, the larger grains grow at the expense of smaller grains, in a polycrystalline network [26]. In AGG, on the other hand, some specific grains have grain boundary energy, and mobility advantages should grow faster than the similarly sized grains [27, 28]. However, the driving force for both cases is the decrease in the free energy, which accompanies a reduction in the total grain boundary area. Numerous theoretical, experimental and computer simulation studies have been investigated to unveil the grain growth phenomena and their complexities [29, 30, 31, 32]. Grain growth phenomena are extensively studied for single-phase materials [20, 21]. According to the classical growth law, the mean grain size (grain radius) is characterized by a scaling regime, in which the size follows a power law. In single-phase materials, the isotropic grain growth data can be represented as

$$\bar{R}_t^m - \bar{R}_0^m = K(t - t_0), \tag{2.1}$$

where $\bar{R}_0$ is the mean grain size at the initial time step ($t_0$), $\bar{R}_t$ denotes the mean grain size at a steady state regime ($t$), $m$ is the grain growth exponent, and $K$ represents the grain growth constant.

Although in most cases it is known that the initial grain size is much smaller than the final grain size of the system ($\bar{R}_0 << \bar{R}_t$), there is a simplified relationship for grain growth, which is defined as follows:

$$\bar{R} \approx k t^{(1/m)}, \tag{2.2}$$

where $\bar{R}$ represents the mean grain size, $t$ is the time, $k$ denotes the proportionality constant, and $m$ is the grain growth exponent.

The self-similarity behavior of the microstructural evolution can be determined from the geometrical and topological characteristics, such as normalized mean grain size distribution (GSD) and topological distribution (GTD). In the earlier investigations, several analytical and empirical functions were proposed to approximate the GSD's obtained from the experimental and simulation microstructures [20, 33, 34]. Hillert's theory predicts a quasi-stationary GSD function for grain growth, given by the following equation [20]:

$$F(\rho) = (2e)^{\dot{\beta}} \, \frac{\rho \dot{\beta}}{(2-\rho)^{2+\dot{\beta}}} \, exp\Big(\frac{-2\dot{\beta}}{2-\rho}\Big), \tag{2.3}$$

where $\rho = R/R_c$ represents the relative grain size. The critical grain size assumed $R_c = \bar{R}$ in the two-dimensional case and $R_c = (9/8)\bar{R}$ in the three-dimensional case. Likewise, the shape function defined $\dot{\beta} = 2$ in 2-D and $\dot{\beta} = 3$ in 3-D. The Weibull function can be written as [33]:

$$F(\rho) = \Big(\frac{\tilde{\beta}}{g^{\tilde{\beta}}}\Big) \, (\rho^{\tilde{\beta}-1}) \, exp\Big[-\Big(\frac{\rho}{g}\Big)^{\tilde{\beta}}\Big], \tag{2.4}$$

where $\tilde{\beta}$ is an adjustable parameter and $g = 1/\Gamma(1+1/\tilde{\beta})$.

Several semi-empirical functions can also be used to represent the GSD in a close approximation [35, 33, 36]. Some recent works have been an attempt to derive a unique GSD function, based on self-similar average grain-volume change rate [37].

## 2.3 Concurrent grain growth and coarsening phenomena

The microstructural evolution is more complex in the case of multiphase systems with the presence of additional interfacial energy influences and phase-wise volume conservation constraints [38, 39]. For certain combinations of process parameters and annealing conditions, excellent physical and mechanical properties can be obtained from two-phase systems. For example, dual-phase $Al_2O_3$-$YAG$ composites showed excellent high temperature strength and creep by restricting grain growth and extended diffusion distance for
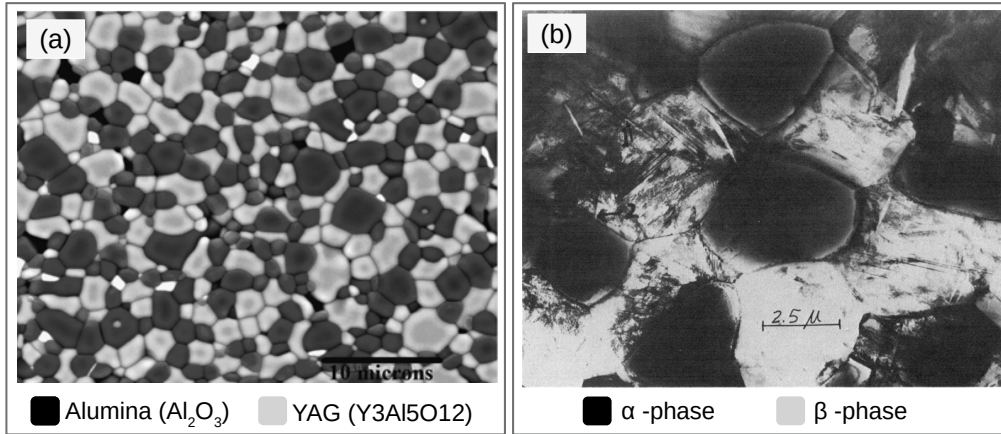
*Figure 2.2:    Two-phase microstructures (a) Scanning electron microscopy (SEM) micrograph of Alumina-YAG (0.5 Al$_2$O$_3$-0.5 Y$_3$Al$_5$O$_{12}$) composite [40] shows a uniform distribution of two phases and homogeneous grain size for each phase. (b) Grain size and microstructural characteristics of recrystallized α-β Titanium alloy having a composition Ti-5.25Al-5.5V-0.9Fe-0.5Cu (0.29α-0.71β) [41]*

distributed phases (Fig. 2.2 (a)) [40]. The α-β Titanium alloys used in chemical plants, marine and aerospace applications due to their exceptional mechanical properties such as strength, toughness and corrosion resistance. Further improvement at high temperature can be achieved by the microstructural modification through heat treatments (Fig. 2.2 (b)) [41]. There have been several attempts, both theoretical and computational, to assimilate such a complex interplay [20, 42]. For instance, in the cases where the second phase is distributed in the form of particles over a homogeneous matrix phase, particle coarsening or Ostwald ripening is studied by Lifshitz, Slyozov and Wagner which is most commonly referred to as LSW theory [43, 44]. While this analysis is developed for very low volume fractions of the distributed phase, an extension was later furnished by Ardell for finite volume fractions [45]. Further, Davis et al. modified the LSW theory to account for the coalescence of the particles [46]. Drawing from all these theories a comprehensive growth rate equation for two phase matrix-particle kind of systems for finite volume fractions was proposed by Calderon et al. [47, 48] as

$$r_\beta^m - r_{\beta 0}^m = \left[ \frac{8f(\phi)D\gamma_{\alpha\beta}C_\alpha(1-C_\alpha)V_M}{9\dot{R}T(C_\beta - C_\alpha)^2[1 + \partial \ln a/\partial \ln C_\alpha]} \right] \cdot (t - t_0), \qquad (2.5)$$

where, β marks the particle forming phase and α is the matrix. $r_\beta$ is the mean particle radius of β at time, t, $r_{\beta 0}$ is an initial mean particle radius, $f(\phi)$ is the functional dependence of the volume fraction $\phi$, $D$ is the bulk diffusivity, $\gamma_{\alpha\beta}$ denotes the energy associated with the α-β interface, $C_\alpha, C_\beta$ are the respective equilibrium concentrations of the α and β phases, $V_M$ is the molar volume of the precipitate, $\dot{R}$ represents the gas constant, $T$ is the absolute temperature and $a$ is the activity coefficient of the rate-limiting solute in α matrix. On the other end of the spectrum, as opposed to LSW type theories, Zener

pinning theories exist in which the focus is the study of grain growth in matrix phase influenced (typically inhibited) by the embedded secondary phase particles [12, 49]. The classical Zener model relates the size (r) and volume fraction (f) of the the minor phase particles to the average size of the primary phase grains (d) as

$$d = 4r/3f, \qquad (2.6)$$

In the original derivation, it was assumed that the secondary particles are spherical, mono-sized, and randomly distributed. However, later experimental and computational investigations accounted for the degree of contact between the grain boundary and the particles, the initial grain size distribution, the shape and distribution of the particles, particle clustering and particle dragging etc by proposing a generalization [50, 51, 52, 53] to Eq. 2.6 in the form

$$d = \acute{k} \left\{ r/f^{(1/q)} \right\}, \qquad (2.7)$$

where $\acute{k}$ denotes the Zener proportionality constant, and $q$ is the generalized Zener exponent. For example, Srolovitz through 2D MC simulations showed that $q = 2$ for non-random particles of $< 5\%$ volume fraction [54]. Hassold et al. proposed that $q = 3$ from three-dimensional simulations with higher volume fractions [55]. Experimentally, structural ceramic composites yielded $q = 3$ for lower volume fractions ($f < 0.15$) [56]. Moelans et al., using a 2-D phase-field model recovered a Zener exponent of $q = 2$ [52]. Interestingly, through large-scale 3-D phase-field simulations, Suwa et al. and Vanherpe et al. obtained $q = 1.14$ and $q = 1.07$, respectively [57, 58]. Although the effect of the second-phase volume fraction and their shape complexities on the Zener relation has been investigated over the past few decades, it is invariably assumed that the pinning particles are inert, i.e., little attention has been paid to the concurrent coarsening of such particles through long range diffusion [59, 60] (one exception is the work of Fan et al. [61]).

## 2.4 Suppressed grain coarsening in multiphase materials

Several efforts have been accompanied to understand the microstructural coarsening of multiphase materials, with the aim of producing better microstructures even after prolonged high-temperature annealing. To further limit grain growth, the same approach can be extended to three-phase microstructures, with an adequate number of alloying elements. However, on the ground of literature, the study of microstructural coarsening in solid solutions with multi-principal elements (>2) and multiphase (>2) is confined [62, 63, 64]. The multiphase ceramic composites are employed for high-temperature applications, where the suppression of diffusion is a prerequisite for microstructural stability
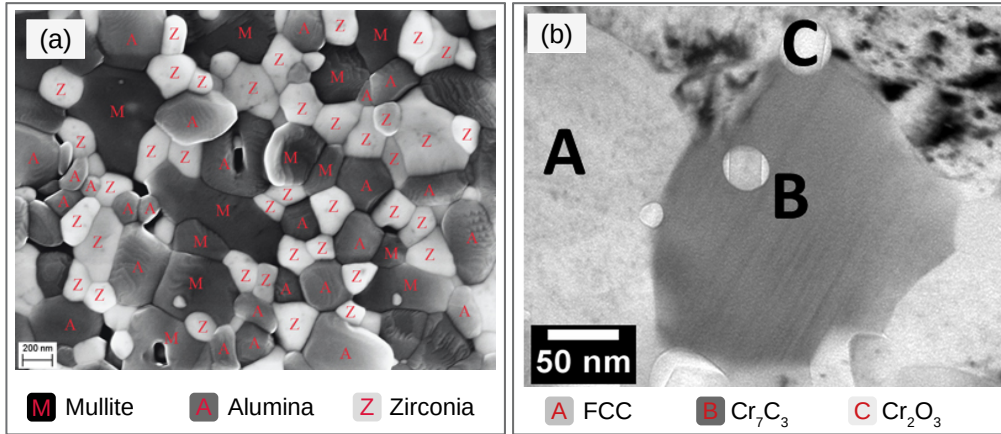
*Figure 2.3:   Three-phase microstructures (a) Equal-volume-percent Alumina-Zirconia-Mullite ceramic composite; three phases homogeneously distributed through- out the microstructure with roughly similar grain sizes seen [68]. (b) Transmission electron microscopy (TEM) micrograph of CoCrFeNi high entropy alloy highlights A-FCC grains, B-Carbide grains and C-Oxide pre- cipitates. Volume fractions of phases 0.70 FCC-0.19 Carbide-0.11 Oxide are in the heat treated sample [73].*

[65, 66]. Kim et al. reported a lower creep rate for triplex (three-phase) composites than did any of its single-phase constituents [40]. The $0.4ZrO_2$-$0.3spinel$-$0.3Al_2O_3$ compos- ite revealed the extensive super-plasticity, due to the intermixing of distinct phases and extended interdiffusion distances, resulting in reduced grain growth [67, 68] (Fig. 2.3 (a)).

High entropy alloys (HEA) are a new class of material that contains more than 4 or 5 principal elements in equal or near equi-molar compositions [69]. Although most HE alloys are referred to as single-phase (BCC or FCC) systems, it has been found that the microstructure of some HE alloys shows multiphase structures [70, 71]. At higher homol- ogous temperatures ($>0.4T_m$), HEA have a better grain stability than conventional alloys [72]. In their experiments, Praveen et al. recently pointed out that higher temperatures lead to an exceptional resistance to grain growth, in the high entropy alloy CoCrFeNi, where the cooperative diffusion of the underlying components is required for the specific phase to grow, which will make the diffusivity sluggish [73]. They stated that the sluggish diffusion, together with the mutual retardation of the grain growth of two-phase systems and Zener pinning, suppress the overall evolution (Fig. 2.3 (b)).

## 2.5   Numerical simulations

Attempts enhancing the understanding of grain growth extend beyond experimental ob- servations to theoretical studies [74, 75, 29, 76]. Approaches that are more pronounced in explicating the microstructural evolution in polycrystalline materials include phase-field

models, Monte Carlo/Potts models, vertex models, cellular automata and front tracking methods [77, 78, 79, 80, 81, 82, 83, 84, 85, 86, 87, 88]. Recently,the phase-field approach has been excessively involved in simulating the microstructural transformation especially in polycrystalline material [89, 90, 91]. Tracking grain boundaries which introduces immense complexity in sharp interface models is appropriately averted by employing suitable phase-field parameters ($\phi_\alpha$). Furthermore, the interface(grain boundary), which is usually few atoms in width, is collectively described with mesoscopic bulk phases (grains) by involving a diffuse interface. The consistency of this approach which is verified asymptotically, e.g [92, 93]. Pioneering works on understanding grain growth through phase-field analysis dates back to 1997 [61]. Interestingly, despite of being one of the early studies and confined to 2-D, a dedicated work is reported on the topological evolution of the grains. Several advancements are reported frequently on the phase-field study of grain growth, such as the introduction of anisotropy to resemble the physical environment [94, 95]. However, recent study comparing the in-situ observation of grain growth in titanium-alloy with the outcomes of an isotropic phase-field simulations ascertains that, at-least from a statistical standpoint, evolution in an isotropic system holds a close resemblance to the ones observed experimentally [84].

Following its outset, phase-field models have been increasing involved in simulating phase transformation accompanying solidification and solid-state transformation [96]. Apart from being thermodynamically consistent, these models ensure the computational and numerical efficiency by circumventing the need for tracking the interface and replacing it with finite-diffuse interface. This diffuse interface separating the bulk phases is defined by a smoothly varying function, evolution of which corresponds to the observed transformation. Furthermore, asymptotic analysis of these diffuse-interface models have shown to recover the outcomes of sharp-interface models, particularly Gibbs-Thomson effect [97]. Therefore, phase-field studies are increasingly involved to gain significant insights, which are otherwise laborious to attain, on complex phenomenon like grain growth. Recent study comparing the evolution of the phase-field simulation with the in-situ observation of grain growth reveals an acceptable degree of convergence between the results [84]. Moreover, theoretical analysis comparing the outcomes of phase-field and Potts Monte-Carlo simulations of isotropic grain growth reveals no significant deviation [98].

Present dissertation explores the microstructural coarsening phenomena in complex polycrystalline materials. Specifically, the intention is to study the effect of phase fraction, number of components on concurrent grain growth and coarsening phenomena. Each of the topics are briefly reviewed one by one to provide a necessary background and the interpretation of the results presented in the thesis.

# Part II
# Methods : Phase-field formulation

# Chapter 3

# Phase-field model for single-phase grain growth

### 3.0.1 Curvature driven grain growth

Microstructural transformation in a physical system, irrespective of its nature, is thermodynamically propelled by the minimization of free-energy. Driving force of a similar configuration is introduced in the present phase-field model through the free energy functional $\mathcal{F}$ [1, 99]. Subsequently, dynamics of the resulting evolution is governed by the minimization of this functional $\mathcal{F}$ which comprises of free-energy contribution from within the grain(bulk phases) and grain-boundary(interface). This free-energy functional of *Ginzburg-Landau type* for a polycrystalline system of $N$ grains is expressed as

$$\mathcal{F}(\boldsymbol{\phi}) = \int_{\Omega} \epsilon a(\boldsymbol{\phi}, \boldsymbol{\nabla}\boldsymbol{\phi}) + \frac{1}{\epsilon} w(\boldsymbol{\phi}) + f(\boldsymbol{\phi}) \mathrm{d}\Omega, \tag{3.1}$$

where $\Omega$ is the volume(area) of the simulation domain under consideration and $f(\boldsymbol{\phi})$ is the free-energy contribution from within the grain. Identity of the $N$ grains involved in the simulation is encompassed in the functional $\mathcal{F}$ through vector-valued continuous phase-field variable $\boldsymbol{\phi}$ of $N$ components $(\phi_1, \phi_2...., \phi_\alpha, \phi_\beta, ..., \phi_N)$, where $\phi_\alpha$ is the state variable representing the volume-fraction of individual grain $\alpha$. Gradient energy density $a(\boldsymbol{\phi}, \boldsymbol{\nabla}\boldsymbol{\phi})$ in Eqn. 3.1 is expressed as the summation of pair-wise interactions between the grains, $\alpha$ and $\beta$, sharing an interface which reads

$$a(\boldsymbol{\phi}, \boldsymbol{\nabla}\boldsymbol{\phi}) = \sum_{\alpha<\beta} \sigma_{\alpha\beta} [a_{\alpha\beta}(q_{\alpha\beta})]^2 |q_{\alpha\beta}|^2. \tag{3.2}$$

Here, $\sigma_{\alpha\beta}$ is the interface energy density of the grain boundary separating $\alpha$ and $\beta$. The form adopted by the interface energy is defined by the term $a_{\alpha\beta}$ wherein anisotropy is conventionally introduced to simulate desired morphology [100]. In Eqn. 3.2, $a_{\alpha\beta}$ is expressed as a function of gradient vector $q_{\alpha\beta}$ which is written as

$$q_{\alpha\beta} = \phi_\alpha \boldsymbol{\nabla}\phi_\beta - \phi_\beta \boldsymbol{\nabla}\phi_\alpha. \tag{3.3}$$

In the present model, multi-obstacle potential $w(\boldsymbol{\phi})$ is involved, as opposed to well-known double-well potential, which reads

$$w(\boldsymbol{\phi}) = \frac{16}{\pi^2} \sum_{\alpha<\beta} \sigma_{\alpha\beta} \phi_\alpha \phi_\beta + \sum_{\alpha<\beta} \sigma_{\alpha\beta\delta} \phi_\alpha \phi_\beta \phi_\delta. \tag{3.4}$$

While all the possible interfaces are encompassed in the first term of Eqn. 3.4, the second term $\phi_\alpha \phi_\beta \phi_\delta$ prevents the formation 'spurious' or third phase, also referred to as 'ghost' phase, in the grain boundary during the evolution. Furthermore, sharp-defined minimas are assigned to the bulk phases(grains) through setting $w(\boldsymbol{\phi})$ to $\infty$ if $\boldsymbol{\phi}$ is not on the Gibbs simplex

$$\mathcal{G} = \left\{ \boldsymbol{\phi} \in \mathbb{R}^N : \sum_\alpha \phi_\alpha = 1, \phi_\alpha \geq 0 \right\}. \tag{3.5}$$

A comprehensive understanding on the numerical and computational efficiency of multi-obstacle potential can be gained from the Refs [92, 101].

Since the present study focuses exclusively on the isotropic evolution of grains, the crystallographic orientation of the grains and influence of the stored energy is overlooked. This consideration implies that the contribution from with the grain(bulk phases) can be ignored. Thus, substituting $f(\boldsymbol{\phi}) = 0$ in Eqn. 3.1 simplifies the functional $\mathcal{F}$ to

$$\mathcal{F}(\boldsymbol{\phi}) = \int_\Omega \epsilon a(\boldsymbol{\phi}, \boldsymbol{\nabla}\boldsymbol{\phi}) + \frac{1}{\epsilon} w(\boldsymbol{\phi}) \mathrm{d}\Omega, \tag{3.6}$$

and the corresponding evolution equation for the grain $\alpha$ through variational derivation can be expressed as

$$\tau\epsilon \frac{\partial \phi_\alpha}{\partial t} = \epsilon \left[ \boldsymbol{\nabla} \cdot \frac{\partial a(\boldsymbol{\phi}, \boldsymbol{\nabla}\boldsymbol{\phi})}{\partial \boldsymbol{\nabla}\phi_\alpha} - \frac{\partial a(\boldsymbol{\phi}, \boldsymbol{\nabla}\boldsymbol{\phi})}{\partial \phi_\alpha} \right] - \frac{1}{\epsilon} \frac{\partial w(\boldsymbol{\phi})}{\partial \phi_\alpha} - \lambda. \tag{3.7}$$

Here, parameter $\epsilon$ determines the thickness of the diffuse interface and $\tau$ is the mean of all the grain-boundary mobilities expressed as

$$\tau = \frac{\displaystyle\sum_{\alpha<\beta} \phi_\alpha \phi_\beta \tau_{\alpha\beta}}{\displaystyle\sum_{\alpha<\beta} \phi_\alpha \phi_\beta}. \tag{3.8}$$

Furthermore, Lagrange multiplier $\lambda$ is incorporated in the evolution Eqn. 3.7 to impose the constraint $\displaystyle\sum_{\alpha=1}^N \phi_\alpha = 1$, which then reads

$$\lambda = \frac{1}{N} \sum_{\alpha=1}^N \left[ \epsilon \left[ \boldsymbol{\nabla} \cdot \frac{\partial a(\boldsymbol{\phi}, \boldsymbol{\nabla}\boldsymbol{\phi})}{\partial \boldsymbol{\nabla}\phi_\alpha} - \frac{\partial a(\boldsymbol{\phi}, \boldsymbol{\nabla}\boldsymbol{\phi})}{\partial \phi_\alpha} \right] - \frac{1}{\epsilon} \frac{\partial w(\boldsymbol{\phi})}{\partial \phi_\alpha} \right]. \tag{3.9}$$

In order to ensure the numerical efficiency of the evolution the parameters involved are appropriately non-dimensionalized. The non-dimensionalization scheme involved in the

present work has already been successfully adopted in numerous theoretical analysis [1, 90]. Furthermore, since the primary focus of the present analysis is to quantify the influence of abnormally large grains on the isotropic grain growth, a constant value is assigned to the mean mobility $\tau$.

# Chapter 4

# Phase-field model for multicomponent multiphase system

### 4.0.1  Binary (two-component) two-phase polycrystalline system

Microstructural evolution is thermodynamically driven by the minimization of free energy. The diverse models adopt diffuse interface techniques where the explicit tracking of the interface movement is obtained through the formulation of partial differential equations. Bulk-free energy functions, related to specific material systems, can be derived from physical principles or can be computed from thermodynamic databases (CALPHAD) [102, 103]. In the present study, the investigation of a binary, two-phase system is based on the grand-potential formulation, proposed in [104], which reads as

$$\mathbf{\Omega}(T, \boldsymbol{\mu}, \boldsymbol{\phi}) = \int_{\Omega} \Big( \mathbf{\Psi}(T, \boldsymbol{\mu}, \boldsymbol{\phi}) + \epsilon a(\boldsymbol{\phi}, \boldsymbol{\nabla}\boldsymbol{\phi}) + \frac{1}{\epsilon} w(\boldsymbol{\phi}) \Big) \mathrm{d}\Omega, \qquad (4.1)$$

where $\mathbf{\Omega}$ is the grand potential functional, $\mathbf{\Psi}$ is the grand chemical potential density, T is the temperature, $\boldsymbol{\mu}$ is the chemical potential, and $\epsilon$ is the interface width. The identity of the $N$ grains, involved in the simulation, is encompassed in the functional $\mathbf{\Omega}$, through the vector-valued continuous phase-field variable $\boldsymbol{\phi}$ of $N$ components $(\phi_1, \phi_2, ..., \phi_m, \phi_n, ..., \phi_N)$, where $\phi_m$ is the state variable representing the volume-fraction of an individual grain, denoted by the subscription $m \in \{1, 2, ..., m, n, ..., N\}$.

We consider a polycrystalline structure which consists of a number of $N(= N_\alpha + N_\beta)$ $\alpha$ and $\beta$ phase grains with different orientations. For the $\alpha$ and $\beta$ phase, we respectively represent the equilibrium composition fields as $c = c_\alpha$ and $c = c_\beta$. The orientation of each phase is represented as

$$\boldsymbol{\phi_\alpha} = (\phi_{\alpha_1}, \phi_{\alpha_2}, \phi_{\alpha_3}, ...., \phi_{\alpha_{N_\alpha}}) \qquad (4.2)$$

$$\boldsymbol{\phi_\beta} = (\phi_{\beta_1}, \phi_{\beta_2}, \phi_{\beta_3}, ...., \phi_{\beta_{N_\beta}}). \qquad (4.3)$$

21
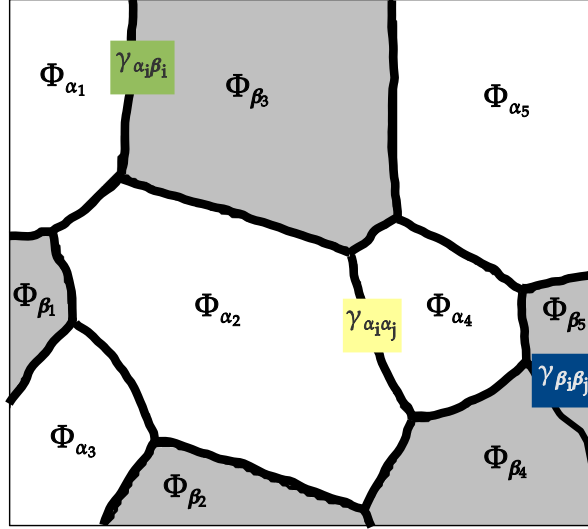
*Figure 4.1: Schematic representation of the two-phase microstructure*

The free energy density contribution $\epsilon a(\boldsymbol{\phi}, \boldsymbol{\nabla}\boldsymbol{\phi})$ is denoted as the gradient energy density, and $\frac{1}{\epsilon}w(\boldsymbol{\phi})$ is represented as the interface potential density of the system. Within each grain $m$, $\phi_m$ equals 1, while $\phi_{m \neq n}$ equals 0. At an interface between the two grains, the respective phase fields $\phi_m^{\alpha,\beta}$ and $\phi_n^{\alpha,\beta}$ change their value smoothly from 0 to 1. A schematic representation of our simulation setup is shown in figure 4.1.

The gradient energy $a(\boldsymbol{\phi}, \boldsymbol{\nabla}\boldsymbol{\phi})$ in Eqn. 4.1 can be expressed by the summation of the pairwise interaction terms between the grains $m$ and $n$:

$$a(\boldsymbol{\phi}, \boldsymbol{\nabla}\boldsymbol{\phi}) = \sum_{m<n} \sigma_{mn}[a_{mn}(q_{mn})]^2 |q_{mn}|^2. \tag{4.4}$$

Here, $\sigma_{mn}$ is the interface energy density of the grain boundary, separating $m$ and $n$. Both the $\phi_m$ and $\phi_n$ grains can be chosen from either phase set in Eq. 4.2 or 4.3. Else, one grain $(\phi_m)$ from set 4.2 and another grain $(\phi_n)$ from set 4.3 can be considered as $\left(\alpha_m \in \{1, 2, ..., N_\alpha\} \text{ and } \beta_n \in \{1, 2, ..., N_\beta\}\right)$. The grain boundary energy term $\sigma_{\alpha_i \alpha_j}$, $\sigma_{\beta_i \beta_j}$ can be used to represent the energy density of the $\alpha_i/\alpha_j$ and $\beta_i/\beta_j$ boundaries, respectively. The anti-phase boundary between the $\alpha_i$ and $\beta_i$ grains can be denoted as $\sigma_{\alpha_i \beta_i}$. In the present study, it is generally assumed that $a_{mn}(q_{mn}) = 1$, to model isotropic systems.

In Eqn. 4.4, $a_{mn}$ is expressed as a function of the generalized gradient vector $q_{mn}$, which is written as

$$q_{mn} = \phi_m \boldsymbol{\nabla}\phi_n - \phi_n \boldsymbol{\nabla}\phi_m. \tag{4.5}$$

Furthermore, a multi-obstacle potential $w(\boldsymbol{\phi})$ is used, including higher order terms:

$$w(\boldsymbol{\phi}) = \frac{16}{\pi^2} \sum_{m<n} \sigma_{mn}\phi_m\phi_n + \sum_{m<n} \sigma_{mno}\phi_m\phi_n\phi_o. \tag{4.6}$$

The first term in the above equation is considered to sum all possible interfaces involved in the system. During the evolution, the second term $\phi_m \phi_n \phi_o$ additionally prevents the formation of a 'spurious' or third phase in the grain boundary, which is also referred to as 'ghost' phase. Sharp minima are assigned to the bulk phases (grains) by setting $w(\boldsymbol{\phi})$ to $\infty$, if $\boldsymbol{\phi}$ is not on the Gibbs simplex, which is defined by

$$\mathcal{G} = \left\{ \boldsymbol{\phi} \in \mathbb{R}^N : \sum_m \phi_m = 1, \phi_m \geq 0 \right\}. \tag{4.7}$$

The numerical and computational advantage of using a multi-obstacle potential was reported in [92]. The present study focuses exclusively on the isotropic evolution of phases or grains, where the crystallographic orientation of the grains and the influence of the stored energy are ignored. We write the grand potential density $\boldsymbol{\Psi}$ as an interpolation of the individual grand potential densities $\Psi_\alpha$, where $\Psi_\alpha$ are the functions of the chemical potential $\boldsymbol{\mu}$ and of the temperature $T$ in the system:

$$\boldsymbol{\Psi}(T, \boldsymbol{\mu}, \boldsymbol{\phi}) = \sum_{\alpha=1}^N \Psi^\alpha(T, \boldsymbol{\phi}) h_\alpha(\boldsymbol{\phi}), \tag{4.8}$$

with

$$\Psi_\alpha(T, \boldsymbol{\mu}) = f_\alpha(c^\alpha(\boldsymbol{\mu}), T) - \sum_{i=1}^{K-1} \mu_i c_i^\alpha(\boldsymbol{\phi}, T), \tag{4.9}$$

where $f_\alpha(c^\alpha(\boldsymbol{\mu}), T)$ is the free energy density of the phase $\alpha$, and $h_\alpha(\phi)$ is an interpolation function, chosen to be a third order polynomial in $\phi_m$. The concentration $c_i^\alpha(\boldsymbol{\mu}, T)$ is an inverse of the function $\mu_i^\alpha(c, T)$, for every phase $\alpha$ and component $i$, $i = 1, 2, ...., K$. Using $\frac{\partial \Psi(T, \mu, \phi)}{\partial \mu_i} = -c_i$, the following relation can be derived from Eqn. 4.9:

$$c_i = \sum_{\alpha=1}^N c_i^\alpha(\boldsymbol{\mu}, T) h_\alpha(\boldsymbol{\phi}). \tag{4.10}$$

As the system under consideration is a two-component system, we reduce the chemical potential vector $\boldsymbol{\mu}$ to $\mu$, which defines an independent chemical potential with respect to $\boldsymbol{c}$. As defined in Eq. 4.2 and 4.3, the phase-field vector contains two individual phases: $\boldsymbol{\phi} = (\boldsymbol{\phi}_\alpha, \boldsymbol{\phi}_\beta)$. The chemical energies of the respective phases are constructed using the parabolic type of functions:

$$f(\phi, c) = f^\alpha h(\phi_\alpha) + f^\beta h(\phi_\beta), \tag{4.11}$$

where

$$f^\alpha = A_\alpha(c - c_{eq}^\alpha)^2 \tag{4.12}$$
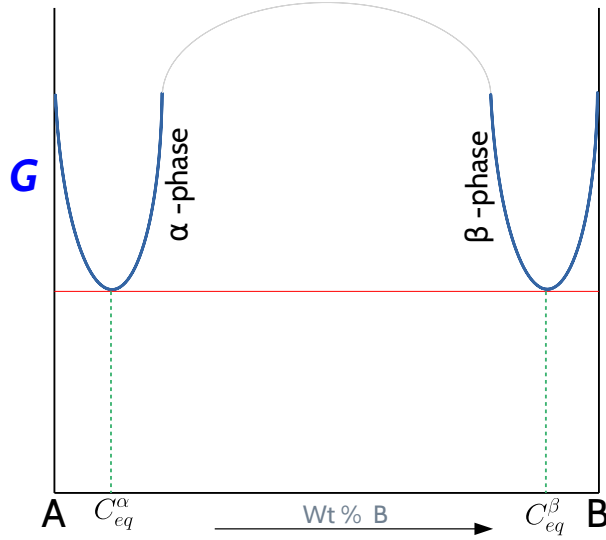
*Figure 4.2: Schematic representation of two-phase equilibrium in the binary system for a given temperature. The chemical potentials of the phases are equal at their equilibrium composition.*

$$f^\beta = B_\beta(c - c_{eq}^\beta)^2, \tag{4.13}$$

and where the coefficients of $A_\alpha$ and $B_\beta$ can be used to determine the steepness of the parabolic free energy. $c_{eq}^\alpha$ and $c_{eq}^\beta$ are the equilibrium compositions of the $\alpha$ and $\beta$ phase. A schematic illustration of the free energy construction appears in Fig. 4.2. A similar type of simple parabolic free energy construction was used in multiphase coarsening studies [105, 106].

For each concentration field $c_i$, the concentration field is obtained from the set of $K-1$ independent concentration variables, using a mass conservation equation, where K is the number of components in the system. The evolution equation for the conserved concentration fields can be expressed as follows:

$$\frac{\partial c_i}{\partial t} = \boldsymbol{\nabla} \cdot \Big( \sum_{j=1}^{K-1} M_{ij}(\boldsymbol{\phi}) \nabla \mu_j \Big). \tag{4.14}$$

Here, $M_{ij}(\boldsymbol{\phi})$ is the mobility of the interface, formulated as follows by an interpolation of the individual phase mobilities:

$$M_{ij}(\boldsymbol{\phi}) = \sum_{\alpha=1}^{N-1} M_{ij}^\alpha g_a(\boldsymbol{\phi}). \tag{4.15}$$

Each of the $M_{ij}^\alpha$ mobilities is defined using the expression

$$M_{ij}^\alpha = D_{ij}^\alpha \Big( \frac{\partial c_i^\alpha(\boldsymbol{\mu}, T)}{\partial \mu_j} \Big). \tag{4.16}$$

The function $g_\alpha(\boldsymbol{\phi})$ interpolates the mobilities. $D_{ij}^\alpha$ are the interdiffusivities in each phase $\alpha$. For both phases, a constant value is assigned to the bulk diffusivity $D$. Both equations,

Eqn. 4.15 and Eqn. 4.16, require information about the chemical potential $\boldsymbol{\mu}$. The evolution equation for the nonconserved $N$ phase-field variables ($\phi_m, m = 1, ...., N$) can be written as

$$\tau\epsilon\frac{\partial\phi_m}{\partial t} = \epsilon\left[\boldsymbol{\nabla}\cdot\frac{\partial a(\boldsymbol{\phi}, \boldsymbol{\nabla}\boldsymbol{\phi})}{\partial\boldsymbol{\nabla}\phi_m} - \frac{\partial a(\boldsymbol{\phi}, \boldsymbol{\nabla}\boldsymbol{\phi})}{\partial\phi_m}\right] - \frac{1}{\epsilon}\frac{\partial w(\boldsymbol{\phi})}{\partial\phi_m} - \frac{\partial\boldsymbol{\Psi}(T, \boldsymbol{\mu}, \boldsymbol{\phi})}{\partial\phi_m} - \lambda. \quad (4.17)$$

Furthermore, the Lagrange multiplier $\lambda$ is incorporated into the evolution equation 4.17, so as to impose the constraint $\sum_{\alpha=1}^{N}\phi_\alpha = 1$, which then reads as

$$\lambda = \frac{1}{N}\sum_{m=1}^{N}\left[\epsilon\left[\boldsymbol{\nabla}\cdot\frac{\partial a(\boldsymbol{\phi}, \boldsymbol{\nabla}\boldsymbol{\phi})}{\partial\boldsymbol{\nabla}\phi_m} - \frac{\partial a(\boldsymbol{\phi}, \boldsymbol{\nabla}\boldsymbol{\phi})}{\partial\phi_m}\right] - \frac{1}{\epsilon}\frac{\partial w(\boldsymbol{\phi})}{\partial\phi_m}\right]. \quad (4.18)$$

In order to ensure the numerical efficiency of the evolution, the involved parameters are appropriately nondimensionalized. The nondimensionalization scheme involved in the present work has already been successfully adopted in numerous theoretical analyses [104, 107].

## 4.0.2 Ternary (three-component) three-phase polycrystalline system

In the present study, the investigation of a ternary three-phase polycrystalline system is based on the grand-potential formulation. A schematic representation of our simulation setup is shown in figure 4.3. We consider a polycrystalline structure which consists of a number of $N(= N_\alpha + N_\beta + N_\gamma)$, $\alpha$, $\beta$ and $\gamma$ phase grains with different orientations. The orientation of each phase is represented as

$$\boldsymbol{\phi_\alpha} = (\phi_{\alpha_1}, \phi_{\alpha_2}, \phi_{\alpha_3}, ...., \phi_{\alpha_{N_\alpha}}) \quad (4.19)$$

$$\boldsymbol{\phi_\beta} = (\phi_{\beta_1}, \phi_{\beta_2}, \phi_{\beta_3}, ...., \phi_{\beta_{N_\beta}}) \quad (4.20)$$

$$\boldsymbol{\phi_\gamma} = (\phi_{\gamma_1}, \phi_{\gamma_2}, \phi_{\gamma_3}, ...., \phi_{\gamma_{N_\gamma}}). \quad (4.21)$$

The gradient energy $a(\boldsymbol{\phi}, \boldsymbol{\nabla}\boldsymbol{\phi})$ in Eqn. 4.1 can be expressed by the summation of the pairwise interaction terms between the grains $m$ and $n$:

$$a(\boldsymbol{\phi}, \boldsymbol{\nabla}\boldsymbol{\phi}) = \sum_{m<n}\sigma_{mn}[a_{mn}(q_{mn})]^2|q_{mn}|^2. \quad (4.22)$$

Here, $\sigma_{mn}$ is the interface energy density of the grain boundary, separating $m$ and $n$. Both the $\phi_m$ and $\phi_n$ grains can be chosen from either phase set in Eq. 4.19 or 4.20 or 4.21. Else, one grain ($\phi_m$) from set Eq. 4.19 and another grain ($\phi_n$) from set Eq. 4.20 or 4.21 can be considered as $\left(\alpha_m \in \{1, 2, ..., N_\alpha\}, \beta_n \in \{1, 2, ..., N_\beta\}\right)$ or $\gamma_n \in \{1, 2, ..., N_\gamma\}$). The grain boundary energy term $\sigma_{\alpha_i\alpha_j}$, $\sigma_{\beta_i\beta_j}$ and $\sigma_{\gamma_i\gamma_j}$ can be used to represent the energy density
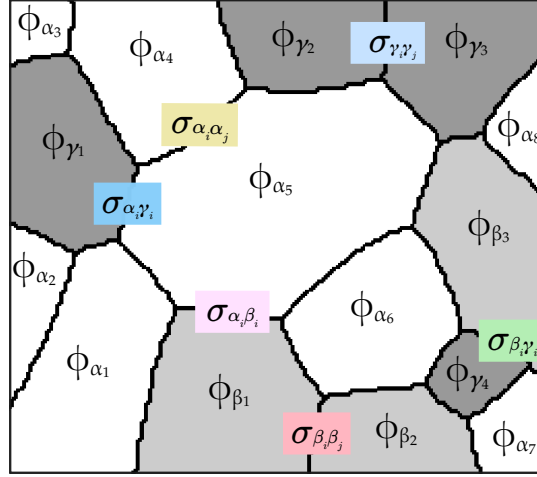
*Figure 4.3: Schematic representation of the ternary (A, B and C), three-phase($\alpha$, $\beta$ and $\gamma$) poly-crystalline microstructure. Each phase can take an appropriate number of grains depending on the initial volume fraction.*

of the $\alpha_i/\alpha_j$, $\beta_i/\beta_j$ and $\gamma_i/\gamma_j$ boundaries, respectively. The anti-phase boundary between the different phased grains can be expressed as $\sigma_{\alpha_i\beta_i}$, $\sigma_{\alpha_i\gamma_i}$ and $\sigma_{\beta_i\gamma_i}$. In the present study, it is generally assumed that $a_{mn}(q_{mn}) = 1$, to model isotropic systems.

As the system under consideration is a ternary system, we reduce the chemical potential vector $\boldsymbol{\mu}$ to $\mu$, which defines an independent chemical potential with respect to $\boldsymbol{c}$. As defined in Eq. 4.1, the phase-field vector contains three individual phases: $\boldsymbol{\phi} = (\boldsymbol{\phi}_\alpha, \boldsymbol{\phi}_\beta, \boldsymbol{\phi}_\gamma)$. The chemical energies of the respective phases are constructed using the paraboloid type of functions:

$$f(\phi, c) = f^\alpha h(\phi_\alpha) + f^\beta h(\phi_\beta) + f^\gamma h(\phi_\gamma), \tag{4.23}$$

The free energies of the given phases are described by the following form (for example $\alpha$-phase case),

$$f_\alpha(c_A, c_B, c_C) = \tilde{A}_\alpha c_A^2 + \tilde{B}_\alpha c_B^2 + \tilde{C}_\alpha c_C^2 + \tilde{D}_\alpha c_A c_B + \tilde{E}_\alpha c_B c_C + \tilde{F}_\alpha c_C c_A$$
$$+ \tilde{G}_\alpha c_A + \tilde{H}_\alpha c_B + \tilde{I}_\alpha c_C + \tilde{J}_\alpha,$$

where $c_A$, $c_B$, $c_C$ are the concentrations of A, B, and C, respectively. The $\tilde{A}$, $\tilde{B}$, $\tilde{C}$, $\tilde{D}$, $\tilde{E}$, $\tilde{F}$, $\tilde{G}$, $\tilde{H}$, $\tilde{I}$ and $\tilde{J}$ are the components at specific temperature. Taking the constraint $c_A + c_B + c_C = 1$, we can rearrange the above equation as follows.

$$f_\alpha = A_\alpha(c_A - c_{A\alpha}^{eq})^2 + B_\alpha(c_B - c_{B\alpha}^{eq})^2 + C_\alpha\left[(c_A - c_{A\alpha}^{eq})(c_B - c_{B\alpha}^{eq})\right] + D_\alpha \tag{4.24}$$

In this study, we assume that swapping of $A$ and $B$ do not change the free energy function. Hence, the coefficients of the paraboloid curve can be taken as $A_\alpha = B_\alpha$. It provides conic section that has the same property of symmetry. Typical paraboloid type free energy construction for a given temperature is schematically presented in Fig. 4.4.
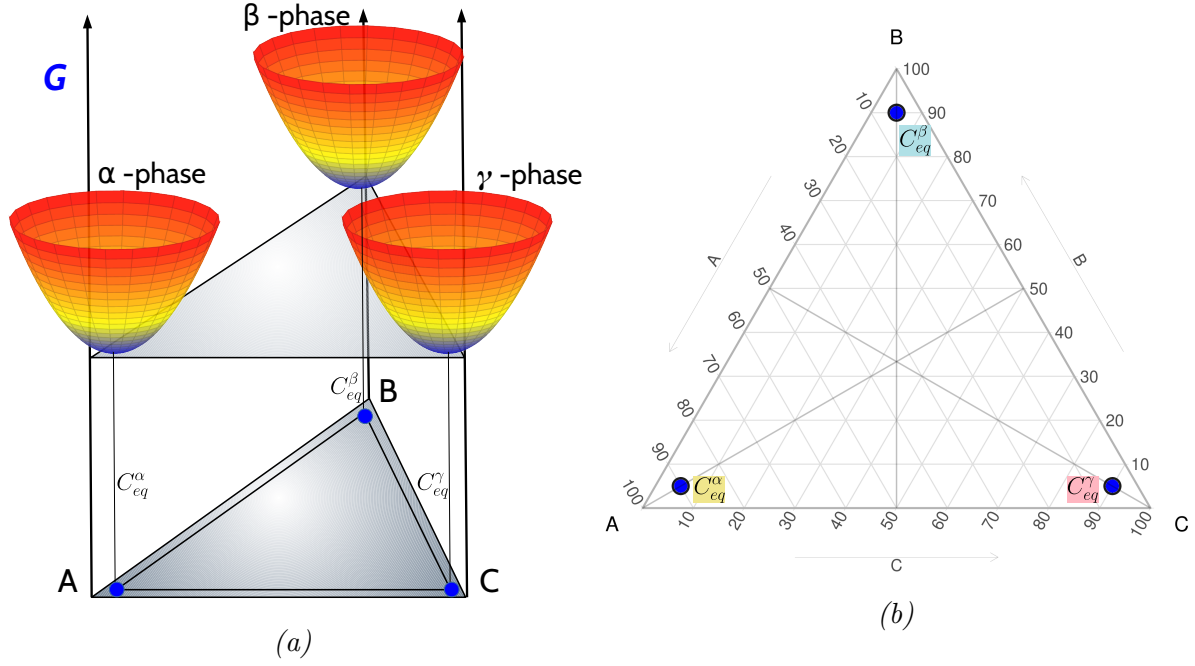
*Figure 4.4: Schematic representation of free energy construction for a given temperature. The chemical potentials of the phases are equal at their equilibrium composition. A three- phase equilibrium in the ternary system (a) 3-D projection (b) 2-D projection*

$$f_\alpha = A_\alpha \left[ (c_A - c_{A_\alpha}^{eq})^2 + (c_B - c_{B_\alpha}^{eq})^2 \right] + C_\alpha \left[ (c_A - c_{A_\alpha}^{eq})(c_B - c_{B_\alpha}^{eq}) \right] + D_\alpha \qquad (4.25)$$

To determine the chemical potential, grand-chemical potential and the relation between concentration and chemical potential, we start by equating the derivatives with respect to the composition as,

$$\frac{\partial f_\alpha}{\partial c_A} = \mu_A = 2A_\alpha(c_A - c_{A_\alpha}^{eq}) + C_\alpha(c_B - c_{B_\alpha}^{eq}) \qquad (4.26)$$

$$\frac{\partial f_\alpha}{\partial c_B} = \mu_B = 2A_\alpha(c_B - c_{B_\alpha}^{eq}) + C_\alpha(c_A - c_{A_\alpha}^{eq}) \qquad (4.27)$$

$$c_A = c_{A_\alpha}^{eq} + \frac{2A_\alpha\mu_A - C_\alpha\mu_B}{4A_\alpha^2 - C_\alpha^2} \qquad (4.28)$$

$$c_B = c_{B_\alpha}^{eq} + \frac{2A_\alpha\mu_B - C_\alpha\mu_A}{4A_\alpha^2 - C_\alpha^2} \qquad (4.29)$$

$$\frac{\partial c_A}{\partial \mu_A} = \frac{2A_\alpha}{4A_\alpha^2 - C_\alpha^2} \qquad (4.30)$$

$$\frac{\partial c_A}{\partial \mu_B} = \frac{-C_\alpha}{4A_\alpha^2 - C_\alpha^2} \qquad (4.31)$$

$$\frac{\partial c_B}{\partial \mu_A} = \frac{-C_\alpha}{4A_\alpha^2 - C_\alpha^2} \qquad (4.32)$$

$$\frac{\partial c_B}{\partial \mu_B} = \frac{2A_\alpha}{4A_\alpha^2 - C_\alpha^2} \tag{4.33}$$

$$\omega_\alpha = f_\alpha - \mu_A c_A - \mu_B c_B \tag{4.34}$$

$$\omega_\alpha = \left( A_\alpha \left[ \left( \frac{2A_\alpha \mu_A - C_\alpha \mu_B}{4A_\alpha^2 - C_\alpha^2} \right)^2 + \left( \frac{2A_\alpha \mu_B - C_\alpha \mu_A}{4A_\alpha^2 - C_\alpha^2} \right)^2 \right] + \right.$$
$$\left. C_\alpha \left[ \left( \frac{2A_\alpha \mu_A - C_\alpha \mu_B}{4A_\alpha^2 - C_\alpha^2} \right) \left( \frac{2A_\alpha \mu_B - C_\alpha \mu_A}{4A_\alpha^2 - C_\alpha^2} \right) \right] + D_\alpha \right)$$
$$- \left[ 2A_\alpha \left( \frac{2A_\alpha \mu_A - C_\alpha \mu_B}{4A_\alpha^2 - C_\alpha^2} \right) + C_\alpha \left( \frac{2A_\alpha \mu_B - C_\alpha \mu_A}{4A_\alpha^2 - C_\alpha^2} \right) \right] \left( c_{A_\alpha}^{eq} + \frac{2A_\alpha \mu_A - C_\alpha \mu_B}{4A_\alpha^2 - C_\alpha^2} \right)$$
$$- \left[ 2A_\alpha \left( \frac{2A_\alpha \mu_B - C_\alpha \mu_A}{4A_\alpha^2 - C_\alpha^2} \right) + C_\alpha \left( \frac{2A_\alpha \mu_A - C_\alpha \mu_B}{4A_\alpha^2 - C_\alpha^2} \right) \right] \left( c_{B_\alpha}^{eq} + \frac{2A_\alpha \mu_B - C_\alpha \mu_A}{4A_\alpha^2 - C_\alpha^2} \right)$$

and where the coefficients of $A_\alpha$, $C_\alpha$ and $D_\alpha$ can be used to determine the steepness of the paraboloid free energy. $c_{A_\alpha}^{eq}$ and $c_{B_\alpha}^{eq}$ are the equilibrium compositions of the components $A$ and $B$ for $\alpha$ phase. A similar type of paraboloid free energy construction was used for the remaining $\beta$ and $\gamma$ phases. For all three phases, a constant value is assigned to the bulk diffusivity $D$. To derive the evolution equations for the conserved concentration field and individual phase, the variational derivatives are derived in the form of Eqn. 4.14 and 4.17, respectively.

# Part III
# Results and Discussion :
# Grain growth phenomena in
# single-phase materials

# Chapter 5

# Formation of first-neighbor topological clusters during the isotropic grain growth

## 5.1 Introduction

Understanding the microstructural evolution in a polycrystalline material is of primary interest to both engineers and material scientists alike. Although superficially, the evolution of the polycrystalline material is governed by the simple principle of reducing the grain boundary area, several factors have been reported to play an influencing role [20]. One such factor with a considerable influence on the evolution is the topological nature of the grains. Mathematically, topology, in itself, is an extensive topic. However, in the context of the polycrystalline materials, these studies are often restricted to the number of faces observed in a grain [108, 109, 110, 111, 112]. This topological feature is referred to as face-class of a grain which is replaced by edge-class in 2-dimensional cases. Irrespective of the dimensions, this topological feature relates directly to the number of surrounding grains. For instance, in 3-D, the face-class of a grain is equal to the number of grains constituting its first neighbor. Thus, when compared to size, this feature inherently includes the nature of its surrounding to certain extent [113, 114, 115]. Seminal work of Aboav-weaire considers face-class of an individual grain and relates it to that of its neighbor[116, 117]. Furthermore, the growth rate of a grain in relation to its topological feature is captured by von Neumanns -Mullins law [118, 119]. This relation, originally postulated for 2D, has been extended to three-dimension by MacPherson and Srolovitz[120]. Moreover, while rendering an extension to Neumanns-Mullins result, this work recognizes and includes the influence of geometrical features like mean-width on the kinetics of grain growth. Despite numerous reports on the topological behavior of the grains, a comprehensive understanding on the temporal evolution of face-class of the grains and its
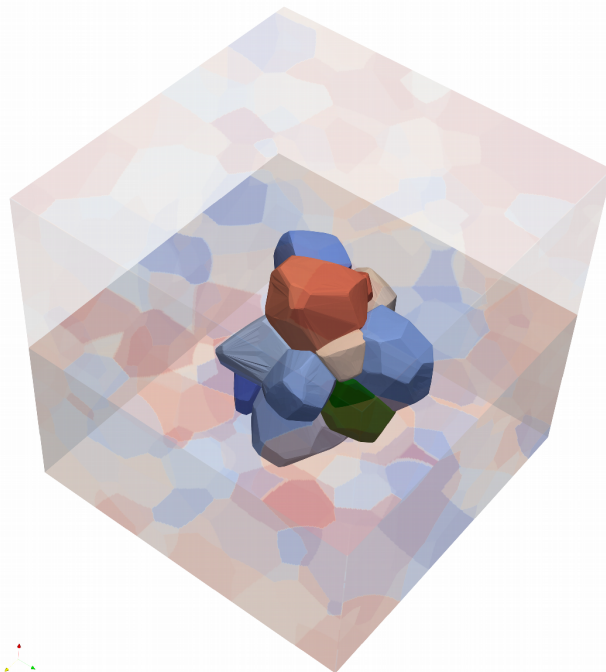
*Figure 5.1: Distribution of grains in a section of 3D simulation domain with a grain and its first-neighbor highlighted.*

neighbors is yet to be attained [121, 122]. Understandably, this inadequacy is primarily due to enormous data-sets that emerge from the evolution of large numbers of grains. Quantitative handling of these data-sets which include both geometrical and topological evolution of the grain and its neighbors is rarely pursued, and is replaced by appropriate mathematical treatment. Although substantial understanding has been gained by this approach, the replacing mathematical-treatments are specifically formulated to address the problem at hand [87, 123]. On the other hand, studies considering fewer number of grains to circumvent the complexity of handling huge data deviate noticeably from the expected analytical predictions [17]. Thus, unique approach is required to analyze the topological evolution quantitatively considering appropriate number of grains. In this study, the topological evolution of the grains along with its neighbours are quantitatively presented using an appropriate statistical tool [124]. Although this well-known tool called heat-maps is hardly used in the analysis of grain evolution, this work intends to provide a framework by highlighting its importance.

## 5.2    Simulation domain set-up

The distribution of grains, in both 2-D and 3-D simulations, is implemented by a Voronoi algorithm wherein the points corresponding to the grains are randomly placed in the domain and allowed to initialize. A 3-D representation of the final arrangements of the

grains obtained by this algorithm is shown in Fig. 5.1. In order to render an indicative statistical study, domains of sizes $4000{\times}4000$ and $870{\times}500{\times}960$ gridpoints with 60000 and 75000 grains are analyzed in 2-D and 3-D, respectively. A separate 3-D simulation of 3000 grains, in a $300 \times 300 \times 300$ domain, with finer time steps is considered to describe certain aspects of the transformations that demand intense investigations. In all simulations, the grain boundary energies ($\sigma_{\alpha\beta}$) and the mobilities ($\tau$) are assumed isotropic and equal to 1.0.

The variational derivative of the functional, $\mathcal{F}$ with respect to the phase-field variable $\phi_\alpha$ and phase-field gradient $\boldsymbol{\nabla}\phi_\alpha$ generates scalar and vector respectively. Thus, an appropriate numerical scheme is adopted to optimize the evaluation. The evolution equation is discretized in an equidistant grid of cell sizes, $\Delta x = \Delta y = \Delta z = 1.0$ by a finite difference method. A consistency within the simulations is attained by fixing the length scale of the diffuse interface width to $\epsilon = 4\Delta\mathrm{x}$. Furthermore, simulations are made computationally efficient by implementing a *Locally reduced order parameter optimization (LROP)* which restricts the number of order parameters solved at each grid point.

## 5.2.1   Identifying the geometrical and topological features of the grain

Topological analysis of grain growth relies substantially on the identification of the face-classes. Thus, to dynamically capture the change in the face-class of the individual grain during its evolution, an approach similar to Sun et al [125] is adapted. Grid points that bear an order parameter are treated as voxels occupying the lattices of simple cubic packing [126]. This depiction of the grains based on grid points in a cube lattice yields stepped faces as shown in the Fig. 5.2a.

Each voxel in a grain is surrounded by 26 other voxels, of which, 6 share the faces, 12 share the edges and 8 share the corners. Within a grain, these contiguous voxels bear identical integers (order parameters). Thus, ambiguity in the identity of any one of these 26 voxels signifies grain boundary. To ascertain a face, the nature of the 6 face-sharing voxels is examined. If any of these six voxels differs from the central voxel, then the corresponding face shared by the non-identical voxel is characterized as the grain face. Therefore, in Fig. 5.2b, face shared with the voxel 3 is the face of the grain, considering all the other voxels are identical. Extending this analysis across the recognized grain-boundary voxels ascertains the face-class of the grain. Identification of the edges necessitates finer probing of the surrounding voxels, particularly, regarding two face-sharing and the abutting voxels. As shown in Fig. 5.2c, when two of three contiguous voxels are different, then the shared edge represents the edge of the grain. Furthermore, in the present study, the geometrical feature of the grain is restricted to its volume. Voxels that belong to a grain, characterized by identical order parameter, is quantified to
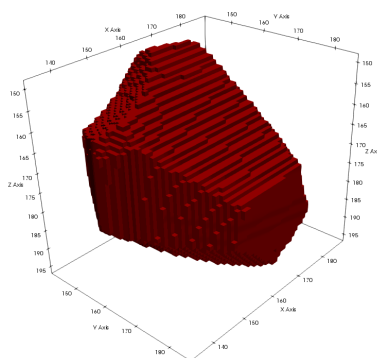
*(a)*
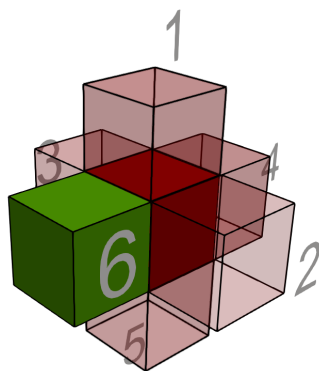


*(b)*
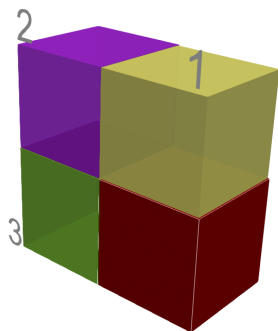


*(c)*

*Figure 5.2: (a) Voxel (or grid point) based representation of a grain wherein the faces appear rugged instead of smooth. (b) The central voxel is located along the face of the grain with five identical face-sharing voxels and one voxel of different order parameter numbered with label 6. Face shared with voxel 6 coincides with the face of the grain. (c) Voxel set-up considered to determine the edge of a grain. To form an edge, two face-sharing voxels 1 and 3 are in contact with an abutting voxel 2 with at least two of three voxels different from the central voxel.*

ascertain its volume.

## 5.3   Results and discussions

### 5.3.1   Extended Aboav-Weaire Law

A single grain chosen arbitrarily from the 3-dimensional simulation domain and its first neighbors are illustrated in Fig. 5.3a. The positions of the surrounding grains are represented by markings, which correspond to the contacting faces. Although the number of grains constituting the first neighbor depends on the face-class (number of faces) of the individual grain, this representation reveals that the face-classes of the surrounding grains vary significantly. Fig. 5.3a is rescaled for the ease of representation, the sizes of the neighboring grains are also different.

An analytical expression relating the face-class of an individual grain to that of its neighbors has been postulated based on 2-D experimental observations [116, 117]. This relation, often referred to as Aboav-Weaire law, reads

$$m(f) = 6 - a + \frac{6 \cdot a + \mu}{f} \tag{5.1}$$

Aboav-Weaire law has been extended to the third dimension in [130] and is written as,

$$m(f) = \langle f \rangle - 1 + \frac{\langle f \rangle + \mu_f}{f} \tag{5.2}$$

where $f$ and $m(f)$ refer to the face-class of the individual grain and the average face-class of its neighbors, respectively $\langle f \rangle$ is the average number of faces in the system, $a$ is a constant and $\mu$ is the second moment of the face-class distribution.

The average face-class of all the first neighbors, $m(f)$ in the present 2-D and 3-D simulations is calculated and plotted against the face-class of the grain ($f$) in Fig. 5.3b. Identical shape of the plot suggests that grains with less number of faces are surrounded by few but higher face-class grains, while neighbors of the large face-class grains are numerous with relatively fewer faces. In 2-D, apart from the slight deviation in the smaller face-class grains, complete agreement with the experimental observation [116, 117] is evident. Fig. 5.3c displays observations of 3-D simulation results in comparison with several theoretical and experimental results [121, 17, 131, 132, 128, 129]. A complete coherency is absent due to the complexity of the 3-D evolution. Significant deviation occur considering less number of grains [17, 131]. To avoid any influence of the domain size, a maximum number of grains is considered, which consequently yields an acceptable consistency, of $\langle f \rangle \approx 14$, with the experimental observation [128].
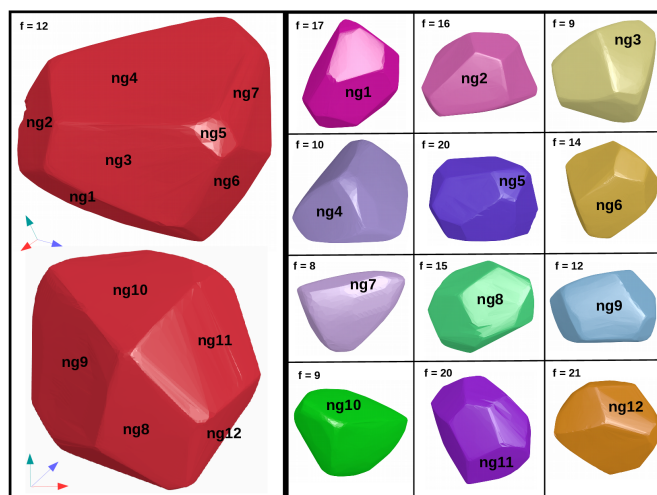
*(a)*
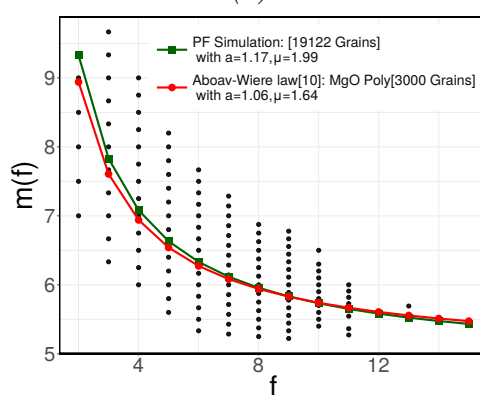


*(b)*
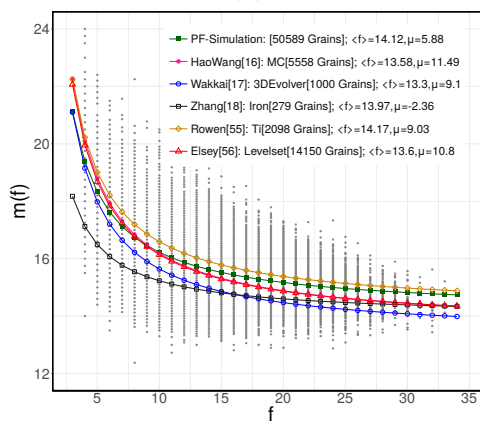


*(c)*

*Figure 5.3: (a) Topological structure of a randomly chosen grain of face-class 12 and its neighbors. The size of the surrounding grains are rescaled for the ease of representation and position is appropriately marked. (b) Average face-class of first-neighbor grains (m(f)) as a function of face-class and in a 2-D simulation is compared with the experimental observation of Aboav et al [116]. (c) f and m(f) distribution in a 3-D simulation domain along with several other existing results which are noticeably non-coherent [121, 122, 127, 128, 129].*

## 5.3.2  Influence of face-class on the kinetics of evolution
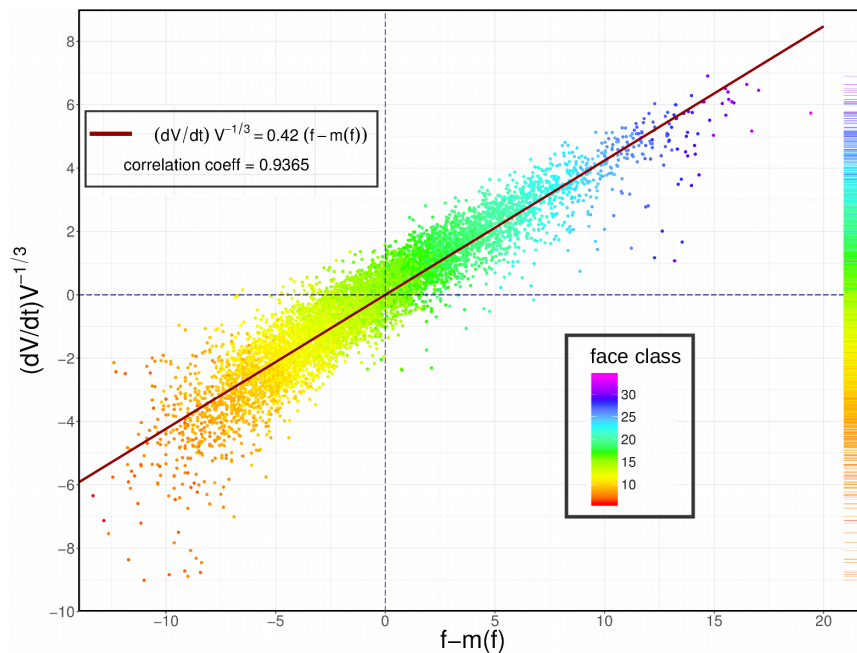


*Figure 5.4: Influence of the topological nature of the grain and its surrounding $(f - m(f))$ on the normalized growth rate, $(dV/dt)V^{-1/3}$.*

Existing experimental and simulation findings suggest that, grain growth involves a competitive interaction between the grain and its nearest neighbors [110, 111, 133, 134, 135, 136]. Influence of this localized topological-atmosphere on the geometrical evolution of the grain expressed as,[121]

$$(dV/dt)V^{-1/3} = CM\gamma(f - m(f))  \qquad (5.3)$$

where the rate of change of volume, $dV/dt$ of a grain is normalized by its voxel-based initial volume,$V$. $M$, $\gamma$ and $C$ correspond to mobility, interfacial energy and fitting constant, respectively. Fig. 5.4 illustrates the transformation rate of the different face-class grains which are distinguished by an appropriate color scheme. This data representing the kinetics of grain-growth is attained by considering two consecutive time-steps, after initialization. X- and Y-axis of this depiction comprise of positive and negative regime to encapsulate both, growth and decay of the grains, respectively. In-keeping with the analytical predictions [137], the grains with the face-class less than the average of its neighbor predominantly decay while grains with $f - m(f) > 0$ grow. Furthermore, it is evident that the rate of transformation is proportional to topological differences between the grain and its neighbor, $f - m(f)$. Parameters that characterize the plot in Fig. 5.4, C and *correlation coefficient* which are 0.42 and 0.9365, respectively, are in thorough compliance with both experimental and theoretical studies [121, 128, 138].

## 5.3.3   Evolution of grains and the influence of first neighbors
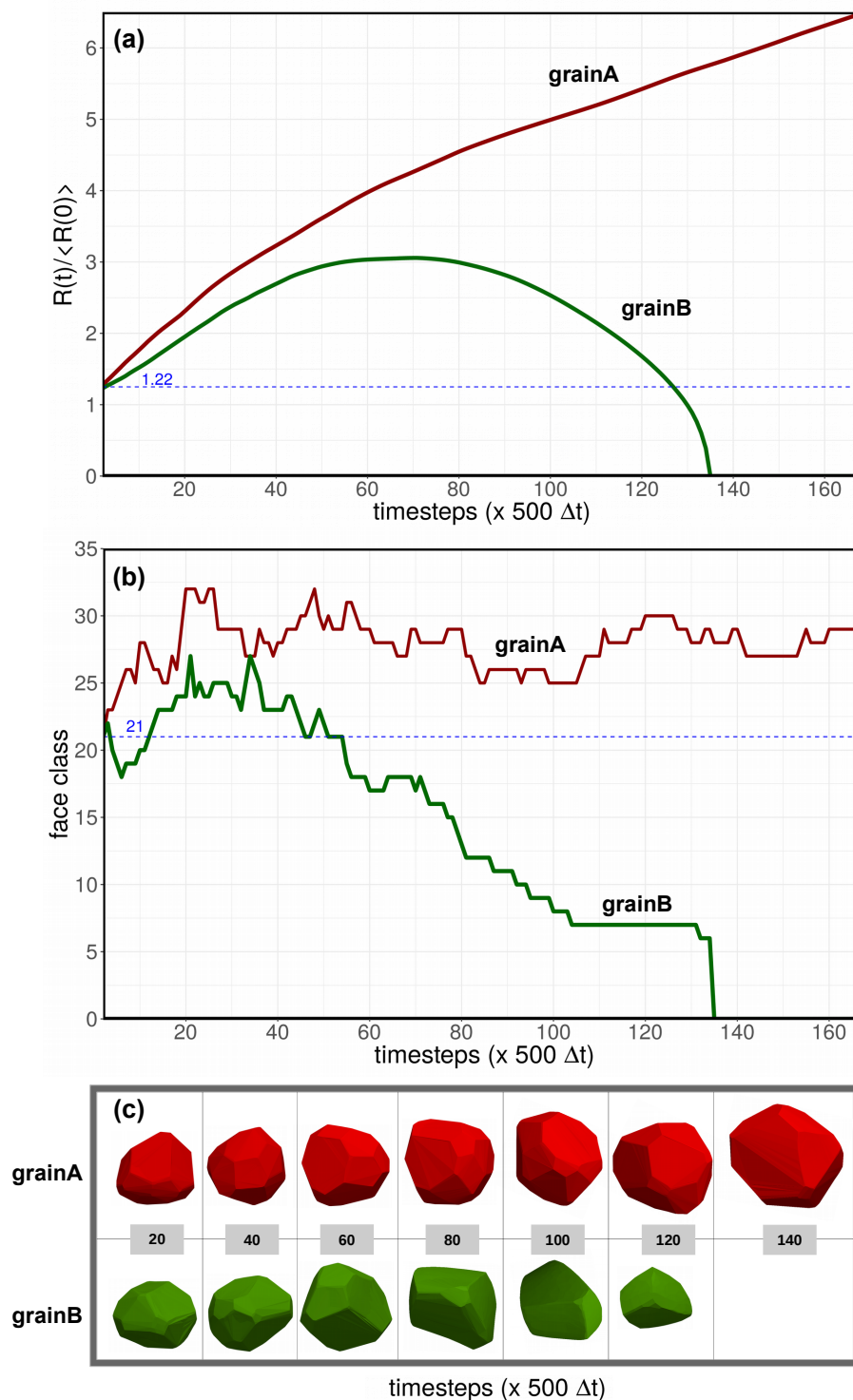


Figure 5.5: (a) Change in the size of the two grains $(R(t)/R(0))$ with identical initial size, $R(0)$ during grain growth. (b) Temporal evolution of the face-class of two topologically similar grains of face-class 21. (c) Visual representation of the topological nature of the identical grains (grainA and grainB) at different time-steps. grainB at time, $t = 140 \times 500\Delta t$ is intentionally left vacant to indicate its disappearance.

A separate 3-dimensional simulation of domain size $300 \times 300 \times 300$ gridpoints with finer time steps and yet, similar parameters is extensively analyzed to describe the geometrical and topological evolution of grains. From the possible 3000 grains, two grains (grainA and grainB) of identical size and face-class are monitored to assess the influence of surrounding first-neighbors. Geometrical evolution of these grains is shown in Fig. 5.5 where $R(0)$ and $R(t)$ correspond to the radii of the grains at time 0 and $t$, respectively. The values of the radii are calculated by considering the grains to be spherical. Gradual increase in size is observed for both grains during the initial stages of the transformation, although the rate of grainA, is noticeably greater than of grainB. As the transformation proceeds, the grain with lower growth rate eventually shrinks and disappears, while its counterpart continues to grow.

Temporal change in the face-class of the grains, grainA and grainB, are discreetly traced to capture the topological evolution illustrated in Fig. 5.5b. Noticeably, the face-class of both grains does not monotonically increase or decrease depending of its geometrical evolution but rather vary haphazardly. Moreover, it is evident that in addition to loss and gain of faces, during certain time intervals, these grains retain face-class without any change. Although, the no-change events are not significantly pronounced, they are significantly dominant in the final stages of the disappearing grain, grainB . Nevertheless, the contrasting behavior exhibited of these topologically and geometrically identical grains indicates the substantial influence of the neighbors on the evolution.

## 5.3.4  Topological evolution of the individual grains

### 5.3.4.1  Face switching events

The topological evolution of grain comprises three distinct events; gain, loss and no-change, often referred to as face switching events [122]. The number density of the different events is plotted against the face-class in Fig. 5.6a. Since the density of the no-change event is dependant on the span of time-steps considered, the graphical representation of this event in overlooked in this analysis. Consistent with the existing study [122], the loss event is numerically dominant over other events irrespective of the face-class. However, irrespective of its nature, both these events are predominantly influenced by the topology of the evolving grain. Interestingly, the disparity between the face-gain and loss events progressively decreases with increase in face-class.

Analysis similar to the switching events with an extensive focus on the behavior of the edges has been previously reported for 2-dimensional case. Sprague et al [139] postulate the affinity of a particular event by introducing $N_i^{I,random}$ representing the expected number of that event for $i$-class grains. Similar approach is extended to calculate the 'switching affinity, $S_i^I$ ' through the following expression,
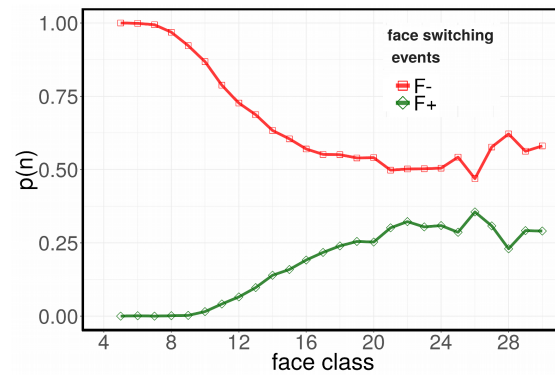
*(a)*
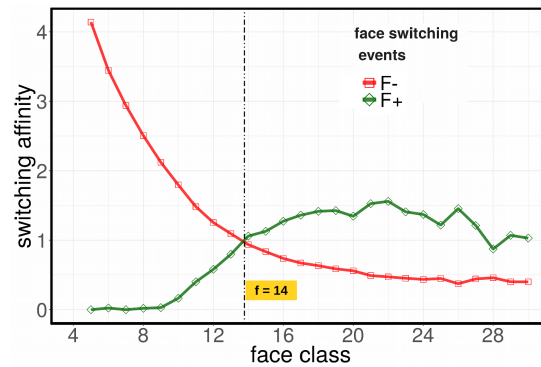


*(b)*
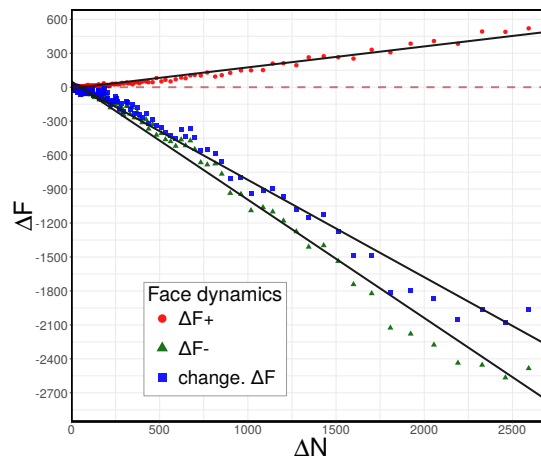


*(c)*

*Figure 5.6: (a) Number-density p(n) based distribution of different face-switching events, which includes face-gain (F+), -loss (F−) and no-change (F0) events, for different face-classes. (b) Inclination towards certain switching events (switching affinity) depending on the face class of the evolving grain. (c) Change in the total number of face, (ΔF) with the disappearance of (ΔN) grains. (ΔF+) and (ΔF−) represent increase and decrease in number of faces, respectively.*

$$S_i^I = \frac{N_i^I}{(N_I)\left(\frac{i.N_i}{\sum_{j=3}^{jmax}(j.N_j)}\right)} \tag{5.4}$$

where $N_i^I$ is the number of grains belonging to face-class $i$ involved in a particular switching event $I$ that includes gain, loss or no-change. $N_I$ represents the total number of switching event $I$, while $i$ and $N_i$(or $j$ and $N_j$) indicate the number of faces and corresponding number of face-class grains respectively. The denominator of the Eqn.(5.4) collectively renders the expected number of events based on the contact, $N_i^{I,random}$ . Affinity, $S_i^I$ of the various switching events for different face-classes is illustrated in Fig. 5.6b. Despite its numerical dominance, Fig. 5.6b suggests that the affinity of the face-loss event, $(F-)$ monotonously decreases with increase in face-class. Additionally, all the face classes above 14 possess a significant preference for face-gain event, $(F+)$. It is also interesting to note that the transition in the preference of face-gain event over face-loss event, which appears at face-class 14 in the present study, is reported to occur at edge-class 6 for 2-D simulations [139].

Total change in the number of faces, $\Delta F$ due to this face-switching events is plotted against the change in the number of grains, $\Delta N$ in Fig. 5.6c. For the ease of representation, the plot is confined to $\Delta N \approx 2600$. Indicative of the previous observation on the numerical dominance of the face-loss event, $(F-)$, the total change in the number of faces,$\Delta F$ lies in the negative regime. Furthermore, from plot 5.6c, the number of face-gain and loss event can be related to the change in number of grains by $\Delta F^+ = \kappa_1 \Delta N$ and $\Delta F^- = \kappa_2 \Delta N$, respectively, where $\kappa_1$ and $\kappa_2$ are fitting parameters. Although, the values of $\kappa_1$ and $\kappa_2$, which depends the initial number of grains, vary considerably when to compared to existing study, the ratio of $\kappa_2/\kappa_1(= -4.644)$ which indicates the relative dominance of face-loss events over gain events is in exact agreement [122].

### 5.3.4.2   Influence of topological evolution on life-span of a grain

Extensive analysis of the topological evolution in Fig. 5.5 indicates that, despite the face-loss events in both the grains, face-class of the surviving grain, grainA is sustained above certain range. In other words, a drastic decrease of face class is seldom observed in grainA and its evolution is mostly confined above face-class 25. For grainB, no face-gain event is observed after the grain reaches the face class 14. Thus, to understand the influence of this topological evolution on the life-span of the grains, a 'Face-switching average, $\langle F_\rho^\alpha \rangle$' is calculated by

$$\langle F_\rho^\alpha \rangle = \frac{\sum_{i=1}^{t_{life}} F_i^\alpha}{t_{life}} \tag{5.5}$$

where $F_i$ is the face class of grain $\alpha$ at time step $i$ and $t_{life}$ is its life-span. This face-switching average is further normalized by $F_\rho^\chi$ expressed as

$$\langle F_\rho^\chi \rangle = \frac{1}{t_{final}} \sum_{i=1}^{t_{final}} \frac{F_i^\chi}{N_i^\chi} \tag{5.6}$$
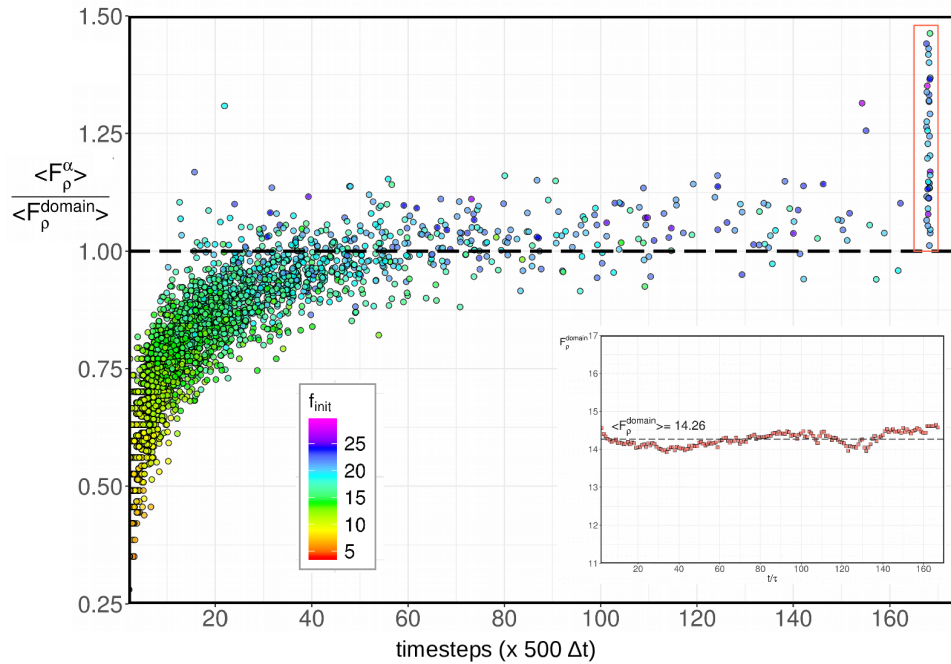
*Figure 5.7: Influence of the topological evolution, captured by the normalized face-switching average,$\frac{\langle F_\rho^\alpha \rangle}{\langle F_\rho^X \rangle}$, on the life span, $t_{life}$ of the grains.*

where the ratio of the total number of faces $(F_i^X)$ to the total number of grains $(N_i^X)$ in Eqn. (5.6) is the mean face-class of the entire simulation domain at time step $i$. The normalized face parameter $\frac{\langle F_\rho^\alpha \rangle}{\langle F_\rho^X \rangle}$ of all the grains and its corresponding life-span is plotted in Fig. 5.7. Increase in the life-span of the grains with increase in normalized face-switching average and the value of $\frac{\langle F_\rho^\alpha \rangle}{\langle F_\rho^X \rangle} > 1$ for all the surviving grains(highlighted in red in Fig. 5.7) cumulatively indicate the following trend. The longer a grain away from the face-class(s) range of $\langle F_\rho^X \rangle \approx 14$ during its topological evolution, stays the greater is its life expectancy. Furthermore, the almost time-invariant nature of the mean face-class $\left(\frac{F_i^X}{N_i^X}\right)$ captured in sub-plot of Fig. 5.7 suggests that the life-span of the grains is prolonged if the respective topological evolution is predominantly beyond $\frac{F_i^X}{N_i^X} \approx 14$. In other words, life expectancy of the grains with the topological evolution around and below face class 14 is considerably short. Although not conclusively, it can be said that face-class 14 appears to be the 'dead-zone' of the topological evolution where a recovering of grains from it is almost improbable.

## 5.3.5 Topological evolution of first neighbors

### 5.3.5.1 Heat-map representation of first neighbors

In most analysis, like in Aboav-Weaire law, face-classes of the first neighbors are averaged to provide a cumulative understanding [116, 117, 140]. Yet, this topological feature can be quantitatively represented as a matrix, wherein the face-class of an individual grain is
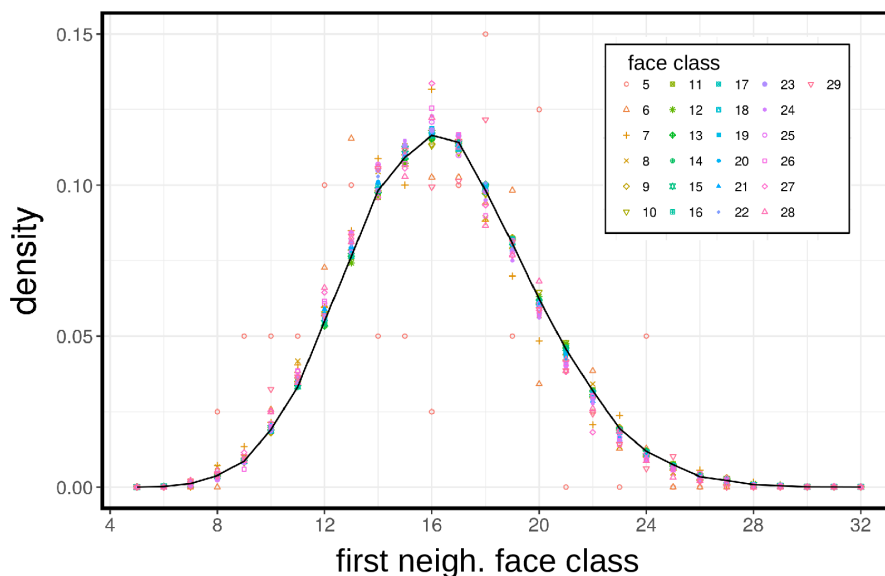
*(a)*
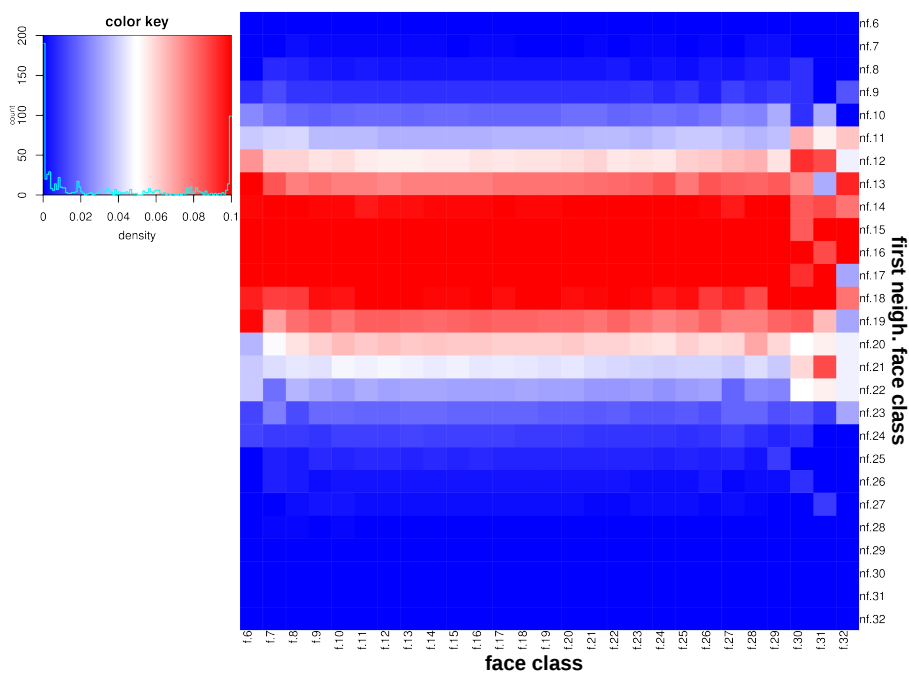


*(b)*

*Figure 5.8: (a) Conventional representation of the topological distribution of the first-neighbors in a large-scale 3-D domain with ≈ 75000 grains. (b) Same data as in (a) depicted in the form of heat-map with individual face-classes and illustrating the topological nature of its first-neighbors represented along the row and columns respectively. The color-scheme and corresponding quantitative values are presented in the sub-set.*

considered as the row and the number density of different face-classes that constitute the first neighbor is presented along the column. These data if represented as in Fig. 5.8a yield approximately 30 plots for each time-step which needs to be thoroughly analyzed to
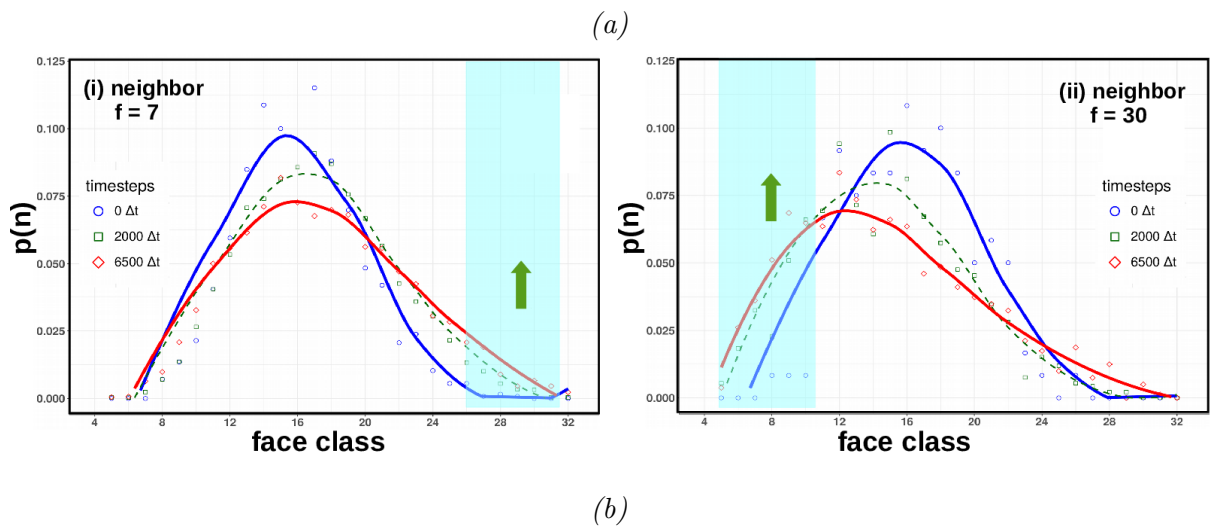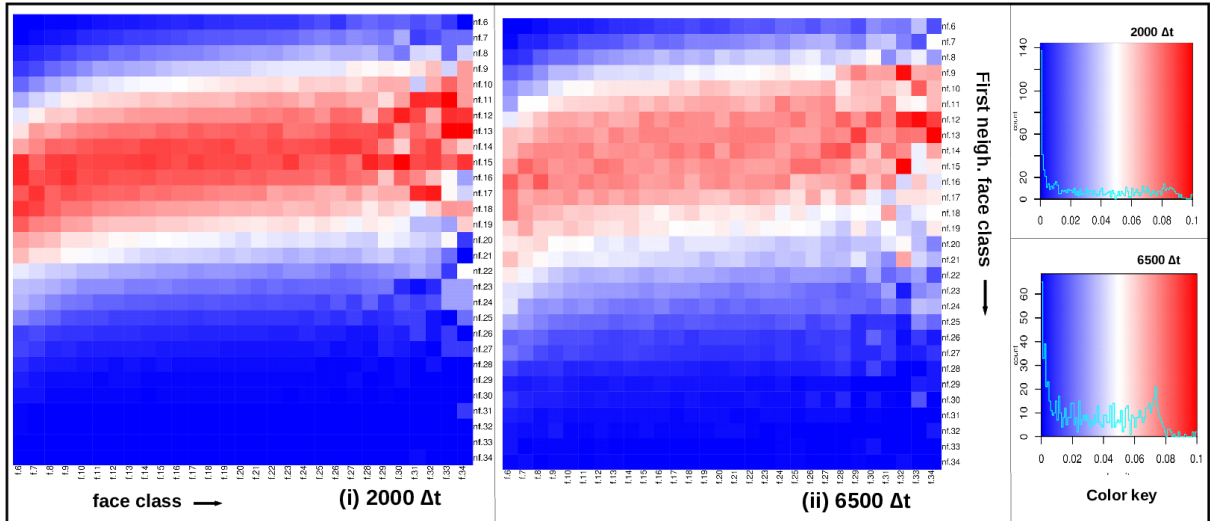
*Figure 5.9: (a) Change in the pattern of the heat-map, reflecting the topological evolution of the first-neighbors, at time, t = 2000 Δt and 6500Δt. (b) Conventional representation of the topological evolution of first-neighbors in face-class 7 and 30 to indicate the change in the pattern observed at t = 2000 Δt and 6500Δt.*

understand the topological evolution of the first-neighbors quantitatively. In this work, this complication is averted by involving a well known statistical tool called 'heat-maps'. These maps provide an efficient visualization by assigning colors to all entries of the matrix. A brief discussion on the heat-map representation is given in the Appendix A.

Heat-map depicting the number-density based contribution of the different face-classes to first neighbors during the initial stage of grain growth is shown in Fig.5.8b. Color palette adopted for this illustration is included as a subset wherein face-classes with low density in the first neighbors are represented in black while face-classes with middle and high contribution are allotted white and red, respectively. This palette is widely preferred due to its ability to encompass and meaningfully distinguish huge data. Reordering of the rows and columns, an important feature of the heat-map representation, is ignored

temporarily.

In addition to a quantitative depiction of the first-neighbors, heat-map in Fig. 5.8b reveals a dense straight-red band comprising of face-classes 13 to 19. This pattern, indicative of almost equal and dominant presence of 13 to 19 face grains in the first neighbors, is attributed to the initial distribution which predominantly consists of these grains (Fig. 5.8a). Topologically, the temporal evolution can be captured by analyzing the change in the contribution of the different face-classes to the first neighbor and thus, the first-neighbor heat-maps at intermediate and final time step are considered in Fig. 5.9a. In comparison with the initial stage, it is evident that the dense red band gets increasingly diffuse with time and the pattern noticeably abates. Furthermore, significant shift at either ends of the heat-map is observed which bends the straight dense region. To elucidate this shift, change in the number density of the face-classes surrounding the grains with 7 and 30 faces are analyzed separately in Fig. 5.9b. Smooth curves are fitted based on the data points for better depiction. Consistent with the heat-map representation, the initial curves at $t = 0\Delta t$ the curves corresponding to both the grains, 7 and 30, are almost identical. But as the transformation proceeds, tail end of the curve pertaining to face-class 7 gradually grows which shifts the curve to the right. On the contrary, no substantial change is observed for the tail end related to face-class 30. The other end, representing the lower face-classes, grows and shifts the curve to the left.

### 5.3.5.2   First-neighbor clusters

Data represented by the heat-maps are often re-ordered to enhance the understanding. In the present study, the rows of the heat-maps are re-ordered by 'clustering' the face-classes with similar contribution to the first neighbors. In order to make these clusters independent of the topological nature of the surrounding grains, the columns remain unchanged by the re-ordering process. A complete description of the different statistical steps involved in re-ordering is given in the appendix. Fig. 5.10 illustrates the re-ordered heat-maps at the initial and final stages of the grain growth. Three distinct 'clusters' with most, medium and least contribution to the first neighbors, henceforth referred to as cluster I, II and III respectively, can be perceived from this representation.

As shown in Fig. 5.10 after the initialization, when interaction is random and entirely based on the distribution, 'clusters I' consists of all face-classes between, and including, 10 and 24. Moreover, face-class 14 exhibits maximum density in the first neighbor. Face-classes, 10 to 24, are considered as 'intermediate', whereas face-classes below 10 and above 24 are referred to as 'minor' and 'major', respectively. This distinction illustrated in Fig. 5.10 facilitates a better description of the clusters and the temporal evolution. Accordingly, while the larger section of the minor face-classes 7-9 and smaller section of the major face-classes 25-29, constitute 'clusters II', the smaller section of minor 5, 6 along with larger section of the major 29 and above form 'clusters III' as shown in Fig.
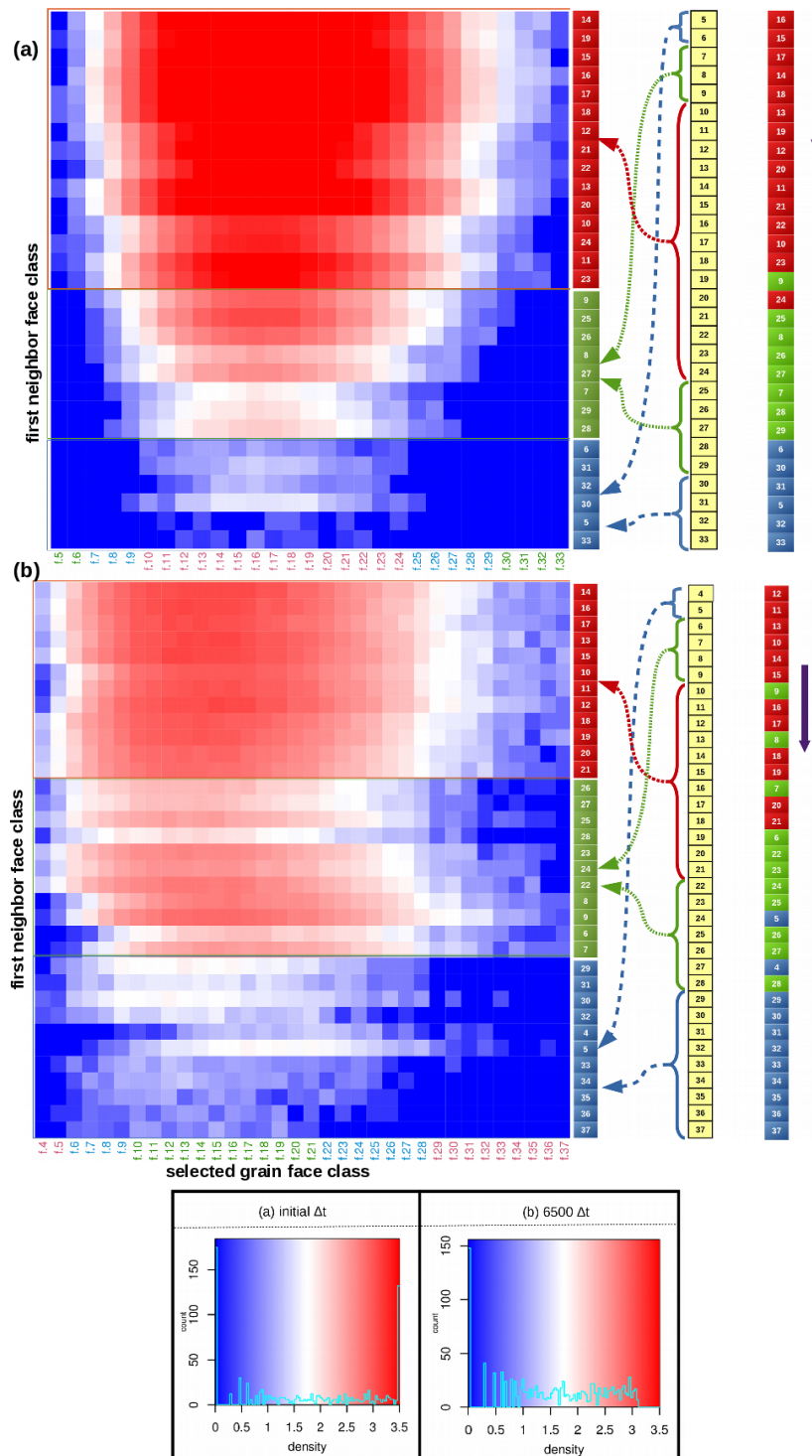
Figure 5.10: *Re-ordered heat maps at time t = 0 Δt and 6500Δt, wherein the rows are statistically-clustered leaving the column intact. The configuration of different clusters is described in-terms of minor, intermediate and major face-classes by the column of face-classes in the center. A deviation from the expected distribution of face-classes based on their availability is presented by the arranging the face-classes in decreasing order of number-density to the extreme right. Appropriate color-scheme is adopted in this representation to capture the deviation.*

5.10 with the help of arrows.
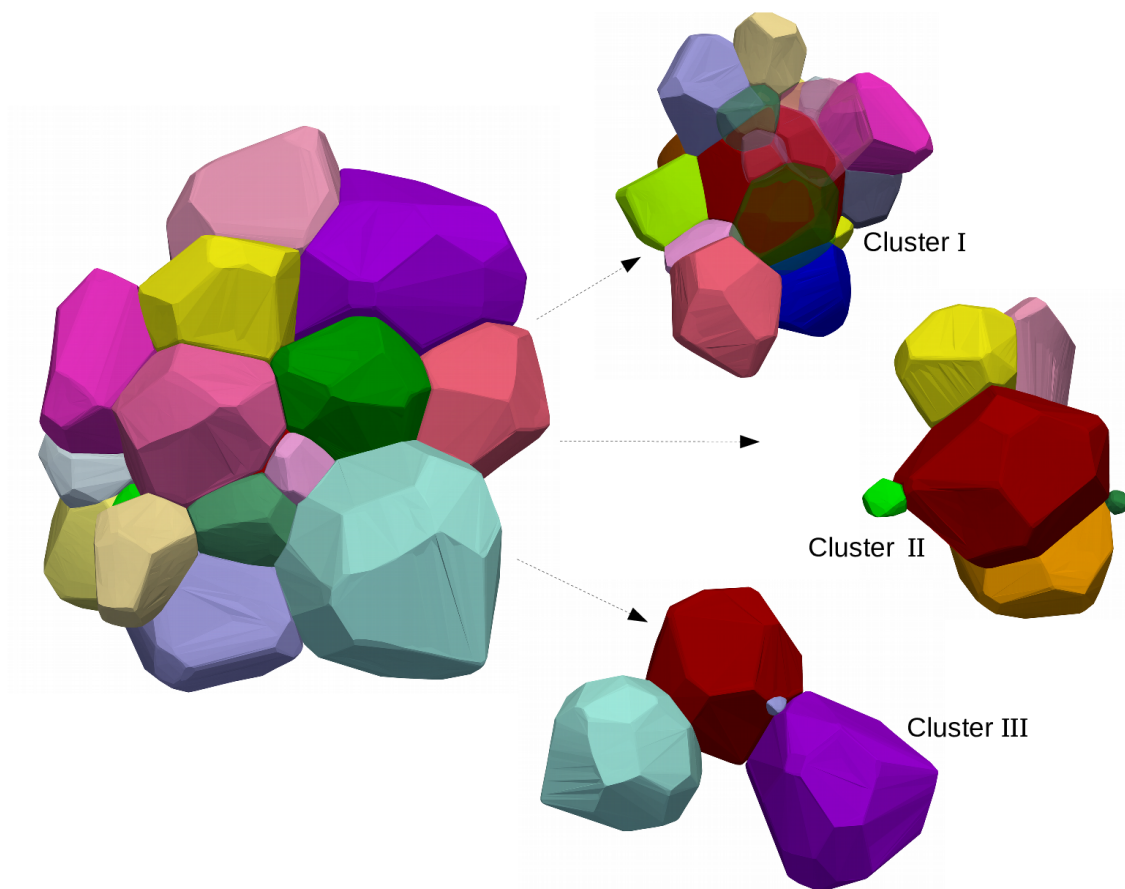


*Figure 5.11: The arrangement of different 'cluster types' on the first-neighbors of an arbitrarily chosen grain is visualized.*

During grain growth, significant shuffling of the face-classes is observed both, within and across these clusters. Although these shuffling events are dominant in the early stages of the transformation, the clusters become stable eventually. The heat map representation at time, $t = 6500\Delta t$ in Fig. 5.10 captures these changes induced during grain growth. Cluster I imparts the larger sections of its intermediate face-classes 22-24 to cluster II, which reduces its size from 15 to 12. Shuffling within the cluster II introduces a definite order in the arrangement of the face-classes. In addition to the shuffling, introduction of new face-classes increases the size of cluster III. Despite these changes, face-class 14 continues to be the dominant first neighbor consistent with the analytical prediction [141, 133].

Furthermore, in order to unravel the inherent influence of the randomness, which is based on the availability of different face-classes, the clusters are comparatively analyzed with the overall distribution. To the far right of the heat-maps in Fig. 5.10, the face-classes are arranged in decreasing order of its number density. At initial time step, it is evident that the face-classes which are higher in number form cluster I and cluster III comprises of the low number density face-classes. Moreover, the ordering of the face-
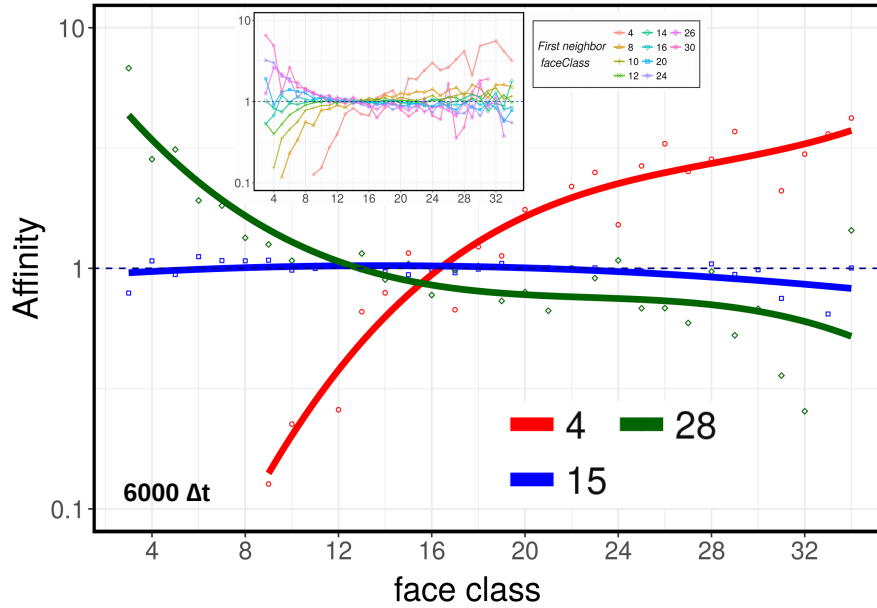
*Figure 5.12: Contact affinity of face-class 4, 15 and 28 grains each representing minor, intermediate and major face-class, respectively. Curves are fitted for the three chosen face-classes while the raw data for all the other grains are presented as a sub-set.*

classes in clusters are noticeably close to its position in the number-density based ordering on the far right of Fig. 5.10. Thus, consistent with the theoretical predictions and previous observations [115, 140, 142], the contribution of a particular face-class to the first neighbors is proportional to its availability in the early stages of the transformation. However, the temporal evolution of the grains introduces significant deviation from the expected configuration of the clusters. At time $t = 6500\Delta t$, the comparison of the number density of face-classes with the clusters reveals that certain face-classes, like 9 and 8, despite its high prevalence, provide only a moderate contribution to the first neighbor face -classes 14, 16 and 17. To visualize the set-up of these clusters in the first neighbor representation, a grain is chosen arbitrarily and the complete arrangement of its surrounding grains is shown in Fig. 5.11. In this illustration, a distinction is made between the grains rendered by each cluster. In complete agreement with the present analysis, a major portion of the first neighbor belongs to cluster I, followed by cluster II and III subsequently. A similar behavior is observed in almost all grains.

### 5.3.5.3  Contact affinity

The formation of clusters in the first neighbors is noticeably different from the expected number density distribution, is attributed to the preferred interaction between the face-classes and referred to as 'contact affinity $(A_{ij})$' [126, 139]. Thus, in order to substantiate this claim, the pair-wise interaction between the faces is calculated by taking the ratio of

number of established contacts ($N_{ij}$) to the possible random contacts (($N_{ij}$)$^{random}$),

$$A_{ij} = \frac{N_{ij}}{(N_{ij})^{random}} \tag{5.7}$$

where the ($N_{ij}$)$^{random}$ is expressed as

$$(N_{ij})^{random} = (i \cdot N_i)\left(\frac{j \cdot N_j}{\sum_{k=3}^{k_{max}}(k \cdot N_k)}\right) \tag{5.8}$$

$N_\eta$ is the number of $\eta$ face-class grains where $\eta$ can be $i$, $j$ or $k$ representing the number of faces.

The contact affinity greater than 1 between a pair of face-classes implies mutual attraction while less than 1 indicates the tendency to avoid. The affinity of three face-classes, each representing the minor, intermediate and major face-classes, is illustrated in Fig. 5.12. Consistent with the existing studies [126, 139], this depiction confirms that face-class 4 prefers the contact of major face-classes while avoiding the grains of minor face-classes. Additionally, the contact affinity of $\eta = 15$ remains almost unchanged and close to 1, indicating the lack of preferential contacts. In contrast to $\eta = 4$, grains representing the major face-class, $\eta = 28$ exhibit attraction towards minor face-classes while avoiding its own. The contact affinity of all the face-classes is included as subset in Fig. 5.12.

### 5.3.5.4   Influence of clusters on growth rate $(dV/dt)V^{-1/3}$

Topologically comparable-environment around almost all grains, is established by the formation of 'first-neighbor clusters', elucidated in the previous sections. However, properties like growth rate, $(dV/dt)V^{-1/3}$ depend on the inherent nature of the evolving grains as well. Thus, the temporal evolution $(dV/dt)V^{-1/3}$ is analyzed by making distinction in the face-classes. Fig. 5.13a displays the distribution of number density, $\rho(n)$ over the growth rate, $(dV/dt)V^{-1/3}$ and its evolution with time, $500\Delta t$ for face-class 11 and 19 using scatter-plot. As the transformation proceeds, the diversity in the growth rate is noticeably reduced and a consolidation of $\rho(n)$ can be observed in both the face-classes. This behavior is distinctly captured in Fig. 5.13b, wherein the raw data are constructed as a histogram. The corresponding fitting curves are plotted at three time steps, $t = 500\Delta t, 1500\Delta t$ and $3500\Delta t$. Evidently, irrespective of the face-class, the curves become sharper with time by reducing their widths. Topologically almost similar surroundings reduce the vast differences in the growth rate and consolidate the distribution of number density, $\rho(n)$. Furthermore, the formation of clusters substantiates the time-invariant nature of the topological evolution of grains reported previously [123]. Additionally, face classes and the time steps considered in this section are specifically chosen to render a definite statistical study.
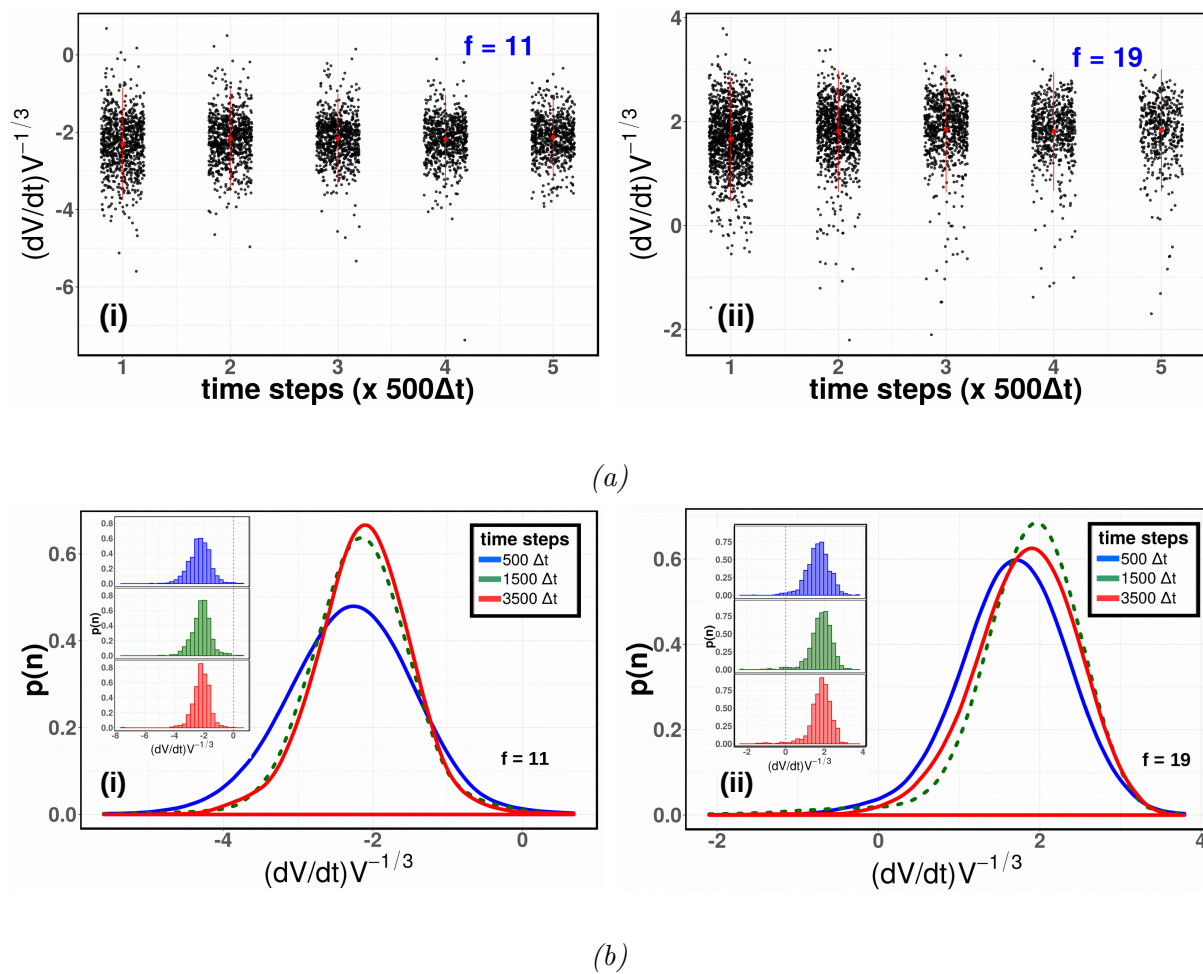
*Figure 5.13: (a) Scatter-plot illustrating the distribution of number density, $\rho(n)$ over growth rate, $(dV/dt)V^{-1/3}$, of face-class 11 and 19 grains and its temporal evolution. (b) Histogram representation of (a) is presented as a subset and the corresponding curves(fitted) are collectively shown to capture influence of time.*

## 5.4   Summary

Microstructural evolution of grain growth encapsulates geometrical (size) and topological (face-class) changes. In the present work, a thermodynamically consistent and well-established multiphase-field approach has been adopted to gain deeper insight into the topological aspects of this evolution. Analysis of face-switching events, that constitute the topological evolution, is often confined to face-gain or loss events [122]. However, this work reveals that no-change event, in addition to other events, renders a considerable contribution to the evolution. Additionally, we discussed that, although face-loss events are numerically dominant, a preference towards these events is dependent on the topological nature of the grains and it decreases with increase in face class.

Influence of topological events on the life-span of the grains has been captured and a 'dead zone' around face-class 14 is identified. It is suggested that the life-expectancy of grains with the topological evolution around or below this zone is significantly reduced.

A comprehensive understanding on the topological evolution of the first-neighbors is uniquely provided by employing an efficient statistical tool called heat-maps. The temporal evolution of these heat-maps is extensively analyzed and a significant deviation from the expected availability-based distribution of face-classes in the first-neighbors has been elucidated.

It is observed that the topological evolution of the surrounding grains which facilitates this deviation, predominantly occurs in the initial stages of the transformation and the topological set-up of the first-neighbors turns time-invariant eventually. By employing statistically coherent approaches, different face-classes constituting this topological set-up are re-ordered into 'clusters' based on their contribution to first-neighbors. The nature of these clusters around a grain are organized such that they remain unchanged irrespective of their face-class. These clusters provide an overall description of first-neighbors independent of the geometrical or topological nature of the grain it surrounds.

In the current work, topological evolution of the grains and first-neighbor analysis has been methodically distinguished and elucidated, yet the influence of size has been overlooked. Thus, a study considering both geometrical and topological evolution of the grains and their mutual interactions during grain growth will be pursued in the following chapters.

# Chapter 6

# Grain size and topological correlations on normal grain growth

## 6.1 Introduction

One of the much physically motivated normal grain growth theories, proposed by Hillert [20], represents the growth rate of grains, in terms of their curvature influence. He observed that the normalized grain size distribution (GSD) is invariant with growth. Although, Hillert's formulationis based on the well known Lifshitz-Slyozov-Wagner (LSW) coarsening theory [43, 44], the distribution significantly differed from most observed GSD's in the literature. Fayad et al. derived a Weibull distribution function from a Johnson-Mell grain structure, using the front tracking model [82]. Besides, there are additional GSD functions (such as log-normal, Rayleigh-type functions), based on physical theories, which provide solid grounds on adjustable fitting variables [143]. It is quite interesting to note that the Weibull distribution matches with the 2-D [144, 145] and the Hillert distribution, which lie in close approximation to the 3-D results [123, 146]. Although the dimensionality effect on GSD's, obtained from the computer simulations, can be seen, the underlying physical theories are unclear. To the best of our knowledge, the previous investigations have paid little attention to this issue.

The growth rate models for single-phase, isotropic materials, where the grain boundary motion is governed by the thermodynamics of the interfaces, can be considered as a modest version of the complex grain growth process in real materials. Hillert's growth law introduced a critical grain size above which the grains grow and below which the grains shrink.

$$R\frac{dR}{dt} = \alpha M \sigma \left( \frac{R}{R_{cr}} - 1 \right),$$

(6.1)

Here, $\alpha$ is a geometrical constant, $R_{cr}$ is a function of the mean grain size $\bar{R}$, $M$ is a grain boundary mobility and $\sigma$ is a grain boundary energy. Hillert proposed that $\alpha = 0.5$ is valid for 2-D and $\alpha = 1$ for 3-D systems.

The long-time growth kinetics in the scaling regime is expressed as:

$$R_t = kt^{(1/m)}, \tag{6.2}$$

where $R$ represents the mean grain size, $t$ is the time, $k$ denotes the proportionality constant and $m$ is the grain growth exponent.

Hillert exercises the mean field approximation, where the change in the size of the isolated grain represents the average influence of the whole array of grains in a system. In a classical particle coarsening mean field theory, the volume fraction of second-phase particles approaches zero and the role of inter-particle distance is important. On the contrary, the volume fraction is unity in grain growth and the grains can interact directly with the neighbors. Therefore, the applicability of the mean field approximation for grain growth has to be doubted. The statistical theories proposed that mutual interactions of the ensemble of grains could control the evolution of individual grains [147]. The spatial correlations have been stated as one of the reasons for the disparity between Hillert's original theory and the observed results. Hunderi and Ryum demonstrated that a size correlation exists between neighboring grains, in one- and two-dimensional computer simulations [148, 149].

Another equally important question is how topological distributions are invariant in microstructures. The Aboav-Weaire law correlates the average number of the topological class of the neighboring grains to the n-sided (faced) grain [150, 151]. This topological correlation behavior has been validated experimentally and by the use of computer simulations [1, 17, 128]. Wang et al. extended this topological correlation from short-range (first layer) to long-range (second and third layer) neighbor interactions [113]. He noticed that long-range neighbor correlations have a weak influence on the grain growth process. However, the short and long-range size correlation study in three-dimensional systems is limited in the literature. A quantitative study is expected to examine the long-range neighbor influences and their invariant behavior during growth.

Furthermore, the two and three dimensions of the grain growth process are also subjected to topological constraints. In 1951, von Neumann suggested a topology-dependent growth rate equation for 2-D systems, in which grains with less than six edges shrink, while those with more than six edges grow [119, 152]. He pointed out that the evaluation of the grains was inferred from their topological features, irrespective of the size. The actual extension of von Neumann's theory to 3-D systems required almost 50 years to solve. In 2007, MacPherson and Srolovitz proposed a mathematically rigorous equation for the rate of change of the volume of each grain in 3-D, in terms of the linear mean width framework [120]. Since this formulation contains some intricate parameters to measure

either in experiments or simulations, the moderate version of 3-D growth rate equations, based on the topology of the grains and their neighbors, have been suggested, following [134, 141, 153]. By considering the nonrandom neighbor interactions, Wang et al. suggested an equation in which the average rate of the growth of a given topological class is determined by the difference between the number of faces of the grain and an average number of faces of its first neighbors [121].

Numerous refinements of the NGG model were proposed by considering geometrically and topologically controlled mechanisms. However, a comprehensive theory which predicts the grain growth law, the grain size distribution, the topological class distribution of the grains and the correlation behavior of the neighbors is still lacking. The normal grain growth phenomena appear quite simple. Yet, the experimental and simulation results cause a conflict with the theoretical models, in many aspects. There are many open questions in our current understanding:

1. How are the transient and steady-state grain growth regimes to be distinguished?

2. Is the linear growth law assumption adequate for 2-D and 3-D systems?

3. Is there any correlation among the grains' neighbors, which means that grains should not be randomly located within the space?

4. What is the influence of the initial microstructures on accomplishing the self-similar state?

The statistical accuracy of the grain growth models typically constitutes a number of grains in an analyzing microstructure. In recent years, much research has been focused on large-scale numerical simulations, using powerful computational tools, which offer more quantitative results. The present study considers NGG on single-phase systems and employs the phase-field simulation to characterize the large grain networks statistically.

## 6.2   Simulation set-up

In order to solve the phase-field evolution equations, a finite difference algorithm with explicit marching scheme (forward Euler scheme) is implemented across a uniform numerical grid [154]. Further, equal grid spacings is assumed in all the dimensions such that $\Delta x = \Delta y = \Delta z = 1.0$. Length scale parameter $\epsilon$ which ascertains the width of the diffuse interface is set to $4\Delta x$ for the simulations. *Locally reduced order parameter optimization (LROP)* is employed to enhance the computational efficiency which optimizes both memory and time consumption of the simulation by limiting the number of order parameters solved at each grid point[155, 156].

The 2-dimensional domain of size $5000 \times 5000$ grid-points and 3-dimensional domain of $600 \times 600 \times 600$ grid-points, with periodic boundaries, are used for the initial large scale studies. Random distribution of about 36000 grains in 2-D and 75000 grains in 3-D is accomplished by Voronoi tessellation as described in Refs. [157]. At this stage, however, all grains in the domain are of the random geometrical and topological arrangements. In the present study, the influence of the initial polycrystalline patterns on NGG behavior is also investigated. To obtain the heterogeneous microstructure, an appropriate number of grains are randomly chosen and presented with different geometrical and topological attributes. Therefore for this non-random fillings, various statistical distribution functions on the Voronoi algorithm are adopted. Additionally, by assigning unique input parameters, for each distribution, randomness in their direction or difference in the size of the grains is obtained. The 2-D domains, sized with $2400 \times 2400$ and 3-D domains, sized with $400 \times 400 \times 400$ grid points, with an adequate number of grains, are exercised for these specific studies.

The time step is chosen well within the numerical stability range ($\Delta t = 0.8$). A constant value is assigned to the mean mobility $\tau = 1.0$ and the interfacial energy as 0.1 to simulate the NGG behavior. The radius of a grain $i$ is expressed as $R_{\phi_i}$, where $\phi_i$ indicates the phase identity. To compute the grain radius, the number of voxel cells inside the grain is counted, and a circle of an equivalent area is assumed for 2-D. Similarly, the equivalent volume of the sphere is considered for 3-D. The simulation domains were computationally enhanced by domain decomposition, using MPI (Message Passing Interface) [107]. The simulations are run long enough to ensure that the steady state grain growth regime reached.

## 6.3 Results and discussions

### 6.3.1 Microstructural features

The initial polycrystalline microstructures, with the predefined number of grains, have been generated in a 2-D and 3-D set-up. The random sequence of grain contacts is apparent from the visual examination. Considering that the grain boundaries take uniform interfacial energy and mobilities, the temporal evolution is controlled by a total grain boundary energy minimization approach. Throughout growth, the total number of grains decreases, while increasing the mean grain size. The larger grains that possess concave boundaries consume the small-sized neighbor (convex boundary) grains, and the growth proceeds. The surviving grains in the microstructure rearrange their local environment, size and shape to compensate the geometrical and topological constraints induced by the adjacent grains. Theoretically, the microstructure should eventually reach a single crystalline structure, where the lowest thermodynamic energy state is favored. Nevertheless,
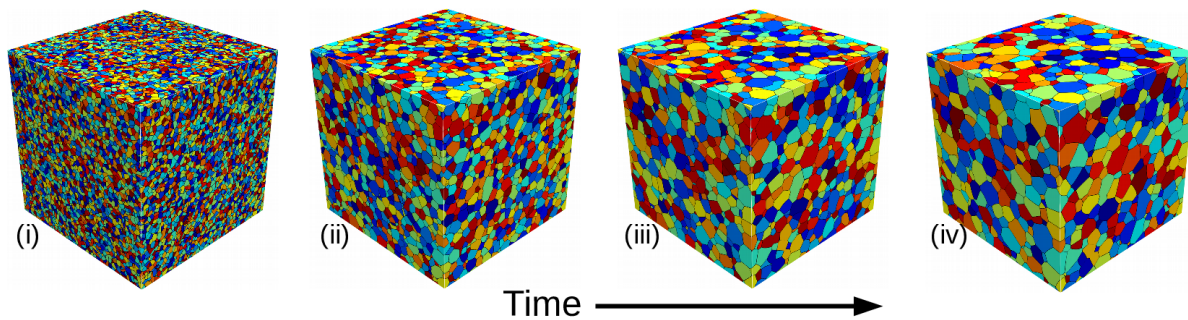
*Figure 6.1: Time evolution of the large-scale 3-D microstructure. The mean grain size progresses with the diminishing number of grains.*

in real materials, we seldom obtain single crystals through heat treatment processes.

The adopted simulation parameters are nearly the same for 2-D and 3-D cases. Hence the direct comparison of both systems is possible here. Fig.6.1 shows the temporal evolution of the large-scale 3-D simulation results. It can be seen that the mean grain size of the system increases with time. A similar grain growth behavior is observed in the 2-D simulations, and the resulted microstructure is not provided here. In both instances, the abnormal type of grains was not present in the microstructure. The quantitative characterization of the obtained microstructure and the neighbor influences will be addressed in the subsequent section.

## 6.3.2   Parabolic growth state

Normal grain growth obeys a parabolic type of growth behavior, $R_t = kt^{(1/m)}$, where $R_t$ is the mean grain size at time $t$, $k$ is the growth rate constant and $m$ is the growth coefficient. The growth coefficient often holds around 2, for the curvature-driven systems. The rate constant $k$ is often observed as a function of process parameters, such as interfacial energy and mobility. The mean grain size obtained from the 2-D and 3-D simulations is plotted in Fig. 6.2 (a) and (b), respectively. The extended linear fit is over-plotted to show the power law kinetics. One can notice that there are two distinct growth regimes in the figure. At the initial stage (regime I), the fit line deviates a lot, compared to the later regime (regime II). The initial random Voronoi filling arrangement is profoundly sensitive and commences the quasi-steady (QS) state shortly. However, the time required to attain a QS state depends on the initial heterogeneity of the microstructure. The dimensionality of the system also extends the complexity of the evolution process.

Numerous analytical models and simulations attempt to describe the QS state on the NGG behavior in a single-phase material [158, 159]. The previous attempts proposed some quantitative ways to represent the size and topological arrangements of the underlying microstructure [160]. The first neighbor correlations and their influence on growth were also studied in detail. However, in the simplest way to indicate the QS state, Nordbakke

noted that the $\bar{R}.(1/\bar{R})$ parameter approach is slightly above 1.3 [161]. Monte Carlo and vertex simulations yield towards 1.33 [149, 162]. With other supporting information, they claimed that the system is already in the QS state. The shape of the grain size distribution (GSD) can be interpreted employing the preceding dimensionless measure.

In the present study, the 2-D simulation attains a QS state at around $30dt$ time steps. The obtained data points follow the exponential type of fit function in Fig. 6.2 (c). It can be seen that there is an abrupt shift at the initial slope, and a later convergence to a constant value. A similar procedure is followed for the 3-D case, and a QS state is noticed at about 10dt time steps 6.2 (d). The discrepancy in the time duration, required to reach the QS state, might indicate the difference in the underlying coarsening mechanisms, due to the dimensionality effect.

In the microstructure, $\bar{R}_{nb}$ is stated as the mean of all the first neighbor grains. It is found that the mean grain size $\bar{R}$ and the parameter $\bar{R}_{nb}$ are not equal. It is indicated that the smaller grains are surrounded by larger ones, and vice versa. The ratio of $\bar{R}_{nb}/\bar{R}$ converges to a constant value, in the QS state. The previous 2-dimensional investigations stated that 1.13 results from MC and 1.22 from vertex simulations [149, 162]. From Fig. 6.2 (e) and (f), we observed that $\bar{R}_{nb}/\bar{R} = 1.09$ results from 2-D and 1.13 from 3-D simulations. While adopting similar input parameters for both systems, the variation in the $\bar{R}_{nb}/\bar{R}$ ratio indicates the effect of surroundings of a grain on its correlation behavior. Hence the detailed study of neighbor interactions, in terms of correlation functions, is demanded. To the best of our knowledge, there is no systematic study to examine the neighbor correlations in 2-D and 3-D microstructures concurrently.

### 6.3.3   Grain size and topological class distributions

The time-invariant behavior of the normalized mean grain size distribution is an implication of a QS state and is frequently reported in the literature [160, 163]. Hillert proposed a critical grain size of $R_{cr}$, in which the growth rate was inferred from it [20]. The transient and QS state regime microstructures are characterized to represent the effect of time on GSD and GTD. Grain size distribution in an isotropic model is usually perceived as a normal distribution type of curve, where the maximum peak occurs at $R/\bar{R} = 1.0$, and a symmetry around their mean. On the ground of literature, substantial number of analytical and mathematical functions is practiced to fit the GSD [34, 164].

However, in this study, only Hillert (solid line) and Weibull (dashed line) formulations are adopted. The Hillert function builds upon the LSW coarsening theory, into which the inter particle distance and the volume fraction hypothesis are incorporated [42]. On the other hand, the Weibull function originated from the mathematical ground (probability theory). Several semi-empirical functions can also be used to represent the GSD in a close approximation [33]. The true nature of the GSD is yet to be derived. Interestingly, the

*(a)*



*(b)*



*(c)*



*(d)*



*(e)*



*(f)*
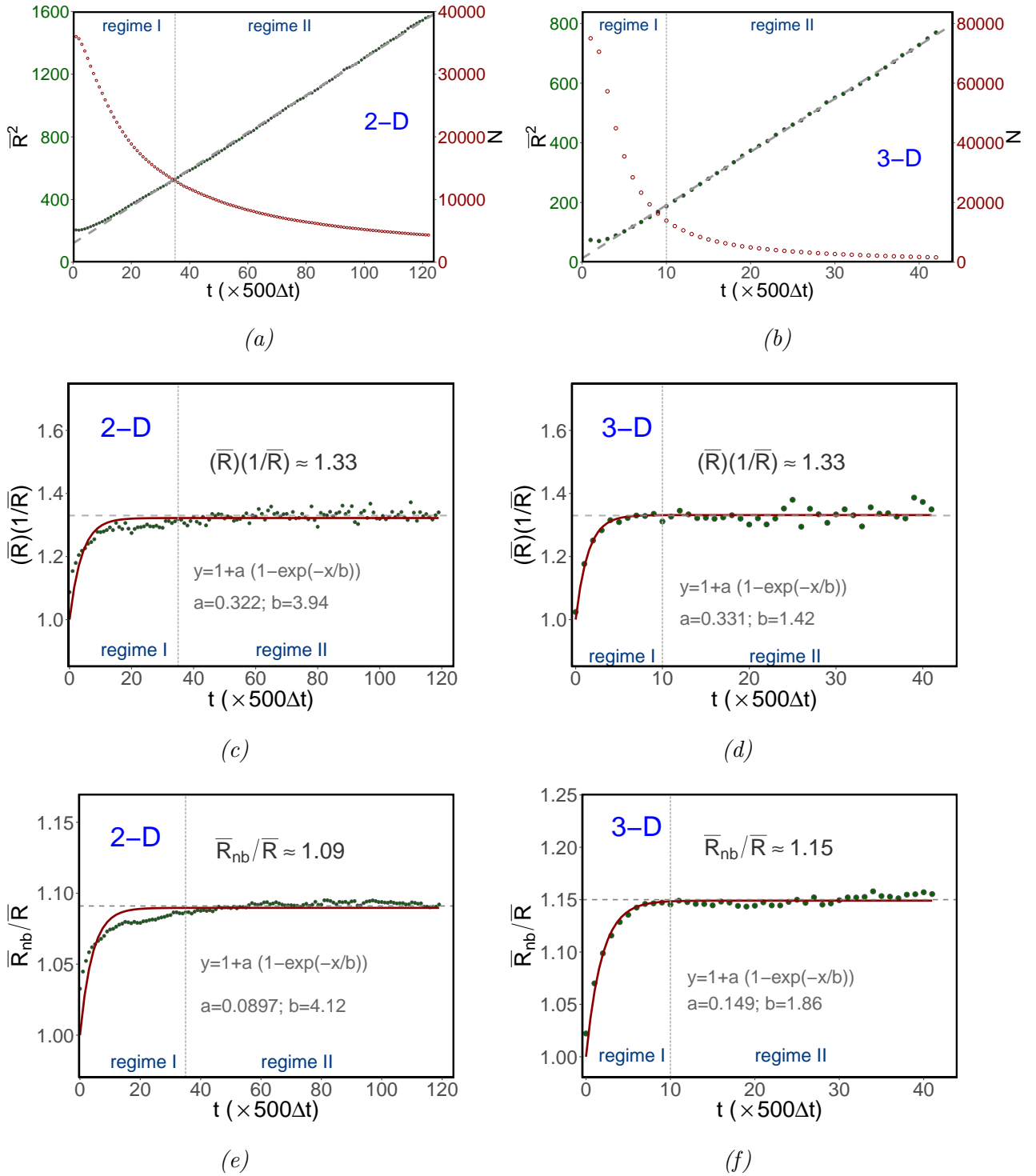
*Figure 6.2: Normal grain growth behavior in 2-D and 3-D systems. The observed datasets can be represented in two distinct regimes, depending on the time span of the transient (I) and the quasi-steady state (II). (a) and (b): Mean grain size evolution. The total number of grains is computed at each time step and is shown in a secondary axis (red in color), (c) and (d) $\bar{R}.(1/\bar{R})$ can be used to represent the shape of the grain size distribution, (e) and (f) $\bar{R}_{nb}/\bar{R}$ display the neighbor interactions.*

obtained 2-D and 3-D grain size distributions contradict each other and accommodate different functional fit parameters. Some recent works have been an attempt to derive a unique GSD function, based on self-similar average grain-volume change rate [37]. In fact, the individual volumetric rate of change can be directly related to the local topology of the selected grain and their neighbor influence.

Since most of the analytical models do not count the neighbor interactions for their distribution calculations, each grain is presumed to be surrounded by the random sized/shaped grains. However, the obtained experimental microstructures generally differ from the random arrangement assumption and yield inconsistency with the analytical fitting parameters. There is no adjustable fit parameter in the Hillert function, whereas the Weibull function has the variable $\tilde{\beta}$. In this work, the Weibull function uses $\tilde{\beta} = 2.7$ for both 2-D and 3-D cases, to keep consistency. The 2-D numerical simulations assert that the Weibull function can be considered as a close approximation to the normalized GSD. The log-normal and Louat function are also claimed for 2-D GSD, in some articles [33].

The initial microstructure confers a GSD with a very sharp peak, and is not approximated by both the Hillert and Weibull function. As time proceeds, the GSD of the transient regime superimposes the Weibull function, which is displayed in Fig. 6.3 (a). However, the shift in their peak position is perceived for microstructures at a later stage. For example, the GSD of the QS state exhibits a small deviation at a time step of $80dt$. Other than certain small peak differences, the larger and smaller grain size ranges, the Weibull fit has a very good agreement with the data points. It is observed that our 2-D distribution is slightly broader than the Hillert distribution. Since all GSD curves are well below the Hillert fit, one can interpret that the Hillert function is not a comprehensive one for the 2-D microstructures.

For our 3-D results in Fig. 6.3 (c), the Hillert function stays in closer approximation than the Weibull function. In particular, the GSD curves of the transient regime superimpose the fit line of the Hillert functional. The GSD peak of the QS state slightly descends at later time steps, and furthermore, the regime of the larger grains broadens. The consistency of Hillert's GSD function for 3-D microstructures has been addressed in the literature. The simulation and experimental microstructures show mixed results [165, 166, 167]. The recent large-scale phase-field study proposed that the Hillert function is only adequate for certain transient periods [123, 146]. The longtime annealed QS-state microstructure exhibits small deviations in Hillert's GSD approximation. From the subplot, the above hypothesis is further verified.

In 2-D microstructures, the topological class of a grain is denoted as the number of edges (n), and in 3-D microstructures, it is denoted as the number of faces (f). To sustain the QS state, the microstructure in a fixed domain size has to satisfy the geometrical and also the topological constraints. Although the well-defined formulations for the GSD are reported in the literature, less attention has been paid to the derivation of the analytical
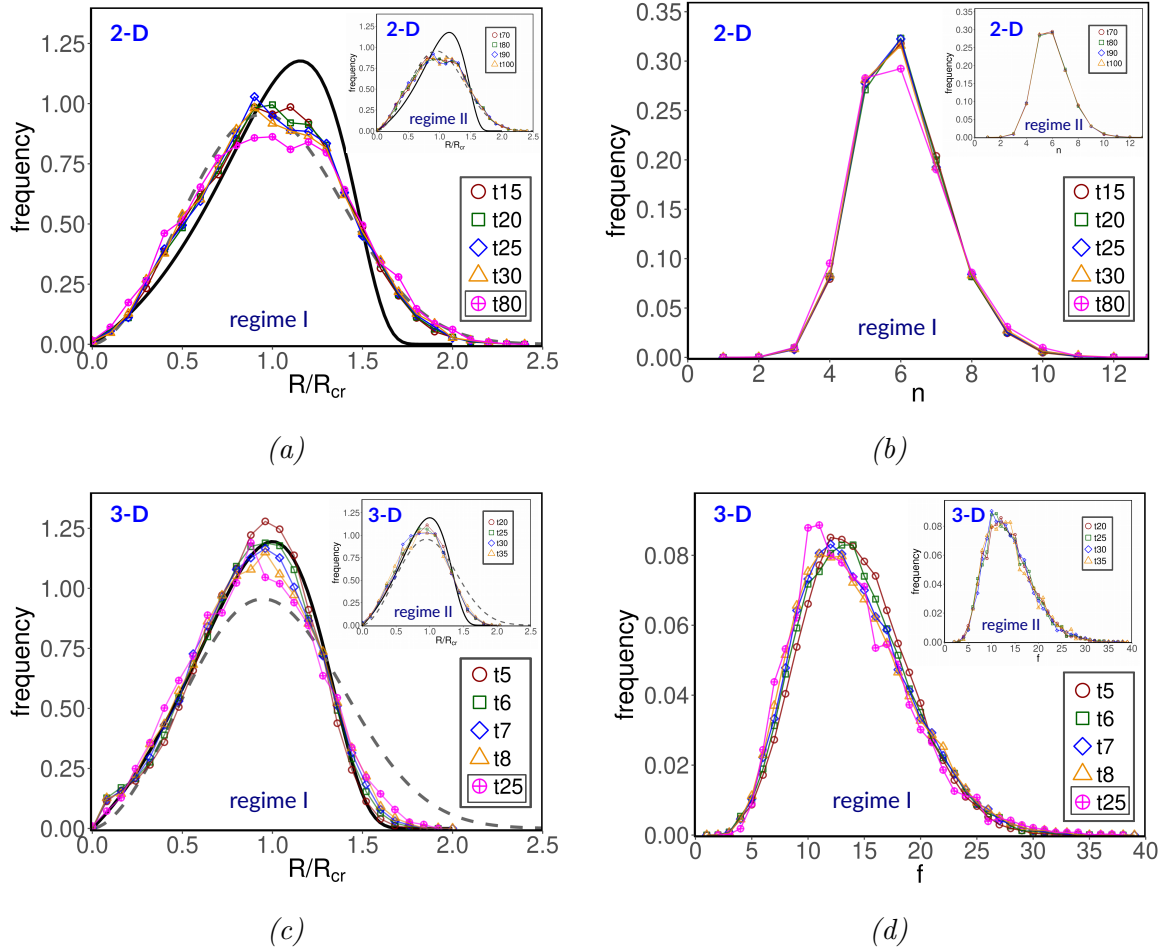
*Figure 6.3: Grain size distributions (GSD) for two grain growth regimes in 2-D (a) and 3-D (c). The solid curve is the Hillert distribution for equivalent spherical grains, and the broken curve is the Weibull functional fit. Grain topology distribution (GTD) at similar time steps, for 2-D (b) and 3-D (d).*

functions, in order to describe the Grain Topological Distribution (GTD). The time-invariant behavior of GTD in 2-D and 3-D simulations is respectively shown in Figs. 6.3 (b) and (d). The peak of the GTD was found at $n \approx 6$ for the 2-D and at $f \approx 14$ for the 3-D QS state. The difference in the transient and QS state GTD is considerably weak, as opposed to the GSD variations in the microstructures.

## 6.3.4   Growth kinetics

Since the classical Hillert theory is based on the mean field approximation, the influence of neighbors is the same for all grains, irrespective of their size and topological feature. Although the linear growth law is generally adopted, the mean field approximation has had some extent of conflicts with the numerical simulation results [123, 146]. Hillert presumes a linear relation among the mean curvature of the grain and its growth rate. The original derivation overlooked the topological influence on grain growth. Moreover,
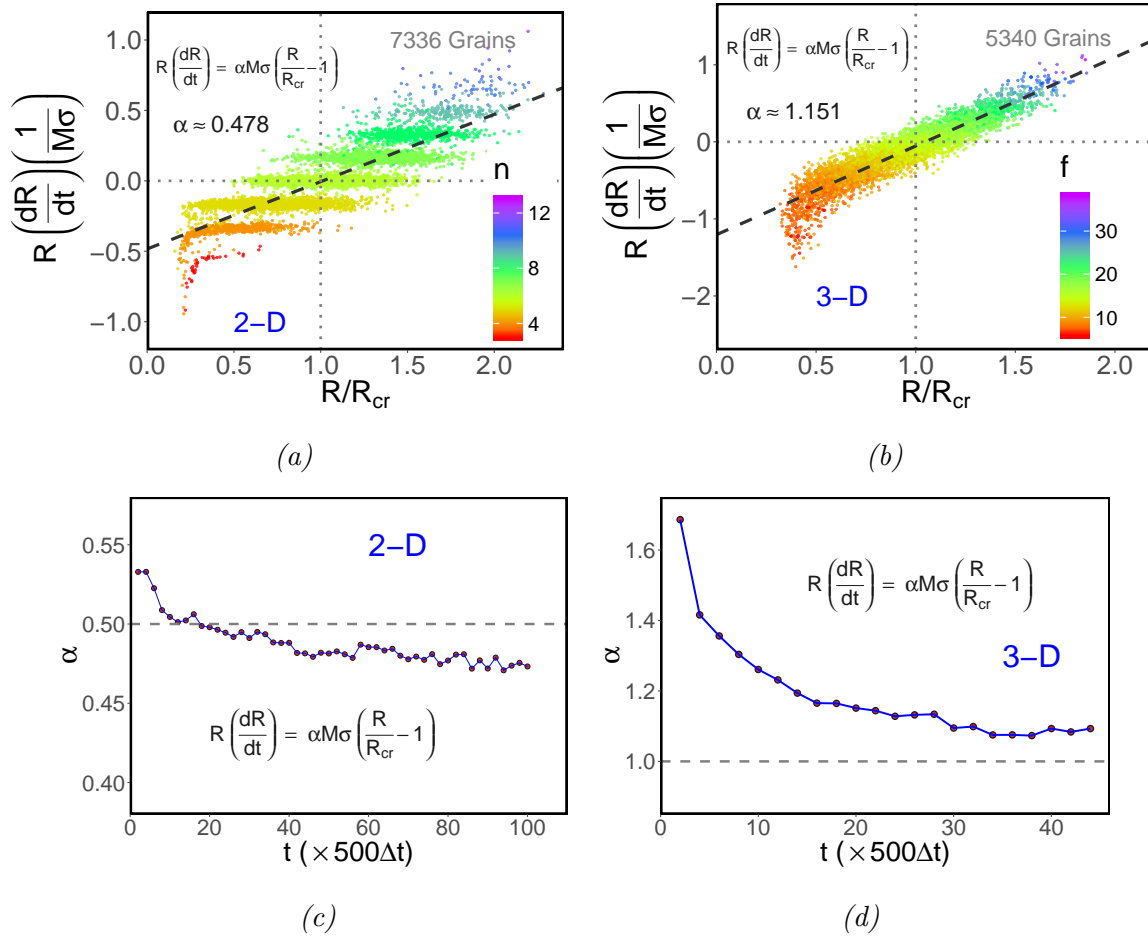
*Figure 6.4: The normalized mean grain size scales linearly with the growth rate. Hillert's linear growth law is shown for the (a) 2-D and (b) 3-D QS microstructures, in each dataset as a function of the topological class. Hillert's linear geometric constant as a function of time, for (c) 2-D and (d) 3-D cases. The dashed lines represent the original values of $\alpha = 0.5$, for 2-D, and $\alpha = 1.0$, for 3-D, from Hillert's derivation. The plot inquires the validity of the linear growth assumption.*

for a reliable statistical measure, the QS state microstructure should accommodate an adequate number of grains.

The classical geometrically mediated growth law has been adopted for our 2-D and 3-D results in Fig. 6.4 (a) and (b) respectively. The color schemes are employed to distinguish the individual topological classes. Despite being scattered in the growth rate dataset, the linear correlation is evident. The obtained geometric parameter found roughly the same in earlier studies [123]. While the linear fit is consistent with the regime $R/R_{cr} > 0.5$, the lower grain size relatively shrinks very fast and slightly deviates from the fit line.

In our previous section, the conflict of the GSD functions in 2-D and 3-D microstructures is addressed. Here, the main motivation is to corroborate whether the linearity hypothesis in Hillert's theory is valid or not. The dimensionality influence on the mean curvature of the grain demonstrates how differently the geometrical parameter ($\alpha$) varies,

and is presented in Fig. 6.4 (c) for 2-D and (d) for 3-D. The analytical models suggested that the value of the geometrical constant $\alpha = 0.5$ is for the 2-D and $\alpha = 1.0$ for the 3-D system. The 3-D geometrical constants are slightly higher than Hillert's prediction ($\alpha = 1.0$), while the 2-D values are lower than the theoretical value ($\alpha = 0.5$).

The linear dependence in Hillert's growth theory implies that the relative velocity of the moving boundary is constant with time. In other words, the geometrical constant $\alpha$ should not change during evolution. The recent publication from Kamachali found that $\alpha$ is not novel and varies with time [123]. His observation infers that the moving boundary velocity fluctuates. The observed $\alpha$ is high initially, and that it converges to a constant value later in time. Consequently, the QS state $\alpha$ approaches roughly 1.13 in their 3-D system. Temporal evolution of $\alpha$ from our 2-D and 3-D microstructure accompany a similar trend which suggests that time-invariant behavior seen for long time annealing. These results might support our hypothesis of a nonlinear growth relation, among 2-D and 3-D cases.

In earlier studies, the correlation theory is derived for 1-D and 2-D systems, by considering the first neighbor grain size interactions [148, 149]. Although $\bar{R}_{nb}$ is not a localized parameter, all neighboring grains were considered to compute this. In other words, the consolidated influence of the first neighboring grains is considered to derive the growth aspects of the selected grain, noted in Fig. 6.5 (a) and (c). The instantaneous transitions of the neighbors geometrical and topological features are difficult to measure through the experiments. In this study, we extend the neighbor correlation in terms of the local variable $R_{nb}$, the first neighbor mean grain size of the individual grain.

The growth rate of a selected grain has a linear relationship with the local environment of the neighbor clusters and is shown in Fig. 6.5 (b) and (d) with a linear fit line. The $\tilde{\alpha}$ outlines a geometrical fitting constant for the neighbor correlation theory, and it is found that $\tilde{\alpha} = 0.521$ for the 2-D case. In a similar way, the localized neighbor mean grain size consideration $\bar{\alpha} = 0.468$ is obtained. On the other hand, for a 3-D simulation, the cumulative neighbor mean grain size equation gives $\tilde{\alpha} = 1.171$, and the localized neighbor mean size equation results in $\tilde{\alpha} = 1.073$.

Since the von-Neumann growth law widely used for 2-D systems, several attempts have been made to quantitatively describe the growth rate of the 3-D grain [152, 119, 134, 136]. MacPherson-Srolovitz's topology-dependent equation predict the exact grain growth rate of individual 3-D grains [120]. On the other hand, the simplified topology-dependent growth equations can be employed to predict the average grain growth behavior [121, 132]. In this study, to get a general idea about the applicability of the topology dependent growth equation, we used the prior microstructures to evaluate the 2-D and 3-D growth equations. The volumetric change of the grain is proportional to the difference in the topological class and the mean number of the first neighbor faces. The summarized results are shown in Fig. 6.6. The topological constant of $\tilde{\kappa} \approx 0.792$ for 2-D and $\tilde{\kappa} \approx 0.44$
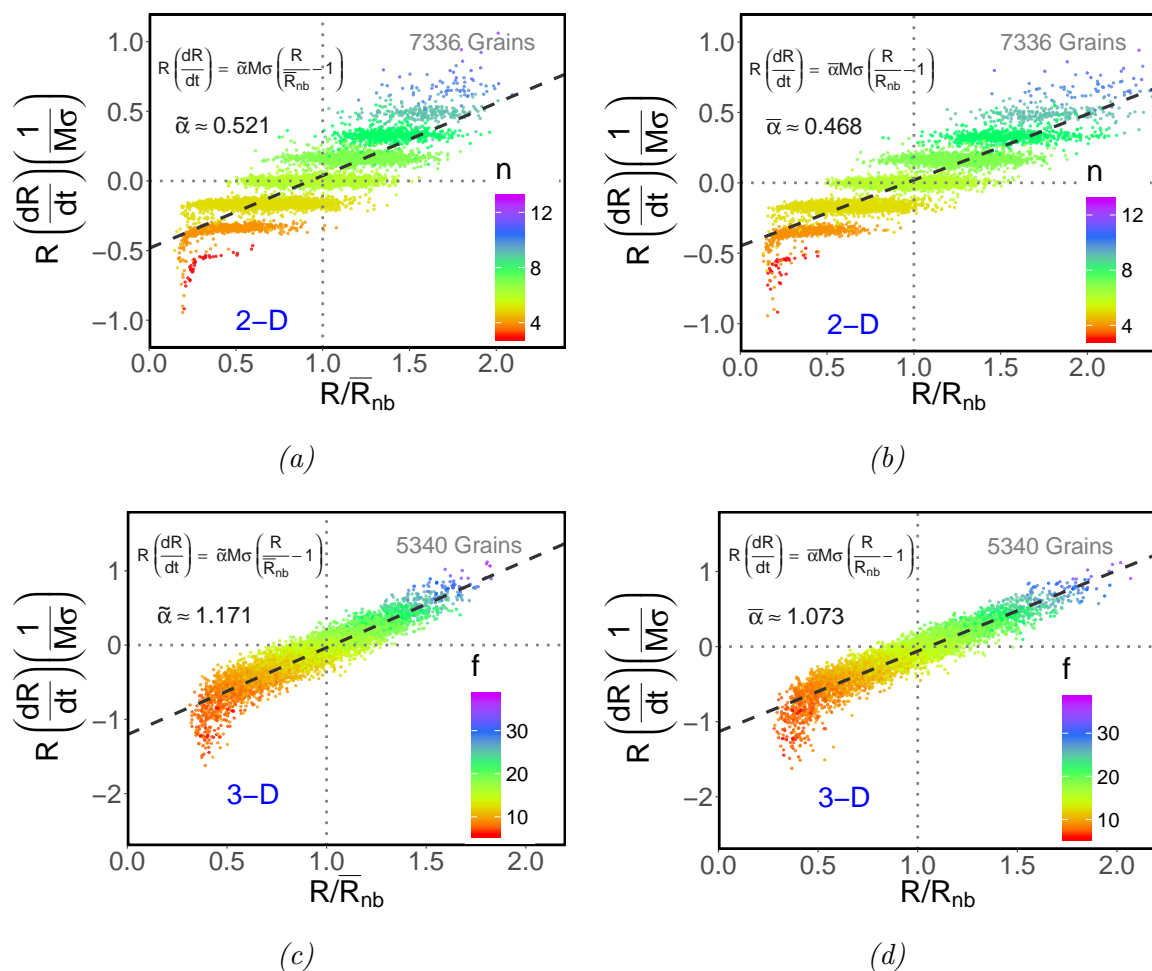
Figure 6.5: The analytical and empirical geometric growth laws show various normalized mean grain size adaptations that may indicate the neighbor correlations. The cumulative mean neighbor grain size ($\bar{R}_{nb}$) interactions are in (a) 2-D and (c) 3-D. The localized neighbor mean size ($R_{nb}$) that confer the growth laws in (b) 2-D and (d) 3-D. The growth transitions are represented by their topological classes.
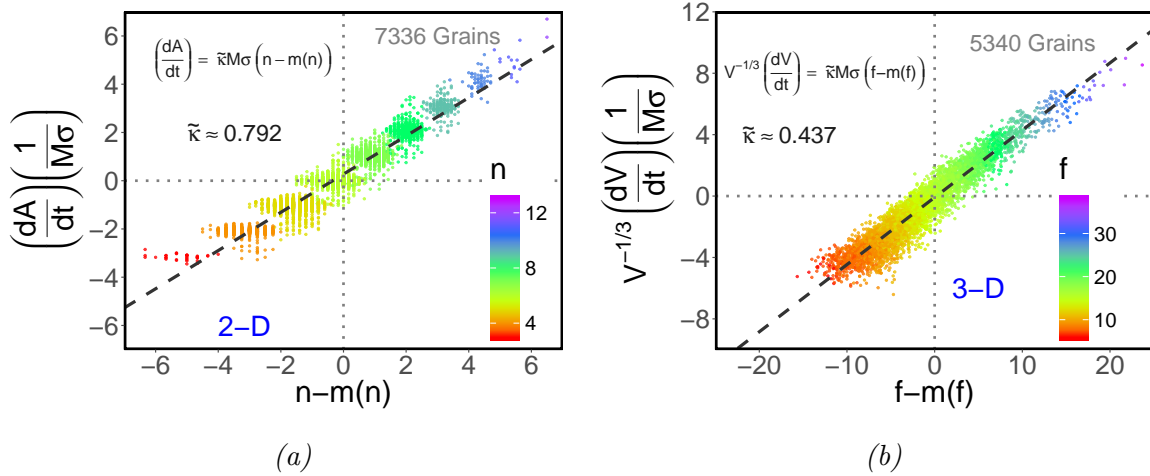
*Figure 6.6: Relation between the average grain growth behavior and their topological interaction where n-m(n) is for 2-D and f-m(f) for 3-D. Dashed line represents the best linear fit. The topologically mediated growth law indicates the consideration of local environment of grains.*

for 3-D are roughly similar to the prior results.

Furthermore, the growth velocity $(dR/dt)/(dR_{cr}/dt)$ can be described as a function of $R/R_{cr}$. This parameter evaluates the relative growth rate of the individual topological classes, with respect to each other. Hillert's linear growth law exaggerated that if the grain approach is infinite in size, the growth rate should be infinite. But the former linear state cannot be reached in numerical simulations where the topological and geometrical constrains govern the microstructural evolution. In order to quantify the relative growth rate in our system, the above drift velocity framework is employed here. The drift velocity of the selected grains is assembled in terms of their topological classes and then fit with the best nonlinear functions for the available dataset in Fig. 6.7 (a) for 2-D.

While the shrinking rate of a smaller edge and smaller-sized grains is very rapid, the larger grains $R/R_{cr} > 0.5$ show a relatively low shrinking rate. The six-sided grains exhibit the random growth characteristics, irrespective of the advantages of their size. The roughly linear fit along the zero lines is plotted, and thus attributed no preferential growth direction. Moreover, several grains shrink and disappear in subsequent time steps. Some grains may grow at the expense of their random neighbors. For the large edge class grains, the increment in grain size may not be advantageous for the growth. It is observed that a larger grain size actually diminish the drift velocity, comparable to average-sized grains of the same class. A similar study has been carried out on 3-D microstructures, and the results are presented in Fig. 6.7 (b) which also asserts nonlinear drift velocity behavior. Some of the selected grains in the lower, intermediate and higher face class groups are furnished in the subplot. The $f = 6$ grains show a moderate size spectrum and confer the complete shrinking response. The grains with the $f = 10$ unveil two distinct drift velocity directions, where the substantial shrinking rate is marked for lower-sized

grains, $R/R_{cr} > 0.5$, and the large grains are moderately weaker than this.

The size factor have a considerable influence on the face class of 14 and 15 grains where the growth direction randomness can be noticed. Besides, the higher face class grains ($f > 20$) are approximately larger than the critical size of the distribution. Therefore, positive growth rate for all grains is expected. However, the larger-size grains in these topological classes show relatively weaker drift velocities than the normal grains. This surprising behavior is compatible with our prior 2-D findings. The randomness in the drift velocity increases by increasing the topological class. It should be noted that the large-sized higher face class grains may grow or shrink irrespective of the advantage of their size, due to the space filling constraint. There is always a thriving growth competition among the neighboring grains. The random walk theory for the NGG model also depicts the nonlinear relationships with the microstructural and geometrical parameters [22, 168].

### 6.3.5 Neighbor correlations

The correlation amongst the neighboring grains can be exercised as a feature to represent the QS state in the microstructure. Previous analytical and simulation studies were evaluated on size correlations, comparing the chosen grain and their first neighbors [147, 160]. They claimed that there is a notable clustering tendency for smaller to larger grains, and vice versa. The intermediately sized grains can often be encompassed by grains of roughly the same size.

The normalized neighbor mean grain size ($R_{nb}/\bar{R}_{nb}$), as a function of a normalized grain size ($R/\bar{R}$), exhibits the clustering bias within the QS microstructure in Fig. 6.8 (a) for 2-D and (b) for 3-D. It can be seen from the subplot that, for the initial Voronoi distribution, the correlation behavior is measured in microstructure is in good agreement with that predicted by the earlier results [160]. With the expectation from the self similar state, that the smaller grains tend to be surrounded by the larger adjacent grains, the intermediately sized grains reveal a random neighbor arrangement. The broader spread in the dataset can be detected in the farthest cases of smaller- and larger-sized grains. A third-order polynomial type of function is used to fit the curve. Interestingly, the captured fitting coefficients are nearly identical for 2-D and 3-D results.

The individual topological class accommodates a broad range of grain size variations. In other words, for a chosen grain, the number of contacts may remain fixed; yet the adjoining grain size may differ considerably. Nordbakke derived an analytical model to express the size correlation in terms of their topological classes, on the basis of their geometrical arrangements [160], as

$$\frac{\bar{r}_{nb,n}}{\bar{r}_n} \approx \frac{sin(\pi/n)}{1 - sin(\pi/n)} \tag{6.3}$$

It has been pointed out that six-sided grains are embedded in the similarly sized neighbor
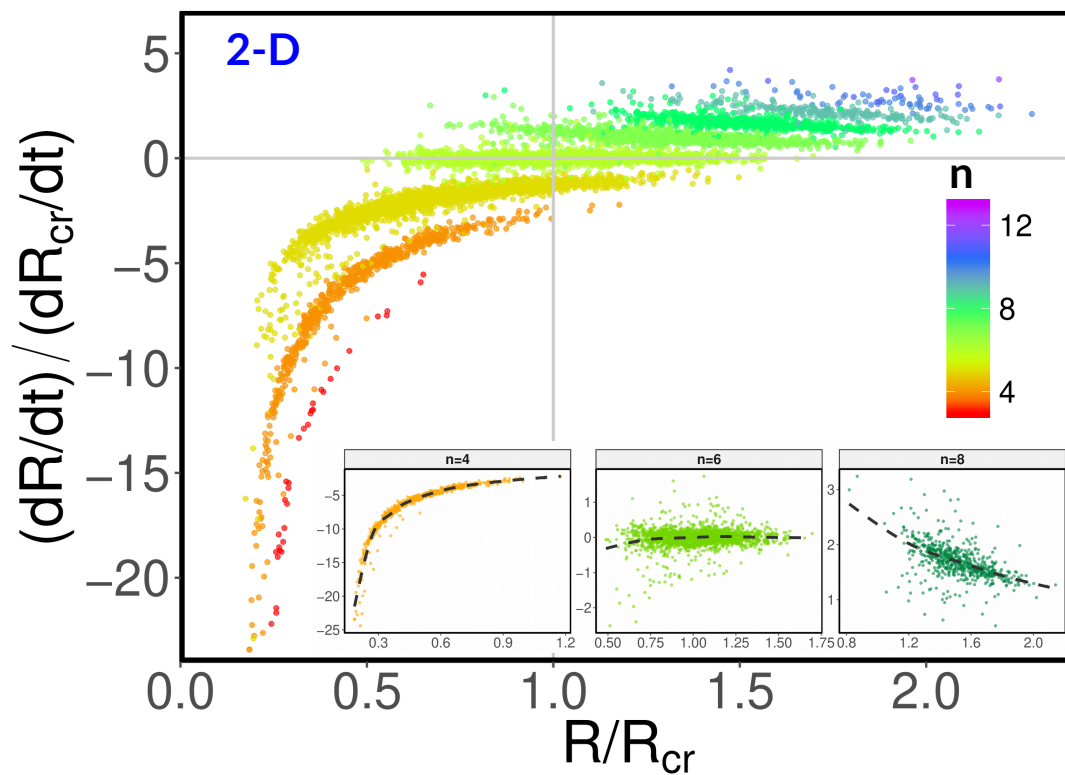
*(a)*
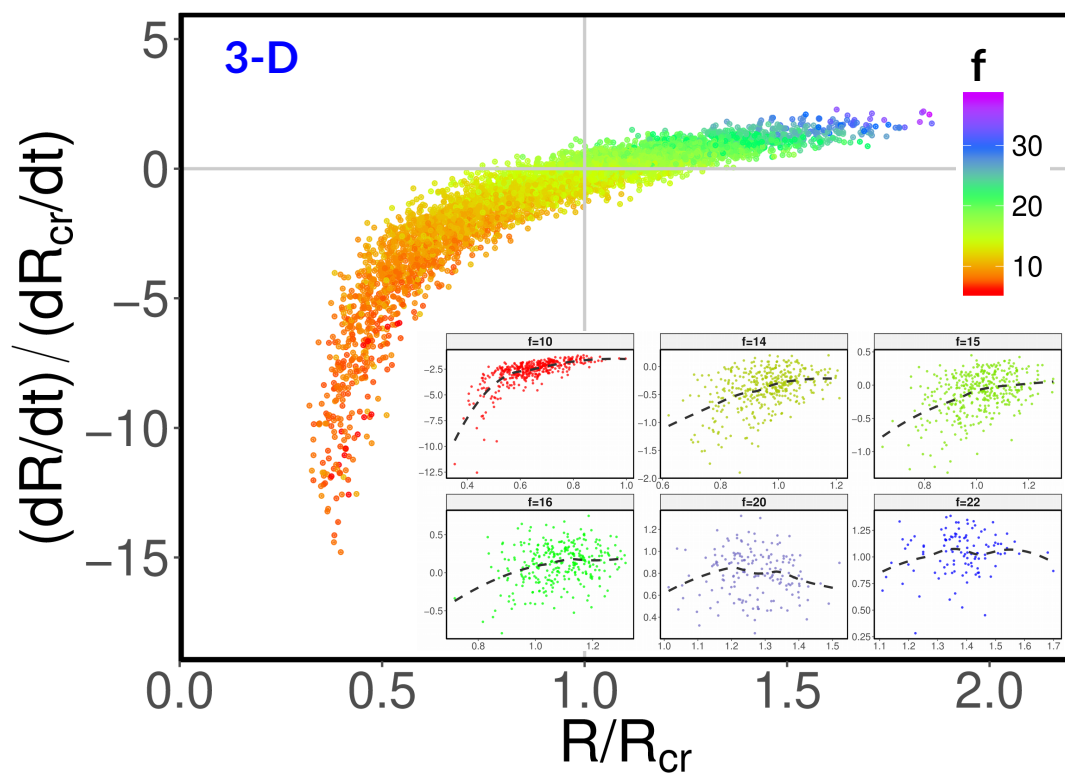


*(b)*

*Figure 6.7: The growth velocity is estimated as a function of topological classes. A substantial decrease in drift velocity is perceived when the normalized grain size is greater than one. The significance of the growth direction, compared to their size, is indicated with a dashed fit line.*

environments, in the 2-D domain. However, on average, the larger topological class grain has a smaller adjacent grain network and vice versa.

These topologically biased correlations in 2-D support the previous section pure size correlation results. However, the direct 3-D extension of the size to topological correlation formulation is not yet apprehended. For this reason, we tried to assess the size-topological correspondence for our 3-D microstructures. The adopted QS state microstructures have been inspected at multiple time steps, so as to draw the time-invariant characteristics of the correlation functions. The summarized results are presented in Fig. 6.8 (c) and (d) for 2-D and 3-D respectively.

It is difficult to ascertain that the analytical function is purely based on their geometrical features for the 3-D microstructures, . Interestingly, the overall trend in the figure seems very similar to the 2-D findings. The topological classes 6 in 2-D and $\approx 14$ in 3-D accommodate similarly sized neighbor grains while the random neighbor interaction indicated using the dashed lines in the figure.

## 6.3.6   Individual size distribution: neighbors

In the previous section, we attempted to explain the correlation behavior among the selected grains and their local mean neighbor sizes. Still, the grains with the same topological class, in different positions, can be encompassed by a broad neighbor size range. Hence, it should be necessary to examine the local neighboring grain size distribution for the chosen topological classes individually. $R_{nb,n}$ means that the average neighboring grain size of the selected topological class is $n$.

In the following calculations, this parameter can be represented as a fraction of $\bar{R}_{nb}$. The topological classes of 3, 6 and 11 have been investigated for a 2-D microstructure, and the results are shown in Fig. 6.9 (a). The lower topological class $n = 3$ shows that the peak of the neighbor GSD is more moderate than the relative neighboring grain sizes. The smaller-sized neighbor grains have a substantial fraction in the higher topological class $n = 11$. For the intermediate case $n = 6$, there are no preferential contacts where the neighbor GSD confers a symmetrical form around the center.

The topological classes of 5, 14 and 32 have been analyzed for 3-D microstructures, and are shown in 6.9 (b). Comparable to the 2-D outcomes, the topology-dependent neighbor grain size correlation can be exposed. The intermediate topological class grains ($f = 14$) possess a stochastic random neighbor arrangement.
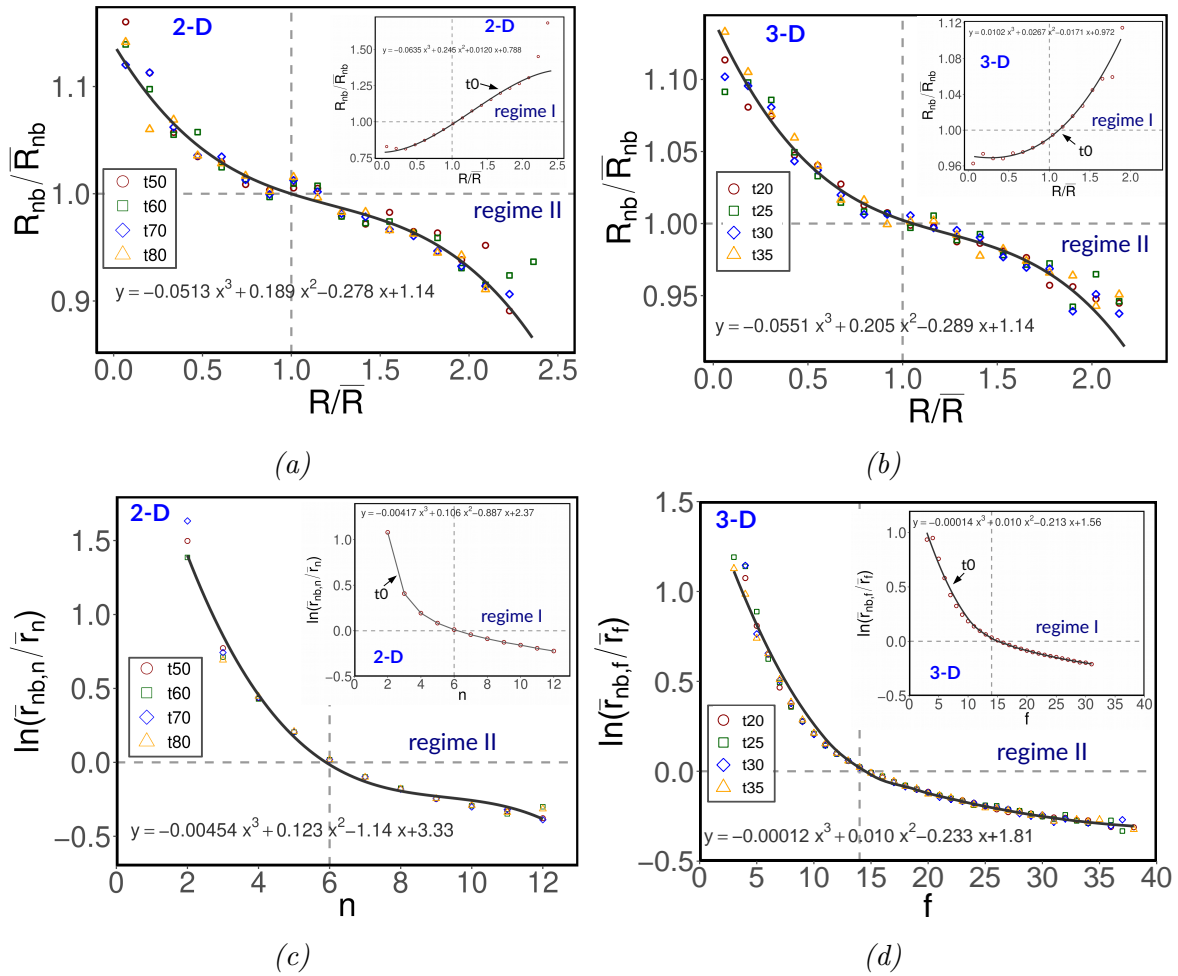
*Figure 6.8: Analysis of first neighbor correlations. The subplot shows the initial microstructure, while the four data points in the main plot show a time-invariant behavior. The small-sized grains are surrounded by large grains, and vice versa, as confirmed by (a) 2-D and (b) 3-D results. The normalized neighbor grain size, as a function of topological classes, reconfirms the correlation theory (a) 2-D and (b) 3-D.*
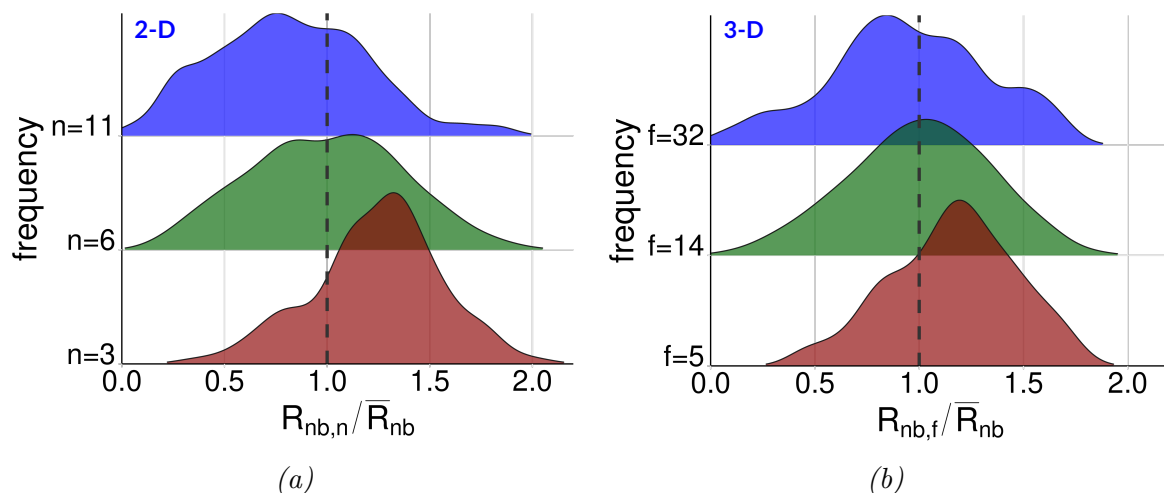
*Figure 6.9: Under the selected topological class, the QS state is well described by normal-type distribution. The lower topological classes have a higher fraction of larger-sized grains and vice versa. (a) 2-D and (b) 3-D.*

### 6.3.7 Size and topology: square root relation

According to the Lewis's law, the mean radius of the grains is proportional to the number of their edges $n$ in 2-D [169]. Similarly, the topologically averaged grain size in 3-D can be derived from their face class $f$. For our 2-D and 3-D microstructures, Fig.6.10 (a) and (c) respectively exhibit the positive correlation among the topological class and the normalized grain size. The grains with larger size tend to have more neighbors than smaller grains. During the evolution, these topological classes yield broader size variations. It should be noted that, the different time step datasets in Fig. 6.10(b) and (d) are computed to show time invariant behavior. It is perceived that a square root-type relationship does exist between them and the linear fit line is overplotted into the figure. While the normalized grain size in the range of 0.5 to 1.5 shows very good agreement with the fit line, the smaller and larger grains show slight deviations.

### 6.3.8 Short- and long-range topological correlations

The size and topological correlations of the first neighbors have been investigated in prior studies [160, 170]. However, the impression caused by the geometrical and topological rearrangement of a particular grain is not only limited to the first neighbors, but should also extend to their long-range neighbors. In other words, one can presume that the local changes of each grain provoke some series of reactions in the microstructure. Hence the long-range interactions have to be specified precisely, to quantify the QS state. Although the experimental investigations of long-range interactions are difficult to measure, the numerical simulations can be used to extract each grain and their short- and long-range neighbors. Recently, Wang et al. reported long-range topological correlations from their
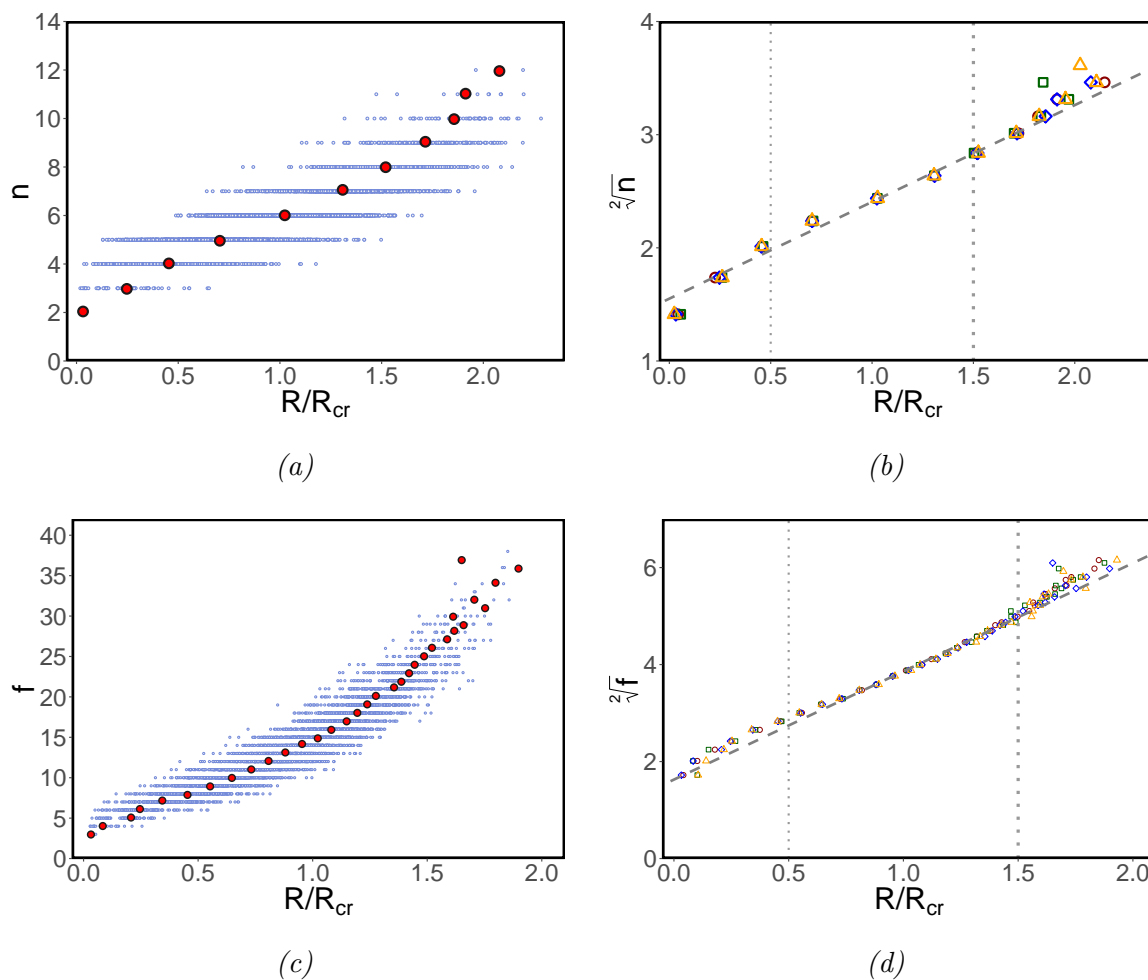
*Figure 6.10: Grain size and topology relationship. The QS microstructures with a linear relation are shown for (a) 2-D and (b) 3-D. Dots represent the mean observations of the individual, topological classes. The time-invariant behavior for 2-D and 3-D is respectively represented by the points in figure (c) 2-D and (d) 3-D.*

MC simulations [113]. They noticed that the long-range interactions exhibit a weak effect on the growth behavior of the central grain.

In our study, the long-range correlations have been extended to up to five layers, which are shown in Fig. 6.11. The schematic representation of short- and long-range neighbors are highlighted with distinctive color schemes in the subfigure. The mean neighbor topological class values are computed and plotted in the right top of the figure for 2-D case. The QS state microstructure indicates that the convergence of short- and long-range neighbors might appear close to the topological class of $n \approx 6$ for 2-D and $f \approx 14$ for 3-D. Nevertheless, there is noticeable difference between short- and long-range neighbor arrangements. If the neighbor layer increases, the convergence rate is quite high. The short-range neighbor grains show the strong topological correlation in the figure. In other words, other than the first neighbor clusters, the long-range grains appear like a mean field approximation (i.e. similar grain ensemble to the central grain).

The sequence of short- and long-range neighbor layers on the leading QS state is compared in Fig. 6.12. Here, the motivation is to check whether there is any dimensionality influence on neighbor layer rearrangements during growth. The initial and QS state microstructures are used to assess the prior hypothesis. The first, second and third neighbor layers of the grains are highlighted for further investigation. It is seen that the topological correlation transformation is quite rapid in 2-D, compared to 3-D systems. This can be attributed to their dimensionality influence on topological arrangements. To this end, this findings slightly contradicts with the geometrically based observations in the previous sections, where it was assumed that the curvature in 3-D systems reconciled much faster than in 2-D systems. Here, however, the topological rearrangement of long-range neighbor grains, during the evolution in 3-D, is slower than the 2-D microstructures. On the whole, the confluence behavior is evident for both 2-D and 3-D cases.

The first neighbor interactions, in terms of the Aboave-Wearie law, exist in the experimental and numerical simulation results [171]. This classical law suggested a linear correlation, examining the topological grain class and the mean of the topological classes of the first neighbors. The long-range interactions have been presented with the fit line in Fig. 6.13. While examining the first neighbors for high-edge grains in 2-D, the low-edge grains ($< 6$) are surrounded by the class grains with a higher edge ($> 6$), and vice versa. On the other hand, the long-range neighboring grains possess a pretty weak influence on the Aboave-Weaire relation. The second and third neighbors reveal a nearly flat fitting line for our dataset.

In a similar way, the grain size correlations for short- and long-range neighbors are investigated and shown in Fig. 6.14. These observed results are compatible with the topological correlation behavior. The second and third neighbors have no size influence over the central grain. The mean neighbor grain size is almost independent of the nature of the central grain. From this long-range correlation study, one can realize the significance
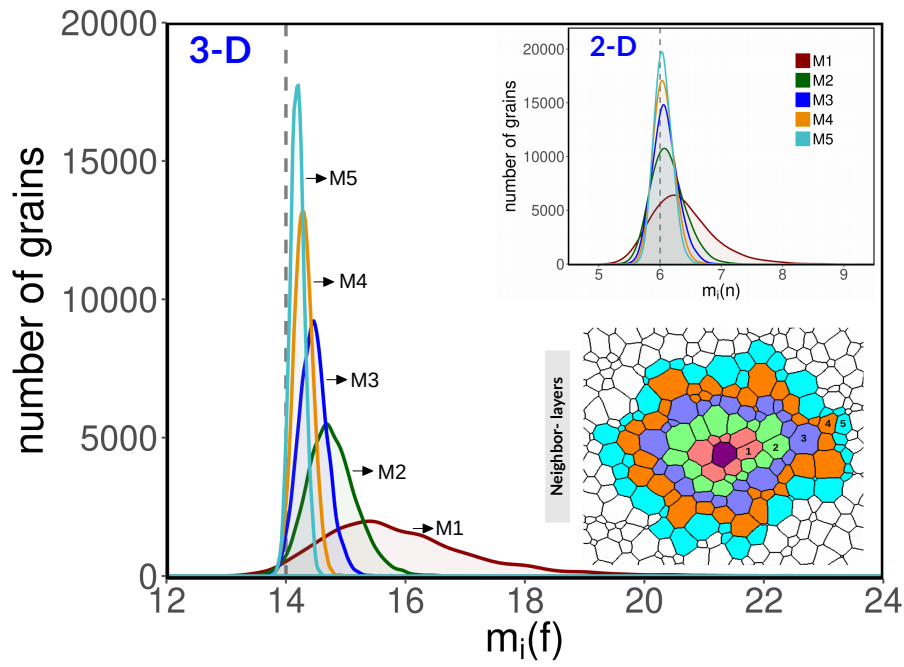
Figure 6.11: *The short- and long-range topological correlations in 2-D and 3-D. The subplot shows the schematic representation of the neighbor layers. Note that the correlation behavior in the QS state clearly depends on the layer of the cells; the short-range neighbors display a strong correlation, while the long-range grains show a random arrangement.*
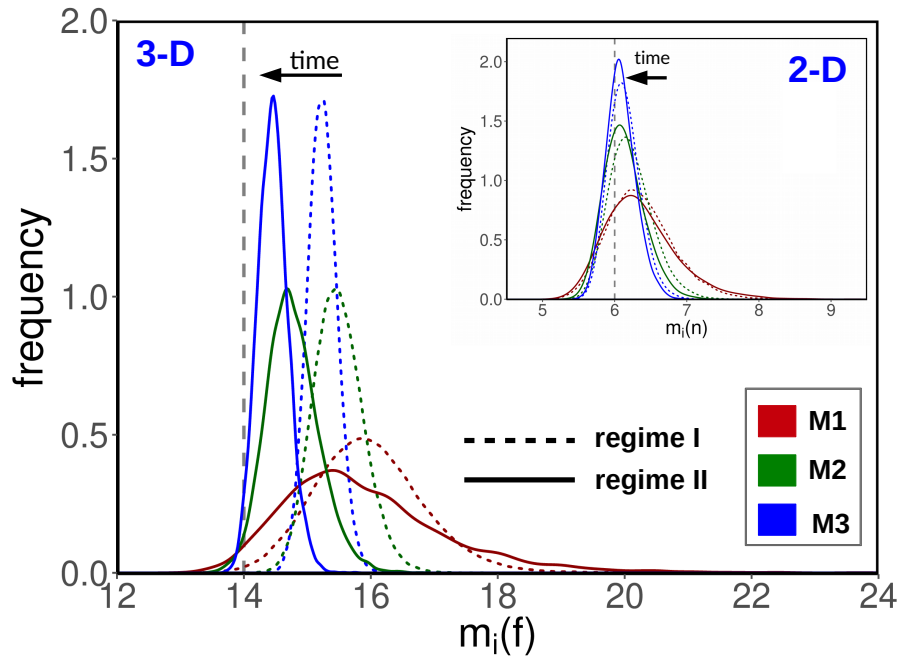


Figure 6.12: *The initial and QS state transition on topological classes. It is observed that the 2-D transition is quite faster than the 3-D results.*
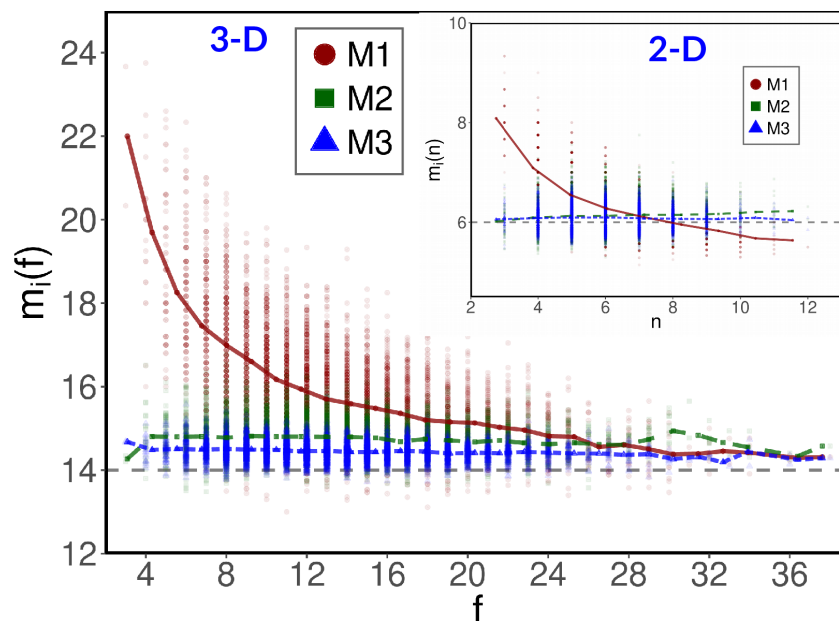
*Figure 6.13: The Aboave-Weaire law for short- and long-range neighbors in 2-D and 3-D. The best-fitted lines are also shown. The long-range neighbors show weaker correlation behavior than first neighbor.*

of the first neighbor clusters over the long-range interactions.

## 6.3.9    Effect of initial fillings

In this section, the influence of initial microstructural variations on NGG circumstances is examined. The Voronoi algorithm has been modified to produce different initial GSD's. In this preliminary work, reaching the QS state with respect to their initial microstructure is only interpreted in terms of their geometrical constituents. The topological correlation investigation is overlooked here. The five microstructures with a different initial Voronoi filling have been presented in Fig. 6.15. Going from left to right, one can qualitatively see the heterogeneity of the microstructures. The gs0 microstructure is roughly comparable to the initial large-scale, random, polycrystalline arrangement, where the primary grain contacts are arbitrary in nature. The gs1, gs2 and gs3 microstructures show a linear increase of the grain sizes in the microstructure, along the y-direction. The gs4 microstructure shows complex grain-grain interactions, in which the larger-larger and smaller-smaller grain contacts are preferred.

The grain size distribution of the initial and QS state microstructures are shown in Fig. 6.16. The initial GSD for gs0 shows a very sharp peak, compared to the remaining cases. The peak of the GSD for gs4 is shifted to the left, while the microstructure comprises two different sets of grain sizes. The general Hillert and Weibull GSD formulations are overplotted. However, our initial GSD's are not approximated by the Weibull and Hillert
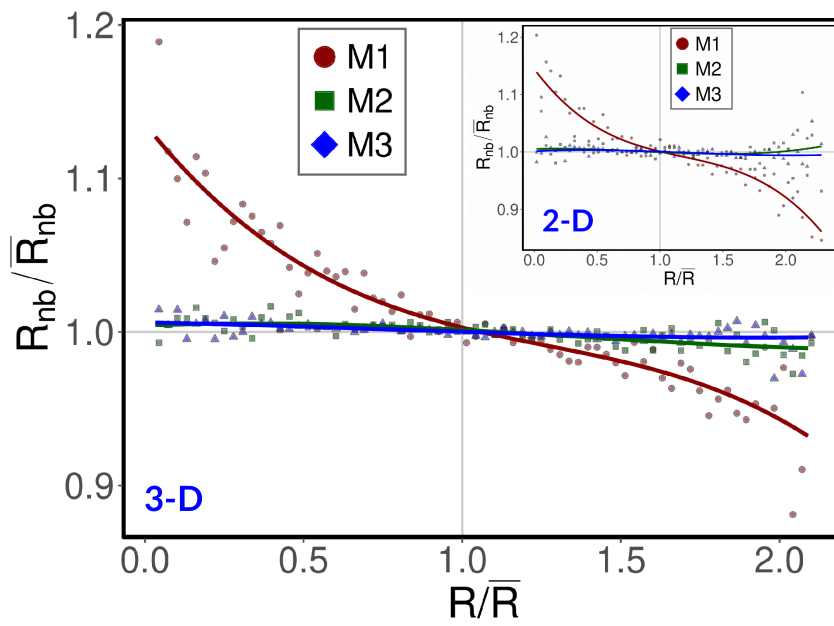
Figure 6.14: Grain size correlations for short- and long-range neighbors. The correlation be-
havior decreases by increasing the neighbor layer arrangement. Solid line represents the fit.
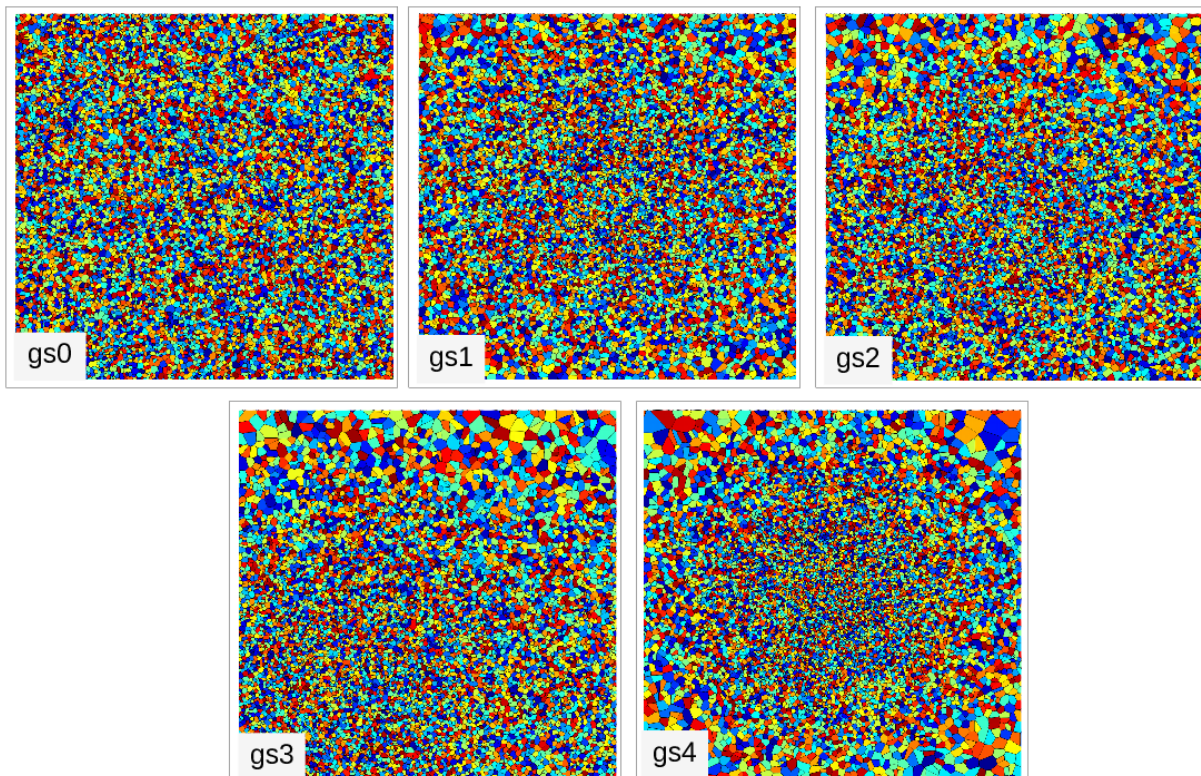


Figure 6.15: Different initial Voronoi fillings for the 2-D simulations.
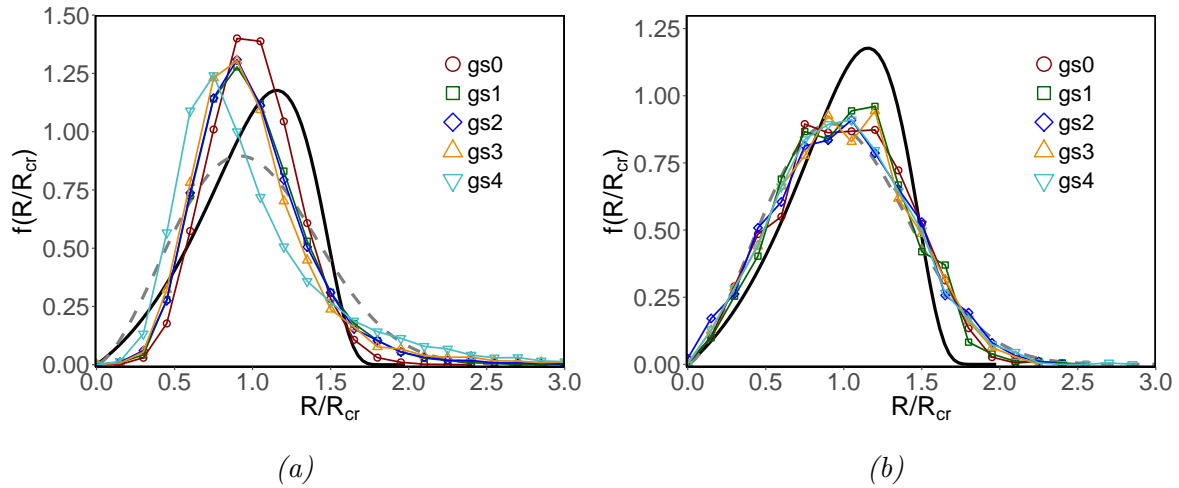
*Figure 6.16: Grain size distribution at 2-D (a) initial and (b) QS state microstructures. The black solid line corresponds to a Hillert function and the dashed line denotes the fit of the Weibull functional.*

functional fit. The microstructures gradually reorder themselves to reach the QS state throughout the evolution process. The above figure asserts that the GSD of the QS state is compatible with the Weibull function. In the earlier section, we also found that the Weibull function can be best suited for the large-scale 2-D results.

The mean grain size evolution of all five cases in the log scale is shown in Fig. 6.17. The two general and distinct grain growth regimes can be perceived. After the transient period, the microstructure approaches the QS state. The linear functional fit is affirmed to draw the steady-state regime. The shape of the GSD, in terms of the $\bar{R}.(1/\bar{R})$ parameter, yields $\approx 1.33$. The $\bar{R}_{nb}/\bar{R}$ ratio narrows down to $\approx 1.09$. These perceived 2-D results are consistent with the parameters of the large-scale distribution functional.

In addition to the standard correlation functions, the statical parameters have also been used to quantify the heterogeneities in the microstructure. The Appendix A on statistical functions includes details of the the formulations of grain size and topological distributions. In this section, the statistical self-similarity of the GSD is analyzed. Hence the coefficient of variation (CV), the skewness and the kurtosis of the grain size distribution are measured and presented in Fig. 6.18. The CV[R] is a nondimensional parameter to establish the variations of the size distribution. By using this nondimensional parameter, a one-to-one comparison is possible among different simulation methods. The analytical and numerical studies rarely report the CV[R], following the normal grain growth hypothesis. The classical Hillert mean field approximation returns $CV[R] \approx 0.33$. However, the previous simulation studies return a value which is slightly higher than the theoretical value. Wang et al. obtained $CV[R] = 0.44$ from 2-D MC simulations and they report that the $CV$ measure of the QS state is independent of the initial microstructure, under NGG conditions [145]. The recent publication from Zöllner stated that the $CV$
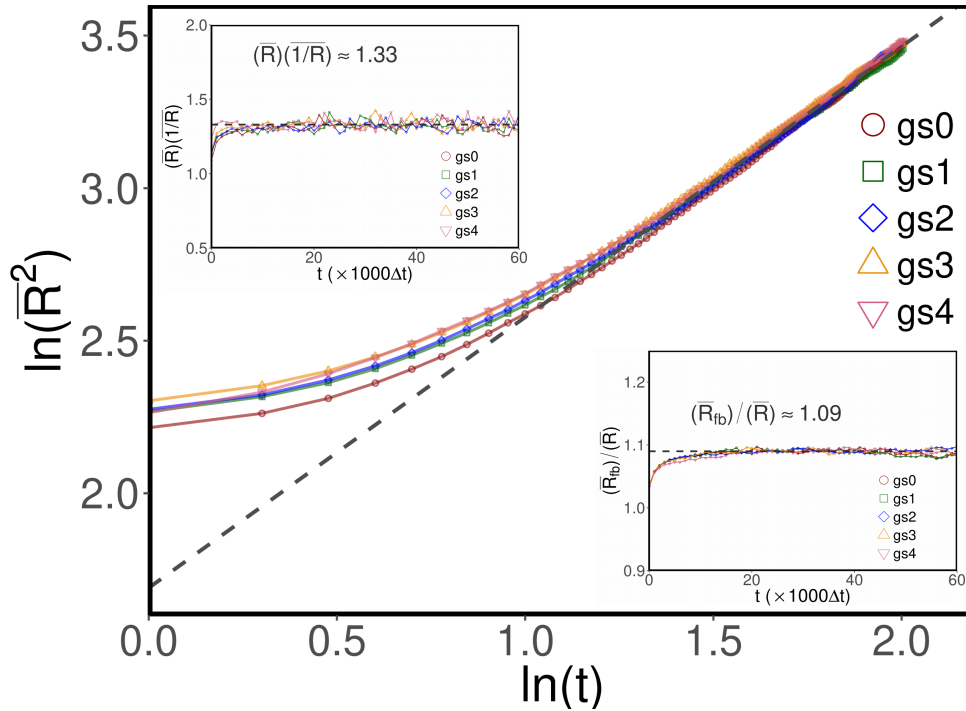
*Figure 6.17: The mean grain size evolution in the log-log scale, for different 2-D initial conditions. The subplot fit parameters of $(\bar{R})(\overline{1/R}) \approx 1.33$ and $(R_{nb}/\bar{R}) \approx 1.09$ are comparable to the large-scale 2-D results in the previous section.*

measure approach to $\approx 0.388$ from 2-D MC simulations [172]. The consequence of the initial GSD only limit the time span to lead a steady-state regime in the microstructure.

We noticed that the microstructural heterogeneities could not induce an abnormal grain growth behavior in our results. The above statement can be backed by the our recent publication [2], where we demonstrated that only the size advantage is not sufficient to provoke the abnormal grain growth. While the absolute growth rate of the pre-existing abnormal grains is fast, their relative growth rate is lower than the normal grains. As time progresses, the larger grains tend towards the distribution of the normal grains. The skewness and kurtosis factor symbolizes the symmetry and tail of the size distribution during the microstructural development. After the transient period, the whole microstructure acts very similarly during further evolution. In the microstructure, the time-invariant behavior perseveres.

The 3-D extension of the study of the disordered microstructure is conducted for four different GSD settings. Fig 6.19 shows the initial Voronoi filling of grains in the gs0, gs1, gs2 and gs3 set-up. The size heterogeneities and the directional configurations of the neighbors can be comprehended qualitatively. During the evolution, the microstructures in the initial and QS state are characterized by adopting similar statistical parameters. The transition in the GSD at the initial and QS state is checked to validate the functional fit hypothesis and is shown in Fig. 6.20. While increasing the heterogeneities in the
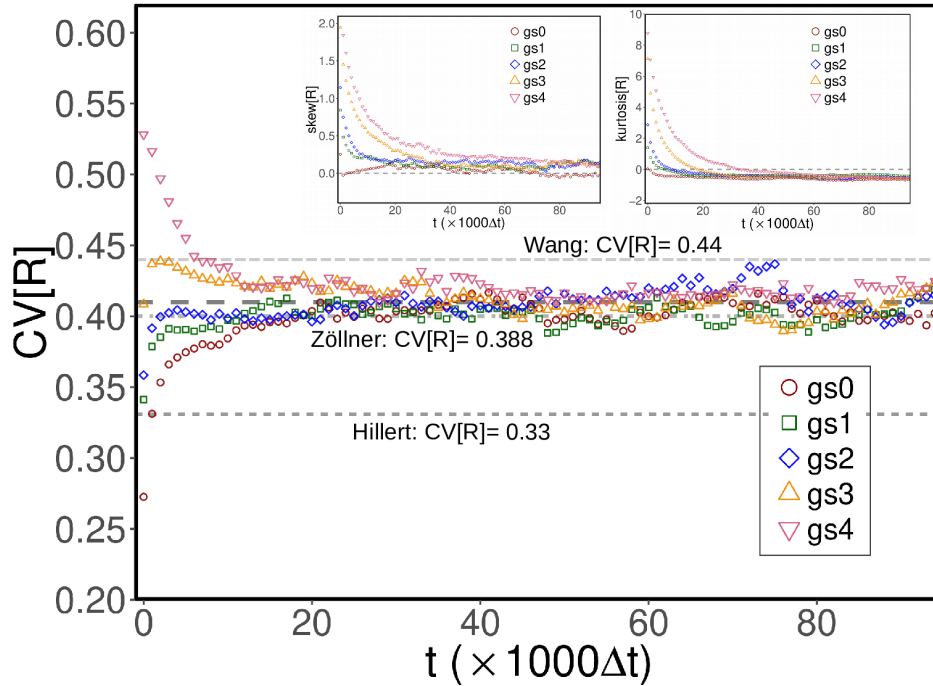
*Figure 6.18: The statistical functions that precisely describe the GSD. The obtained CV[R] is consistent with the MC results. The convergence of skewness and kurtosis confirms the QS state. The time to reach the QS state largely depends on the initial heterogeneities of the material.*

microstructure, the initial GSD curve shifts towards the left-hand side and the peak value drops considerably. Examining the transient regime, the GSD sustains the Hillert regime for some intermediate time. Nevertheless, the provided GSD at the QS state reasonably demonstrates that the Hillert and Weibull functions are not a perfect approximation for them.

The log-scale grain size evolution shows the transient and QS state regimes in Fig. 6.21. The time taken to attain a QS state is largely influenced by the initial heterogeneities. $\bar{R}.(1/\bar{R}) \approx 1.32$ and $\bar{R}_{nb}/\bar{R} \approx 1.15$ are consistent with the results from the previous section. The present 3-D results in Fig. 6.22 yield $CV[R] \approx 0.40$, which is similar to the 2-D results. The skewness and kurtosis values asserted that the microstructure already reached a QS state, in terms of their geometrical features. Certainly, the topological behavior of self-similarity is also expected from the microstructure. With this in mind, the short- and long-range neighbor correlations under initial heterogeneity conditions will be focused for the future works.

## 6.4   Summary

The microstructure of a polycrystalline material exhibits a self-similar state. In the absence of any phase transformation, it thus invariably includes a 'transient and QS state
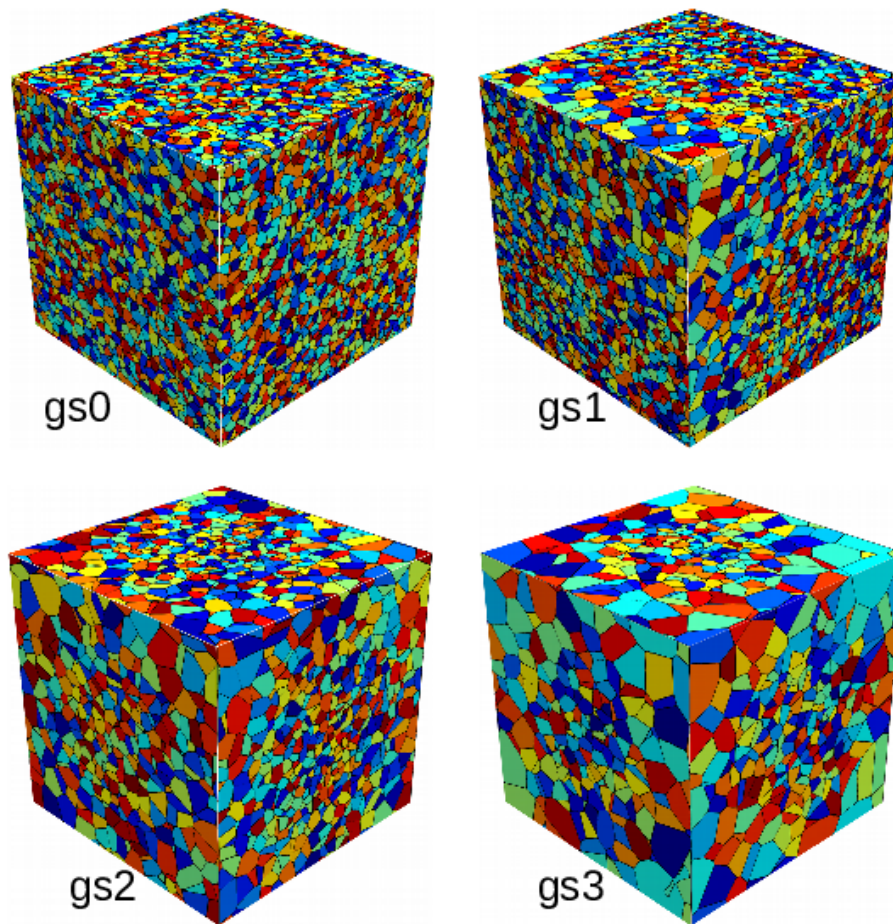
Figure 6.19: *Different initial Voronoi fillings for 3-D simulations. The nonrandom arrangement of grains can be seen.*
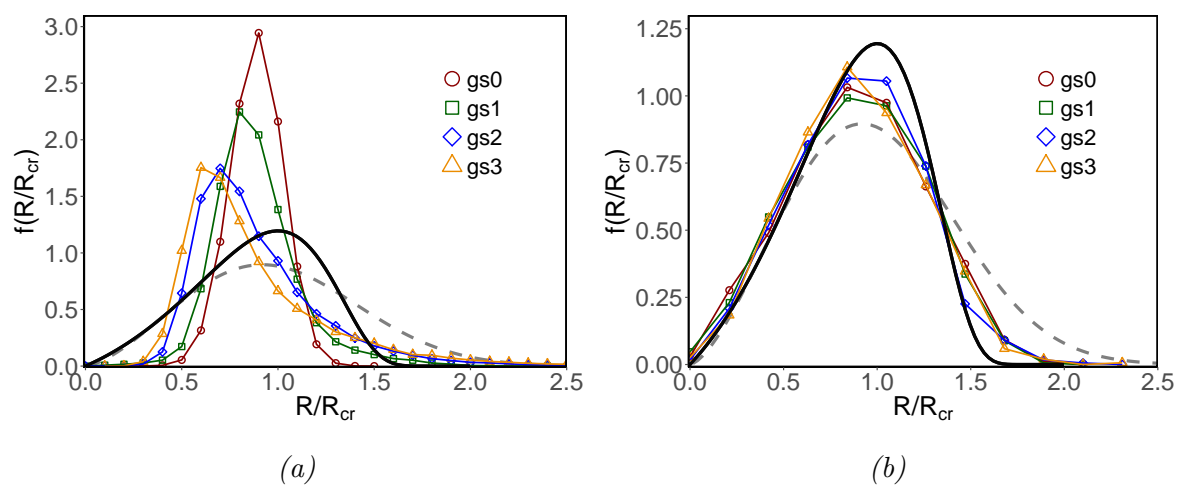


Figure 6.20: *Grain size distribution at (a) initial and (b) QS-state microstructures in 3-D. The black solid line corresponds to a Hillert function and the dashed line denotes the fit of the Weibull functional.*
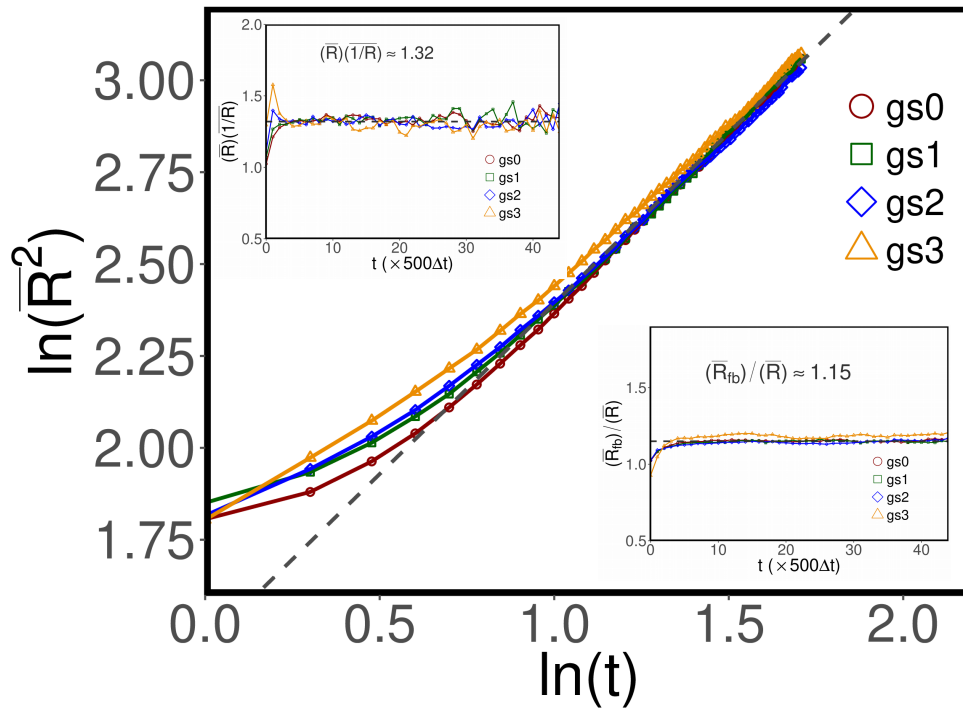
Figure 6.21: *Mean grain size evolution in the log-log scale, for different 3-D initial set-ups. The subplot fit parameters of $(\bar{R})(1/\bar{R}) \approx 1.32$ and $(R_{nb}/\bar{R}) \approx 1.15$ are consistent with the large-scale 3-D results.*
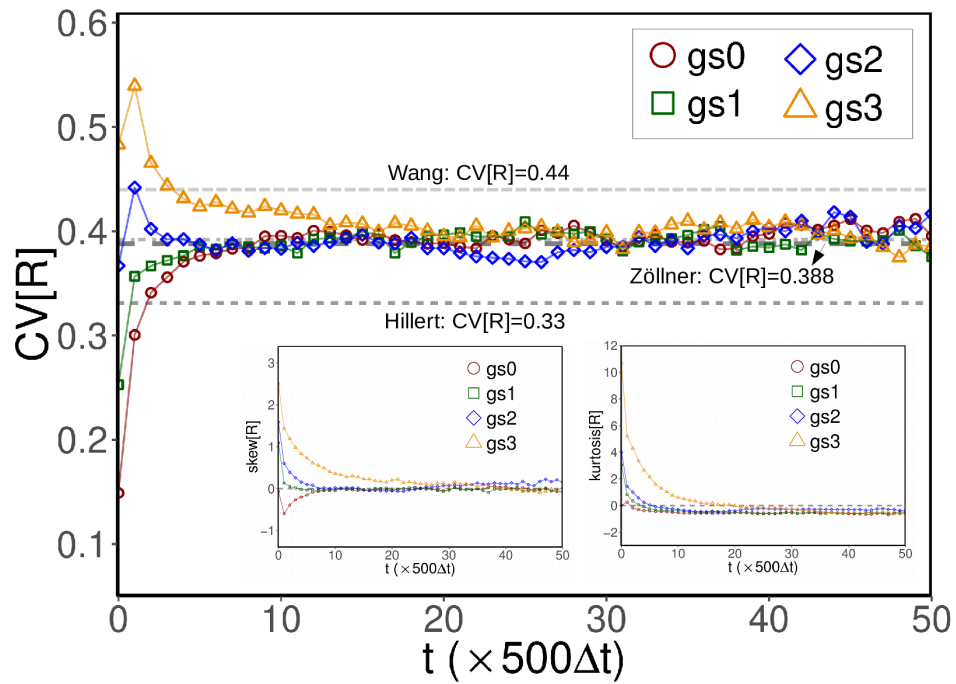


Figure 6.22: *Statistical parameters to quantify the GSD with time.*

growth regime', during which the microstructure gradually attains a time-invariant distribution. However, during this growth period, owing to the increase in the critical grain size $R_{cr}$, the number of grains eventually decreases. Thereby, the microstructure should satisfy the geometrical and topological constraints.

Following the postulation of the linear growth behavior of the grains, theoretical studies claim that these grains develop similarly in 2-D and 3-D systems, as the evolution proceeds, which is described by the time-variant distribution or correlation functions. In the present work, a thermodynamically consistent phase-field approach is concurrently applied for the extensive analysis of the NGG behavior in 2-D and 3-D. Considerably different from the existing studies, this work characterizes microstructures with precise geometrical and topological correlation functions.

In our study, the analysis of the transition and QS state microstructures reveals fluctuations in their distribution functions, which are in complete agreement with the existing research. While in 2-D, the GSD forms close to a Weibull functional, the Hillert approximation is quickly reached in 3-D, which slightly contradicts the GSD developing at a later time. In other words, it is identified that the longtime annealing ensures that neither the Hillert nor the Weibull function corresponds to the exact 3-D GSD. When the dimensionality of the system changes, the kinetics of grain growth does not strictly follow the linear growth behavior. This can be demonstrated by computing Hillert's geometrical constant in 2-D and 3-D, for different time steps. The observed geometrical constant values are roughly comparable with earlier findings. Moreover, from our simulations, the empirical growth laws, based on the first neighbor correlations, have also been proposed.

A comprehensive understanding of the correlations of the short- and long-range neighbors is presented by employing efficient statistical methods. It is perceived that the geometrical and topological evolution of the first neighbor grains, which shows the strong correlation, predominantly weakens for the long-range interactions. This correlation behavior of the surrounding grains eventually exhibits a time-invariant behavior. In order to quantify the influence of the initial arrangements of the grains, on reaching the self-similar state, a considerable number of simulations is investigated. With an increase in the initial heterogeneities of the microstructure, the duration of the transition period increases. Finally, when the microstructure reaches the QS state, describing the statistical parameters, grains significantly accompany the time-variant distribution.

# Chapter 7

# Transient phenomena induced by 'abnormally' large grains during isotropic grain growth.

## 7.1 Introduction

In the absence of phase transformation, microstructural evolution in polycrystalline material is governed by the thermodynamical ability of the system to reduce its grain boundary energy per unit volume. Owing to the extensive influence of the microstructure on the behavior of the material, grain growth is analyzed both theoretically and experimentally, to gain substantial understanding. Despite the influence of several factors, geometrical and topological, which convolute the dynamics of grain growth, it is identified that the grain size distribution remains unaltered all through the evolution during normal grain growth [173, 74, 174]. This time-invariant behavior is simply accounted by the consideration that the entire evolution is governed by the difference in the principal curvature and thus, the larger grains grow at the expense of the smaller ones without noticeably disturbing the size distribution. Hillert, in his seminal work, invokes this consideration and presents an analytical treatment for grain growth as a special case of Ostwald ripening [20]. Accordingly, the approach postulated by Lifschitz and Slyozov [43] and Wagner [44] is extended to encapsulate the evolution of grains in a polycrystalline system. In addition to several other deductions, this approach yields a size distribution function of the form

$$P(u) = (2e)^{\beta} \cdot \frac{\beta u}{(2 - u)^{2+\beta}} \cdot \exp \frac{-2\beta}{2 - u}, \tag{7.1}$$

where $u = R/R_c$ with $R$ and $R_c$ representing the radius of the grain and the critical radius above which transition from shrinkage to growth occurs, respectively. In a 2-dimensional set up, the parameter $\beta = 2$ and $R_c = \overline{R}$, while in 3-D ($\beta = 3$) this relation is expressed as $R_c = (9/8)\overline{R}$. In 2-D, 'normal' grain growth, characterized by the distribution func-

tion in Eqn. 7.1, posits a restriction that maximum grain size can never be greater than twice the average grain size, owing to its mathematical stability. Thus, it was postulated that 'abnormally' large grains with geometrical feature $R > 2R_c$ grow predominantly at the expense of other smaller grains disrupting the time-invariant distribution [20]. However, subsequent theoretical studies on pure polycrystalline systems which overlook the influence of crystallographic orientation and pinning, show that the size-advantage of the 'abnormally' large grains (referred to abnormal grains henceforth) does not induce 'abnormal' grain growth, wherein few grains grow at the expense of the others. On the contrary, it has been identified that the abnormal grains induce a transient period during which the evolution tends towards steady-state growth [27, 24, 25]. Conventionally, this steady-state grain growth is recognized by the time-invariant behavior of the size distribution and adherence of the growth kinetics to the power law, although few deviations in the power-law have been reported [29].

Microstructures resulting from the manufacturing processes rarely exhibit complete adherence to a well-defined grain size distribution. Therefore, heat treatment techniques that induce grain growth in such polycrystalline structures invariably involve a transition period over which self-similar transformation is achieved [175, 176]. Owing to its practical implications, theoretical studies attempting to relate the influence of the initial microstructure on these transient phenomena have increasingly been reported [177, 25, 178]. Simulation studies in addition to the analytical approaches have been vital in explicating the physics undergirding grain growth. Moreover, initial report on the onset of a transition period in the presence of abnormally large grains, contradicting the view of abnormal grain growth, pertains to Monte-Carlo simulations [27].

Often these early attempts were limited owing to the computational restriction. For instance, the aforementioned simulation study analyses a small regime of the microstructure with a single abnormal grain fixed in the center. However, advancements and increased availability of the computational resources enable the simulation of the polycrystalline structures that resemble physical microstructures. Recently, Zöllner et al. by employing one such advanced simulation technique, (Potts types Monte-Carlo) distinguished and analyzed the transient phenomena observed in a supposedly random microstructure [172]. Despite the role of the abnormally large grains in governing the evolution of the microstructures, studies have been predominantly focused on abnormal grain growth induced by difference in the grain boundary energy and mobilities [179, 180, 181, 182]. Thus, investigations on the influence of the abnormally large grains on the dynamics of grain growth have not been sufficiently reported yet. Thus, in the present study, a different but well-known approach, referred to as phase-field modeling, is employed to elucidate the behavior of abnormal grains during an isotropic grain growth. Thus, in the present work, a thermodynamically-consistent phase-field approach is employed to understand the transient phenomena induced by the size-advantage abnormal grains.

## 7.2   Domain set-up

The variational derivative of functional $\mathcal{F}$ in Eqn. 3.7 generates scalar and vector entities corresponding to the derivatives with respect to phase field variable ($\phi_\alpha$) and gradient ($\boldsymbol{\nabla}\phi_\alpha$), respectively. In order to solve the phase-field evolution equations, a finite difference algorithm with explicit marching scheme (forward Euler scheme) and a domain decomposition for scalable parallelization is implemented across an uniform numerical grid [100, 154]. Moreover, equal grid spacings are assumed in each spatial dimensions, such that in 2-D $\Delta x = \Delta y = 1.0$. The length scale parameter $\epsilon$ which ascertains the width of the diffuse interface is set to $4\Delta x$ for all the simulations after initial optimization. *Locally reduced order parameter optimization (LROP)* is employed to enhance the computational efficiency which optimizes both memory and time consumption of the simulation by restricting the number of order parameters solved at each grid point [58, 156, 183].

In order to ascertain an optimum domain size, so that the statistical spread is sensible all through the evolution, three domain sizes $1024\times1024$, $2048\times2048$ and $3000\times3000$ gridpoints are considered. Monitoring the evolution of the grains in all three domains, the size of $2048 \times 2048$ is identified to be optimum. Random distribution of about 24000 grains, as depicted in Fig. 7.1a, is achieved by Voronoi tessellation, as described in [184, 157]. For all the simulations involved in the present analysis, periodic boundary conditions are assigned to the domain boundaries. The statistical spread on each simulation is separately included in the supplementary data.

Generally, the abnormally large grains are introduced into the random polycrystalline structure in the form of the spherical grains of desired size [27, 185, 186]. However, in almost all existing studies, the abnormal grains in a given microstructure are assumed to be geometrically identical. Since, this consideration deviates from the physical observations, in the present study, abnormal grains with varying degree of abnormality and distance between them, as shown in the Fig 7.1a, are considered. To achieve this random distribution of the abnormal grains, two parameters $R_{s_i}$ and $d_0$ are assigned, where $i$ can be $1, 2, 3...n$ and $n$ is the total number of abnormal grains in the domain. The radius of an abnormal grain $i$ is expressed as $R_i^{ab} = 2\overline{R} + R_{s_i}$, where $R_{s_i}$ governs the degree of abnormality. For a given microstructure, a maximum value for $R_{s_i}$ is defined and a condition $R_{s_i} > 0$ is set. Since the grains of size $R_i^{ab} = 2\overline{R}$ belong to the tail-end of the quasi-stationary distribution in Eqn. 7.1 *i.e* largest of the normal grains, the aforementioned condition introduces abnormal grains. Additionally, by assigning unique and random values of $R_{s_i}$, for each abnormal grain, randomness in the degree of abnormality or difference in the size of the abnormal grains is achieved. Furthermore, varying-distance between the abnormal grains is established by involving a parameter $d_0$. If the distance between two abnormal grains is expressed as $d_l + d_0$, then fixing the least distance between a pair of abnormal grains ($d_l$) and defining a range for $d_0$ yields random distribution of the abnormal grains upon iteration of the scheme over the domain grid points.
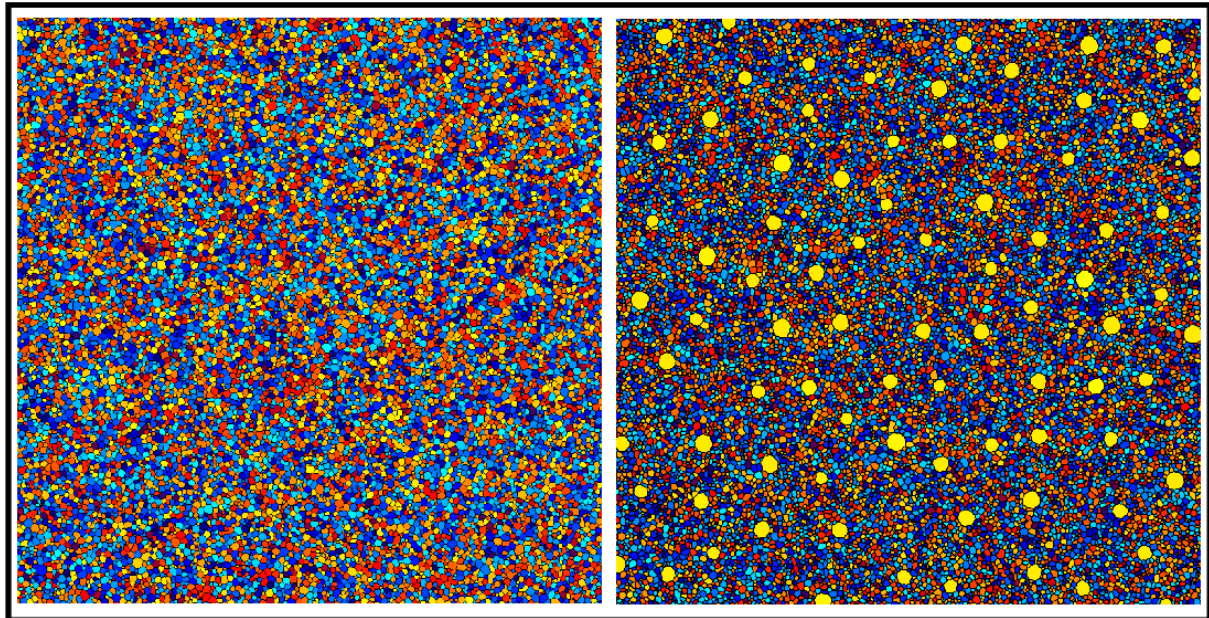
*(a)*
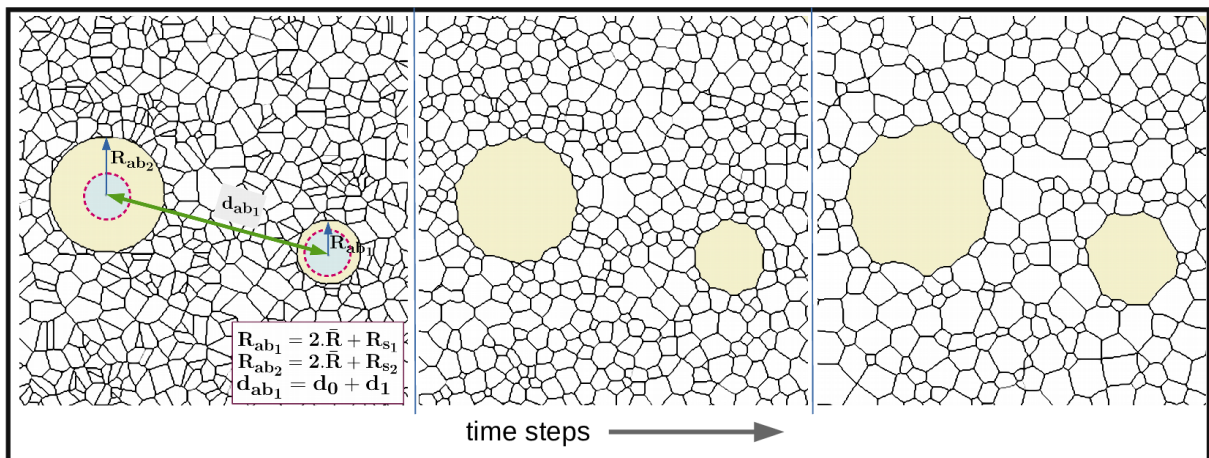


*(b)*

*Figure 7.1: (a) Normal grain distribution achieved through the Voronoi tessellation (left) and randomly distributed abnormal grains in a polycrystalline structure (right) of 2-dimension. (b) Topological re-adjustment of the abnormal grains in the initial stages of the grain growth, which facilitates the adaptation of these grains in accordance with its neighbors.*
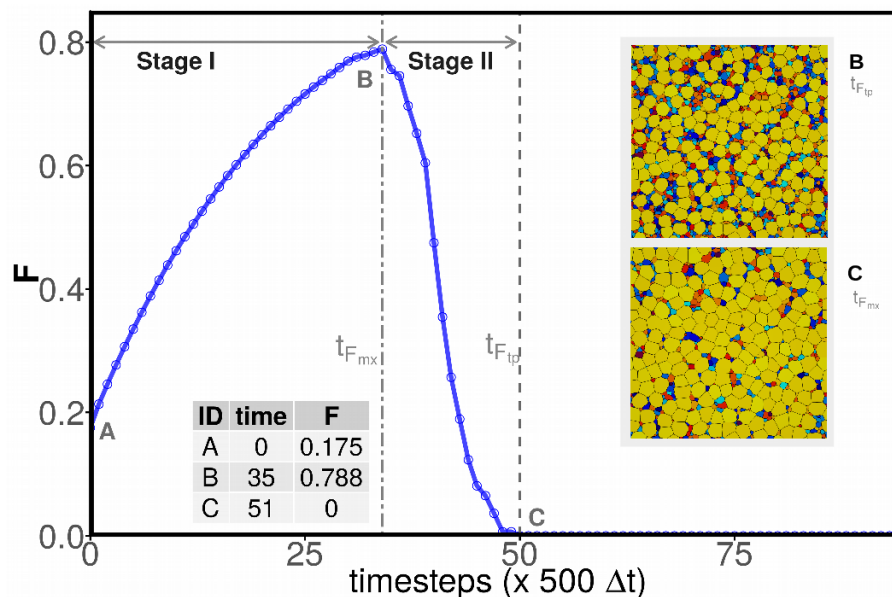
Figure 7.2: Change in the volume fraction of the abnormal grain ($F$) with time as the average grain size $R_c$ monotonically increases in a microstructure with the initial volume-fraction of abnormal grains about $0.175$ (simA).

The abnormal grains introduced onto the random distribution of normal grains are circular and appear topologically favorable owing to its relatively increased number of neighbours. However, this topological-strength is diminished in the early stages of the evolution when the abnormal grains adapt a physical shape as shown in Fig. 7.1b. This topological re-adjustment of the abnormal grains, during which the non-physical circular shape of the grain is replaced with a shape compatible with the geometrical and topological nature of its neighbors, is similar to the observations made earlier [27, 185, 186].

## 7.3    Results and discussions

### 7.3.1    Temporal evolution of the volume-fraction of the abnormal grains

Benson and Wert, in their theoretical work [178], investigated the transient phenomena by monitoring the volume fraction of the abnormal grains ($F$) during grain growth. Since by definition, the abnormal grains and their volume-fraction $F$ depend on the ever-increasing average grain size $R_c$, which encompasses both normal and abnormal grains, the transition period is characterized by the disappearance of the abnormal grains, signified by $F$ becoming zero. A similar approach is employed in the present phase-field study, and for a microstructure simA with an initial volume-fraction of $0.175$ ($F_o = 0.175$), the temporal evolution of $F$ is monitored and plotted in Fig. 7.2. Consistent with the analytical and
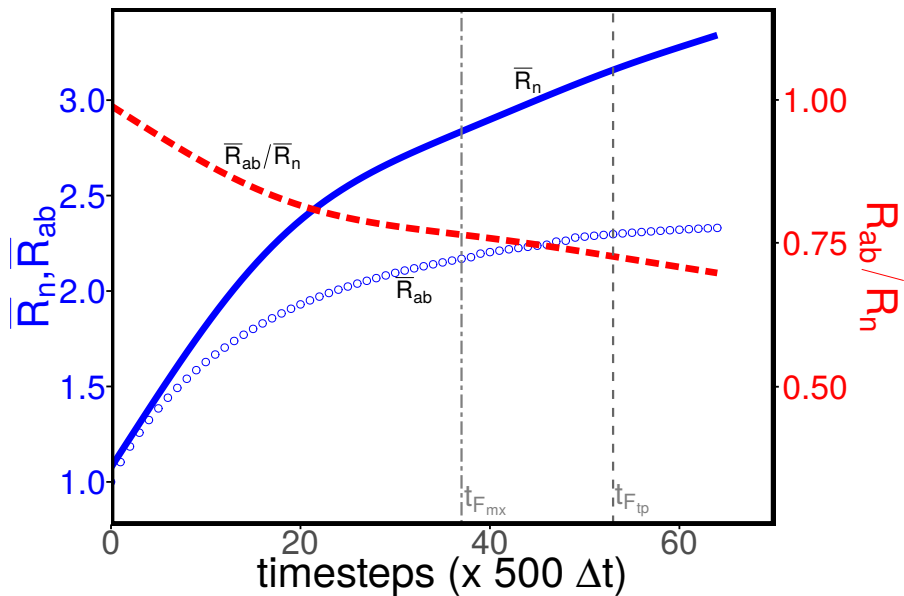
*Figure 7.3: a) Normal and abnormal grains are distinguished in simA. Increase in the average size of the normal grains $\overline{R}_n$ is compared with the change in $\overline{R}_{ab}$, average size of the abnormal grains with time. b) Relative growth of the abnormal grains is illustrated by plotting the ratio of $\overline{R}_{ab}$ and $\overline{R}_n$.*

simulation results [24, 25, 27, 178, 187], Fig. 7.2 indicates that the presence of abnormally large grains, rather than initiating an abnormal grain growth, induces a period of transition during which the volume-fraction $F$ becomes zero. Although, this dissolution of the abnormality in the large grains is expected in a deterministic model based on Hillert's distribution [178], this behavior has not been reported in any phase-field simulations yet. Furthermore, consistent with the theoretical prediction, Fig. 7.2 shows that the temporal evolution of $F$ consists of two stages, *stage*-I and *stage*-II, highlighted by segments $AB$ and $BC$, respectively [178] . In stage-I, the volume-fraction of the abnormally large grains increases monotonically, while $F$ rapidly descends to zero in stage-II. The transition between these two stages occurs at point $B$ wherein volume-fraction of abnormal grains is at its maximum ($F = 0.788$). The graphical representation of the microstructure at point $B$ and $C$ have included in Fig. 7.2. This depiction indicates that, despite the consequential decrease in the volume-fraction of normal grain in *stage*-I, surviving grains exhibit noticeable growth. Influence of this growth of the normal grains is analyzed further to elucidate its role in the transient phenomena.

## 7.3.2   Growth kinetics of normal and abnormal grains

Different from the statistical techniques that exclusively analyze the evolution of the grain size distribution [25, 178], the phase-field study facilitates the investigation of individual grains during grain growth [1]. This distinctive feature of the present approach is in-

voked to understand the temporal change in the volume-fraction of the abnormal grains ($F$) illustrated in Fig. 7.2. Upon distinguishing the normal and abnormal grains, that constitute the microstructure $simA$ of $F_o = 0.175$, the increase in the average radius of these grains are normalized and plotted distinctly in Fig. 7.3. For this illustration, the average size of the normal ($\overline{R}_n$) and the abnormal grains ($\overline{R}_{ab}$) are normalized by their corresponding values at initial time-step, $\overline{R}_n^o$ and $\overline{R}_{ab}^o$, respectively. In complete agreement with the theoretical predictions [24, 25, 27], the average size of the normal grains $\overline{R}_n$ increases more rapidly when compared with the abnormal grains $\overline{R}_{ab}$. The study on relative growth kinetics of single pre-existing abnormal grains in matrix of fine grains are shown in Appendix C. This behavior accounts for the lack of abnormal grain growth in the presence of large grains ($R > 2R_c$). To unravel the evolution exhibited by $F$ in Fig. 7.2, points $B$ and $C$ wherein the $F$ reaches its maximum ($F_{mx}$) and zero ($F_{tp}$), respectively, are overlaid in Fig. 7.3. In contrast to the normal grains which continue to grow progressively, the growth kinetics of the abnormal grains get saturated eventually. However, it is evident that in the initial stages of the grain growth, similar to the normal grains, the abnormal grains exhibit a rapid growth till the maximum volume fraction is attained $F_{mx}$. Therefore, based on Fig. 7.2, it can be stated that the monotonic increase in $F$ during stage-I, is caused by this initial rapid growth of the abnormal grains. As this growth rate gradually subsides beyond $F_{mx}$, stage-II initiates and $F$ rapidly turns zero. Furthermore, to verify the coherence of the present simulation, the relative growth of the abnormal grains, determined by the ratio of $\overline{R}_{ab}$ and $\overline{R}_n$, is plotted in Fig. 7.3. Consistent with the analytical predictions [24, 188, 189], the relative growth of the abnormal grains $\frac{\overline{R}_{ab}}{\overline{R}_n}$ follows a negative slope. This investigation of the growth kinetics definitively indicates that the accelerated coarsening of the normal grains, rapidly increases the average grain size $R_c$ when compared to its abnormal counterparts, which ultimately drives the evolution of $F$ to zero.

### 7.3.3   Change in the grain size distribution

The overall evolution of the microstructure during grain growth can be expounded from the temporal change in the grain size distribution. Thus, the size distributions of the normal and pre-existing abnormal grains are analysed to capture the transformation accompanying the transient phenomena induced by the abnormal grains. The overall grain size distribution of the microstructure $simA$ at the initial time step is illustrated in Fig. 7.4a, wherein the distribution of the normal grains are distinguished from the abnormal ones. The histogram representation of this distribution is included as an inlay in Fig. 7.4a. This representation of the microstructure introduces an additional parameter $\overline{U}_{max}$ which is the ratio of the mean radius of the abnormal grains $\overline{R}_{ab}$ and the overall average radius $R_c$. This parameter $\overline{U}_{max}$, referred to as the degree of abnormality, describes the geometrical nature of all the abnormal grains present in simulation setup. It is evident from Fig. 7.4a
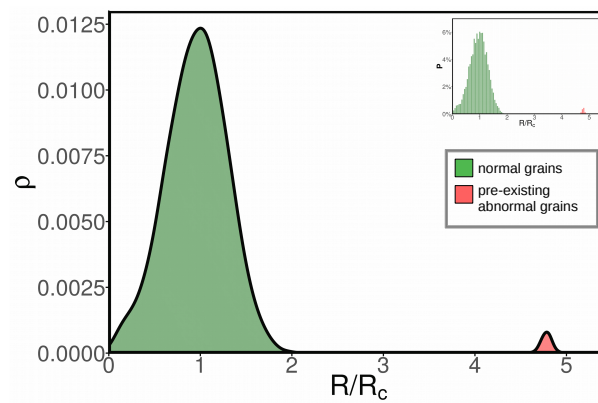
*(a)*
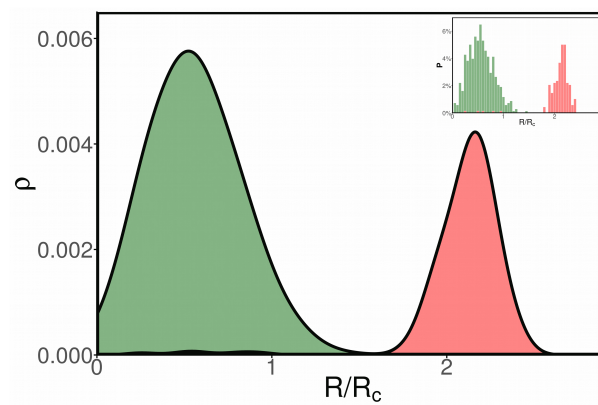


*(b)*
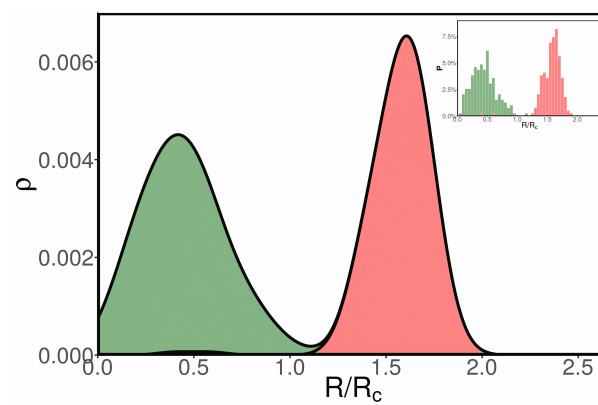


*(c)*

*Figure 7.4: Temporal evolution of the grain size distribution of simA at (a) $t_{F_0}$, (b) $t_{F_{mx}}$ and (c) $t_{F_{tp}}$. Increase in the dominance of the abnormal grains is presented by distinguishing the normal and abnormal through appropriate color scheme.*

that for $simA$, the degree of abnormality $\overline{U}_{max}$ is approximately equal to 5.

In the early stages of the grain growth, both normal and abnormal grains grow progressively, as elucidated in Sec. 7.3.2. However, the increased rate of coarsening exhibited by the normal grains, significantly influences the overall increase in the average grain size $R_c$. Since this enhanced temporal evolution of the average grain size is noticeably greater than growth rate of the pre-existing abnormal grains, the distribution of the abnormal grains shifts to the left. Additionally, the growth of the abnormal grains at the expense of the normal (smaller) grains increases its dominance in the distribution plot. The size distribution at $F_{mx}$, when the volume fraction of the abnormal grains $F$ is at its maximum, is presented in Fig. 7.4b. This illustration coherently indicates the shift in the size distribution and an increased dominance of the abnormal grains, collectively accomplished by growth of the normal and abnormal grains. Although the present observation contradicts the claims of the deterministic analysis [178], which states that in stage-I grain growth operates towards the formation of unimodal distribution, it is in complete agreement with the statistical predictions on the formation of bimodal distribution [25, 177]. Furthermore, as shown in the Fig. 7.4c representing the grain size distribution at $F = 0$, the continued increase in the average grain size shifts the distribution of the abnormal grains to the right within $2R_c$. This shift in the size distribution of the abnormal grains ensures the complete lack of grains with size greater than $2R_c$, characterizing the 'apparent' onset of steady-state grain growth. However, it is evident that the size distribution at $F = 0$ significantly deviates from the expected unimodal stead-state distribution but exhibits bimodal distribution with 'pre-existing' abnormal grains, grains with size greater than $2R_c$ at the initial time step, asserting equal dominance. This analysis suggests that the complete disappearance of the abnormally large grains at $F_{tp}$ does not correspond to the onset of normal grain growth, characterized by the self-similar or time-invariant grain distribution. Therefore, it is important to note that, the transient phenomena considered in the present work exclusively indicates the section of the grain growth during which the volume-fraction of the abnormal grains ($F$) becomes zero, although a steady-state grain growth is not attained.

### 7.3.4   Dominance of pre-existing abnormal grains

As the grain growth proceeds, the dominance of the pre-existing abnormal grains continues to increase in the grain size distribution. Ultimately, as shown in the Fig. 7.5a, the microstructure attains a unimodal distribution entirely comprising of pre-existing abnormal grains with a scant traces of the normal grains. This behaviour indicates that, despite the role of the transient period in eliminating the abnormality of the large grains, by confining it within $2R_c$, the pre-existing abnormal grains prevail through the grain growth and ultimately, govern the resulting microstructure. Furthermore, to account for the influence of this pre-existing abnormal grains on the kinetics of the grain growth, the

*(a)*                                                                          *(b)*



*(c)*
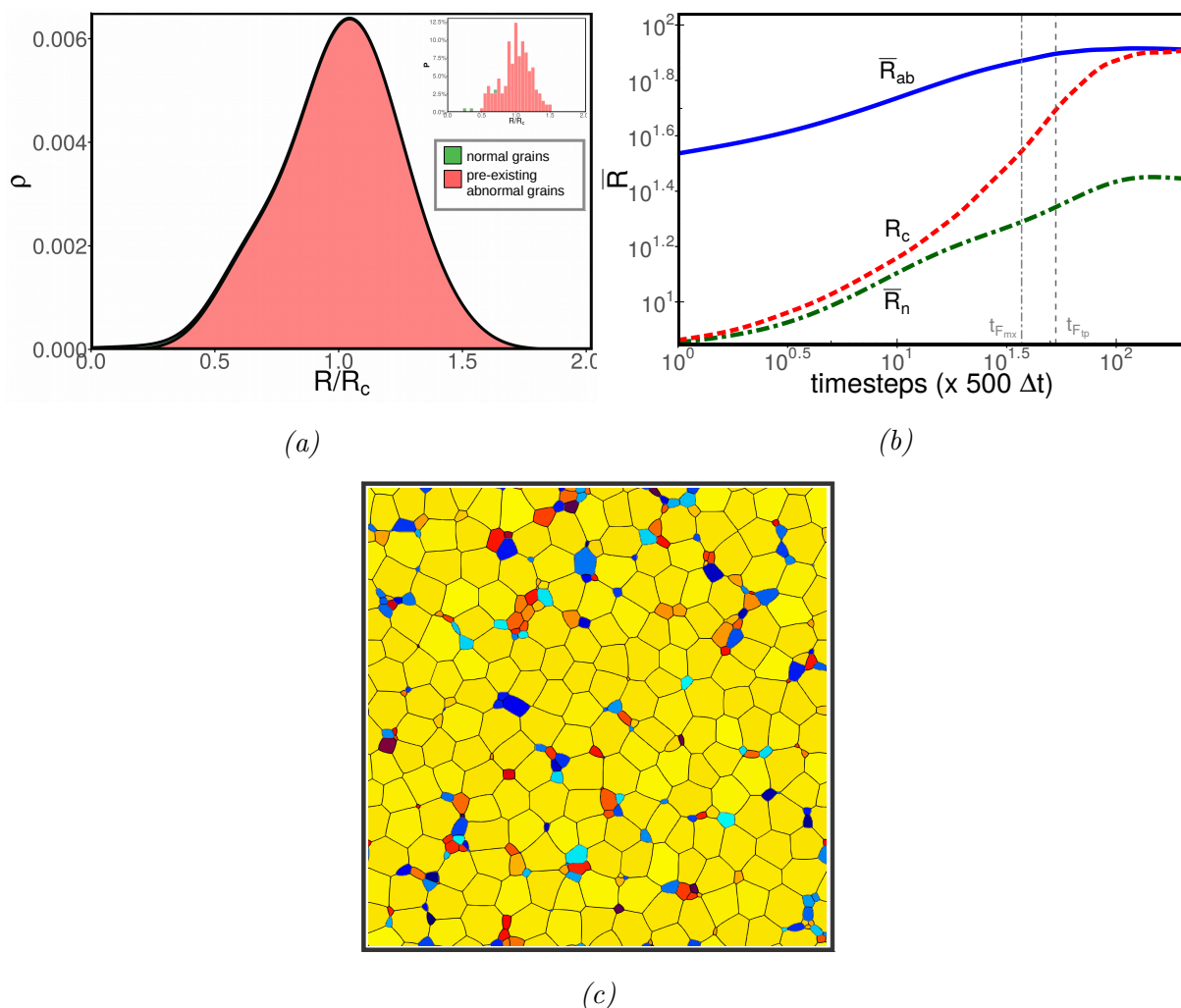
*Figure 7.5: (a) Grain size distribution of simA when unimodal distribution is achieved. Color scheme used in Fig. 7.3 is employed to highlight the dominance of the pre-existing abnormal grains. b) Increase in average grains size of normal and abnormal grains, $\overline{R}_n$ and $\overline{R}_{ab}$ respectively, without normalization. Corresponding change in the average grain size $R_c$ is included to illustrate its dependence on normal and abnormal grains. c) Polycrystalline structure of simA when unimodal distribution is attained. All the pre-existing abnormal grains are assigned yellow color.*
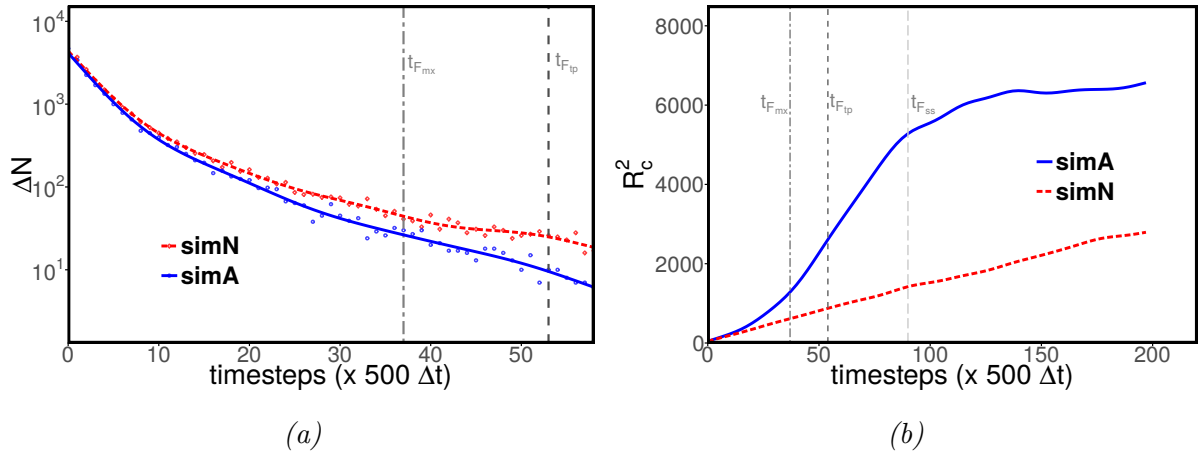
*Figure 7.6: (a) Comparison of the number of disappearing grains $\Delta N$ at each time for simA and a normal grain distribution. (b) Adherence of simA to the power-law from $t_{F_{ss}}$, characterizing the onset of steady-state grain growth, and its deviation from disappearance of abnormally large grains $t_{F_{tp}}$. $R_c$ is the critical radius of the microstructure.*

change in average size of the abnormal $\overline{R}_{ab}$ and normal grains $\overline{R}_n$ with time are plotted along with the critical radius $R_c$ in Fig. 7.5b. This illustration reveals that in the initial stages of the grain growth, the kinetics is considerably influenced by the normal grains. But as the transformation proceeds, the evolution of the overall mean radius $R_c$ progressively shifts towards $\overline{R}_{ab}$. This shift in the evolution of $R_c$ substantiates the gaining influence of the pre-existing abnormal grains on the growth kinetics [25, 177].

The microstructure corresponding to the grain size distribution illustrated in Fig. 7.5a is shown in Fig. 7.5c. The pre-existing abnormal grains, assigned yellow, noticeably dominate the final microstructure with the small remnant of the normal grains. Since these abnormal grains are introduced in the form of topologically favorable circular grains, an additional advantage over the normal grains is expected. However, the role of this topological advantage on the dominance of the pre-existing abnormal grains can be considered minimal because, as these abnormal grains grow at the expense of the other grains, its topological feature (edge-class) is reduced with decrease in the number of surrounding grains, eventually making it topologically indistinguishable. This factor indicates that the dominance of the pre-existing abnormal grains in the microstructure is solely governed by its geometrical nature (size). In other words, it can be stated that, although the size-advantage of abnormal grains does not warrant an increased growth kinetics, it ensures the progressive dominance of the pre-existing abnormal grains in the microstructure.

### 7.3.5   Overall kinetics of the evolution

Akin to the change in the average grain size ($R_c$), the kinetics of grain growth can also be assessed by the change in the number of grains [20, 172]. The difference in the number of grains , *i.e*, the number of grains vanishing, at each time-step is monitored and plotted for *simA* and normal microstructure *simN* (Fig. 7.1a) in Fig. 7.6a. Although in the very early stages, the number of disappearing grains $\Delta N$ appears to be unaltered by the presence of abnormal grains in *simA*, a difference is introduced in the following time-steps. As the grain growth proceeds, the number of disappearing grains in the normal microstructure becomes greater than *simA*. This disparity between the normal microstructure and *simA* continues to increase progressively with the microstructural evolution. In order to understand the difference in $\Delta N$, the growth kinetics of *simA* and *simN*, in terms of the temporal change in critical radius $R_c$, is compared in Fig. 7.6b. Consistent with the analytical predictions, the normal grain distribution *simN* evidently follows power-law $R_c \propto t^{0.5}$. However, as elucidated in the previous sections, an expeditious increase in $R_c^2$ is observed in *simA*, owing to the accelerated growth of the normal grains in the abnormal grains (Fig. 7.3). In *simA* the number of disappearing grains $\Delta N$ is entirely restricted to the normal grains, owing to the size-advantage of the abnormal grains. But the accelerated growth of these normal grains counteracts the disappearance of the grains, thereby exhibiting a low $\Delta N$ when compared to a normal microstructure. In other words, the interplay between the accelerated growth of the normal grains and the growth of the abnormal grain at the expense of smaller grains introduces the disparity in $\Delta N$ observed in Fig. 7.6a. Additionally, Fig. 7.6b substantiates the claim that the complete disappearance of the abnormally large grains ($F_{tp}$) deviates significantly from the adherence of *simA* to the power-law $F_{ss}$, which characterizes the onset of steady-state growth. As recognized in the previous section, this noticeable deviation is due to the existence of bimodal size distribution when $F$ becomes zero. As this distribution transforms to unimodal as shown in Fig. 7.5a after $t_{F_{ss}}$, the growth kinetics in *simA* begin to follow the characteristic power-law of normal grain growth. This behavior indicates that the disappearance of the abnormally larger grains with size greater $2R_c$ cannot be ascertained from the evolution of $R_c^2$.

### 7.3.6   Influence of $F_o$ and $\overline{U}_{max}$ on the transient phenomena

In order to capture the influence of the initial volume-fraction of the abnormally large-grains $F_o$ on the induced transition period, the temporal evolution of $F$ for four different $F_o$ corresponding to various microstructures (*simA*, *simB*, *simC* and *simD*) with constant degree of abnormality, $\overline{U}_{max} = \frac{\overline{R}_{ab}}{R_c} = 5$, is presented in Fig. 7.7a. It is evident from this depiction that with the increase in the initial volume fraction $F_o$, the time-taken for the disappearance of the abnormally large-grains decreases [178]. As elucidated in the

*(a)*

*(b)*

*(c)*
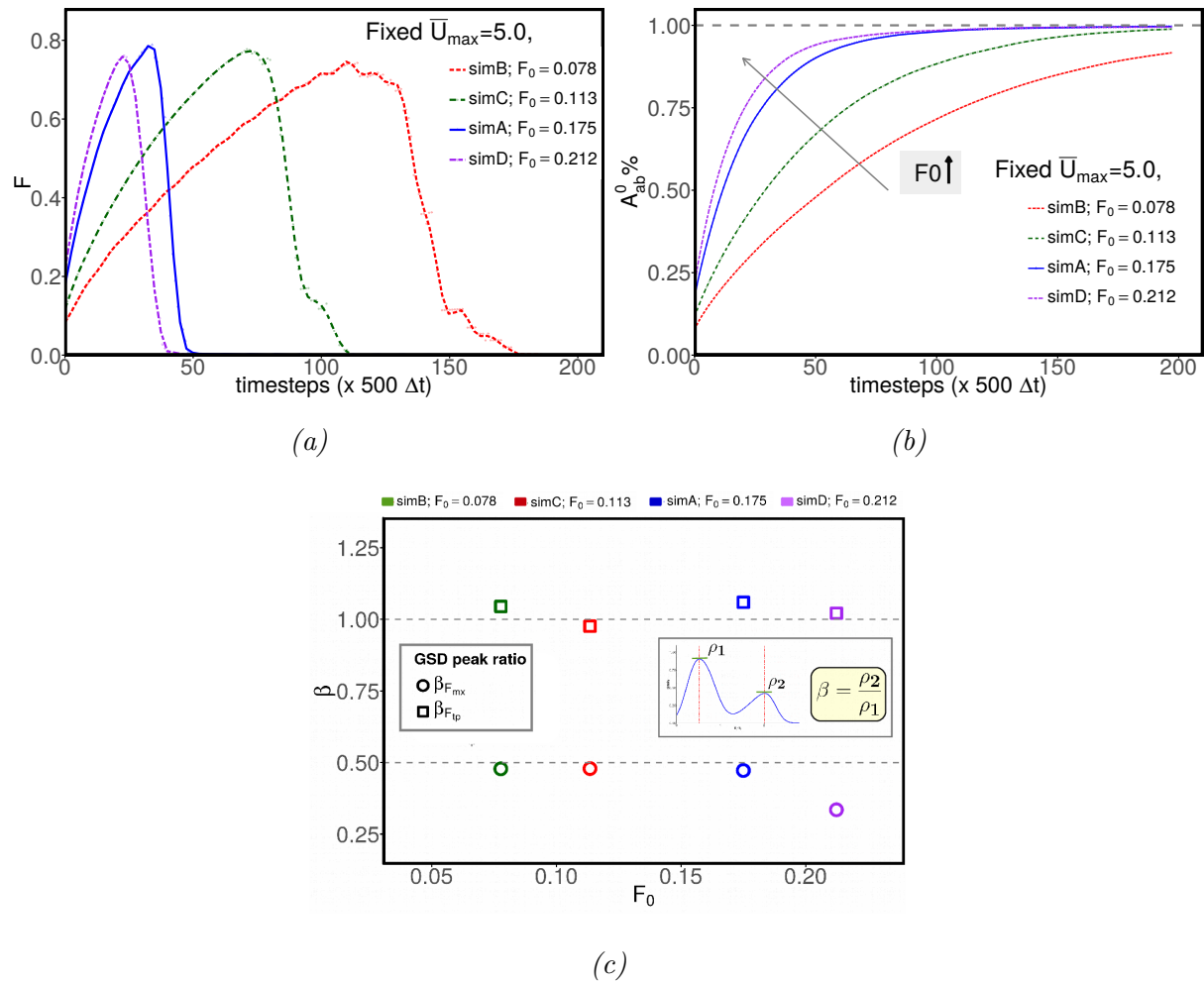
Figure 7.7: *(a) Change in the duration of the transient phenomena as the initial volume-fraction of the abnormal grains $F_o$ changes. With increase in $F_o$, the time taken for the disappearance of the abnormal grains decreases. (b) Relative dominance of the pre-existing abnormal grains $\beta$, illustrated by the ratio of dominance of the abnormal ($\rho_2$) and normal ($\rho_1$) grains, at $F_{mx}$ and $F_{tp}$. (c) Increase in the volume fraction of the pre-existing abnormal grains $A_{ab}^o$ with time for different initial volume fraction of abnormal grains $F_o$.*

previous section, the transition period involves accelerated growth of the normal grains accompanied by the increase in the dominance of the abnormal grains which establishes a bimodal distribution. When the initial volume fraction of the abnormal grains $F_o$ is increased, the corresponding volume fraction of the normal grains is lowered. Thus, minimal growth of the abnormal grains, at the expense of the normal grains, rapidly increases its dominance in the size distribution. This behavior augmented with the accelerated growth of the normal grains which confines the distribution of the abnormal grains to $2R_c$, reduces the duration of the transition period as seen in the Fig. 7.7a. Furthermore, the peak at which the stage-I of the transition region switches to stage-II remains considerably unchanged for all four microstructures. This behavior indicates that the distribution at the peak and end of the transition remain similar if $\overline{U}_{max}$ remains constant, despite influence of $F_o$ on the kinetics of the transient phenomena. This similarity in the distribution at the peak and end of the transition period is illustrated in Fig. 7.7b through the parameter $\beta$. It is interesting to that note, irrespective of the initial volume-fraction of the abnormal grains, $F_{mx}$ is achieved when its dominance in the distribution plot is half of the normal grains. Moreover, the transition period ends, $F$ becomes zero, when both normal and abnormal grains exhibit equal dominance in the distribution plot.

The volume fraction of the pre-existing abnormal grains $A_{ab}^o$ during the grain growth is determined and plotted in Fig. 7.7c for different microstructures with varying $F_o$. Here, it is important to distinguish the evolution of $F$ from $A_{ab}^o$. The volume fraction of the abnormal grains $F$ is defined based on average grain size $R_c$ and changes correspondingly with the evolution of $R_c$. However, the volume-fraction $A_{ab}^o$ refer to the volume fraction of a set of grains with initial grain size greater than $2R_c$. Thus, the evolution of $R_c$ does not directly influence the $A_{ab}^o$. Furthermore, as opposed to $F$, $A_{ab}^o$ progressively increases in agreement with the continued increase in the dominance of the abnormal grains in the microstructure. Fig. 7.7c shows that this dominance of the abnormal grains is achieved more rapidly in microstructure with utmost $F_o$. In $simB$, wherein the initial volume-fraction of the abnormal grains is the least, the increase in $A_{ab}^o$ is gradual, whereas in $simD$ of maximum $F_o$, an abrupt increase in the volume fraction of the abnormal grains is seen in the initial stages. Irrespective of the differences in $F_o$, the pre-existing abnormal grains tend to occupy the entire microstructure as the transformation proceeds.

An approach, employed to understand the influence of $F_o$ on the transition period is extended to capture the effect of the degree of abnormality, $\overline{U}_{max}$. With the initial volume-fraction of the abnormal grains fixed ($F_o = 0.12$), its average size is varied to determine the influence of $\overline{U}_{max}$ on the kinetics of grain growth. Fig. 7.8a shows the transient phenomena exhibited by four microstructures, $simE$, $simF$, $simG$ and $simH$, with constant $F_o$ and varying $\overline{U}_{max}$. In contrast to the influence of $F_o$, it is evident that the increase in $\overline{U}_{max}$ prolongs the time taken for the abnormally large grains to disappear. Furthermore, the peak observed in the evolution of $F$, which characterizes the maximum volume fraction of the abnormal grains in the transition period, remains
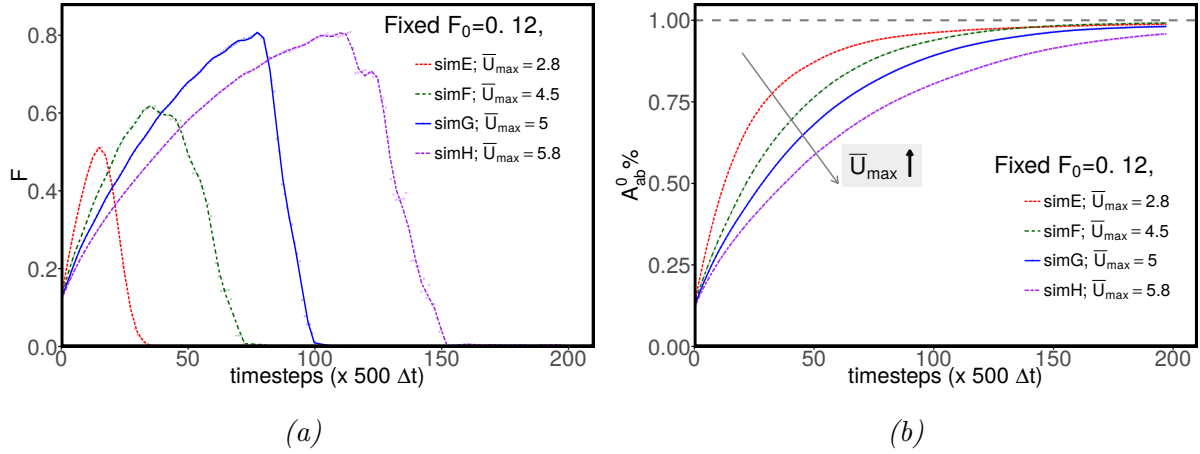
*Figure 7.8: (a) Change in the time-taken for the disappearance of the abnormally large grains $F_{tp}$ as the degree of abnormality changes ($\overline{U}_{max}$). With increase in $\overline{U}_{max}$, span of the transition period increases. (b) Increase in the volume fraction of the pre-existing abnormal grains $A_{ab}^o$ with time as $\overline{U}_{max}$ varies.*

independent of $F_o$ and raises with increase in the degree of abnormality $\overline{U}_{max}$, as shown in Fig. 7.8a. Increase in $\overline{U}_{max}$ shifts the distribution of the abnormal grains to the far left in the distribution plot. Thus, to confine these grains within $2R_c$, considerable growth in the normal grains is expected. Despite the accelerated growth kinetics of the normal grains, the magnitude of shift required to confine the abnormal grains within $2R_c$ leads prolongation of the transient period. Owing to this extended survival of the abnormal grains, its growth kinetics is varied and consequently, maximum volume-fraction during the transition period is altered.

The change in the volume fraction of the pre-existing abnormal grains $A_{ab}^o$ during grain growth for different microstructures of varying $\overline{U}_{max}$ is plotted in Fig. 7.8b. Recurrently, as opposed to the influence of $F_o$, the microstructure with least degree of abnormality *simE* exhibits a rapid increase in volume-fraction of the pre-existing abnormal grains while $A_{ab}^o$ in *simH* with maximum $\overline{U}_{max}$ increases gradually. However, similar to $F_o$, dominance of the pre-existing abnormal grains progressively increases with time. The complete statistical results are tabulated in Appendix B.

*Table 7.1: Parameters $f_1$ and $f_2$ governing the duration of the transient period.*

| $\overline{U}_{max}$ | $f_1$ | $f_2$ |
|---|---|---|
| 3 | 5.02463 | 1.09687 |
| 4 | 6.57384 | 1.10712 |
| 5 | 6.74043 | 1.20537 |

Since the initial volume fraction of the abnormal grains $F_o$ and degree of abnormality $\overline{U}_{max}$ vary significantly with the manufacturing technique, a quantitative understanding of its cumulative influence on the duration of the transition-stage $\chi$ is of vital importance.

(a)                                                                (b)
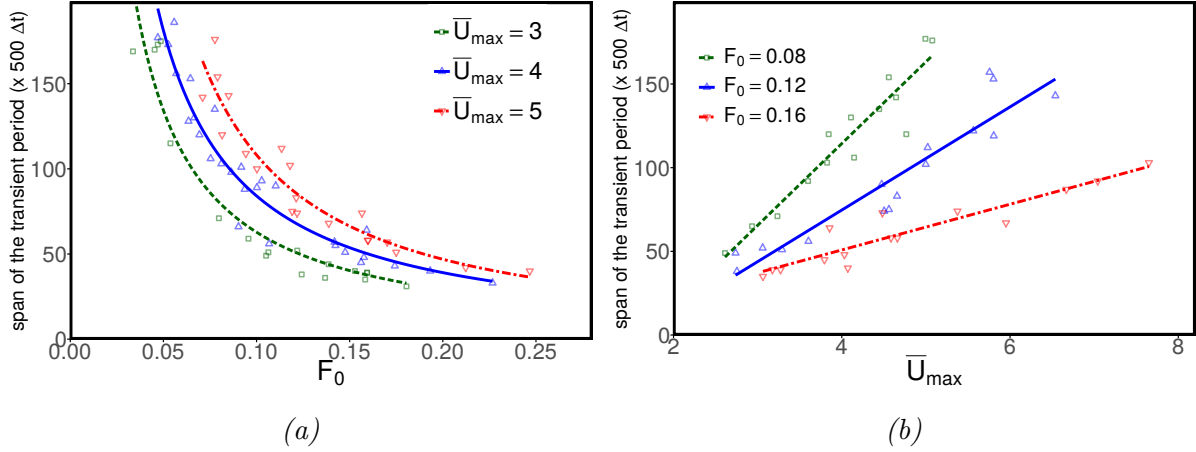
*Figure 7.9: (a) Influence of initial volume-fraction of abnormal grains $F_o$ on time taken for their disappearance $F_{tp}$. Microstructures for this illustration are categorized based on $\overline{U}_{max}$ through color scheme. (b) Influence of degree of abnormality $F_o$ on span of the transition period $F_{tp}$. Change in $F_{tp}$ for different microstructures are distinguished based on $F_o$.*

Thus, over hundred microstructures with different $F_o$ and $\overline{U}_{max}$ are analyzed to quantify the influence of these parameters. A change in the span of the transient phenomena with increase in $F_o$ is presented in Fig. 7.9a, wherein the data-points are categorized based on the degree of abnormality $\overline{U}_{max}$ owing to its augmented influence. Consistent with the above discussion, the length of the transient period decreases with increase in $F_o$. For the $\overline{U}_{max}$ of 3, 4 and 5, the influence of the $F_o$ on the transition period can be expressed as

$$\chi_{(\overline{U}_{max})} = \exp\left(f_1(\overline{U}_{max})\right) \times F^{-f_2(\overline{U}_{max})}, \tag{7.2}$$

where the parameters $f_1$ and $f_2$, which are the function of $\overline{U}_{max}$, are tabulated in Table. 7.1. Analyzing these, $\overline{U}_{max} = 3$, 4 and 5, and other simulations, a generalized expression that relates $F_o$ with $\chi$ is extracted, which reads

$$\chi_{(\overline{U}_{max})} = \exp\left(0.14 \times \overline{U}_{max} + 1.2\right) \times F^{-(0.05 \times \overline{U}_{max} + 0.9)}. \tag{7.3}$$

Furthermore, the plots corresponding to $\overline{U}_{max} = 3$, 4 and 5 apparently overlap as the $F_o$ increases. Therefore, it can be suggested that beyond a certain $F_o$, the influence of $\overline{U}_{max}$ on $\chi$ diminishes.

Figs. 7.8a and 7.9a indicate that, with increase in the degree of abnormality $\overline{U}_{max}$, the time taken for the disappearance of the abnormally large-grains $\chi$ increases. However, to capture the proportionality of this dependence, the change in $\chi$ with increase in $\overline{U}_{max}$ is plotted in Fig. 7.9b. Like Fig. 7.9a, the data-points are distinguished based on the similarity in $F_o$. This illustration reveals that, for a fixed initial volume-fraction of the abnormal grains, the time taken for $F_o$ to become zero increases linearly with increase in the degree of abnormality $\overline{U}_{max}$.

### 7.3.7    Transient growth behavior in 3-D

In this section, we highlight the effect of PEA grains on grain growth dynamics, associated with 3-dimensional polycrystalline systems. The domain size of $300 \times 300 \times 300$, filled with approximately 19000 grains are used. To maintain a consistency in our results, these 3-D simulation input parameters are very similar to the previous 2-D setup. The volume fraction $F_o$, abnormality $U_{max}$ and the inter-grain distance have been systematically varied to quantify the influence of initial PEA grains on transient growth regimes. For a selected simulation condition $F_o = 0.019$, the overall evolution of the microstructure can be seen in Fig. 7.10. The PEA grains assigned yellow, depending on the initial volume fraction, are randomly distributed over the normal grains (grey-scale representation) in the microstructure. In complete agreement with the 2-D results, the closely situated PEA grains consume the neighbor normal grains and continue to grow progressively. In the early stages of grain growth, both normal and abnormal grains grow concurrently. However, the abnormal grains exhibit a rapid growth until the loss of the remaining normal grains. Furthermore, at the later time steps, this growth rate gradually subsides and can be noticed in Fig. 7.10.

The corresponding temporal evolution of $F$ is monitored and plotted in Fig. 7.11. Consistent with the prior 2-D results, the presence of PEA grains also induces a period of transition and later, the volume fraction ($F$) becomes zero. The temporal evolution of $F$ consists of two stages, where $F$ firmly increases in *stage-I* (*A-B*) and $F$ quickly drops to zero in *stage-II* (*B-C*). The volume fraction of abnormal grains at A, B, and C have indicated in Fig. 7.11.

For a better understanding of the dominance of PEA grains embedded in the finer grain matrix (3-D), the size and number of PEA grains are varied. After a certain period, the microstructure retains only the closely filled initial PEA grains while the neighbor normal grains are entirely consumed throughout the evolution. The progression of volume coverage ($X$) by PEA grains can be interpreted by plotting the fraction of the microstructure that is PEA grains vs. the simulation time and results in sigmoidal shaped curves as shown in Fig. 7.12. The sequence commences with an initial volume fraction $X_0$, accompanied by an increasing rate of volume fraction as PEA grains consume neighbor normal grains, then a linear region of rapid growth, and ends with a decreasing rate due to the growth impingement of PEA grains on each other. The perceived growth behavior can be quantified using the well known Johnson and Mehl, and Avrami (JMA) type relationship that relates X, the volume fraction of PEA grains, to simulation time, t [27]:

$$X = 1 - b\,e^{-at^p}, \tag{7.4}$$

where $a$, $b$ and $p$ are the fitting parameters. The extracted values by fitting the simulation data in Fig. 7.12 to equation Eqn. 7.4 are measured. It is found that the $X$ values confer the systematic relationship with the initial volume fraction of PEA grains. However, the
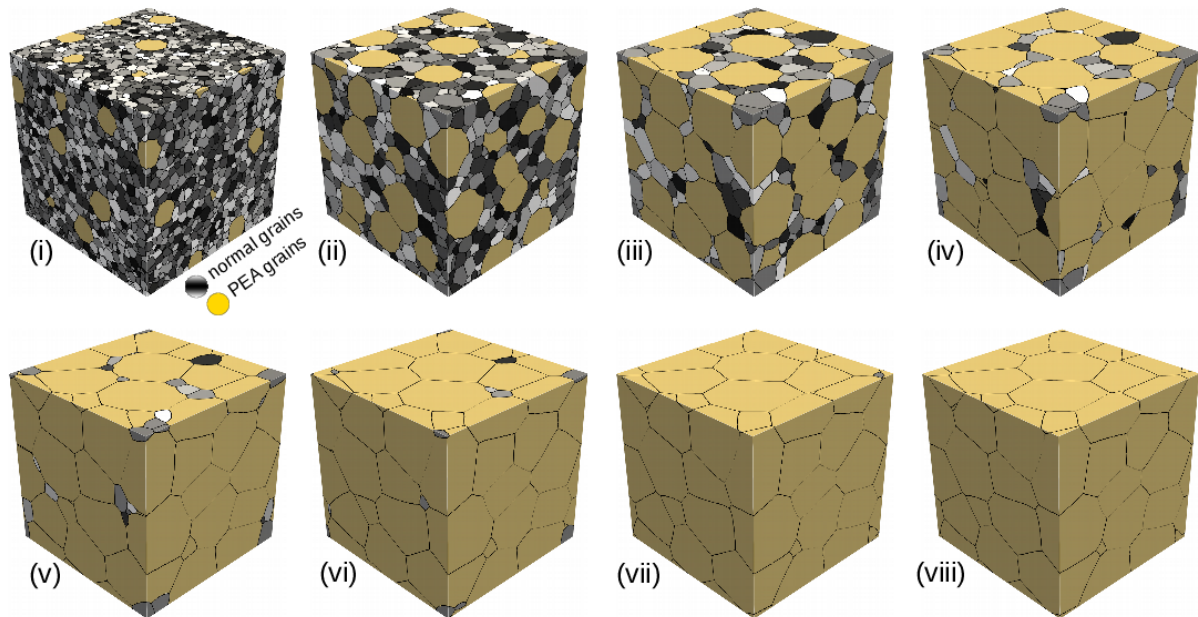
*Figure 7.10:   Temporal evolution of the $F_o = 0.019$ microstructures, as obtained from 3-D phase field simulations. (i) 2dt, (ii) 10dt, (iii) 20dt, (iv) 30dt, (v) 40dt, (vi) 50dt, (vii) 60dt and (viii) 70dt. where $dt = 400 \times \Delta t$*

effect of PEA grain size variation is overlooked here.

## 7.4   Summary

The microstructure of a polycrystalline material involved in a manufacturing process rarely exhibits a self-similar size distribution. Thus, subsequent heat treatment of the material, in the absence of any phase transformation, invariably includes an 'early growth regime' during which the microstructure attains a time-invariant distribution [172]. Presence of abnormally large grains, which in 2-D corresponds to the grains with sizes greater than twice the average (critical) grain size $R_c$, prolongs this regime by introducing a transition period. During this transition period, owing to the increase in the average grain size $R_c$, the size of these 'pre-existing abnormal grains' eventually become less than $2R_c$, thereby indicating the lose of 'abnormality'. Although theoretical studies following the postulation of the abnormally large grains claim that as the evolution proceeds these grains lose their abnormality [27, 24], the end of this transition period is considered to be the onset of normal grain growth, which is characterized by time-invariant grain size distribution or adherence to power law [178]. In the present work, a thermodynamically consistent phase-field approach is employed for the first time to render an extensive analysis of this transient phenomena induced by the abnormal grains. Preliminary analysis of the transition period, by monitoring the temporal evolution of the volume-fraction of the abnormal grains ($F$), reveals two stages in complete agreement with the existing
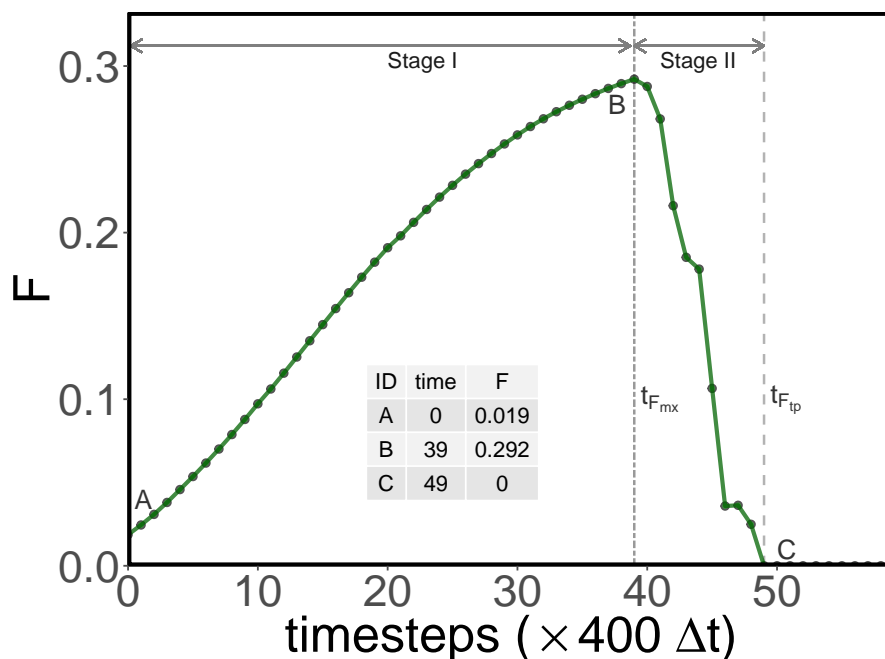
Figure 7.11: *Change in the volume fraction of the abnormal grains (F) with time for 3-D microstructure. The $F_o = 0.019$ system reaches at its maximum ($t_{F_{mx}}$) and turns zero ($t_{F_{tp}}$).*
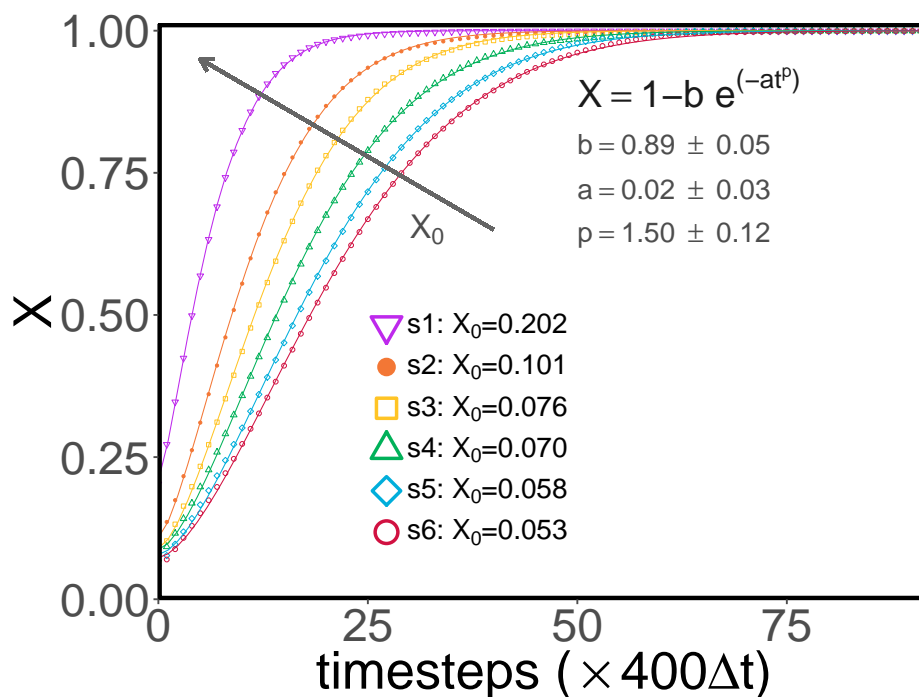


Figure 7.12: *Volume coverage (X) of PEA grains during evolution. The best fitted non-linear lines (JMA equation) are superimposed to the dataset.*

observation [178]. While in stage-I the volume-fraction of the abnormal grains gradually increases to a peak, in stage-II it rapidly reaches zero, characterizing the end of the transition period. In contrast to the existing conception [178], subsequent investigations indicate that when $F$ becomes zero, the microstructure exhibits a bimodal grain size distribution rather than an unimodal time-invariant distribution. In other words, it is identified that the end of the transition period, that ensures the complete disappearance of the abnormality, does not correspond to the onset of normal grain growth. This claim is additionally substantiated by analysing the adherence of this evolution to the power law.

In order to quantify the influence of the initial volume-fraction of the abnormal grains $F_o$ and the degree of abnormality $\overline{U}_{max}$, which is the ratio of average size of the abnormal and normal grains at initial timestep, close to hundred different phase-field simulations have been analysed. All the simulation domains were computationally optimized by domain decomposition using MPI (Message Passing Interface). Simulations, on average, took 4 hours for completion, with each involving 37 CPUs. With increase in the initial volume fraction of the abnormal grains, the duration of the transition period decreases. However, a reduction in the span of these transient phenomena is noticed only when the degree of abnormality is reduced. Furthermore, the pre-existing abnormal grains are distinguished from the normal grains and the evolution of its volume fraction is examined. Although $F$, which depends on $R_c$ becomes zero at the end of the transition period, the volume fraction of the pre-existing abnormal grains continues to increase. Ultimately, when the microstructure reaches the unimodal distribution, characterizing the normal grain growth, this pre-existing abnormal grains significantly dominate the grain distribution. In other words, although abnormality of the pre-existing abnormal grains are lost during the transition period, these grains continue to grow and dominate the microstructure when the steady-state condition is reached. Moreover, it has also been identified that in microstructures with marginal degree of abnormality, $\overline{U}_{max}$ slightly greater than 2, and $F_o < 0.01$, the transient phenomena is not distinctly perceivable.

# Part IV

# Results and Discussion : Microstructural coarsening of multiphase materials

# Chapter 8

# Concurrent grain growth and coarsening of binary two-phase microstructures

## 8.1 Introduction

The microstructure of materials serving practical purposes are generally polycrystalline in nature, and the constituent phases are distributed amongst the grains. That is, it is seldom the case that one of the phases is homogeneous throughout the device or is encapsulated in a matrix. Grains of both the phases influencing each others growth behavior is to be expected. No theories, as per our knowledge, exist for such multiphase polycrystalline structures where both the phases have to be treated on an equal footing. Ankem and Margolin fitted their experimental data on two phase grain growth of $\alpha$-$\beta$ Ti alloys to two different equations (one for each phase) of the form Eq. 2.1 [190, 191]. Investigating the temporal evolution of the microstructure through conventional experimental treatments is a laborious task. Therefore, theoretical techniques are largely adopted to complement the experimental observations and deepen the understanding. Limited computational studies exist which interpreted the results in terms of single phase like power laws [192, 193, 194]. However, the influence of parameters like volume fraction, diffusivity and inter-phase and inter-grain interfacial energies is unexplored in these studies. Further most of the conducted studies employed small domain sizes thus statistical discrepancy may arise. The current chapter aims at filling these gaps through an implementation of a state of the the art phase-field modeling approach for performing the large scale simulations.

## 8.2    Simulation set-up

Two-dimensional domains, sized with $2048 \times 2048$ grid points, with periodic boundaries, are employed for all simulations of the current study. About 10000 grains are randomly distributed over the domain, through a Voronoi tessellation, as described in [1]. At this stage, however, all grains in the domain are of the single phase. To obtain a mixed microstructure with a controlled volume fraction of the second phase, an appropriate number of grains is randomly chosen and assigned with different properties. The initial fillings obtained are shown in Fig. 8.1. The radius of a grain $i$ is expressed as $R_{\phi_i}$, where $\phi_i$ indicates the phase identity. To compute the radius, the number of voxel cells inside the grain is counted, and a circle of an equivalent area is used.

The composition variables at each grid point are set equal to those of the equilibrium values ($C_{eq}^{\alpha} = 0.2A0.8B$ and $C_{eq}^{\beta} = 0.8A0.2B$). The $\alpha_i/\alpha_j$ and $\beta_i/\beta_j$ grain boundary energies are chosen to be 1.4 and 0.97, respectively. The interfacial energy of the $\alpha/\beta$ interphase is taken as 1.0. These values are adopted from a previous work [61]. The bulk diffusivity is varied from 0.01 to 1.0, while holding the grain boundary mobility constant.

In order to solve the phase-field evolution equations, a finite difference algorithm is implemented across a uniform numerical grid [154], using an explicit time-stepping (forward Euler) scheme. Equal grid spacings are assumed in both directions, i.e., $\Delta x = \Delta y = 1.0$. The diffuse interface width $\epsilon$ is set to $4\Delta x$, for all simulations, ensuring a sufficient resolution of the diffuse interface region, and a time step is chosen well within the numerical stability range ($\Delta t = 0.01$). The simulations are run long enough to ensure that the steady state grain growth regime is reached. Computational efficiency has been improved by introducing the *Locally reduced order parameter optimization (LROP)* method, which optimizes both memory and time consumption [156, 183, 155].

The simulation domains were computationally enhanced by domain decomposition, using MPI (Message Passing Interface) [107]. On average, each simulation took 28 hours for completion, with 82 CPUs. The total computation time for this study is around 1456 hours ($\approx 60$ days).

## 8.3    Results and discussions

### 8.3.1    Microstructural features

The starting configurations with the $\beta$ phase volume fractions, which range from 10% to 90% and are employed for the simulations, are assembled in Fig. 8.1. The grains shown in yellow correspond to the $\alpha$ phase, and the ones shown in blue correspond to the $\beta$ phase. The distribution is random and uniform throughout the domain, with all grains

being roughly the same size. All grains lie "next to each other," as opposed to a setting where a grain is embedded into another. Also, at very low volume fractions ($< 0.1$, not shown in Fig. 8.1.), the minor phase grains are mainly detected at the triple, quadruple, etc. junctions of the major phase grains.

The temporal evolutions of the microstructures corresponding to the 10%, 30%, and 50% volume fractions of the $\beta$ phase are presented in Fig. 8.2. From the micro-graphs, it is readily evident that the average grain size increases with time. The main governing mechanisms of the growth are an interface re-adjustment around the grain junctions of similar phases, Ostwald ripening, and coalescence. Growth-hindering mechanisms like pinning and dragging also occur concurrently. In the case of 0.1, an appreciable size difference develops between the $\alpha$ and $\beta$ grains, with the latter phase regions still remaining isolated. In this system, self-diffusion of the $\beta$ phase is sufficient enough for the grains to continue to remain at the $\alpha$-grain junctions, as the growth progresses. Evans et al. reported that minor phase particles, exhibiting sufficient self-diffusion, will act like pores during sintering [195]. On the other hand, the size difference in the microstructure of the volume fraction 0.3 is not as much pronounced, but a continuous clustering of similar phase grains, i.e., network-like structures, is observed. Furthermore, the 0.5 volume fraction system resembles an interpenetrating (duplex) composite structure, where the $\alpha$ and $\beta$ grains lie next to each other, forming a chessboard-like pattern [196] with no or little size difference. Such clustering bias continues until a volume fraction of 0.7 is reached, after which it begins to cease, as the $\beta$ phase starts to assume the role of a matrix, and the $\alpha$ grains tend to get isolated. Since different interface and grain boundary energies are used, a considerable number of quadruple junctions additionally appears in the microstructure [197]. However, their lifespan is seen to be limited, and they quickly split into two triple junctions, in the course of the evolution.

The normalized grain size distributions (GSD) of all grains in the 10%, 30%, and 50% volume fraction $\beta$ phase systems are shown in Fig. 9.7a. It is observed that the steady state regime begins after an initial transition time. It can be noticed that the distribution of the 10% $\beta$ system is slightly wider than the distribution of others. Here, the $\beta$ phase grains are at the grain boundaries of the $\alpha$ grains, resulting roughly in a bimodal-type distribution. As the volume fraction of the $\beta$ phase grains increases, the GSD converges to its mean. Interestingly, individual $\alpha$ and $\beta$ phase GSD are approximately identical in shape. Due to a small difference in the interfacial energies of the $\alpha$ and $\beta$ grains, the GSD peaks are slightly shifted. Since the analytical models were mainly derived for single-phase systems, these two-phase systems follow a complex size distribution. Thus, the characteristics of GSD is affected by the initial volume fraction of constituting phase grains.
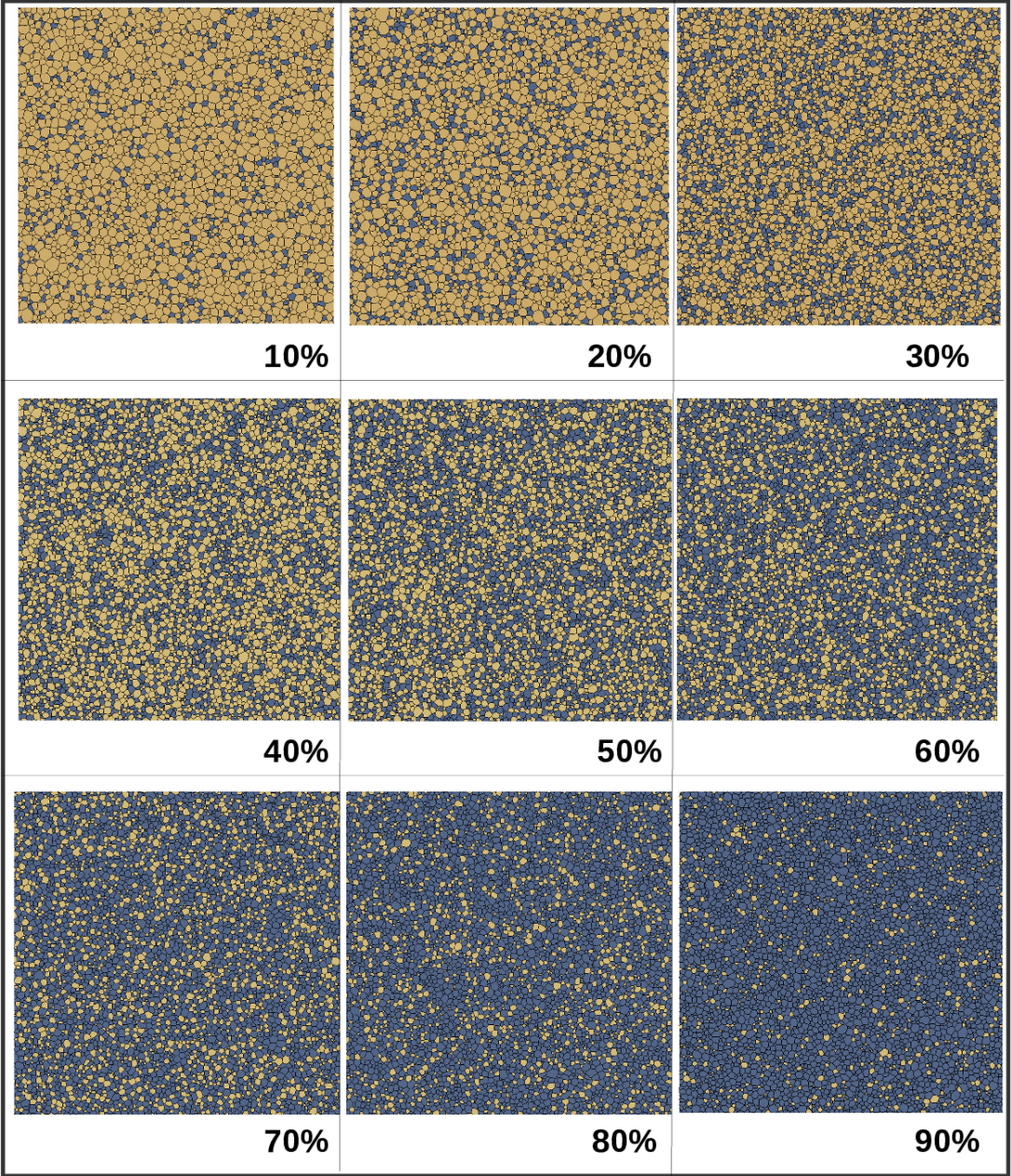
Figure 8.1: Initial simulation setup for a two-phase (α-β) system, with various volume fractions of β phase grains.
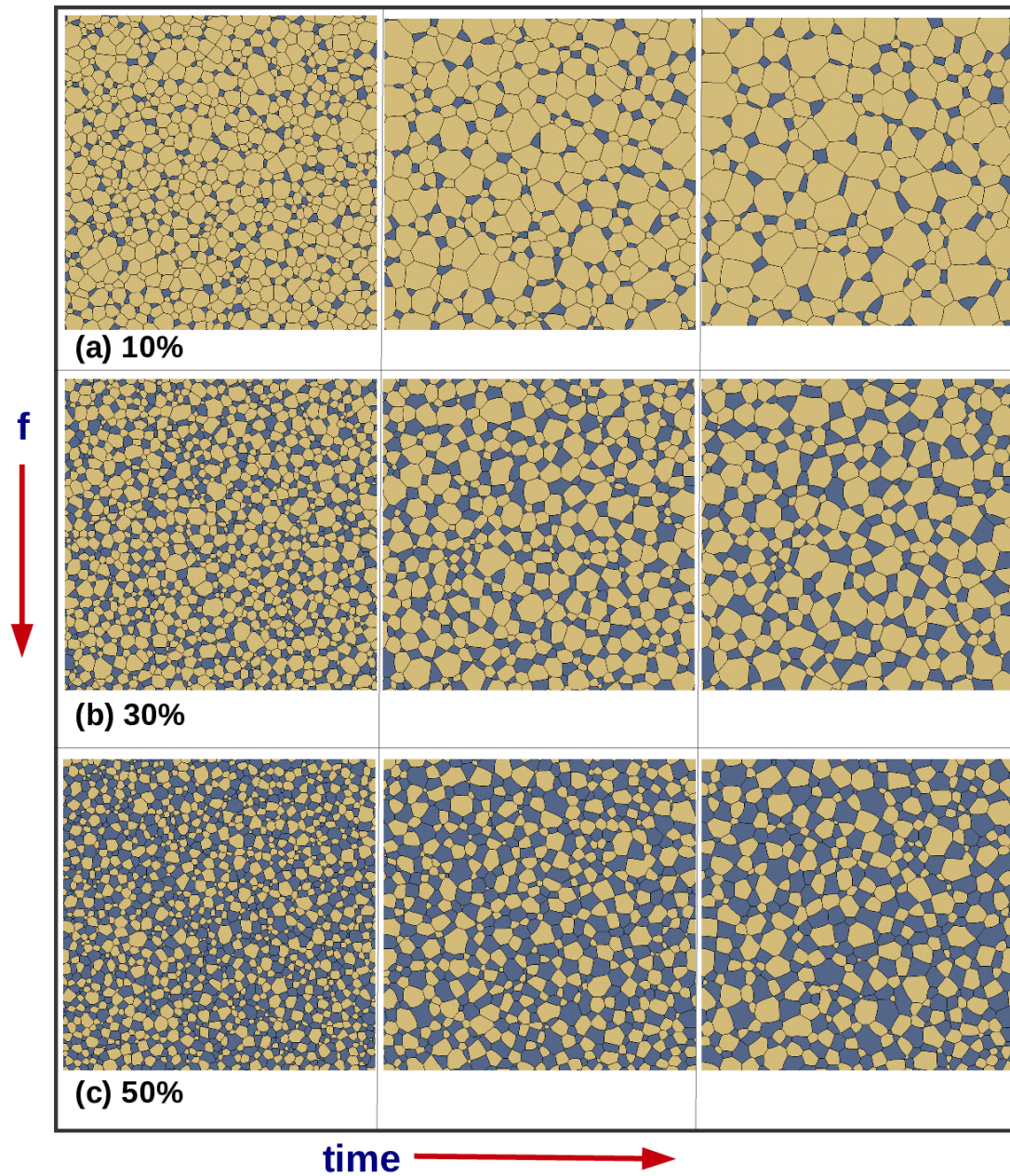
Figure 8.2: Microstructures obtained at $t = 5000$, $t = 15000$, and $t = 25000$ time steps (first, second, and third columns, respectively).
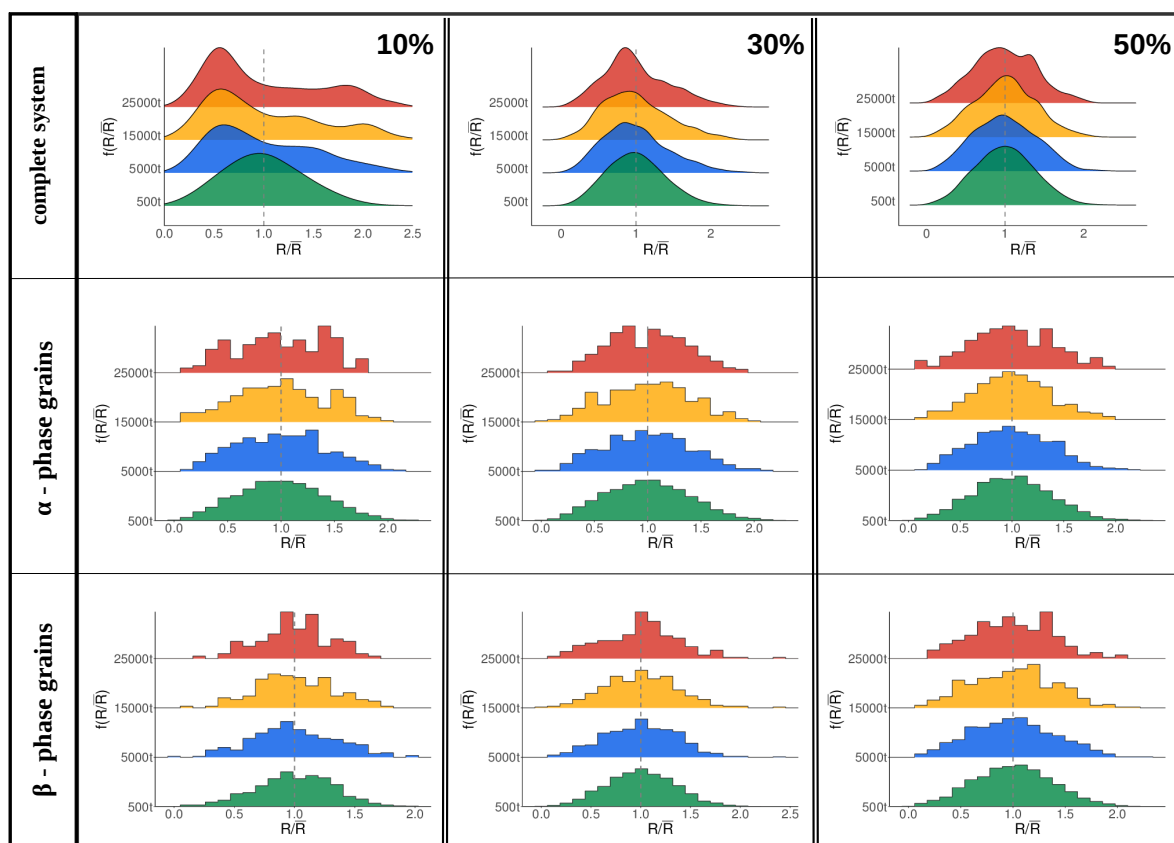
Figure 8.3: *Grain size distributions obtained at* $t = 500$, $t = 5000$, $t = 15000$ *and* $t = 25000$ *time steps. Volume fraction of* $\beta$ *phase grains* 10%, 30% *and* 50% *for first, second and third columns, respectively.*

## 8.3.2   Grain size evolution: nonconserved versus conserved systems

In this section, we highlight the differences in the grain growth dynamics, associated with conserved and nonconserved two-phase systems. In the phase-field terminology, conserved systems are those in which the volume fraction of the individual phases remains constant throughout the evolution, in the absence of a bulk driving force, while nonconserved systems are those in which one phase could consume or be consumed by the other, even in the absence of a bulk energy difference. In physical terms, the chemically homogeneous systems correspond to the latter. A nonconserved situation, for example, is commonly observed during recrystallization, where some set of grains can hold distinct (texture) interfacial energies, compared to the rest. Such highly textured grains acquire their distinctive properties in the processing route, and can consume (or be consumed by) their neighbors. Similarly, in abnormal grain growth systems, the interfacial energies or mobilities for those grains differ from the normal ones. Often the relative growth rate is accelerated for such abnormal grains, and their volume fraction is not preserved over the course of the evolution [197].

Simulations are carried out for various volume fractions of the $\alpha$ and $\beta$ phases in the conserved and nonconserved setting. Typically, smaller time steps are required for the stability of the conserved phase-field model, compared to the nonconserved one. For a better comparison, however, the same time step (the smallest of the two) is employed for both kinds of simulations. We have plotted the mean grain size evolution ($\bar{R}_t$) for selected volume fractions in Figs. 9.5a and 9.5b, for nonconserved and conserved cases, respectively. The inset shows the plots for all studied volume fractions.

In the nonconserved case, the growth rate of the pure $\alpha$ system is higher, compared to the rest. The reason for this can be ascribed to the higher interfacial energy of the alpha grains, which provide a higher driving force for the system, so as to minimize the overall energy. In contrast, when the microstructure is mixed, some of the interfaces ($\alpha/\beta$ and $\beta/\beta$) will have reduced energies, which thus results in a reduced driving force and a slower evolution. A naive extension of this argument, namely, as the volume fraction of the $\beta$ phase increases, the number of interfaces with less energies proportionately increases, and thus the growth rate should steadily decrease, is, however, partly contradictory to the observed behavior: From the curves in the inset of Fig. 9.5a, one can see that the growth rates do not follow a monotonic pattern, with respect to the volume fraction, and sometimes even cross over each other. Furthermore, it could be seen that except for the volume fraction 0 (pure $\alpha$), all other curves cluster around each other, staying close to that of the pure $\beta$ curve. This could be explained from the fact that as the system is nonconserved, and as the $\beta$ phase grains form interfaces with lower energies, the $\alpha$ phase grains convert into them over the period of time, and the microstructure becomes predominantly $\beta$-rich. This is readily evident from Fig. 8.5, (conserved and nonconserved

system) where the $\beta$-phase volume fractions are plotted as a function of time. Thus, the naive argument, if at all, works only for the initial time steps.

On the contrary, two things are characteristically different in the conserved case. In the nonconserved case, they are always on one side of the pure $\beta$ curve (above), as the $\beta$ volume fraction increases, although the growth rates do not follow a steady trend, whereas the growth rates drop considerably below the pure $\alpha$ curve, when increasing the $\beta$ phase fraction from zero to 5% (Fig. 9.5b). Secondly, they do so steadily until a phase fraction of 0.5 is reached, after which they rise up monotonically. This behavior is a clear evidence of the diffusion mechanisms taking over the interface control. When the microstructure is predominantly a single phase, the number of regions, in which the grain clusters of such phases occur, are more and the evolution in these regions does not require diffusion to mediate the growth. Hence, the growth is governed by the interface. However, as the phase fractions tend towards the volume fraction of 0.5, such regions drop, and the diffusion mechanism is operative throughout the microstructure.

### 8.3.3   Grain size evolution: diffusivity effect

While the investigations of prior section are carried out at a fixed diffusivity, we next change it and study its effect on growth kinetics. Diffusivity exhibits an Arrhenius type of relation, with respect to temperature. Hence, the simulations performed at various values of diffusivity can be roughly considered to be a study of temperature influence on growth kinetics. The other thermo-physical parameters of the system, such as free energies and the interfacial energies, also change upon a change of temperature. In the current study, however, we assume the latter to be small, compared to the diffusivity gradation. In Fig. 8.6a, the mean grain size evolution is depicted for the case of a 0.1 volume fraction of the $\beta$ phase system and for various bulk diffusivity values, ranging from $D = 0.01$ to $D = 1.0$.

It is readily seen from Fig. 8.6a that diffusivity has a considerable effect on the growth rate. The higher the diffusivity, the faster the coarsening. For the case of $D = 0.01$, it can be observed that the growth rate is very sluggish, and that the microstructure looks almost stagnant with time. This is in agreement with the coarsening law [48], which relates the velocity of the moving boundary to the curvature, the diffusivity, and the interfacial energy of the grains, with the dependence being proportional to the diffusivity. However, this law is derived in a simplified setting, where only the effect of the two grains forming the contact is taken into account and the influence of the neighboring grains is ignored. In this case, the law stated in the introduction (Eq. 2.5) could be a better relation. It is very well argued that when the growth exponent is of the order 2, it is controlled by the interface, and as it approaches 3, it implies that the limiting mechanism is diffusion. In view of this, we compare our results of Fig. 8.6a with Eq. 2.5 and obtain the respective
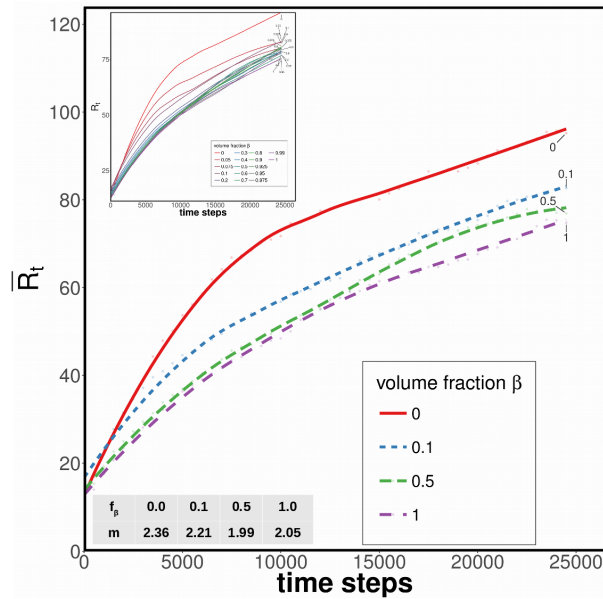
*(a)*
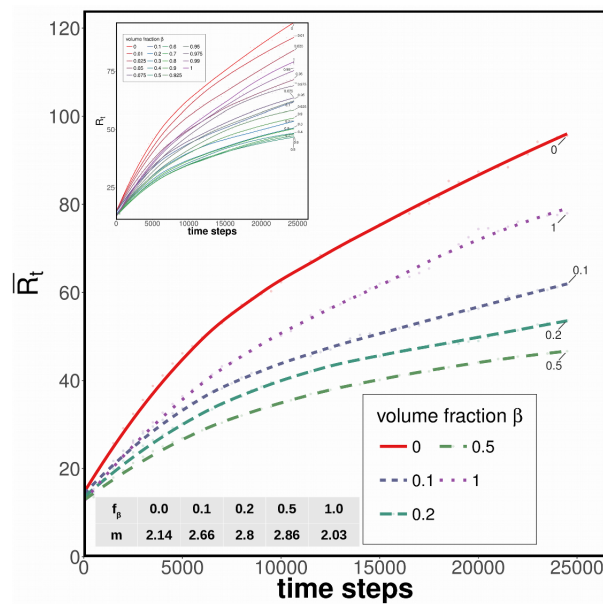


*(b)*

Figure 8.4: *The mean grain size evolutions for (a) the nonconserved and (b) conserved simulation setup are plotted as a function of time, with selected volume fractions. Each fitted line corresponds to the value of the best fitting power law coefficient $(\bar{R}_t^m - \bar{R}_0^m = K(t - t_0))$. The insets show the plots for all studied volume fractions. (For the color interpretation in this figure, the reader is referred to the web version of this article.)*
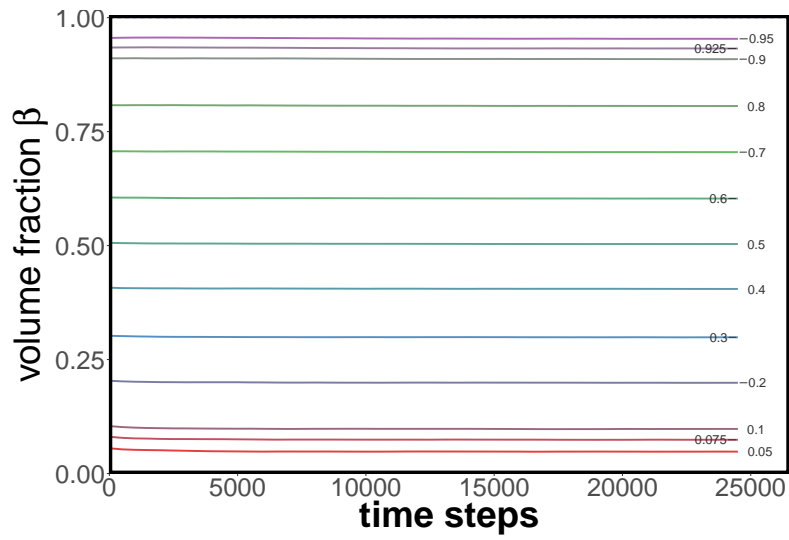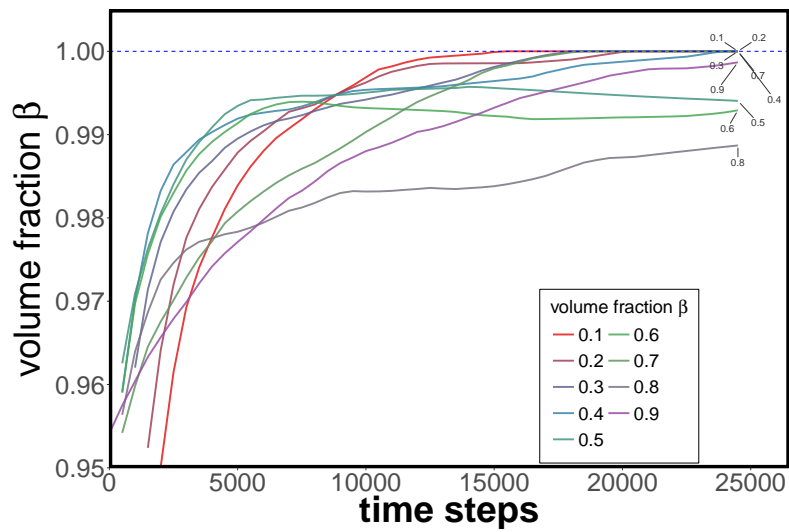
*Figure 8.5: Temporal evolution of the overall $\beta$ phase volume fraction in (a) conserved and (b) nonconserved systems, for various initial fractions.*

exponents. For the four studied cases, a constant value is chosen for the growth coefficient, as a basis for comparison, in keeping with the common practice employed in the grain growth studies [198]. The exponents given by the inserted table in Fig. 8.6a attain values around 3, confirming that the growth is diffusion-controlled. This is strengthened further by increasing the volume fraction to 0.5, and the diffusional processes accordingly, which reduce the growth rate (see Fig. 8.6b).

As it is established that the evolution is diffusion-controlled, we fix the value of the growth exponent at 3, so as to compare the relative growth kinetics for various diffusivities, as well as volume fractions considered in the current study; i.e., compare the growth coefficient values [194]. The results are reported in Fig. 8.7. Notice that although the curve corresponding to a higher diffusivity lies above the lower one, the growth coefficients for the pure phases are identical. This is not surprising, considering the fact that the diffusion mechanism does not play a governing role in the microstructure evolution of the pure systems. Furthermore, a sudden drop and spike respectively occur at the left and right ends of the plot, along with an almost flat trend in the 0.2 to 0.8 range, indicating a characteristically different behavior of the evolution of near pure microstructures, compared to the mixed ones. Finally, the lowest growth rate is observed at a volume fraction of 0.5, irrespective of the diffusivity. The above tendencies are in good agreement with the previously obtained experimental [198] and computational results [61].

### 8.3.4   Grain size evolution: Individual phase kinetics

To compare the individual growth kinetics of the $\alpha$ and $\beta$ phases, the results of the $\alpha$-rich simulations are analyzed. The $\beta$-rich side exhibits a similar behavior. In Fig. 8.8a, the individual phase-specific growth rates ($\bar{R}_\alpha$ and $\bar{R}_\beta$) and total ($\bar{R}_t$) mean grain size evolutions are reported for the $\beta$ phase case with a volume fraction of 0.4. It is noteworthy that the individual phase evolutions also follow the same trend (i.e., a power law) as that of the overall microstructure. Hence, the curve for one of the phases always lies above and the other always below that of the curve for the total system. This behavior is in agreement with the existing literature 9.5. For the sake of a better comparison, $\bar{R}_t$ is plotted in Fig. 8.8a, for the volume fraction 0.5. Next, the individual phase growth rates for various volume fractions are compared in Fig. 8.8b. It can be seen that the curves for the mean grain size of the $\alpha$ and $\beta$ phases diverge from each other with time. Furthermore, the amount of divergence decreases as the volume fraction gets close to the equal phase fraction of 0.5. This is in good agreement with the results of previous experimental and computational studies [198, 199]. As the relative amounts of the phases differ markedly, the mean intergrain distance is high for the low volume fraction phase, compared to that for the major phase, as the distribution of the grains is uniform throughout the domain, which explains the difference in the growth rates for the individual phases. Thus, a diffusion over longer distances is required for the coarsening of the low volume fraction
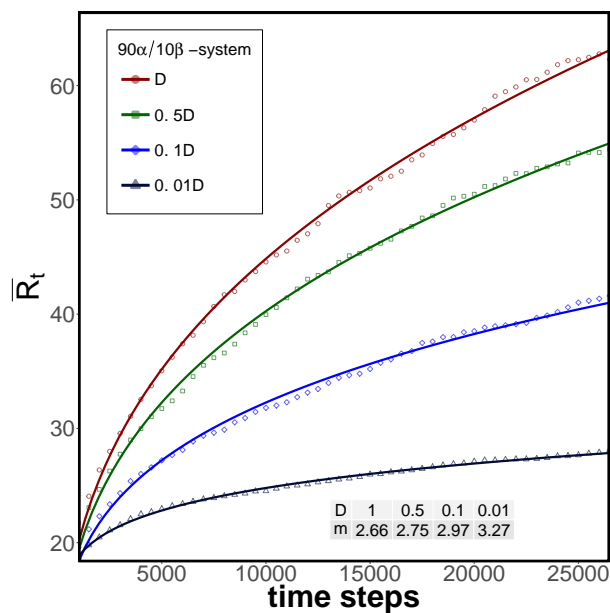
*(a)*
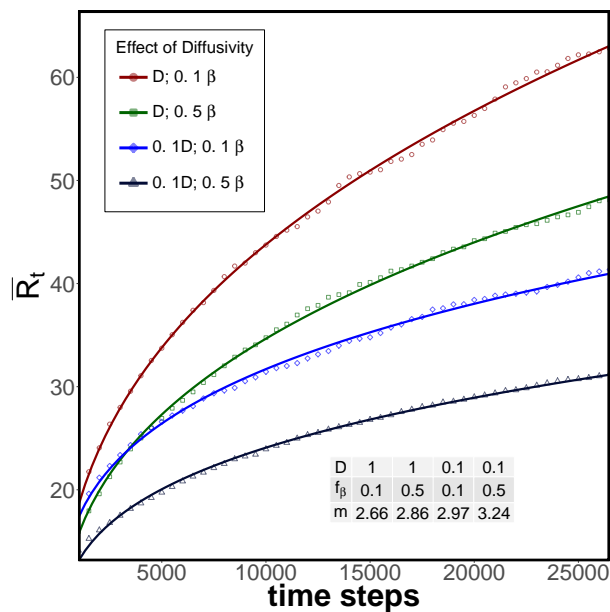


*(b)*

*Figure 8.6: Mean grain size evolution, corresponding to the volume fraction of 0.1 β phase grains, with varying bulk diffusivity conditions (D = 1, D = 0.5, D = 0.1, and D = 0.01, respectively) and (b) to the volume fractions 0.1 and 0.5 in comparison.*
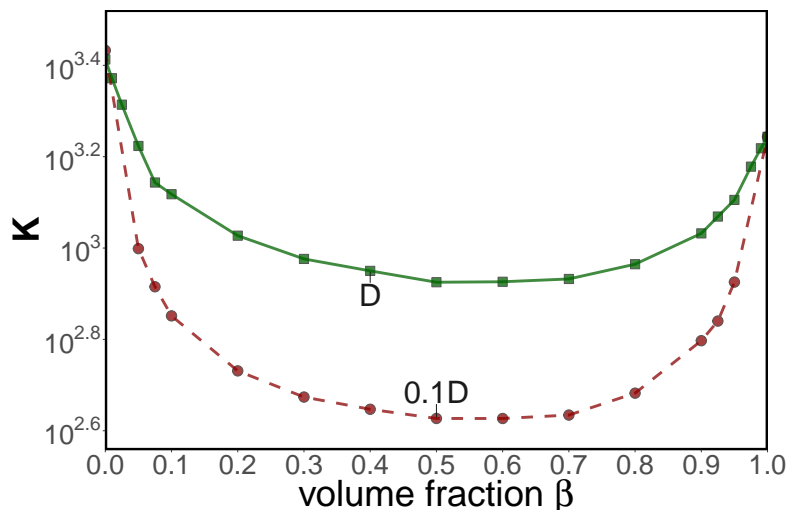
*Figure 8.7: Values of the grain growth coefficient, extracted from the phase field, with a diffusivity condition of D = 1.0 and D = 0.1, and for a wide range of volume fractions (β from 0.0 to 1.0). In this case [$\bar{R}_t^m - \bar{R}_0^m = K(t - t_0)$], the grain growth exponent m is assumed to be 3, to directly compare the growth kinetics of each system.)*

phase, which takes longer and results in the corresponding slower growth. This also explains the relative growth kinetics of a given phase for various volume fractions. The above reasoning implies that for the volume fraction of 0.5, the curves for $\bar{R}_\alpha$ and $\bar{R}_\beta$ (and hence $\bar{R}_t$) should lie on each other, as the intergrain distances are the same for both phases. This, however, is not the case, which becomes evident from Fig. 8.8b. There is still a difference in the growth rates of the $\alpha$ and $\beta$ phases of the equi-volume fraction case. This is due to the difference in the interfacial energies of the two phases.

### 8.3.5  Relative growth rate of $\alpha$ and $\beta$ phase grains

For each volume fraction, the ratio $\bar{R}_\alpha/\bar{R}_\beta$ is found to be roughly invariant with time. This means that the microstructural changes occur in a way that preserves the relative sizes of the grains on average. Furthermore, the ratios decrease with the increasing volume fraction of the second phase, as depicted in Fig. 8.9a. This behavior is in good agreement with the experimental findings for the $Al_2O_3$-$ZrO_2$ system [200, 201]. The computed mean $\bar{R}_\alpha/\bar{R}_\beta$ values are 2.25, 1.75, 1.48, and 1.3 for the volume fractions 0.1, 0.2, 0.3, and 0.4 of the $\beta$ phase, respectively. In addition, the ratio of the maximum mean grain size ($\bar{R}_{max}$) and that of the individual phases ($\bar{R}_\alpha$, $\bar{R}_\beta$) also stays close to a constant. The simulation results are roughly similar to the previous reports from a comparable grain growth study of $Al_2O_3$-$ZrO_2$ ceramic systems [200, 201].

The ratio of the maximum grain size to the mean grain size of the phases serves as a rough measure for the grain size abnormality in the system. Kurtz et al. developed a detailed statistical theory for isotropic grain growth systems and predicted a maximum
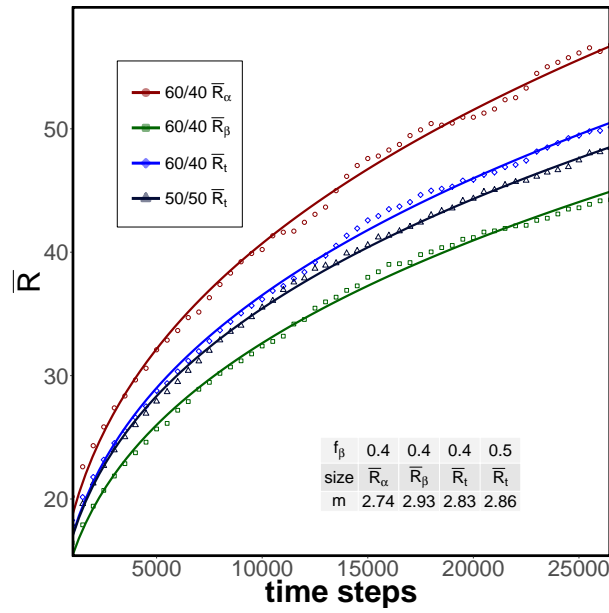
*(a)*
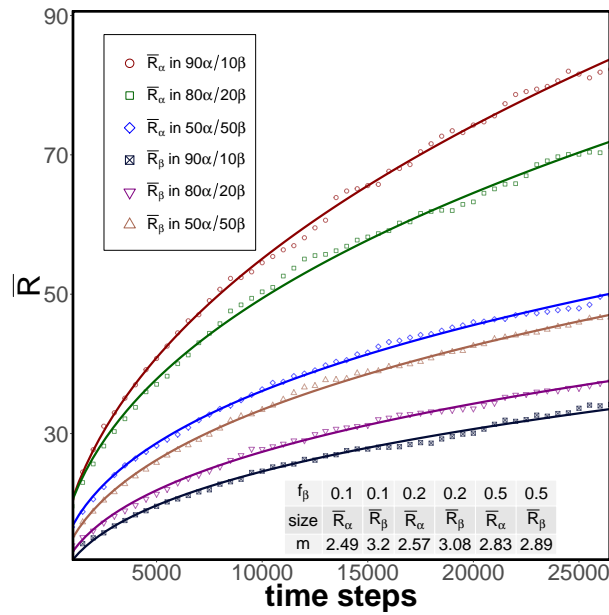


*(b)*

*Figure 8.8: Mean grain size evolution $\bar{R}_\alpha$, $\bar{R}_\beta$ of the $\alpha$ and $\beta$ phase grains: (a) The relative growth kinetics $\bar{R}_\alpha$ and $\bar{R}_\beta$ of $\alpha$ and $\beta$ is chosen for the volume fraction 0.4. The system related to the volume fraction 0.5 is included for consistency with the previous studies. (b) The influence of the volume fraction on the individual phase kinetics is represented here. The incorporated tables summarize the phase-dependent growth exponent of the considered volume fractions.*

grain size that is $e(=2.7183 \times \bar{R})$ times the growth rate of the median grain size [166]. It is also postulated that grains of larger size ($> 2.7183 \times \bar{R}$) do not occur during normal grain growth. A previous experimental study on Alumina-Zirconia composites revealed a linear relationship between $\bar{R}_{max}$ and $\bar{R}$ [198]. The ratio was attained as $\bar{R}_{max}/\bar{R} = 3$ for their system, with a volume fraction of 0.1, 0.2, 0.3 and 0.4. We computed these quantities for our model system, and the results are shown in Fig. 8.9b. The values are normalized with the overall mean size. A linear correlation is obtained for our data set, with $\bar{R}_{max}/\bar{R} = 2.5$. However, the ratio is slightly lower than the prior results, which might be due to the fact that $\bar{R}_{max}/\bar{R}$ is very sensitive to the initial microstructure and the number of remaining grains in the system [155].

For various volume fractions, the effect of diffusivity on the relative growth rates is reported in Fig. 8.10. It is straightforward that in the case when all interfaces have the same energies, $\bar{R}_{\alpha}/\bar{R}_{\beta}$ should be unity for the volume fraction 0.5, irrespective of the diffusivity, due to the interchangeability of the phases. However, from Fig. 8.10, it is readily evident that for $\bar{R}_{\alpha}/\bar{R}_{\beta}$ at 0.5, the distribution is not identically unity. Furthermore, the curves for different diffusivities do not intersect for an equi-volume fraction. This is a direct consequence of the difference in the energies among the $\alpha/\alpha$, $\alpha/\beta$, and $\beta/\beta$ interfaces. However, the curves are almost coincident at the center of the figure. That is, the effect of diffusivity is prominent on the relative growth rate, when the microstructure is dominated by one of the phases. In addition, the mean growth rate of the primary to the secondary phase is high when the diffusivity is reduced. Thus, the growth behavior of the two phases is not affected proportionately, due to a change in diffusivity. The diffusional processes, the interfacial readjustment, and the pinning and dragging that govern the microstructure evolution are hard to decouple from one another. Hence, the observed behavior cannot be readily attributed to any of them, and is believed to be the outcome of the complex interplay among them.

### 8.3.6 The Zener relation

#### 8.3.6.1 Two-phase microstructures with $D = 1.0$

The main findings of the previous subsection can be summarized as follows, as the volume fraction of one of the phases increases, the growth rate of the other phase decreases, and, the ratio of major phase grains' mean radius to that of the minor phase is inversely related to the volume fraction of the latter throughout the course of evolution. The second of these is reminiscent of the Zener pinning law which connects the stagnant state mean radius of the matrix phase to the embedded particles' size and volume fraction. It is probably for this reason that many a time in the literature, the two-phase polycrystalline microstructure coarsening results are fitted to the classical Zener law or after some modifications to it [51]. However, it has to be cautioned that the Zener law is derived for
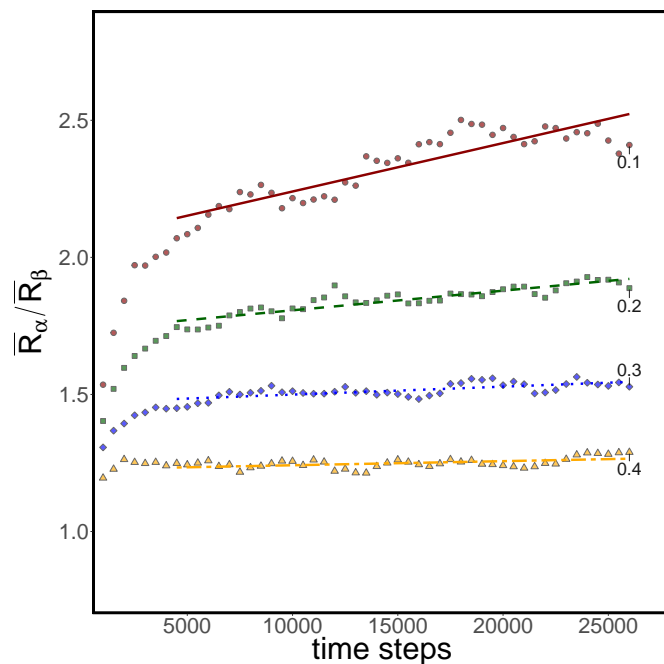
*(a)*
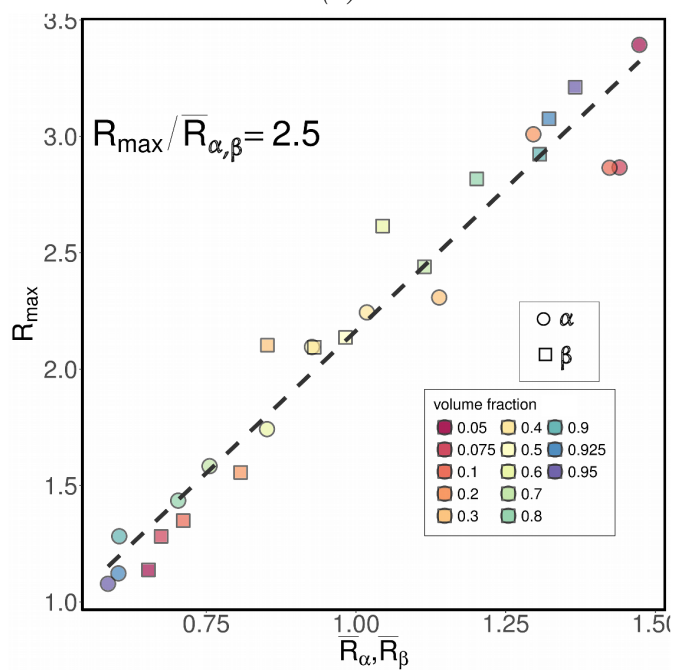


*(b)*

*Figure 8.9: (a) A temporal evolution of a relative growth rate is reported in terms of $\bar{R}_\alpha/\bar{R}_\beta$. As the volume fraction increases, $\bar{R}_\alpha/\bar{R}_\beta$ decreases. (b) The growth rate of the mean to maximum grain size versus the growth rate of individual phases, revealing a linear correlation with $\bar{R}_{\max}/\bar{R} = 2.5$. Their isotropic growth behavior can be revealed by the ratio of $\bar{R}_{max}/\bar{R} = 2.5$.*
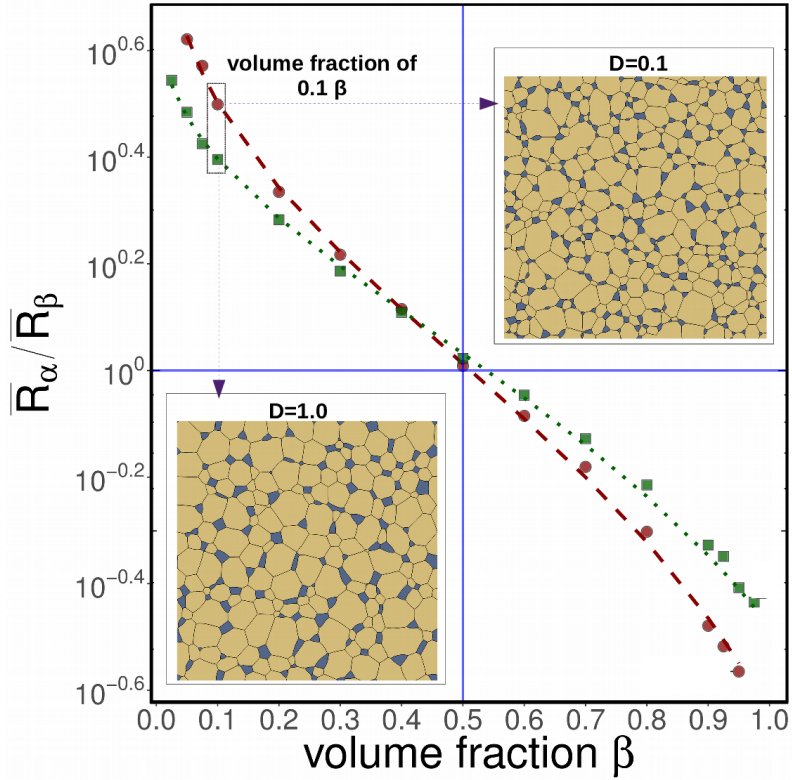
*Figure 8.10: The influence of diffusivity on the $\bar{R}_\alpha/\bar{R}_\beta$ ratio, as a function of the $\beta$ volume fraction.*

situations which are entirely different from the current case of multiphase grain growth where complete pinning or stagnation does not occur, in principle. Hence, such a move has to be understood as borrowing analytical tools from a different domain in the absence of exact analytical theories for the problem under consideration, which is a common practice in applied science. In spite of this, we compare our computational results by fitting them to a generalized Zener relation with some previously proposed exponent values and also obtain a best fit value for our data set. It is interesting to note that in all the prior studies constant values for Zener exponents are proposed, however, we believe that such a thing, which may be true for actual pinning phenomenon, does not carry over to multiphase microstructural coarsening where various parameters like diffusivities, interfacial energies have a role to play. Thus the growth exponents and growth co-efficients have to be functions of these quantities; we test this in the following.

The mean grain sizes of the primary and secondary phases are related through various previously proposed modified Zener relations and are depicted in Fig. 8.11 for various volume fractions $f$. In case of a Zener exponent of $1/q = 1$ prescribed in [49] for non-random inert particle distribution, the fitting lines are completely deviant from one another, i.e. the slopes are quite varied. The values $1/q = 0.5$ and $1/q = 0.33$ suggested in [50] and [202], respectively, show some interesting behaviors when adopted to our data set. Fitting with $1/q = 0.5$ leads to the volume fractions 0.2, 0.3 and 0.4 to overlap, however, the

volume fraction 0.1 deviates from the main fitting. This is in contradiction to a previous similar study on growths involving coarsening minor phase grains [61]. In contrast, the $1/q = 0.33$ case shows very good agreement for 0.1, 0.2 and 0.3 volume fractions, but the higher volume fraction 0.4 deviates from them. When a Mean Square Error (MSE) method was employed to select the best fitting exponent for our data, a value of $1/q = 0.43$ is obtained with a positive correlation of 0.95 and a standard error of 0.0070.

To verify the consistency of our results, we also computed the effect of the volume fraction of the $\alpha$ phase in the $\beta$ matrix. It can be seen from Fig. 8.12 that the fitting parameter of $1/q = 1$ shows a non-consistent behavior. Furthermore, we observe that the volume fraction 0.1 of the $\alpha$ phase deviates from the rest, when $1/d = 0.5$, and similarly the volume fraction 0.4 deviates for $1/q = 0.33$. An MSE method to determine the best fitting line for all volume fractions from 0.1 to 0.4 $\alpha$ yields a value of $1/q = 0.42$ for our dataset, which is in close proximity to $\beta$ in the $\alpha$ matrix case.

### 8.3.6.2   Two-phase microstructures with $D = 0.1$

Diffusivity seems to have a considerable effect on the fitted Zener relations. Fig. 8.13 shows the findings of the analysis of section 3.6.1, when repeated for the diffusivity case of $D = 0.1$. In the case of $1/q = 1$, however, the fitting curves for 0.3 and 0.4 overlap, whereas the fractions 0.1 and 0.2 are separated. Furthermore, the volume fractions 0.1, 0.2, and 0.3 are superposed with the deviated fraction 0.4, when $1/q = 0.5$. For the case of $1/q = 0.33$, all selected volume fractions follow different trend lines with varied slopes. The MSE method provides a best fitting parameter of $1/q = 0.61$. Although the least errors are statistically provided by a best fit, small variations are observed at the volume fraction 0.1.

In Fig. 8.14, similar sets of calculations have been done on $\alpha$ in $\beta$ matrix systems. The fitting for $1/q = 1$ results in approximately parallel lines that are separated from one another. $1/q = 0.5$ exhibits a deviation for the volume fraction of 0.4. Furthermore, $1/q = 0.33$ shows completely incoherent fitting lines. The MSE method results in a Zener exponent of $1/q = 0.6$, which is due to the fact that for the high diffusivity $D = 1.0$, the $\beta$ in the $\alpha$ matrix case and the $\alpha$ in the $\beta$ matrix case behave similarly with respect to the fitting parameter $1/q$.

### 8.3.6.3   Minor phase particle inclusions

A low volume fraction of pinning particles is preferred for high temperature applications, where ideally high strength materials with single-phase microstructures are desired. The $\leq 10\%$ systems of the current work are analyzed in this section, in regard to their consistency with the Zener relation. The fittings of the MSE method, for the volume fractions 2.5%, 5%, 7.5%, and 10%, are demonstrated in Fig. 8.15; the corresponding best fit values
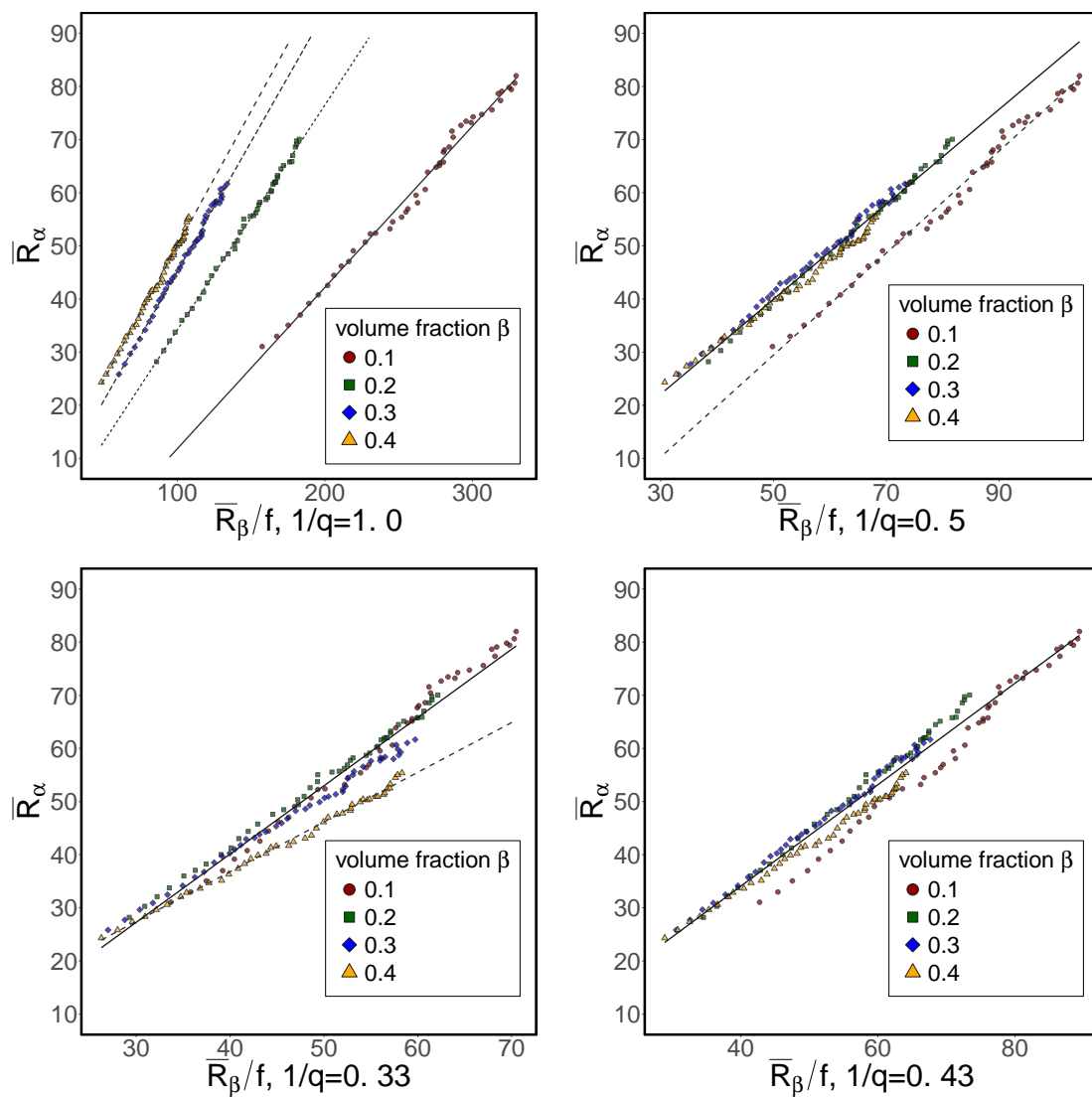
Figure 8.11: Modified Zener equation with the reported fitting values for the diffusivity $D = 1.0$ and for $\beta$ phase grains embedded, in the $\alpha$ matrix $(R_\alpha = SR_\beta/f_\beta^{1/q})$.
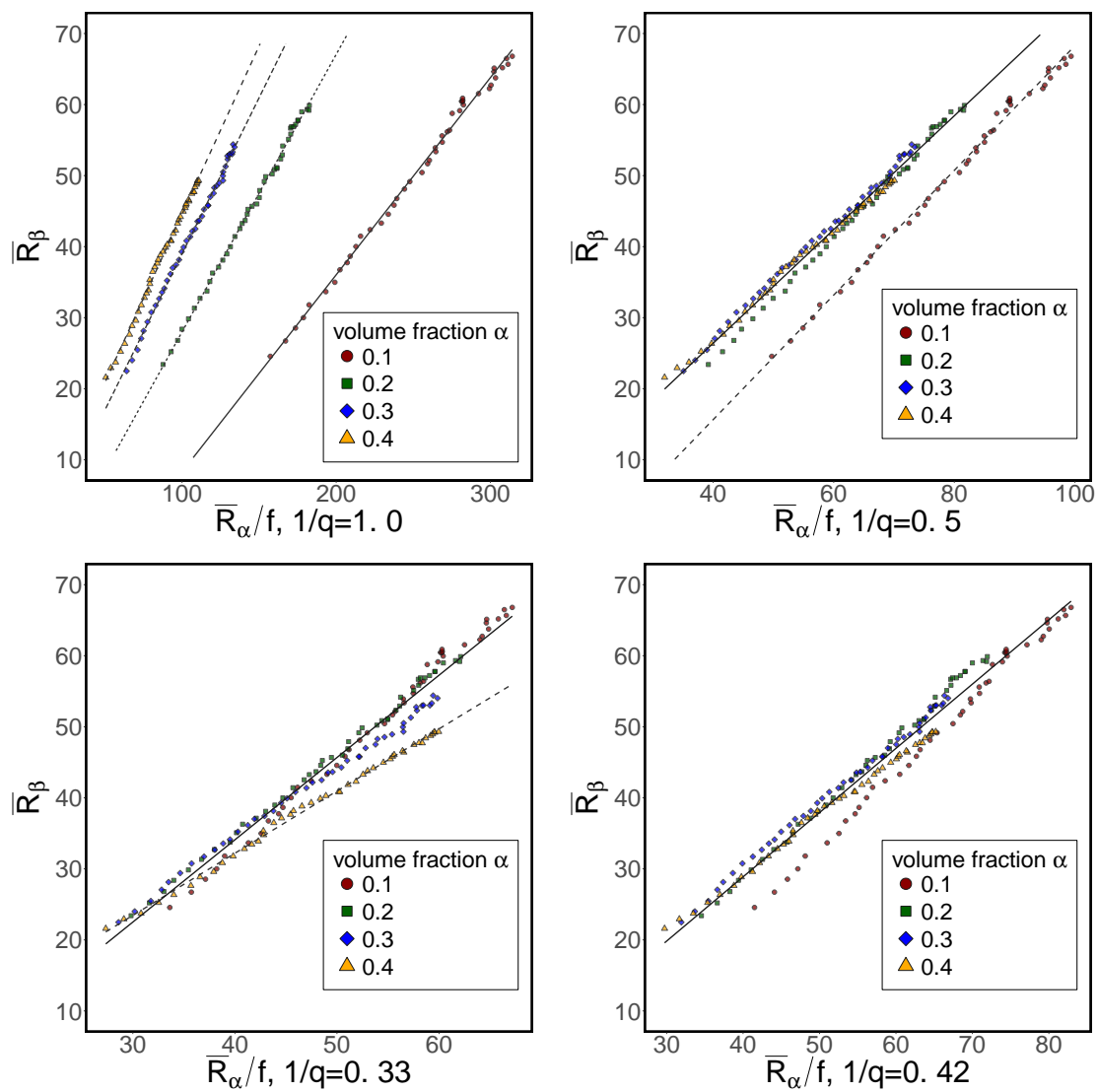
Figure 8.12: *Modified Zener equation for the diffusivity $D = 1.0$ and for $\alpha$ phase grains, embedded in the $\beta$ matrix $(R_\beta = SR_\alpha / f_\alpha^{1/q})$.*
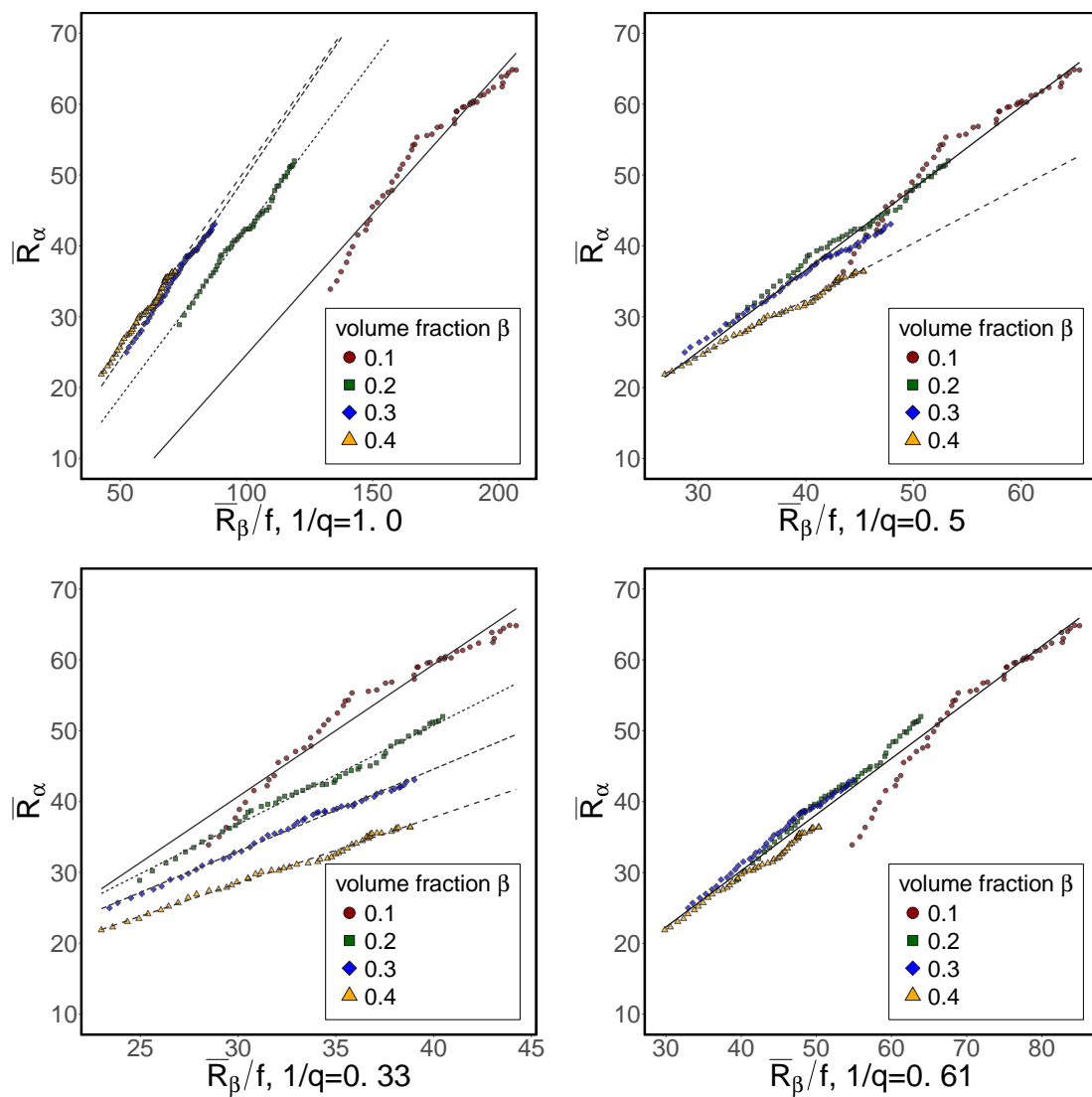
Figure 8.13: *Modified Zener equation for a diffusivity of $D = 0.1$ and for the $\beta$ phase grains embedded in the $\alpha$ matrix ($R_\alpha = SR_\beta/f_\beta^{1/q}$).*
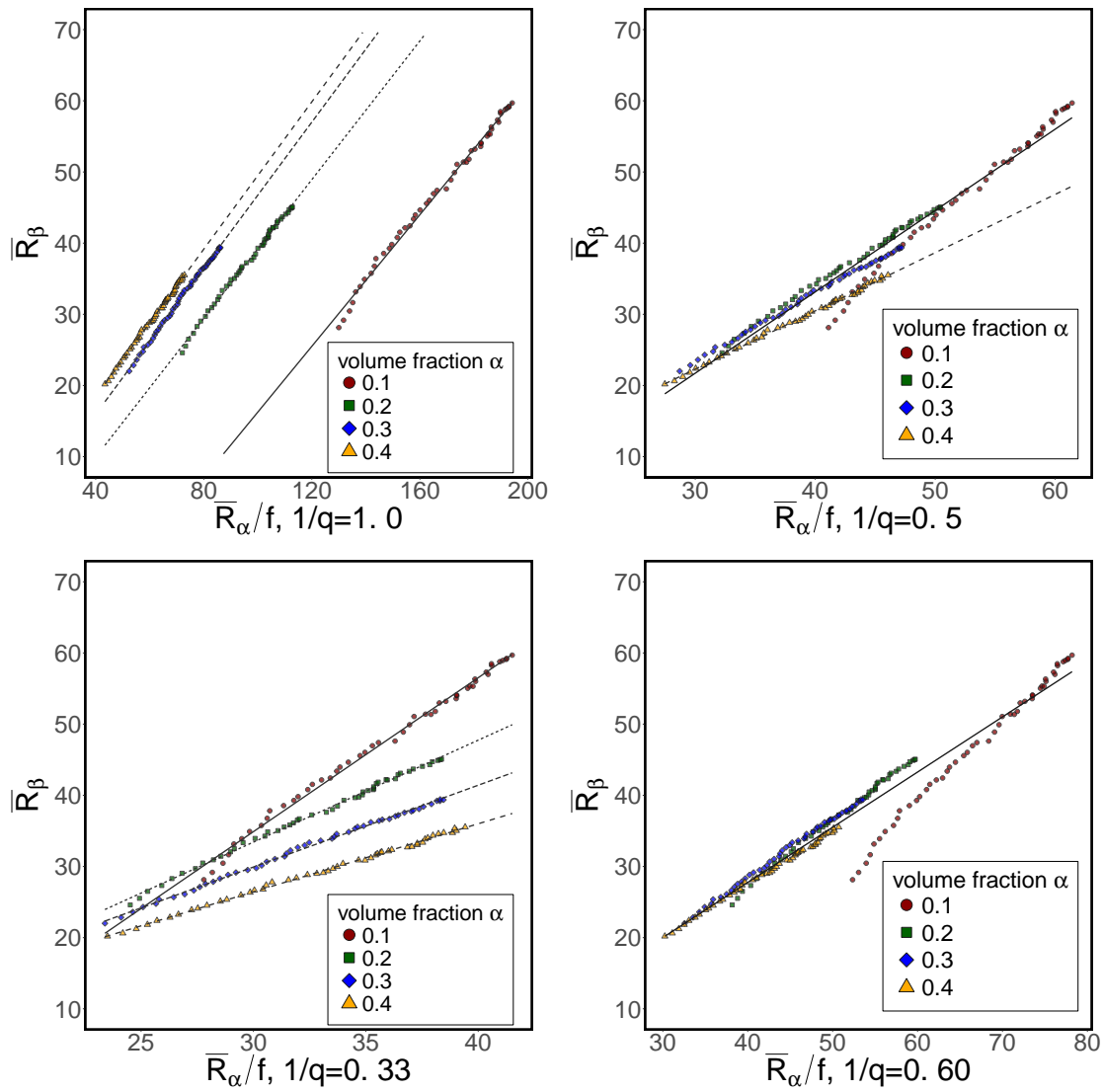
Figure 8.14: Modified Zener equation for a diffusivity of $D = 0.1$ and for the $\alpha$ phase grains embedded in the $\beta$ matrix ($R_\beta = SR_\alpha/f_\alpha^{1/q}$).
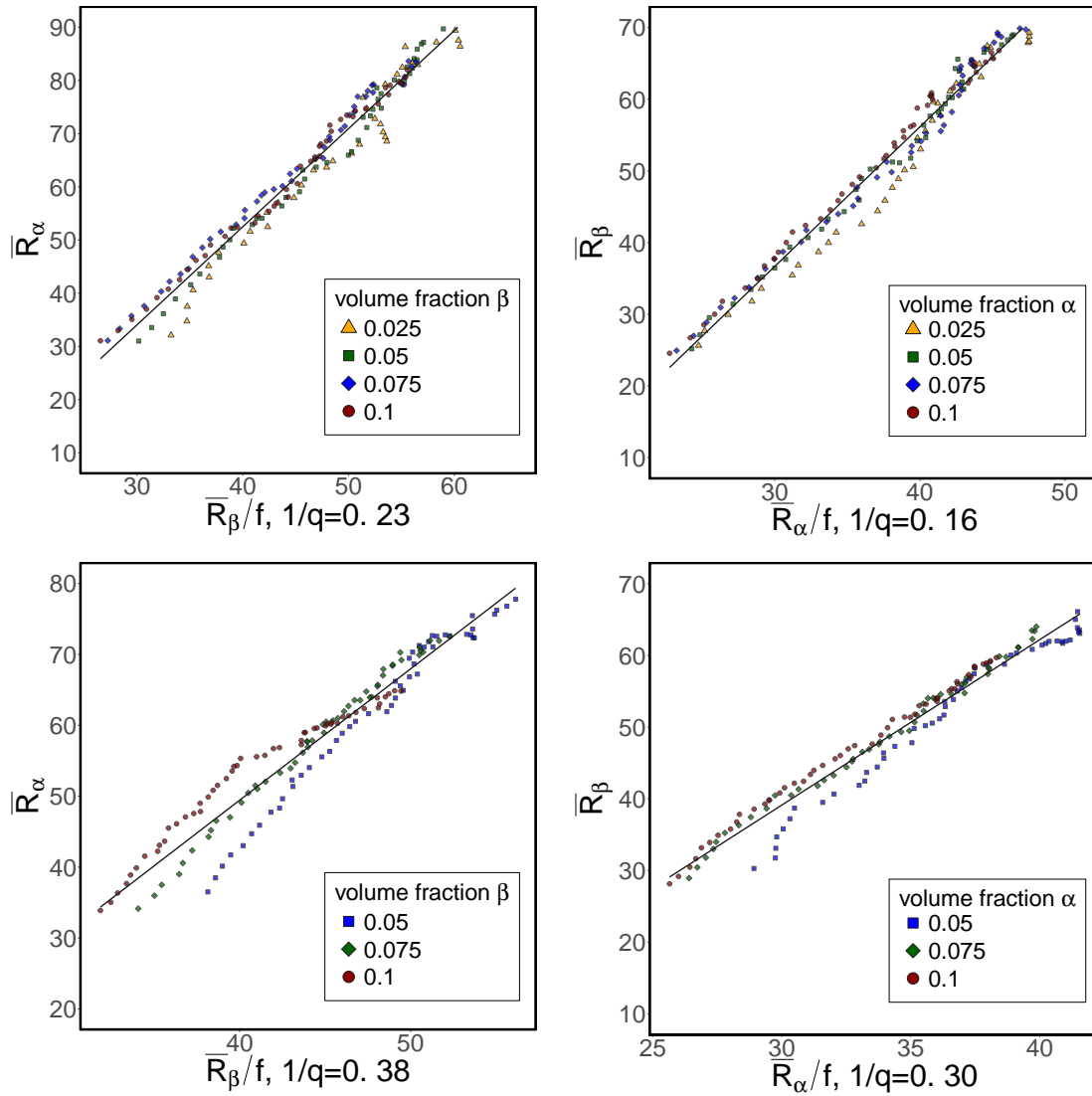
*Figure 8.15: Modified Zener equations for low volume fraction studies (a) $D = 1.0$ (b) $D = 0.1$.*

for $1/q$ are reported in Table 8.1. Notice that unlike the case of two-phase microstructures with high volume fractions, the $\beta$ in $\alpha$ and $\alpha$ in $\beta$ cases exhibit a dissimilar behavior.

### 8.3.6.4   Discussion

Through the aid of simulation studies, a Zener exponent of $1/q = 0.5$ has been previously suggested in the literature for two spatial dimensions. Most of these works dealt with low volume fractions ($<10\%$) assuming inert characteristics and predefined geometries for the secondary phase. This means that right from the beginning of the simulation, the pinning grains have a widely different size compared to the primary grains. Moreover, they are allowed to be embedded inside the major phase grains as opposed to being adjacent to them, as in the current study, while in other investigations, the same exponent value

| | **High f : $1/q$** | | **Low f : $1/q$** | |
|---|---|---|---|---|
| | $\alpha$ in $\beta$ | $\beta$ in $\alpha$ | $\alpha$ in $\beta$ | $\beta$ in $\alpha$ |
| **D = 1.0** | 0.43 | 0.42 | 0.23 | 0.16 |
| **D = 0.1** | 0.61 | 0.60 | 0.38 | 0.30 |

*Table 8.1: Best fitting Zener exponents, obtained from our 2-D simulations*

is predicted, albeit for high volume fractions and an evolving secondary phase. The dependence on diffusivity, however, has not been explored before. In contrast, however, it can be observed that in the current investigation, the Zener exponent $1/q$, for high volume fractions, is clearly dependent on the diffusivity, although it stays close to 0.5, while for low volume fractions, it varies considerably from this value. In the latter cases, it is furthermore found to be independent on interfacial energies, alongside the diffusivity. Such wide discrepancies among the various proposed exponents tend to point out that in the Zener relation, a constant value for $q$, originally derived for inert pinning particles, cannot be directly adopted in the case of two-phase polycrystalline systems. This casts serious doubts on the mechanisms proposed to explain the pinning ability of coarsening secondary grains that follow from a comparison of the Zener co-efficient obtained for such systems through fitting methods with the classically derived one for inert particles.

Nevertheless, some useful information about the growth dynamics can be drawn from such an exercise of fitting to Zener law. For instance, the difference in the fitted $1/q$ values for low and high volume fraction cases can be interpreted as an indication of the presence of a difference in the dominant mechanism (i.e., interface-controlled vs. diffusion-controlled) in the respective regimes. The presence of a difference in the $1/q$ value for $\alpha$ in the $\beta$ case compared to $\beta$ in the $\alpha$ case, for low volume fractions and the lack thereof in the high volume fraction systems, in the presence of different interfacial energies for the two phases, gives strength to this hypothesis. Thus, a comparison with the Zener relation, though inconclusive about the mutual growth retarding behavior, points out the principal governing mechanism of grain growth in the two-phase polycrystalline systems.

### 8.3.7 Abrupt change in local growth behavior due to topological events

Topological events are often accompanied by a sudden change in the local growth behavior [122, 166, 203]. Fig. 8.16a shows a local region in the microstructure evolution for the volume fraction 10% of the $\beta$ case. The Ostwald ripening of the $\beta$ phase grains, encircled in red, is abruptly accelerated, following the topological event of an $\alpha$ grain dissolution, leading to a joining of the $\beta$ grains. This is because the distance over which the atoms have to be transported for coarsening is decreased. When the joining grains have the same orientation, an additional coalescence can be observed, and the size of the grains is

even more pronounced.

A local region, exhibiting a particle drag phenomenon, is depicted in Fig. 8.16b. A long $\beta$ particle, surrounded by four $\alpha$ grains forming four $\alpha/\beta/\alpha$ triple junctions, changes its shape by sequentially reducing its number of faces. In a first step, two of the $\alpha/\beta/\alpha$ junctions join, and the resulting quadruple junction splits, forming an arrowhead-shaped $\beta$ grain, with an $\alpha/\beta/\alpha$ triple junction at the apex and an $\alpha/\alpha/\alpha$ junction. This is followed by a similar event, in which the remaining two of the original triple junctions of the $\beta$ grain finally result in a lens shape. Such topological events spontaneously change the growth rate around the daughter junctions, as compared to the parent junctions. The similar movement of the phase triple junctions can proceed through an interface readjustment, whereas the mixed triple junction dynamics should necessarily be associated with mass redistribution, i.e., a diffusion-controlled mechanism. Experimental evidence of such events was found in $ZrO_2$ inclusions in the $Al_2O_3$ matrix [204], and pore dragging was found during sintering [195].

The details of the frequency of such topological events, their distribution throughout the microstructure, and their effect on the global growth behavior have not been investigated in detail in the phase-field framework. Moreover, the role of relative phase-fractions and diffusivity, with respect to local and global topological changes in the microstructure, makes up for an interesting study, and will be taken up in future investigations.

## 8.4   Summary

The multiphase-field model has been employed to study grain growth and coarsening phenomena in two-phase materials. The 2-D microstructural evolution examined by phase coarsening with a wide variety of volume fractions and varying diffusivity conditions. The obtained results are as follows:

1. Microstructural evolution considerably differs between nonconserved and conserved systems. A stable interpenetrating (duplex) microstructure was obtained for an equal volume fraction case.

2. The kinetics of grain coarsening does not strictly follow the diffusion-controlled or interface-controlled mechanism, when the volume fraction of the minority phase varies. For a critical volume fraction, the rate-limiting step is bulk diffusion, and the observed growth exponent is $m \approx 3$.

3. The ratio between the mean grain size of the $\alpha$ and $\beta$ phase decreased with an increasing volume fraction of the $\beta$ phase. These results are consistent with experimental findings.
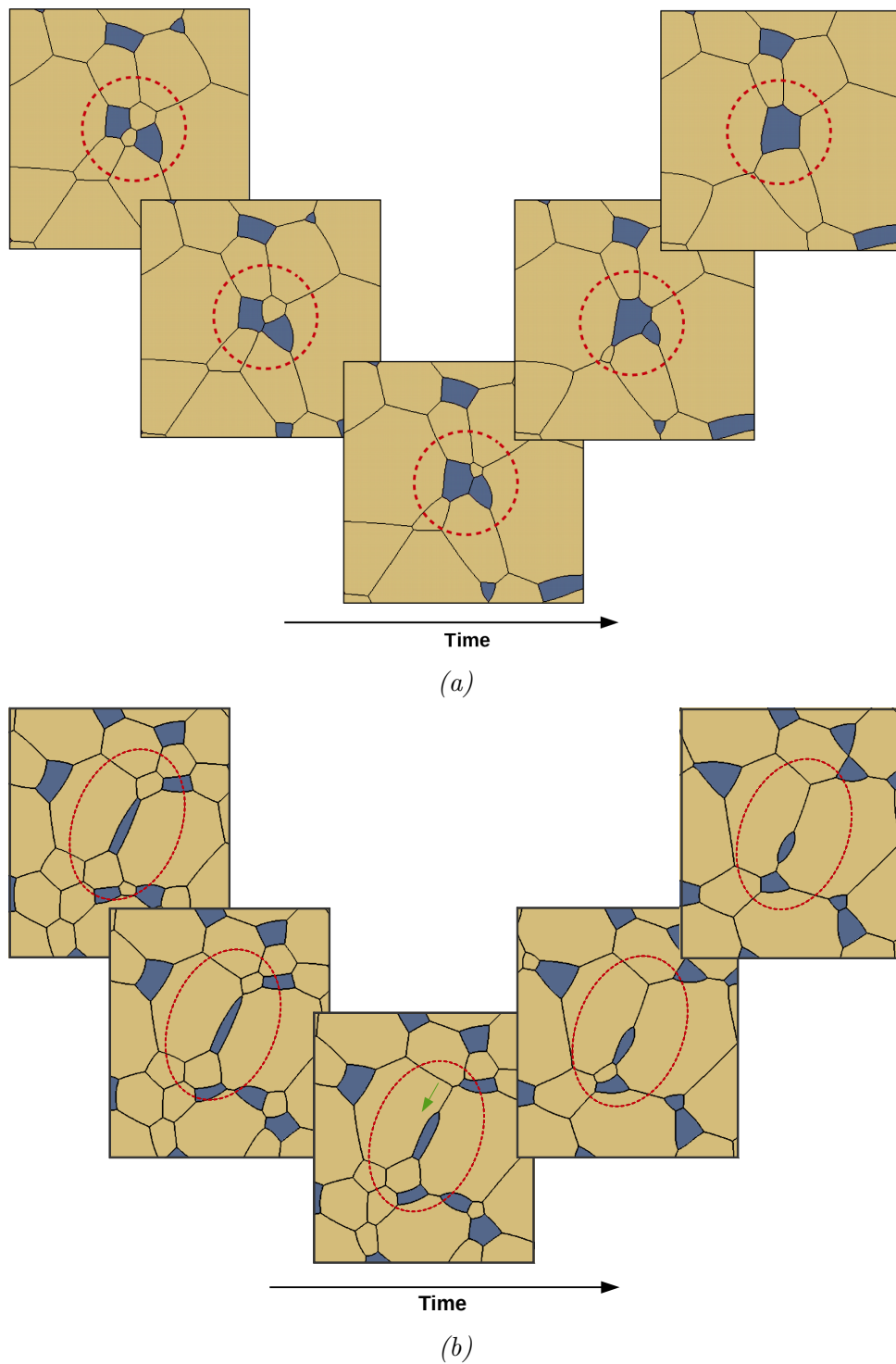
*Figure 8.16: Different particle coarsening mechanisms in a two phase polycrystalline microstructure with (a) topological changes of neighboring grains and (b) a particle dragging event*

4. The diffusion over longer distances is required for the coarsening of the low volume fraction phase and results in a slower growth rate. This can be demonstrated by the relative growth kinetics of a given phase for various volume fractions.

5. The growth rates of the $\alpha$ and $\beta$ phases of the equivolume fraction case are different, since the inter-grain distances are the same for both phases. This is due to the difference in the interfacial energies of the two phases.

6. Grain growth of the $\alpha$ phase was adequately controlled by $\beta$ phase grains and vice versa. The mean grain size of the primary phase can be predicted by the revised Zener relation.

# Chapter 9

# Microstructural coarsening of equivolume fraction duplex materials

## 9.1 Introduction

In the previous chapter, concurrent grain growth and coarsening of the two-component, two-phase (immiscible) system have been investigated while varying the phase volume fraction, diffusivity and interfacial energy parameters [3]. It was found that mean grain size of the system supports a well-known power law kinetics with $m \approx 3$ (volume diffusion controlled). The equivolume dual-phase microstructure holds the highest probability of the number of $\alpha$-$\beta$ contacts where the diffusion length is significant for both phases. In several cases, especially for duplex microstructures, the grains of one or both phases remain either interconnected or distributed throughout the microstructures [197]. In particular, the $0.5\alpha$-$0.5\beta$ system reveals some interesting features where the relative growth rate of both $\alpha$ and $\beta$ phase grains are found to be nearly the same. Thus, the ratio between the mean grain size of $\alpha$ and $\beta$ phase stays close to one. We also observed that the mean grain size ratio $(\bar{R}_\alpha/\bar{R}_\beta)$ of $0.5\alpha$-$0.5\beta$ system is more or less independent to the bulk diffusivity of the system [3]. Ohnuma et al., have also derived a similar linear relationship between $\alpha$ and $\beta$ phases as a function of volume fraction and interfacial energy parameters [205]. Some of the experimental data is found to be consistent with their model of two dimensional simulations with anisotropic boundary energy combinations [4, 5, 206].

Diverse microstructural patterns can be obtained by varying the differences in inter-phase, inter-grain interfacial energies. It is an interesting problem that has been previously addressed by Chan [207]. Later Holm et al., attempted to validate Chan's microstructure maps using their two dimensional Monte Carlo simulations while holding a non-conserved hypothesis [197]. Most recently Change et al. attempted a similar study employing phase-field simulations for the non-conserved two-phase systems [193]. Though the prior studies were concentrated on non-conserved systems, it could also be extended to the conserved

(real) systems where the long range diffusion is operative.

The energy ratio of $\alpha$ and $\beta$ phase grains can be derived as $ER_\alpha = \frac{\sigma_{\alpha_i \alpha_j}}{\sigma_{\alpha\beta}}$ and $ER_\beta = \frac{\sigma_{\beta_i \beta_j}}{\sigma_{\alpha\beta}}$ respectively. For an isotropic system ($ER_\alpha = ER_\beta = 1$), the balance of the grain boundary tensions requires that the edges meet at an angle of $2\pi/3$. Moreover, the quadruple junctions are not thermodynamically stable. Nevertheless, throughout the evolution, a considerable number of the quadruple junctions have been developed. But, the life span of these quadruple junctions are short and can quickly split into stable triple junctions in order to maintain their equilibrium angles at the junction [92, 208]. In contrast to the isotropic cases, at some higher energy ratio combinations, stability of the quadruple junctions are thermodynamically favored while the splitting of triple junctions may cause additional energy contributions.

The stability criteria for triple junctions were discussed by Gibbs, the possibility of stable quadruple junctions in two-phase polycrystalline materials was established by Cahn [207]. The interfacial energy balance should determine the angles at which the boundaries intersect triple junctions. However, it was suggested that angles at quadruple junctions may not be derived only by the interfacial energy balance. However, to sustain these quadruple junctions, the geometric fact that the angles around them must sum to $2\pi$. The balance of interfacial energies at the quadruple junctions requires that the four-grain angles be the same. The stability microstructural maps are summarized and shown in the ($ER_\alpha$-$ER_\beta$) plane [207, 197].

In many systems, particularly in the case of alloys, the phases that develop a duplex microstructure hold the interfacial energy ratios roughly independent of temperature [209, 210, 211]. On the other hand, in ceramics and composites, by choosing the proper constituting phases with the desired energy ratios, the optimum microstructure with appropriate properties can be achieved [212, 213]. The interfacial energy of individual grain/phase combination through $\alpha$-$\alpha$, $\beta$-$\beta$ and $\alpha$-$\beta$ can be easily controlled in numerical simulations. This work attempts to answer some of the open questions in the microstructural coarsening of duplex materials with a wide range of interfacial energy ratios by conducting large scale two-dimensional phase-field simulations.

## 9.2   Domain set-up

We performed two-dimensional (2-D) simulations, with the domain size of $2048 \times 2048$ grid points and periodic boundary conditions are adopted for both directions. Roughly 10000 grains are randomly distributed over the simulation domain, through a Voronoi tessellation algorithm, as described in [1]. At this initial filling stage, all grains in the domain are of the single phase. Simulation of mixed microstructure with 50% second phase, an appropriate number (5000) of grains is randomly assigned with desired prop-

erties. The initial distribution is random and uniform throughout the domain, with all grains being roughly the same size. The radius of a grain $i$ is expressed as $R_{\phi_i}$, where $\phi_i$ indicates the phase identity. The number of voxel cells inside the chosen grain is counted, and a circle of an equivalent area is used for computing individual grain radius. The composition variables at each grid point are set equal to those of the equilibrium values ($C_{eq}^{\alpha} = 0.2A0.8B$ and $C_{eq}^{\beta} = 0.8A0.2B$).The interfacial energy of the $\alpha/\beta$ interphase is taken as 1.0. In this study, the energy ratios of $\alpha$ and $\beta$ phase are systematically chosen to accomplish the desired duplex microstructure. The bulk diffusivity is fixed as 1.0 while holding the grain boundary mobilities are constant.

That one may to solve the phase-field evolution equations, a finite difference algorithm is implemented across a uniform numerical grid [154], using an explicit time-stepping (forward Euler) scheme. Equal grid spacings are assumed in both directions, i.e., $\Delta x = \Delta y = 1.0$. The diffuse interface width $\epsilon$ is set to $4\Delta x$, for all simulations, ensuring an adequate resolution of the diffuse interface region, and a time step is chosen well within the numerical stability range ($\Delta t = 0.01$). Computational performance has been enhanced by introducing the *Locally reduced order parameter optimization (LROP)* method, which optimizes both memory and time consumption for the simulations [155, 156, 183]. The simulation domains were computationally enhanced by domain decomposition, using MPI (Message Passing Interface) [107]. The simulations are run long enough to ensure that the steady state grain growth regime reached. On average, each simulation took 28 hours for completion, with 82 CPUs. The total computation time for this study is around 952 hours ($\approx 40$ days).

## 9.3   Results and discussions

### 9.3.1   Microstructural features

The conserved systems (CS) are those in which the volume fraction of the individual phases remains approximately constant throughout the evolution, while nonconserved systems (NCS) are those in which one phase could consume or be consumed by the other in the absence of a bulk driving force. For example, a nonconserved situation commonly observed in abnormal grain growth systems where the interfacial energies or mobilities for some of the grains differ from the normal ones. Often the relative growth rate is accelerated for such abnormal grains, and thus their volume fraction is not preserved during evolution [197]. Thus NCS can be considered as a single component multi-phase polycrystalline material. On the other hand, most of the engineering materials, e.g. super alloys, steels, high entropy alloys, consist of multi-component multi-phase polycrystalline microstructures and have been treated as conserved systems (CS). The bulk free energy contribution is significant and one may infer that the heat treatment may reveal a tendency

for concurrent grain growth and coarsening behavior.

Temporal evolutions of the equivolume (0.5$\alpha$-0.5$\beta$) duplex microstructures corresponding to different interfacial energy ratios of $\alpha$ and $\beta$ phase combinations with respect to ($ER_\alpha$ & $ER_\beta$) are shown in Fig. 9.1 for non-conserved and Fig. 9.2 for conserved systems. The grains are shown in yellow correspond to the $\alpha$ phase, and the ones are shown in blue correspond to the $\beta$ phase. From the visual observation, it is readily evident that the mean grain size increases with time. The principal governing mechanisms of the growth are a short range interface re-adjustment around the grain junctions of similar phases, and/or long-range bulk diffusion (Ostwald ripening).

The growth competition among $\alpha$ and $\beta$ grains always persist throughout evolution. As shown in the classic work of Holm et. al [197], several interesting microstructural patterns appeared in the duplex non-conversed system at the outcome of the interfacial energy ratio parameter variations. In the present study, motivated from the prior attempts, the utilized interfacial energy ratios can be grouped into four different regimes to discuss the following results.

1. zone1: ($ER_\alpha = ER_\beta < 1.0$)

2. zone2: ($ER_\alpha < 1.0 \neq ER_\beta$)

3. zone3: ($ER_\beta < 1.0 \neq ER_\alpha$)

4. zone4: ($ER_\beta = ER_\alpha > 1.0$)

In general, the overall thermodynamical energy minimization drives the microstructural evolution. In zone1, the simulation of ($ER_\alpha = 0.51$ and $ER_\beta = 0.51$), inter-grain boundary energy of $\alpha/\alpha$ and $\beta/\beta$ are lower than the $\alpha/\beta$ inter-phase interfacial energy. Thus, the lower energy grain-grain contacts are thermodynamically preferable over the higher energy phase boundary contacts. Such a way that the clustering bias is achieved for the system, as the similar phased ($\alpha/\alpha$ and $\beta/\beta$) grains start to form a network like structure, and the neighboring $\alpha/\beta$ grains re-arrange themselves to minimize the number of anti-phase contacts [197, 207]. The difference between the inter-grain and inter-phase interfacial energies is responsible for the rate of clustering tendency in the system. However, for the above case, the difference is not as much pronounced, the resultant microstructure with a continuous clustering of similar phase grains can be reached with the prolonged time.

On the other hand, the energy ratio of the $\alpha$ phase is always lower than the $\beta$ phase counterpart in zone2 simulations. For example, the system with energy ratio of ($ER_\alpha = 0.51$ and $ER_\beta = 1.0$) case is chosen. In this system, whenever the $\alpha$ meets the $\beta$, the lower energy phase might consume the higher energy phase. The energy difference is, therefore, sufficient enough for the $\alpha$ phase grains to continuously consume the neighbor

$\beta$ phase grains during evolution. Over a period of time, the resultant microstructure accommodates only a lower energy phase grains, in this case, the $\alpha$ phase grains can only persist. After this transition period, the evolution should solely build upon on the survival phase grains interfacial energy minimization mechanism. By choosing the ($ER_\alpha = 1.0$ and $ER_\beta = 0.51$) parameter in zone3 setup, the $\beta$-phase grains could completely absorb the $\alpha$ phase grains with time, where the lowest $\beta$-$\beta$ energy contacts are favored. In both cases, the identical simulation parameters are used, other than in place of $\alpha$, the $\beta$ was treated. Henceforth, the overall growth kinetics of both system should behave similarly. The resultant microstructures in Fig. 9.1 indicated that the mean grain size of system looks more or less the same.

The choice of the parameter ensures that the microstructural complexity is much higher than the typical experimental observations. Therefore, at this parametric study, higher energy ratios were tested. For example, in zone4 setup, the system with ($ER_\alpha = ER_\beta = 2.1$) energy ratios is selected. During the evolution, the chessboard-like pattern is gradually revealed from the initial random grain arrangement. We found that an analogous simulation parameters in [197] were also resulted in a complex network like microstructures for two-phase systems. Note that even for a nonconserved condition, this steady-state microstructure consists of roughly equal volume fraction of $\alpha$ and $\beta$ phase grains.

As a result of diverse energy ratios used, the microstructures with a mixed fraction of triple and quadruple junctions are possible [197]. In most cases, the lifespan of quadruple junctions is seen to be limited and quickly split into two triple junctions, in the course of the evolution. However, for some appropriate interfacial energy ratio combinations, considerable fraction of stable quadruple junctions have also been seen in the microstructure (zone4).

While the initial investigations are carried out for the non-conserved system, we next focus on more realistic conserved systems. Hence, the simulations performed at various values of interfacial energy ratios that can be approximately considered to be a study of microstructural coarsening in duplex ceramics/composites. When compared to the NCS case, the steady state microstructures show much more complicated patterns. Because the transformation of one phase (higher energy) to another (lower energy) is not favored and the volume fraction of individual phases are roughly preserved. The summarized results of duplex CS microstructures are shown in Fig. 9.2. The resulted microstructural patterns appear like an interpenetrating (duplex) composite structure, where the $\alpha$ and $\beta$ grains lie next to each other, forming a complex network with little size difference [196].

It should be noted here that the energy ratio parameters for NCS and CS simulations are same. Therefore, the steady-state zone1 CS microstructures can be directly comparable to the NCS results. The clustering tendency among similar phased grains can be observed from the resulted microstructures. It can be seen that the effect of energy
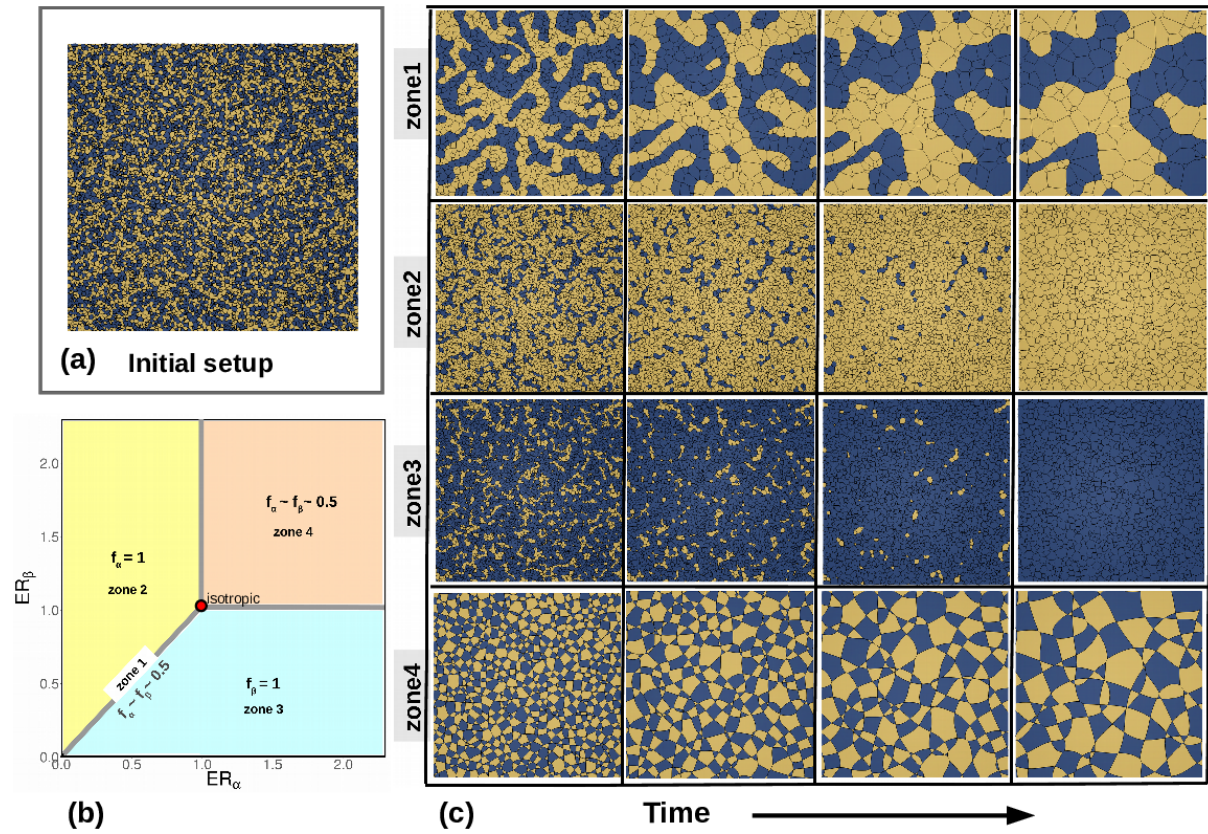
Figure 9.1: (a) Initial simulation setup of $50\alpha$-$50\beta$ system where yellow color represents $\alpha$ and blue represents $\beta$ phase grains (b) The microstructural catalog of two-phase non-conserved microstructures with varying interfacial energies of $\alpha$ and $\beta$ phase grains. (c) Microstructural evolution of selected non-conserved systems.
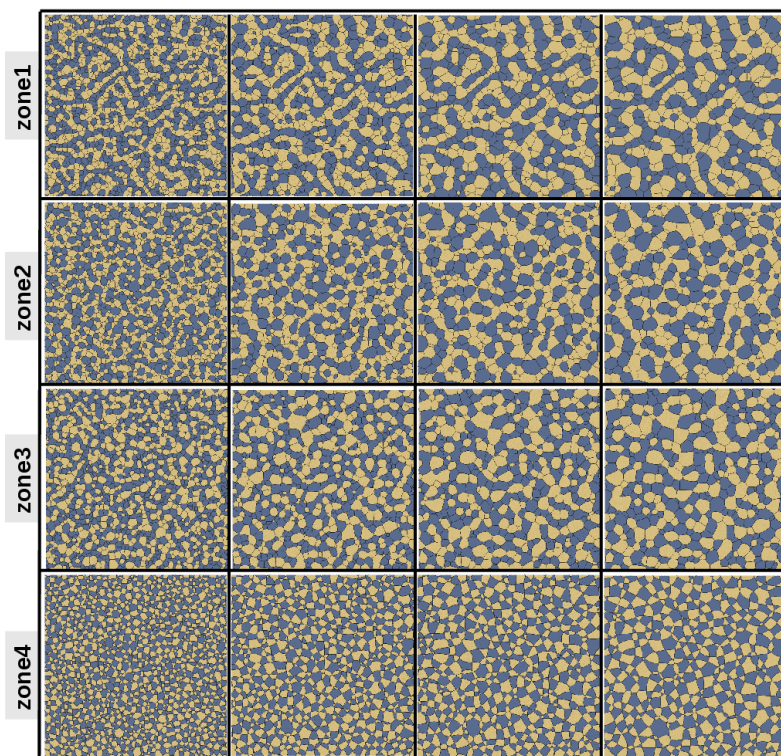
*Figure 9.2: Temporal evolution of some selected conserved system simulations. The volume fraction of the individual phase grains remains approximately constant value.*

ratio on phase transformation of $\alpha$ to $\beta$ and vice versa is restricted by the volume conservation behavior. Again, for higher energy cases, both CS and NCS system result in the chessboard-like microstructures. It is known that the fraction of quadruple to triple junctions is very sensitive to energy ratio parameters. The above results demonstrate that using a thermodynamical model with the anisotropic energies of $\alpha$ and $\beta$ phases are essential to design the interpenetrating composites with the required microstructures.

In the prior simulations, we have tested how the interfacial energy ratio could influence the microstructure by developing an initial pattern into a structured layout. In order to systematically investigate the morphological evolution of duplex structure, a series of energy ratio-dependent simulations are performed. The outcome of the simulated microstructures are shown in Fig. 9.3 for NCS and Fig. 9.4 for CS systems. Holm et al. derived the energy ratio conditions for the thermodynamically stable triple junctions of $\alpha\alpha\alpha$, $\alpha\alpha\beta$, $\beta\beta\beta$ and $\alpha\beta\beta$ and quadruple junction of $\alpha\beta\alpha\beta$ from his nonconserved two dimensional MC simulations [197]. The derived regimes of stable microstructural features (triple and quadruple junction regimes from Holm et. al) are superimposed with our results and more detailed discussions that follows.

As expected that, the clustering tendency among similar phased grains are observed in the $ER_\alpha < 1$ and/or $ER_\beta < 1$ simulations. The interfacial energy $\sigma_{\alpha\alpha} = \sigma_{\beta\beta} = \sigma_{\alpha\beta} = 1$ is fixed for an isotropic case simulations. Though, the initial randomness of the
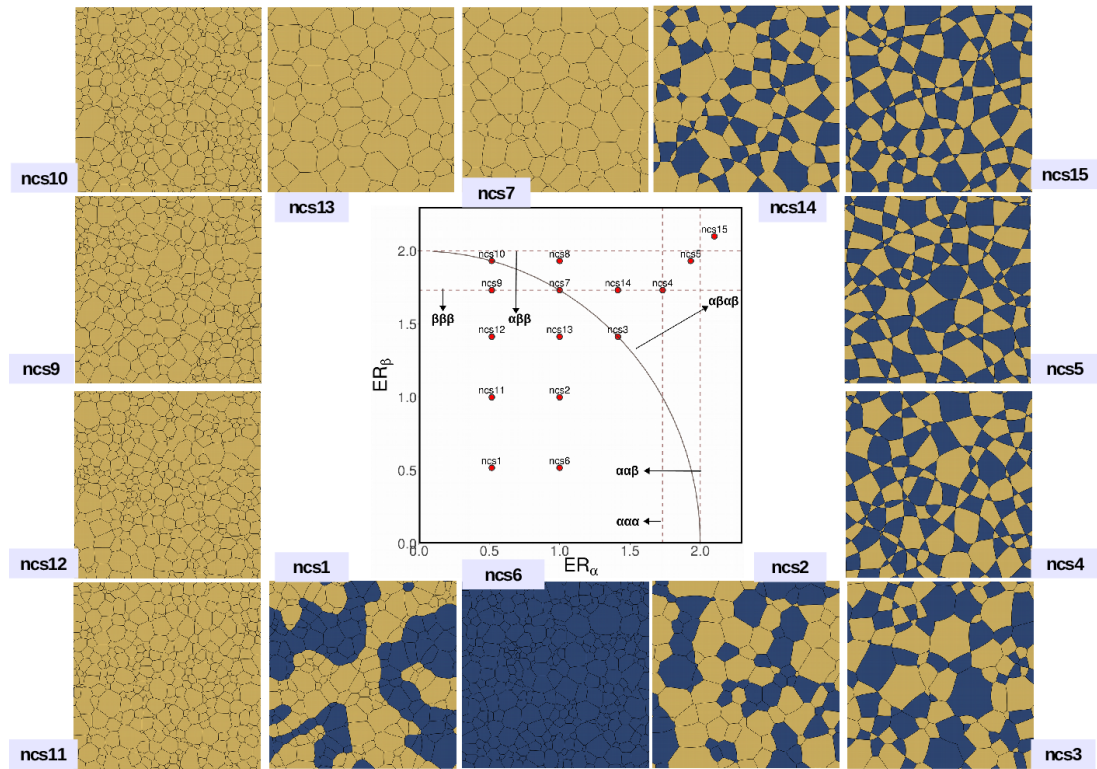
*Figure 9.3: Microstructural map of non-conserved systems with energy ratios. Various stable triple and quadruple junction regimes were reproduced from the Ref. [197].*

microstructural arrangements of $\alpha$ and $\beta$ grains might initiate the small clustering bias among the similar phase grains. Presumably, the conversion of $\alpha$ to $\beta$ and vice versa is not much pronounced. In a microstructure, to generate a single triple junction there should be three different grains making contact. But, in zone4 simulation, the probability of formation of $\alpha$-$\alpha$-$\beta$ and $\beta$-$\beta$-$\alpha$ contacts are not preferred, where as the stable quadruple junction of $\alpha$-$\beta$-$\alpha$-$\beta$ is favored.

We found that, certain quadruple junctions may generate throughout the evolution in lower energy cases, but their life span is short. In contrast, the higher energy ratio simulations, the developed quadruple junctions overcome the excessive free energy contribution and indulge triple junction breakdown. Therefore, we can estimate that the overall microstructure can hold the quadruple junctions depending on the used initial interfacial energy ratio. Sometimes there might be a change in the topological properties of grains to sustain the local quadruple junction criteria. In addition, isolated $\alpha$ and $\beta$ grains are also observed in some microstructures. In the following chapters, we use quantitative characterization tools to be able to more clearly distinguish the different microstructural features.
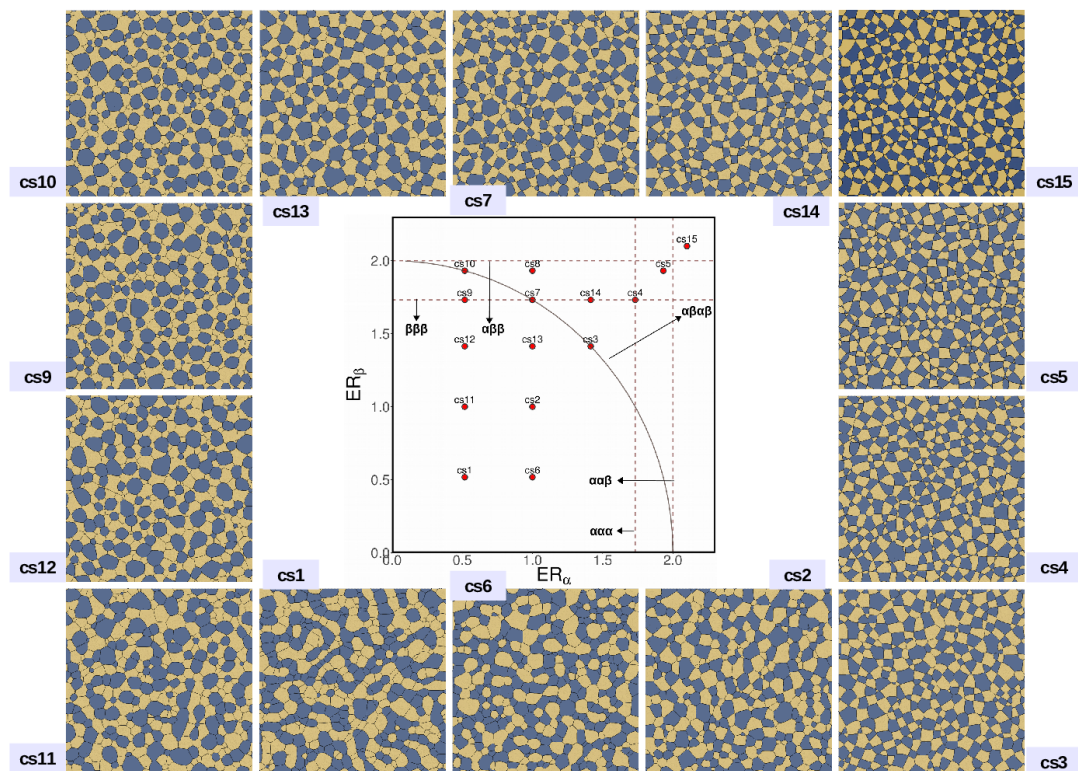
*Figure 9.4: Microstructural evaluation map for the conserved system simulations. The clustering tendency among the similar phased grains can be seen. Besides, the stable quadruple dominated systems develop for some extreme energy ratios.*

### 9.3.2  Mean grain size evaluation

In this section, we highlight the differences in the grain growth dynamics, associated with the nonconserved and conserved two-phase systems. The mean grain size of the individual phases and the whole system progressively increases with time for all the simulations. In general, the bulk diffusion controlled ($m = 3$) systems are much slower than the short-range interface controlled ($m = 2$) systems [3, 194]. By using a general power law kinetics, the best-fitted lines for the dataset are over plotted as solid lines in the Fig. 9.5a. The large differences in the grain growth kinetics are induced by the diverse interfacial energy ratios. This interpretation might provide an information regarding the rate of coarsening relative to one another with respect to their energy ratio parameters.

In NCS, the interfacial energy minimization proceeds through curvature driven grain growth process. The growth rate constant ($k$) implies a linear relationship with the inter-grain interfacial energy of the single phase system. This particular statement can also be valid to a multiphase polycrystalline system where the bulk free energy has not been included in the growth process. Hence, the growth kinetics of the system is instantly linked to the interfacial energy ratios employed in dual-phase systems.

As can be seen from the Fig. 9.5a, the slowest growth kinetics perceived for the zone2 and zone3 simulation conditions. The earlier microstructural observations reveal that phase transformation process of $\alpha$ to $\beta$ and vice versa in some NCS cases. Beyond a short initial period, the phase transformation rate increases with increasing time. Such phenomena indicates that the steady state microstructure after a transition period should only consist of lower energy phase grains. When the system turns into a single phase $\alpha$ polycrystalline microstructure, the driving force typically build on the interfacial energies of the remaining phase ($ER_\alpha = 0.51$).

Whereas in the zone1 regime, the $ER_\alpha = ER_\beta = 0.51$, the growth mechanism by diffusion is slightly faster than the zone2 and zone3 setup. The inter-phase contacts of ($\alpha$-$\alpha$) and ($\beta$-$\beta$) show the preference over the $\alpha$-$\beta$ contacts. The formation of similar phased cluster requires number of rearrangement of grains where the sluggish growth rate was observed immediately after the initial setup. Once the system reaches steady state, the relative growth kinetics is faster where the $\alpha/\beta$ inter-phase holds a higher energy. This phenomena indicated that the later inter-phase arrangement was responsible for the coarsening.

At zone4 ($ER_\alpha = ER_\beta = 2.1$) simulation, results a relatively leading growth rate than the former cases. Here, the $\alpha$-$\alpha$ and $\beta$-$\beta$ contacts are not preferred and the $\alpha$-$\beta$ contacts tends to stick together. Fig. 9.5a also exhibits the change in volume fraction, which however is not much pronounced. The interfacial energy balance results a complex network like structure where the stable quadruple junctions developed over the time.

In the isotropic simulation, the grain boundary energies ($\sigma_{\alpha_i\text{-}\alpha_j}$ & $\sigma_{\beta_i\text{-}\beta_j}$ ) are equal to

the inter-phase interfacial energy ($\sigma_{\alpha\text{-}\beta}$). Hence, all the observed inter-grain and inter-phase arrangements are random in nature. The volume fraction of individual phases roughly equal and conversion of one phase to another is not happening. In the anisotropic cases, presiding phase grains may reorient, assemble, or consume neighbors to form bigger grains. While this may be true for anisotropic interfacial energies, such a clustering bias and related phenomena of undergoing thermodynamical processes could not be prevail in isotropic case. Hence the extra demand for the thermodynamical energy is not needed and the utmost growth rate is noted for the isotropic simulation.

When the higher interfacial energy ratio used, the maximum growth rate could be expected for the zone4 simulations. Because, the overall growth kinetics build upon on the interfacial energies used for $\alpha$ and $\beta$ phases. However, the growth kinetics of zone4 simulation found to be slower than the isotropic case and somewhat higher than the remaining regimes. It should be related to the microstructural features in that the higher fraction of quadruple junction over the triple junction which cause the lower growth rate.

In a conserved system, the mean grain size evolution of zone2 and zone3 simulations behave similarly whereas the least growth rate is noted for zone4 setup. The zone1 result lies in between the zone3 and zone4 regimes. The observed growth kinetics of conserved system be in conflict with the nonconserved system whereas the underlying long-range diffusion mechanism could be responsible for this. The grain boundaries are mediated by the applied interfacial energy for the curvature driven systems. But in the conserved case, the rate limiting step is a bulk diffusion through the matrix where the complex diffusion paths along the grain junction result in sluggish diffusivity.

From the above results, it is worth mentioning that although the isotropic cases have performed well than the remaining simulations for non-conserved and conserved systems, their microstructures are much random because the energy demand impose even less stringent conditions for achieving steady state. However, it should be reminded that the microstructural features presented in earlier studies were mainly for non-conserved systems, not the model for conserved phase-fraction case in which the simulation parameters (i.e., diffusivity, interfacial energy, initial filling) between the $\alpha$ and $\beta$ phase grains participating the coarsening process has to be investigated in detail.

### 9.3.3 Grain size distribution

The normalized mean grain size distribution (GSD) computed throughout the evolution for all the simulations. However, for the ongoing discussion, we focus on the GSD evolution for the more realistic conserved systems (CS). Often, the steady-state microstructural regime commences after the initial transition period. Fig. 9.6 shows some of the selected triple and quadruple junction driven simulation results at steady state regime.

Several analytical and empirical functions were proposed to approximate the GSD's
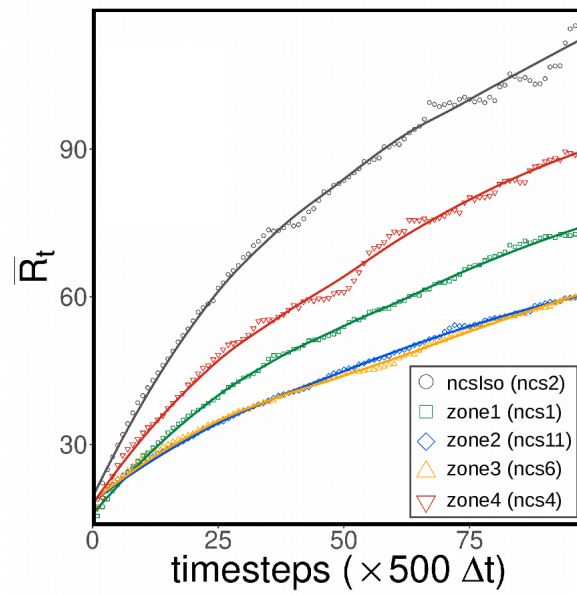
(a)
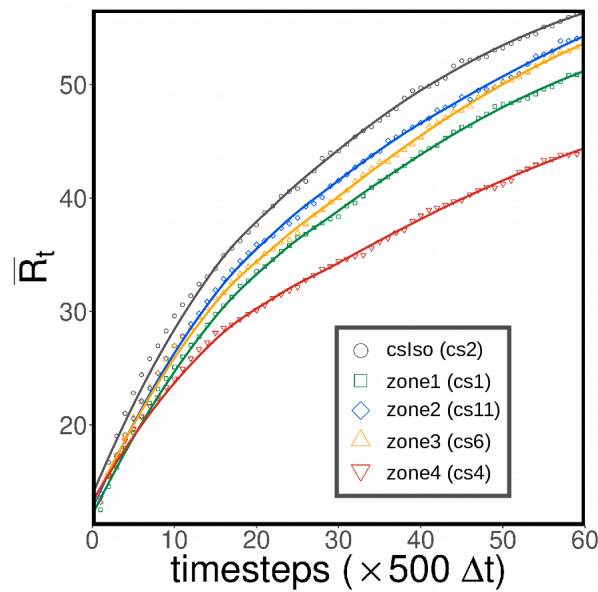


(b)

*Figure 9.5: Mean grain size evolutions for (a) the non-conserved and (b) conserved simulation setup with the selected energy ratios are plotted as a function of time. Each fitted line corresponds to the value of the best fit power law coefficient. (For color interpretation in this figure, the reader is referred to the web version of this article.)*

obtained from the experimental and simulation microstructures [20, 33, 34]. In our study, the classical Hillert and Weibull functions are indicated in solid and dashed lines respectively in the figure. The corresponding phases in each microstructure are also examined individually and shown in the subplot.

Time-Invariant behavior is ascertained for all the selected GSD's. The results reveal that the Weibull distribution with adjusting parameter ($\tilde{\beta} \approx 2.7$) is closely approximated for the triple junction dominated systems. Similar kind of normal distribution behavior is usually seen in the isotropic materials [194]. However, for the anisotropic conditions, the consequence of randomness in the clustering bias among the associated phase grains could marginally modify the relative growth rate of individual phases. Therefore, the GSD peaks of the individual phases are somewhat deviated from their overall system mean. Additionally, the drift in relative growth rate of $\alpha$ and $\beta$ grains might induce slight size differences. The equivolume fraction of $\alpha$ and $\beta$ phases match well with the Weibull functional fit. Interestingly, the classic Hillert type distribution is nowhere supported by our 2-D simulations.

In order to understand the relative evolution for the triple and quadruple systems, the summarized quasi steady state GSD's are shown in Fig. 9.7a. It is noted that much more complicated GSDs are perceived for the quadruple junction systems and these can not be approximated by the available analytical models. As an increasing fraction of quadruple to the triple junctions in the system, the peak value of GSD noticeably deviates from its mean size. The selected quadruple junction governed systems show wider GSD than the triple junction systems. During evolution, due to the growth competition among geometrical and topological factors, considerable number of smaller grains are trapped at the grain boundaries, resulting approximately in a bimodal-type distribution for these higher energy ratio simulations.

Though the previous analytical models were mainly derived to characterize the GSD of single-phase isotropic materials, the dual-phase microstructures might not be fitted by the known equations. However, the obtained GSD can be interpreted by using the statistical tools such as coefficient of variation (CV), kurtosis and skewness factors. Hillert derived an analytical model for an ideal single-phase grain growth systems and showed that CV[R] of 0.33 [20]. For all that, his model assumes non-random neighboring grains and are not very well suited in a real system consideration. Most recently Dana Zollner reported CV[R] of 0.388 from an isotropic MC grain growth simulations [172]. In addition to the CV[R], the above mentioned statistical parameters that describe the GSD have been computed for our simulations and summarized in Fig. 9.7b. The triple junction dominated simulations are in fit with the previous results ($CV[R] = 0.42$), but, the quadruple junction governed systems yield CV[R] of 0.52.
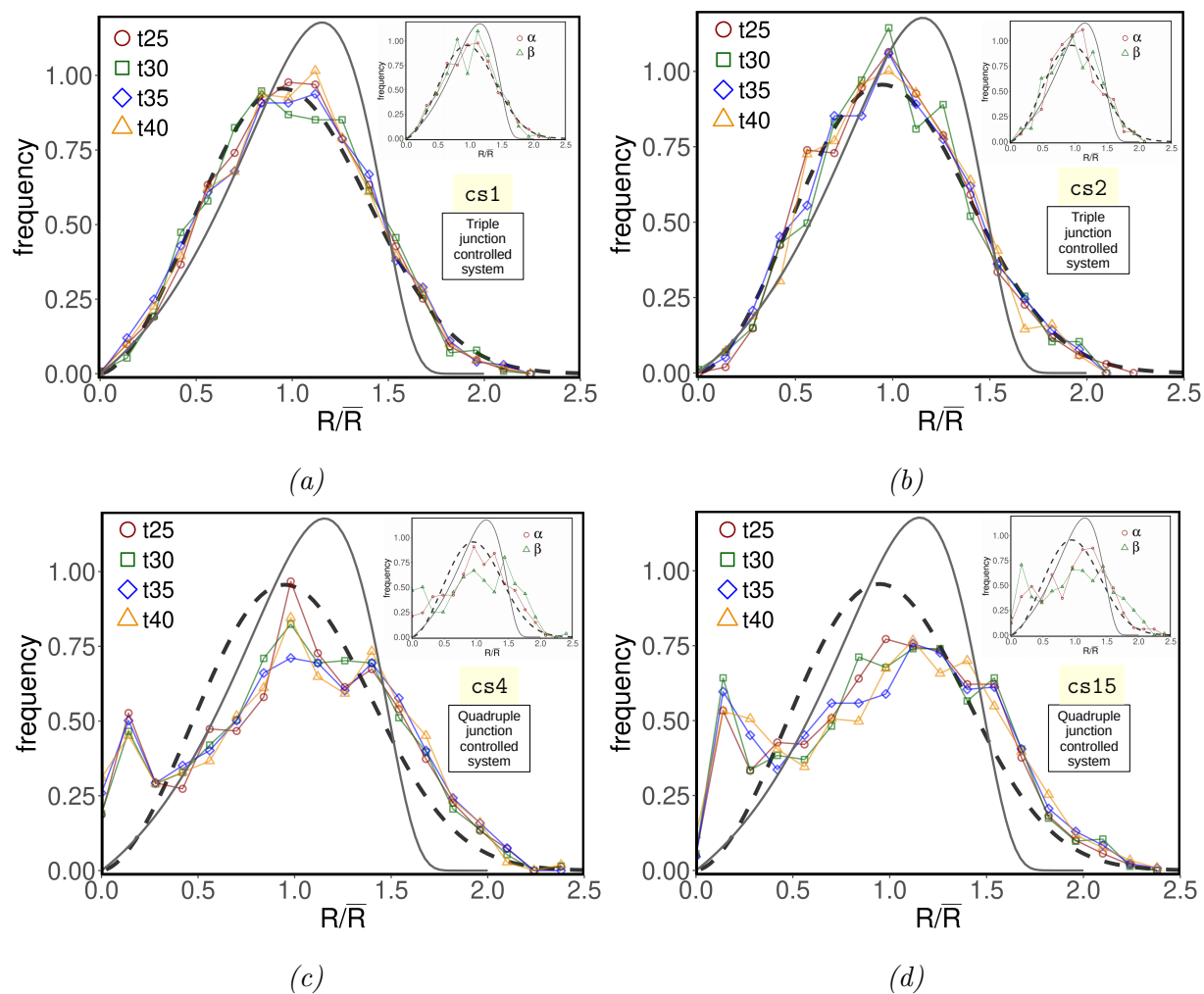
*Figure 9.6: Evolution of the normalized mean grain size for different simulation cases. Comparison to the theoretical models (solid line: Hillert and dashed line: Weibull function) for the grain-size-related aspects. The inset shows the corresponding individual phase GSD's, along with the theoretical fit functions. (a) cs1 (b) cs2 (c) cs4 (d) cs15*
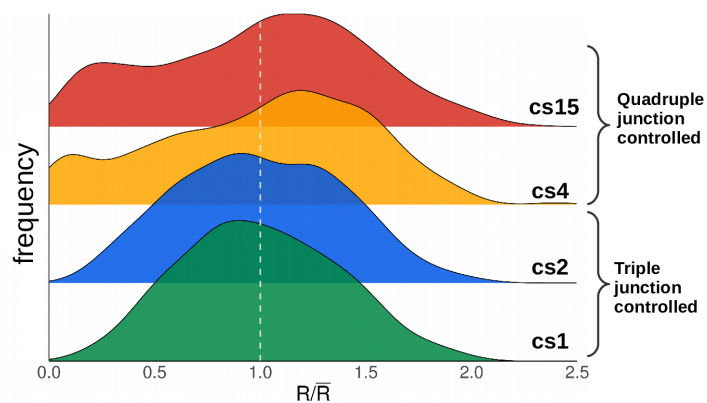
*(a)*
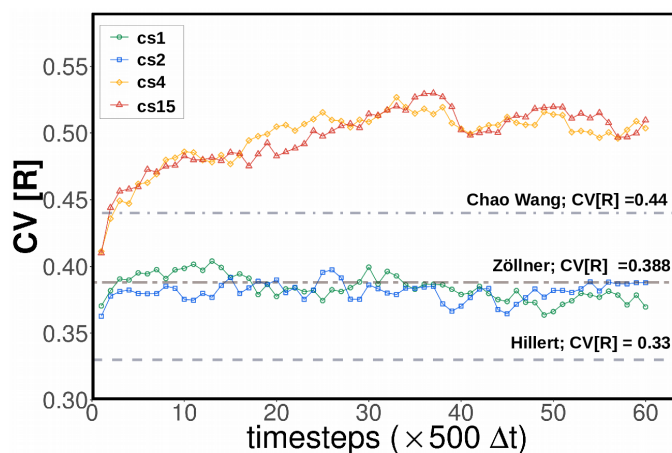


*(b)*

*Figure 9.7: (a) Normalized mean grain size distribution (GSD) were computed for some selected triple and quadruple junction dominated systems. The overall GSD were reported in a steady state regime. (b) Coefficient of Variation (CV) for a grain size distribution is shown here. The previously obtained isotropic case results were overlaid.*
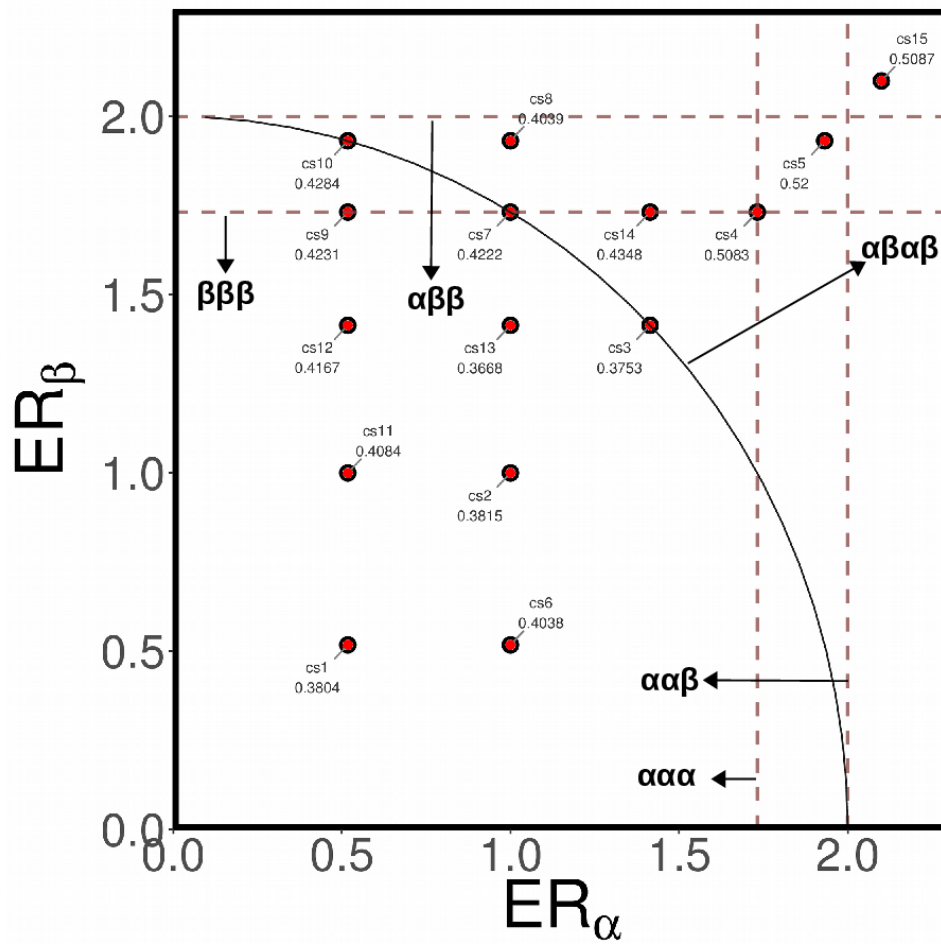
*Figure 9.8: The steady state CV[R] were computed for all the CS simulations. The triple junction controlled systems more or less follow an isotropic distribution case whereas quadruple junction systems do not follow simple CV[R] condition*

### 9.3.4  Growth kinetics: conserved system

For the long range volume diffusion-controlled systems, the obtained growth coefficient lies around $m \approx 3$. The agreement between theoretical models and the existing fitting formula experimental data is certainly interesting, despite numerous degrees of freedom in choosing values for the processing parameters. It should be noted here that the general power law consists of two unknown fitting parameters. Therefore, this set of parameters by no means is the only choice, nor could it be asserted to represent the relative growth kinetics of the multiphase systems. In other words, it is not deal to simply derive the growth rate of multiphase systems from single phase setup by varying both parameters simultaneously.

However, in order to preserve the model consistency, the relative growth kinetics can be computed from the power law by assuming the growth exponent of 3 for our CS simulations. Similar power law fitting description for the two-phase system is recently discussed by Yadav [194]. The fitting method is widely used for studying coarsening of real polycrystalline materials in which multiple phases are employed [3, 214].

Fig. 9.9 shows the summarized growth coefficient results in the $\alpha$ and $\beta$ energy ratio plane. The isotropic system ($cs2$) exhibits the highest growth rate among others. However, the microstructure with the clustering tendency of similar phased grains show an imperceptibly modest coarsening rate. Here the quadruple to triple junction fraction is less. Whenever the stable quadruple junctions develop in the microstructure, the system enters into a sluggish growth regime. The chess board like microstructure exhibits a lowest growth kinetics. These quadruple dominated systems prevail topologically complex structure and additionally, the compound inter-phase diffusion paths make slow growth in nature. Eventually the relative fraction of quadruple to triple junctions in the system can be an approximate tool to predict the microstructural coarsening trends.

### 9.3.5  Relative growth rates of $\alpha$-$\beta$ grains

To estimate the individual growth kinetics of $\alpha$ and $\beta$ phases, the results of CS simulations are discussed in this section. Few decades back, Ohnuma et al., derived an analytical model to express the relative growth rate of dual-phase microstructures [205]. The individual phase specific growth rates ($\bar{R}_\alpha$ and $\bar{R}_\beta$) with the effect of volume fraction and the interfacial energies were investigated. He postulated that, the linear relationship should appear among mean grain size of $\alpha$ and $\beta$ phase grains. However, he did not provide the simulation support to his anisotropic case findings. Some of the experimental results of stainless steels were used in his original paper for the validation [4, 5]. In order to verify the above hypothesis, we have computed the normalized mean grain size of individual phases as a function of interfacial energy and volume fraction. The outcome follows a linear trend with the positive correlation coefficient of 0.95. The previously published
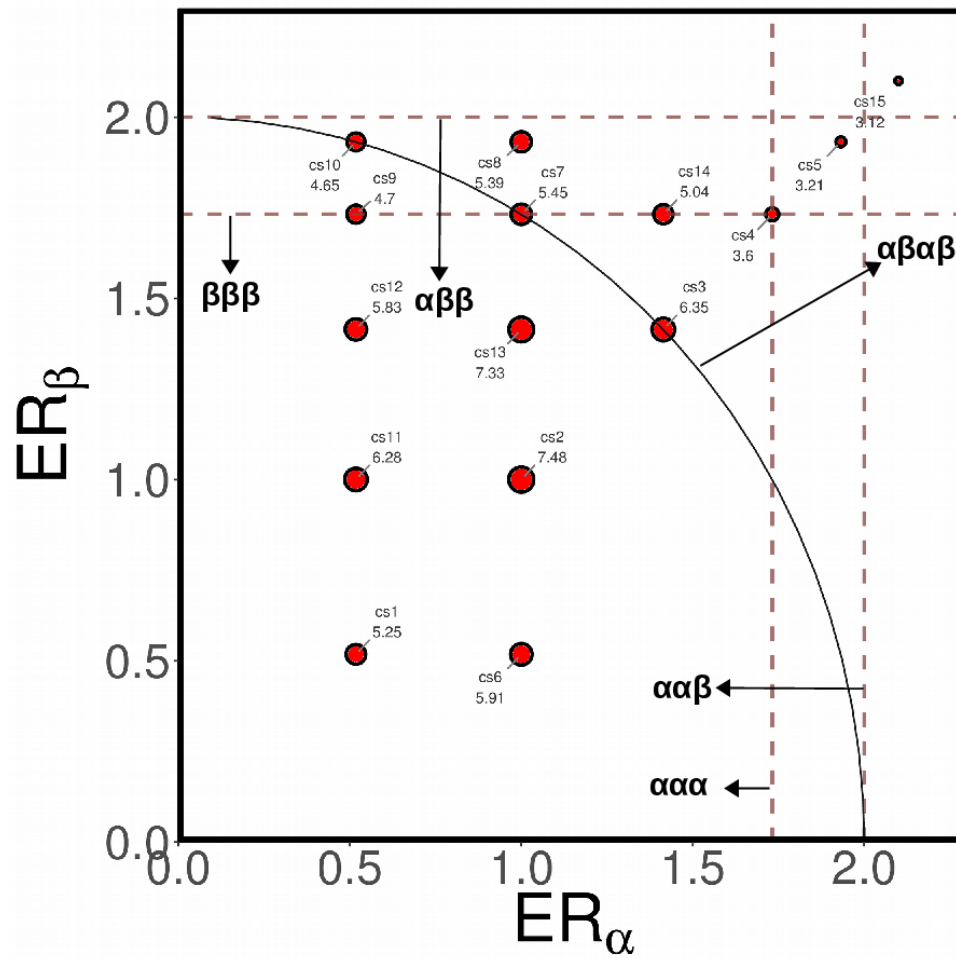
Figure 9.9: *The relative growth kinetics of the various conserved systems can be obtained while fixing the $m = 3$ in a generalized power law $R \approx kt^{(1/m)}$ for the diffusion controlled systems.*
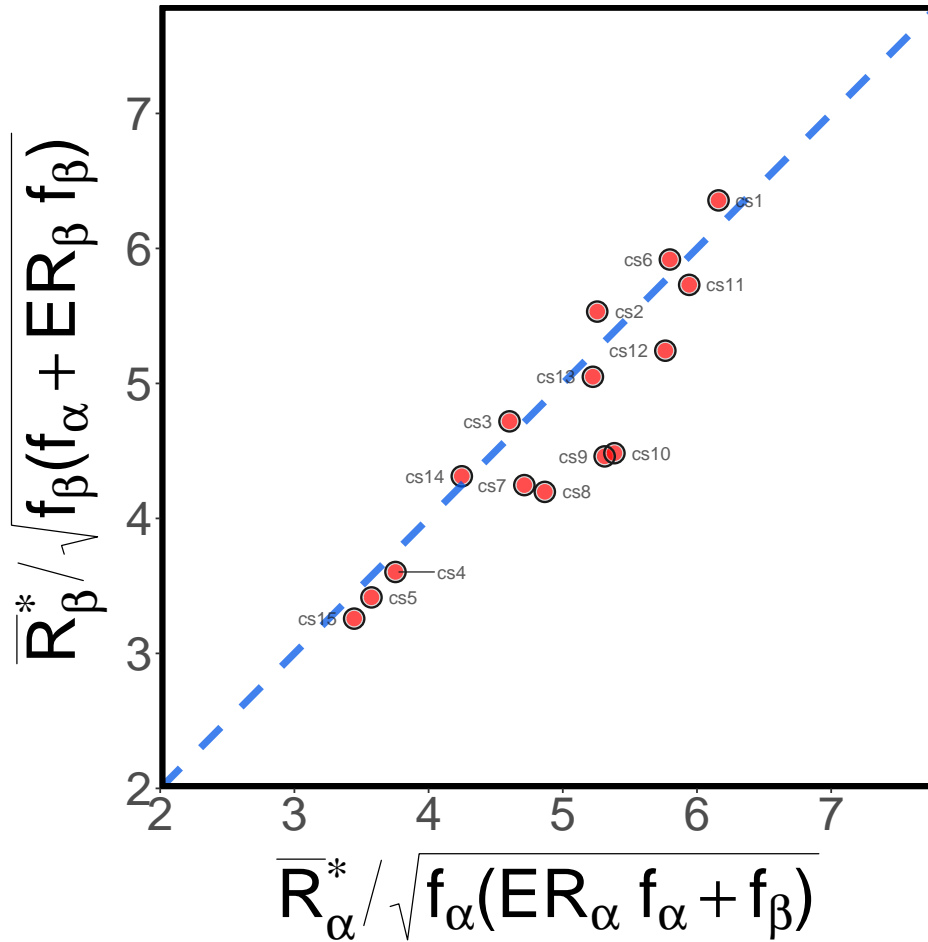
*Figure 9.10: Relation between the mean radii of α and β grains in dual-phase microstructures. The positive correlation can be seen in the figure where as the dotted line is the earlier stainless steel experimental results [4, 5].*

experimental linear curve is overlaid (solid line) in the Fig. 9.10. At a minor note, we also observe small deviations for the quadruple dominated equivolume systems.

### 9.3.6   Quadruple junction migration

In high energy ratio simulations, during evolution, the movement of individual stable quadruple junctions among $\alpha$ and $\beta$ phase grains remain unclear. The magnified region from a selected zone4 case is depicted as temporal evolution of stable quadruple junctions in Fig 9.11. To further emphasize, the moving direction of multiple quadruple junctions of a shrinking grainE is highlighted. It should be clear from these pictures that the equilibrium angles at quadruple junctions should persist during the evolution. Initially, the corners of $\alpha$ phase grainE hold four $\alpha\beta\alpha\beta$ quadruple junctions. These quadruple junctions are quite stable during evolution.

With a chosen interfacial energy ratio combination, the microstructure obtained sug-
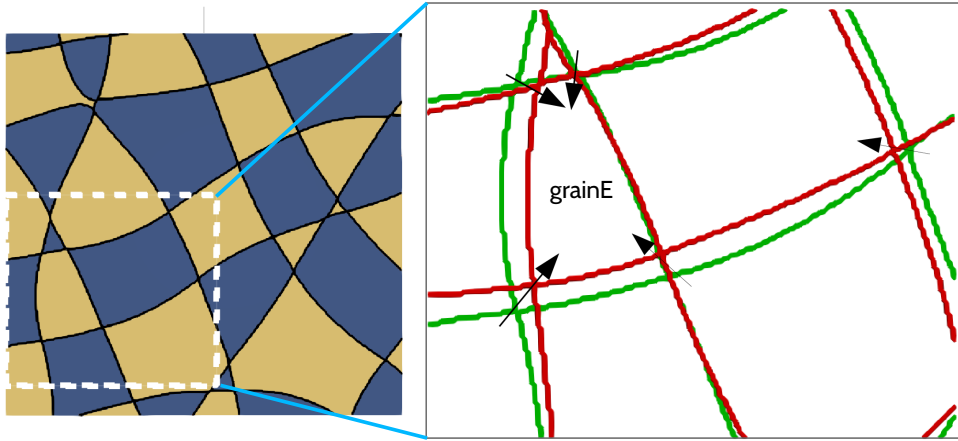
*Figure 9.11: The stable quadruple junctions in a chess board like two-phase microstructure. The magnified regime shows the temporal evolution of quadruple junctions. The selected microstructure holds highest relative fraction of quadruple to triple junction ratio.*

gests more difficulties in dissociating quadruple junction due to thermodynamically more unfavorable formation of triple junctions. The above result shows that in steady state grain growth regime, without a favorable balance of energies, it is unlike that the quadruple junction can dissociate in to triple junctions regardless of the involved process parameters. This thermodynamic perspective is of course interconnected to kinetics, since without long rage diffusion, there is no coarsening even if the energetic conditions are very favorable for microstructural evolution. These results were complemented by an interesting theoretical mechanism proposed by Chan et al.[207]. Moreover, since the zone4 regime simulations can hold the higher fraction of quadruple junctions, the movement of these junctions should be similar. Under very high energy ratios, the overall coarsening behavior is decreased significantly, and the quadruple movement is diminished with geometrical complexity.

To facilitate the discussion, the detailed evolution map of another triple sided $\alpha$ phase grainF is shown in Fig. 9.12. At first, the grainF consist of three $\alpha\beta\alpha\beta$ quadruple junctions at their grain corners. As time progresses, the grainF shrinks and disappear. When three neighbor $\beta$ grains meet at the junction, the coalescence behavior is expected. However, in such a situation, the other $\alpha$ phase neighbors should restrict the formation of $\alpha\beta\alpha$ contacts. Therefore, it is almost impossible to generate triple junction fulfilling such a demanding thermodynamical condition.

This will also lead to splitting behavior of unstable junctions. This kind of behavior will also be found frequently. In our simulation, the higher energy junction quickly splits into two $\alpha\beta\alpha\beta$ quadruple junctions. The chemical potential map is also furnished here to highlight the local chemical heterogeneities around the junctions. This confined data even explains the possible changes in diffusion pathway for $\alpha$ and $\beta$ phases because of disappearance of grainF, which are otherwise inaccessible to measure experimentally and
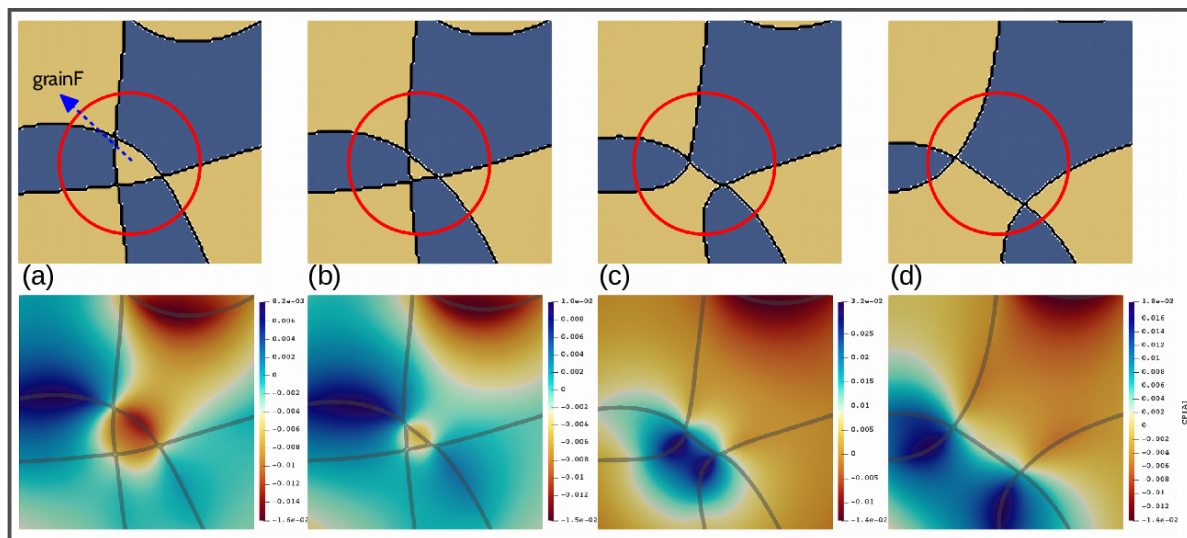
*Figure 9.12: The temporal evolution of a grainB. (a) and (b) consists of the three stable $\alpha\beta\alpha\beta$ quadruple junction corners. While vanishing grainB, the generated triple junction regime is not stable and quickly develop $\alpha\beta\alpha\beta$ junction in (c) and (d).*

explains the influence of short-lived triple junctions.

### 9.3.7 Quadruple and Triple Junction statistics: conserved system

As already shown, the two-phase microstructure can consist of different fraction of triple and quadruple junctions depending on the interfacial energy ratios used. However, there are set of predefined analytical models to assess the microstructure in terms of possible contacts between them. Here, an attempt has been made to quantitatively compute the number of triple and quadruple junctions in the simulated microstructure at a stationary state. However, in this preliminary study, the higher ($> 4$) stable junctions of $\alpha$ and $\beta$ phase grains are omitted. The relative fraction of quadruple to triple junction is computed for each simulation and the summarized results are shown in Fig. 9.13.

For an isotropic case ($cs2$), the microstructure largely consists of triple junctions with very less stable quadruple junctions. Therefore, the obtained relative ratio is the lowest compared to the remaining simulations. By simultaneously increasing both $\alpha$ and $\beta$ phase interfacial energies, the fraction of quadruple junctions increases along in diagonal direction of the graph. It should be noted that for a $cs1$ case, the clustering tendency developed considerable number of quadruple junctions when compared to the $cs2$ (isotropic) case. The outer circle of $\alpha\beta\alpha\beta$ line could elucidate the possible observation of quadruple junctions in the system. In our simulations, the maximum relative ratio is observed for a $cs15$ case. One can estimate the interfacial energy ratio dependent relative junction frac-
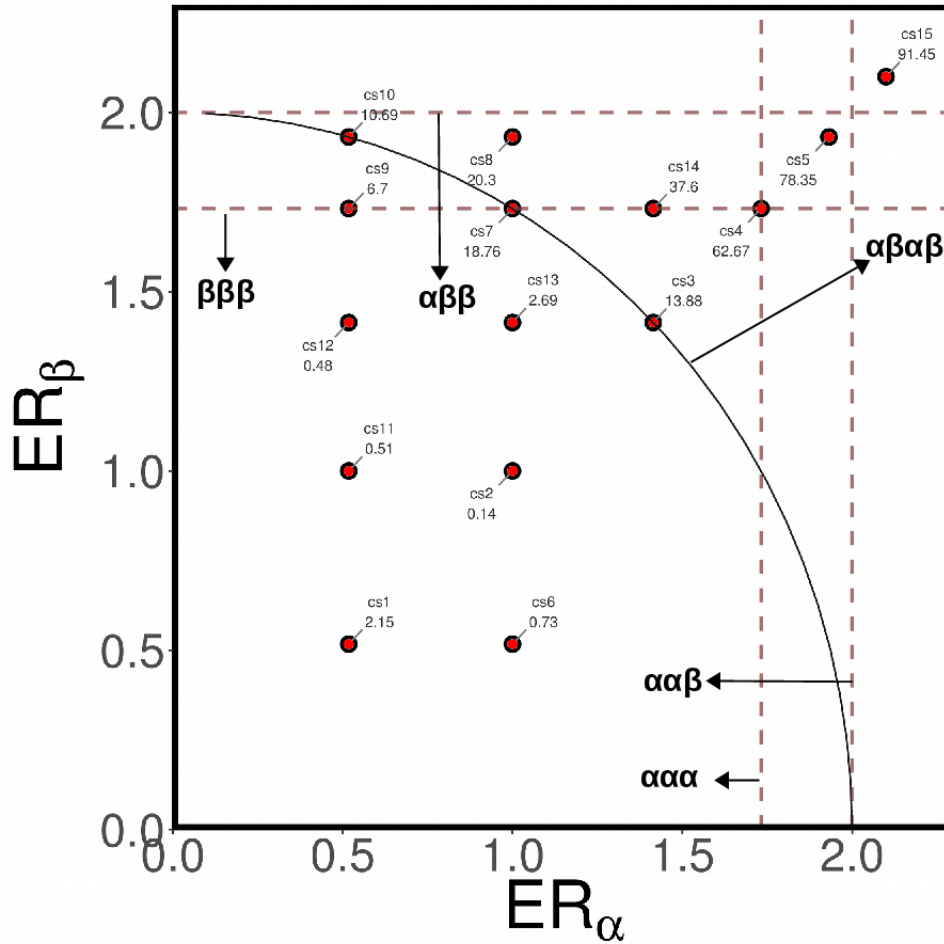
*Figure 9.13: Stable quadruple to triple junction number ratio obtained for the CS simulations.*

tion only if an ideal volume fraction is used. It further indicates that in the equivolume case, the microstructure may appear more homogeneous at different locations. In case of non-equivolume cases, the heterogeneities will be attainable and one need to compute the location dependent relative junction ratio following similar steps.

## 9.3.8   Parallel-coordinate property charts

Visualization of a multidimensional data set is an intricate process step for the researchers. In the present study, the input parameters and the computed simulation results manifest a multidimensional data problem. There are various data science strategies available to strive for this issue. One such tool is a parallel-coordinate plot where the individual parameters are organized in a sequence of vertical lines and followed by data points pass among them. This data analytics approach is recently introduced to the material science community for visualizing large amounts of data and speed up the materials discovery process [215]. The hidden pattern among our data points can be qualitatively apparent in the resultant figure.

The energy ratio of the given system can be considered as an input and the remaining computed parameters can be considered as an output from the microstructure. A proper analysis of this multidimensional dataset may help to eliminate processing complexity to design the dual-phase composites with the required final microstructural properties.

For example, if we choose a system with $ER_\alpha = 2.1$ and $ER_\beta = 2.1$ as the input parameters, the obtained quadruple to triple junction ratio should be more than 90%, the $CV[R] > 0.5$, the $skewness[R] = 0.8$ and the relative growth rate is the least among other simulations. Thus it is understood that the above initial input parameters should result in a complex quadruple dominated system with the sluggish microstructural evolution. Certainly, this tool will be helpful for systematic studies on the effect of many coupled input and/or output variables, while operating in high-dimensional property space. To the best of our knowledge the uniqueness of computational solution for such a multi-parameter microstructural design problem  i.e. the determination of the appropriate energy ratio combinations from the known $\alpha$-$\beta$ plane and the corresponding coarsening kinetics  was not studied so far.

## 9.4   Summary

In the present study, a basic understanding of a complex microstructural evolution in equivolume $\alpha$-$\beta$ material is presented. The outcomes are as follows:

1. Temporal evolution considerably differs between nonconserved and conserved systems. For the NCS simulations, the lowest energy phase grains among $\alpha/\beta$ system should survive in the final microstructure. Volume fraction of $\alpha$ and $\beta$ phase in CS is almost invariant with time.

2. The kinetics of grain coarsening follow the general power law kinetics for $m = 2$ (interface-controlled) for NCS and $m = 3$ (diffusion controlled) for CS simulations.

3. The maximum grain coarsening rate is observed for the isotropic case where the extra demand for the thermodynamical energy is not needed.

4. While varying the interfacial energy ratios, the increasing fraction of quadruple to the triple junctions in the system is observed. The quadruple junction governed systems show wider GSD than the triple junction dominated systems.

5. The ratio between the mean grain size of the $\alpha$ and $\beta$ phase is roughly one which is independent of interfacial energy ratio. These results are consistent with the previous experimental findings.

6. The parallel-coordinate plot is a perfect tool for qualitative assessment of multi-dimensional process parameters and to validate the importance of cross-correlations
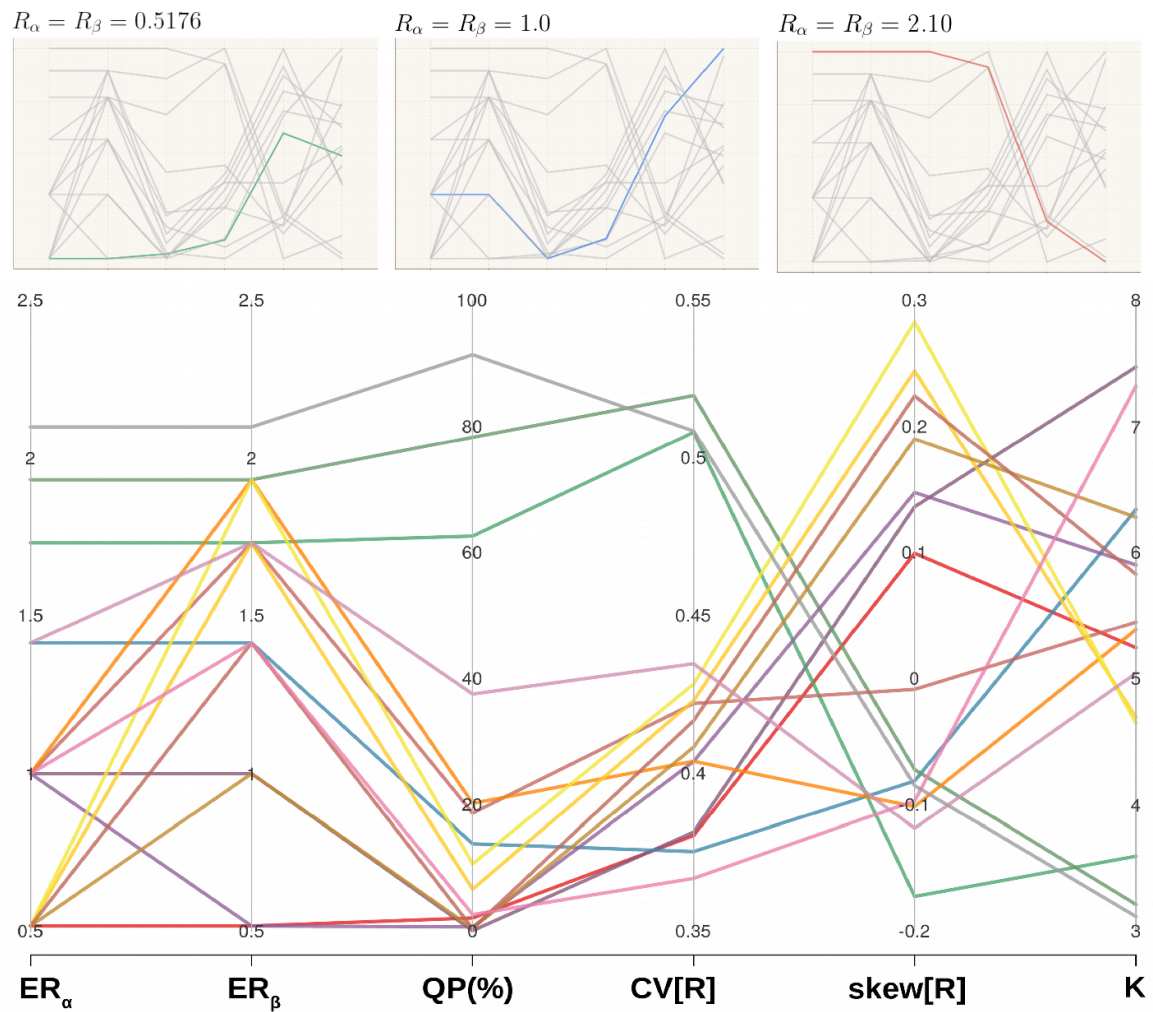
*Figure 9.14: Parallel plot representation for our multi-dimensional dataset. The diagonal energy ratio simulations are shown at the top, to highlight the importance of the hidden pattern among the dataset.*

between various features for microstructural optimization of a duplex material.

# Chapter 10

# Microstructural coarsening of ternary two and three-phase polycrystalline materials

## 10.1   Introduction

During thermomechanical heat treatment processes, microstructural coarsening occurs, in which the size distribution and shape modification of the constituting phases are apparent [8]. Depending on the underlying microstructures, the apprehended grain growth exponent ($m$) varies from 2 to 10 [216]. Specifically for the two-phase system, in the cases where the second phase is distributed over a homogeneous matrix phase, in the form of particles, particle coarsening or Ostwald ripening is studied by Lifshitz, Slyozov, and Wagner, which is most commonly referred to as LSW theory [43, 44]. While this may be valid for low volume fraction cases, later investigations accounted for the finite volume fractions, the coalescence of particles, etc. [45, 46, 47]

On the contrary, a number of technologically relevant materials have grains of both phases influencing each others growth behavior [217, 218, 7]. When we introduce the grains of the second phase into the polycrystalline matrix, the underlying microstructure can be classified as low volume fraction ($f_{minor} < 0.2$) and high volume fraction ($f_{minor} > 0.2$) systems [3]. In the first case, for instance, the low volume fractions of the minor phase constituents are distributed into the matrix as particles that might hinder the grain boundary movement of the matrix phase during growth. Few decades back, Zener-Smith proposed this grain growth hindrance phenomenon, and it became commonly known as Zener pinning/drag effect [12, 49].

The particles of the second phase can be either stable or coarsen with time. The resultant matrix grain size largely depends on the process parameters, such as volume

fraction, particle size, particle shape, and their distribution [50, 53, 52]. In addition, the diffusivity and interfacial energy also show an influence when particle coarsening takes place simultaneously [3, 219]. The optimum volume fraction of finely distributed inert particles can effectively pin the matrix grain growth. Thus, by controlling the characteristics of the minor phase particles, one can decrease the matrix grain size that aids to improve the mechanical properties such as strength, hardness, and toughness of the material [220, 221].

Next, the mutual retardation on the grain growth of each phase is affirmed in the high volume fraction case, by means of experiments and simulations [48, 59, 191]. Previous studies manifested the suppressed grain growth in two-phase composites, in which the volume fraction of each phase varied, due to the difference of the diffusion distances for the two phases [3, 194]. Interestingly, the equivolume ($0.5\alpha$-$0.5\beta$) of the interconnected microstructure reveals the lowest growth kinetics, where the extended diffusion path length is maximum [3, 198]. The long-order interdiffusion is strongly limited to two-component, two-phase microstructural coarsening. Besides, the overall growth coefficient ($m \approx 3$) is generally adopted for these materials [61, 194]. Several efforts have been accompanied to confirm the concurrent grain growth and coarsening phenomena in these materials, with the aim of producing better microstructures, even after prolonged high-temperature annealing.

Recently, multicomponent multiphase materials have been adopted for high temperature applications with the suppressed microstructural coarsening effect, especially multiphase ceramics and High entropy alloys (HEA) which show exceptional mechanical properties at high homologous temperatures [40, 64, 222, 223]. In this work, ternary two and three-phase polycrystalline microstructures were simulated using the multiphase-field model. The characteristics of the resultant microstructures were statistically quantified.

Several changes are incorporated into the phase-field study of grain growth, such as the introduction of anisotropy, to resemble the physical conditions [224, 225]. However, in the present work, phase-field simulations under isotropic conditions are examined, with a particular focus on growth kinetics. To the best of our knowledge, no theories are available for such multiphase polycrystalline structures, where all phases have to be treated on an equal footing. In addition, one has to understand the sluggish diffusion concept affiliated with multi principal elements, which cause much delayed microstructural coarsening. The current paper tries to fulfill these gaps by examining the large-scale simulations over an extensive set of volume fraction conditions.

## 10.2   Domain set-up

We perform two-dimensional (2-D) simulations, with the domain size of $2048 \times 2048$ grid points, where periodic boundary conditions are adopted for both directions. Roughly 10000 grains are randomly distributed over the simulation domain, through a Voronoi tessellation algorithm, as described in [1]. The radius of a grain $i$ is expressed as $R_{\phi_i}$, where $\phi_i$ indicates the phase identity. The number of voxel cells inside the chosen grain is counted, and a circle of an equivalent area is used to compute an individual grain radius. The interfacial energies of the grain boundary and antiphase boundaries are taken as 1.0. The composition variable at each grid point are set equal to those of the equilibrium values ($C_{eq}^{\alpha} : 0.9A0.05B0.05C$, $C_{eq}^{\beta} : 0.9B0.05C0.05A$, and $C_{eq}^{\gamma} : 0.9C0.05A0.05B$). The bulk diffusivity of 0.1 and 1.0 are used, while holding the grain boundary mobility constant. To solve the phase-field evolution equations, a finite difference algorithm is implemented across a uniform numerical grid [154], using an explicit time stepping (forward Euler) scheme. Equal grid spacings are assumed in both directions, i.e., $\Delta x = \Delta y = 1.0$. The diffuse interface width $\epsilon$ is set to $4\Delta x$, for all simulations, ensuring an adequate resolution of the diffuse interface region, and a time step is chosen well within the numerical stability range ($\Delta t = 0.1$). Computational performance has been enhanced by introducing the *locally reduced order parameter optimization (LROP)* method, which optimizes both memory and time consumption for the simulations [155, 156, 183]. The simulation domains were computationally enhanced by domain decomposition, using MPI (Message Passing Interface) [107]. The simulations are run long enough to ensure that the steady-state grain growth regime is reached. On average, each simulation took 28 hours for completion, with 257 CPUs. The total computation time for this study is around 560 hours ($\approx 24$ days).

## 10.3   Results and discussions

### 10.3.1   Grain growth power law kinetics

In this section, we highlight the difference in the grain growth dynamics, associated with binary ($A$-$B$) and ternary ($A$-$B$-$C$) multiphase polycrystalline systems. In the phase-field simulations, two-component two-phase systems ($C2P2$) are those in which the volume fractions of the individual phases remains equal (conserved) similarly three-component two-phase ($C3P2$) and three-component three-phase ($C3P3$) systems are also be extended. For this $C2P2$ simulations, parabolic free energy function was taken to be equal for both phases, as reported in our earlier work [3]. Moreover, simulations are also carried out for different bulk diffusivity values to assess the rate determining step during growth. Generally, diffusivity displays an Arrhenius type of relation with respect to temperature.

With this in mind, to concede the temperature influence on growth kinetics, the simulations can be performed at various values of diffusivity. The temperature does not only influence on diffusivity but also the other physical parameters of the system, change upon a change of temperature. However, the latter effect is assumed to be small, compared to the diffusivity gradation in this study. Fig. 10.1 shows the mean grain evolution of the different volume fraction systems for bulk diffusivity values of $D = 0.1$ and $D = 1.0$. It is readily comprehended from the figure that diffusivity has a considerable effect on the grain growth rate. The faster coarsening observed for higher bulk diffusivity values ($D = 1.0$). For the case of $D = 0.1$, the growth rate is relatively sluggish, and the microstructure predominantly governs by long-range diffusion. Insights into the effects of diffusivity can be gained by comparing our results to the coarsening law, which relates the velocity of the moving boundary to the curvature, diffusivity, and the interfacial energy of the grains.

The best-fitted values for growth power law exponent and rate constant are given by the inserted table in Fig. 10.1. The growth exponent attains values approximately $3 < m < 4$, depending on the bulk diffusivity values, validating that the growth is long range diffusion-controlled. In all the cases, the growth rate of $C3P3$ system is lower compared to $C3P2$ and $C2P2$, irrespective of the diffusivity. The reason for this can be ascribed to the incorporation of $\beta$-grains, which provide additional complication to the microstructural evolution, so as to depreciate the overall growth. Conversely, when the two-phase microstructure is associated with the addition of component 3, the slight decrease in the rate constant is seen. When the diffusivity decreases, the growth rate should follow a similar trend, is, however, partly contradictory to the observed behavior: From the curves in Fig. 10.1, one can see that lower the diffusivity, higher the coarsening rate variation. This could be explained from the argument of Kuehmann et al., [226] that the presence of a third alloying element yield adjusted Gibbs-Thompson effect and the coarsening rate of the system is a function of diffusivities of elements. Nevertheless, most of the Ostwald ripening studies dealt with low volume fractions assuming predefined geometries for the second phase particles. While this may be true for simple systems, the analytical extension cannot be directly adopted in the case of multiphase polycrystalline systems. In addition, the concomitant of alloying elements and diffusivities, however, has not been fully understood. Our simulation results attempt to elucidate some of the open questions on the mechanisms proposed to explain the multicomponent phase coarsening in such complex systems. Moreover, some useful information about the relative growth dynamics can be drawn from such an exercise of fitting to the growth power law.

## 10.3.2   Microstructural features

Temporal evolution of the microstructures can be used to qualitatively estimate the relative growth kinetics. Fig. 10.2 shows the microstructural evolution of pure $\gamma$, $C2P2$, $C3P2$ and $C3P3$ systems at different time steps. The grains shown in red, blue, and
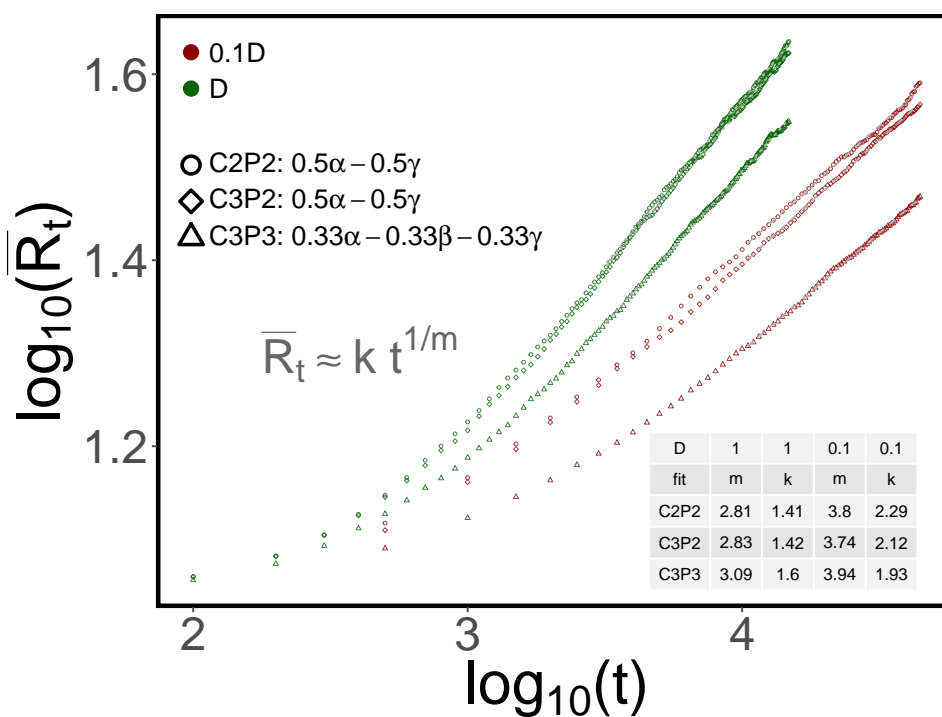
*Figure 10.1: .Temporal evolution of the mean grain size, as obtained from phase field simulations for bulk diffusivity of $D = 0.1$ and $D = 1$. When a diffusivity is decreased, grain growth is sluggish. The addition of the $\alpha\&\beta$ phase in the ($\gamma$-matrix) microstructure suppresses the evolution.*

yellow correspond to the $\alpha$, $\beta$, and $\gamma$ phase, respectively. At the beginning, the more or less equally sized grains are randomly distributed throughout the domains. Then, the corresponding number of grains, equal to the required volume fraction, is assigned to the specific phase properties. In most cases, different phase grains lie 'next to each other' in the mixed microstructure. However, in some low volume fraction cases (not shown here), the minor phase grains have been detected at the triple and quadruple junctions of the major phases. It is observed from all the microstructures that the grain size increases with time, but yields different growth rates.

The main governing mechanism of the pure $\gamma$ system is the interface readjustment around the grain junctions. While decreasing the number of grains in the system, the overall grain boundary energies are reduced. In this particular case, there is no role of diffusion during evolution. On the other hand, the $0.5\alpha$-$0.5\gamma$ system maintains an equal volume fraction of $\alpha$ and $\gamma$ phase grains during growth. In this case, the governing mechanisms of growth are short-range interface readjustment and long-range diffusion (Ostwald ripening). For instance, ternary case, the growth of each $\alpha$ grain should fulfill the equilibrium concentration of A, B, and C components, where the cooperative diffusion is operative. On the other hand, the binary $0.5\alpha$-$0.5\gamma$ case, the growth of $\alpha$ grains only requires the long-range diffusion of component A and B [3]. Hence one would expect that the ternary system coarsens slightly slower than in the binary case. Consequently, the overall coarsening rate for both systems seems relatively lower than the pure system. Since we use the similar interfacial energies for grain boundaries and phase boundaries, the clustering bias among the $\alpha$-$\alpha$ and $\gamma$-$\gamma$ system is not seen in the microstructures.

The triplex $0.33\alpha$-$0.33\beta$-$0.33\gamma$ system further delays the overall growth. The $\alpha$, $\beta$, and $\gamma$ grains are randomly dispersed over the domain. The mutual retardation of grain growth is uniformly expected from each phase. However, by minimizing the interfacial energy, the neighbor arrangement of similar phase grains can be beneficial for their localized growth. The obtained microstructures also demonstrated the weaker clustering tendency amongst the similar phase grains. The grain size of this triplex system did not change very much with time (sluggish), as compared with that of pure systems.

## 10.3.3   Effect of volume fraction

The individual volume fractions of the phases influence the overall microstructural evolution in a ternary polycrystalline systems, which needs to be investigated in detail. The following simulations were carried on bulk diffusivity of $D = 0.1$ consideration. The large scale simulations are categorized into five different groups, based on the initial volume fractions.

1. Case 1: equivolume fractions; (pure $\gamma$, $f_\alpha = f_\gamma$, $f_\alpha = f_\beta = f_\gamma$)
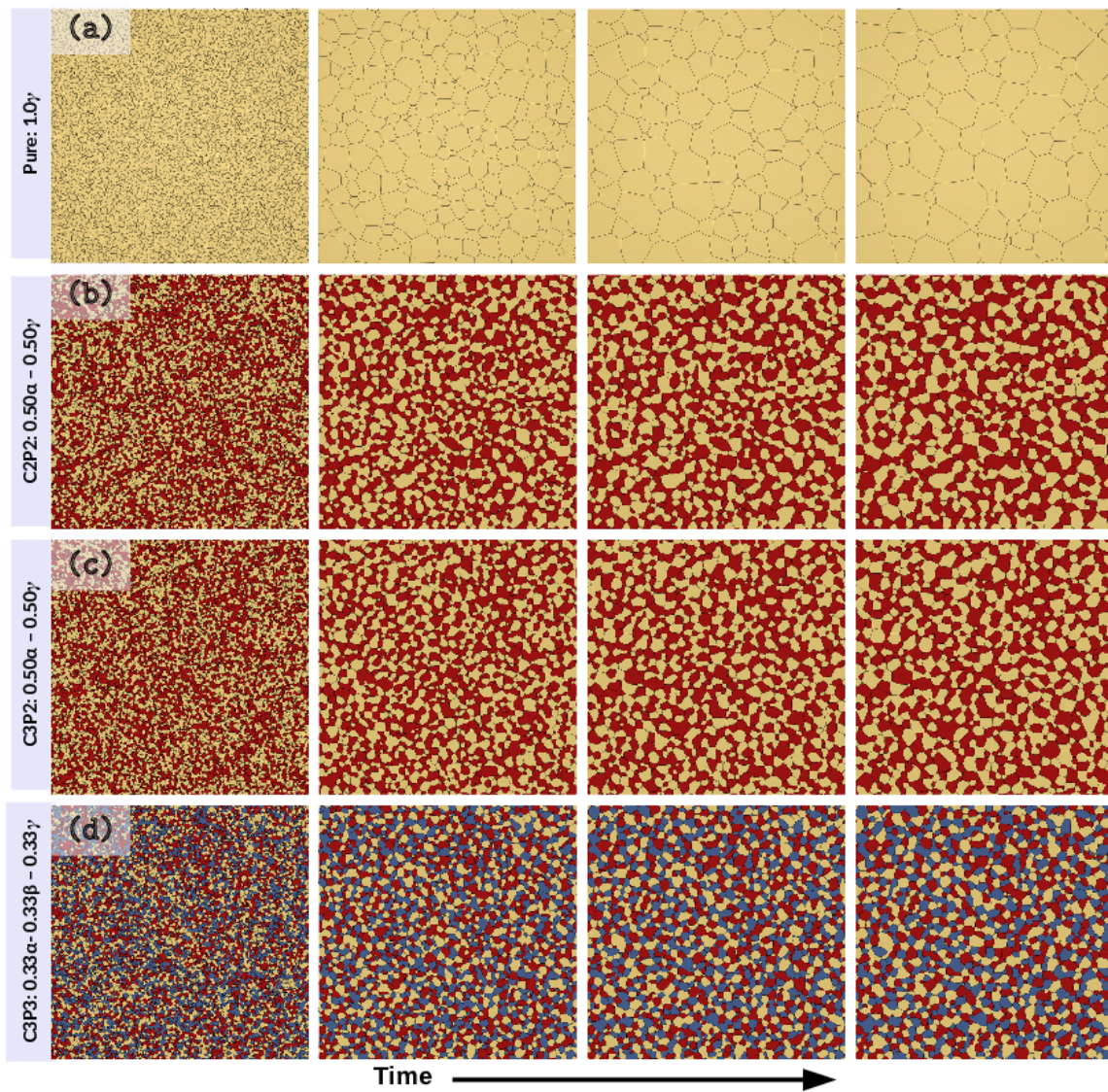
Figure 10.2: *Microstructural evolution of (a) pure:* $1.0\gamma$, *(b)* $C2P2 : 0.5\alpha\text{-}0.5\gamma$, *(c)* $C3P2 : 0.5\alpha\text{-}0.5\gamma$, *and (d)* $C3P3 : 0.33\alpha\text{-}0.33\beta\text{-}0.33\gamma$. *As can be seen, the mean grain size increases, while decreasing the total number of grains. The addition of the* $\alpha$ *and* $\beta$ *phase in the microstructure suppresses the grain growth.*

2. Case 2: $f_\alpha = f_\beta \neq f_\gamma$; and $\gamma \propto matrix\,phase$

3. Case 3: $f_\alpha = f_\gamma \neq f_\beta$; and $\beta \propto minor\,phase$

4. Case 4: $f_\alpha \neq f_\beta \neq f_\gamma$; and $\gamma > \alpha > \beta$

5. Case 5: $f_\beta = 0$; and $f_\gamma > f_\alpha$

### 10.3.3.1   Case 1: equivolume fractions

In this section, we highlight the differences in grain growth dynamics, associated with interface-controlled and diffusion-controlled systems. We have plotted the mean grain size evolution ($\bar{R}_t$) for the selected volume fractions in Fig.10.3 (a). The inset shows the best fitted power law coefficients for the chosen volume fractions. It is noted that the growth rate of the pure $\gamma$ system is higher, compared to the rest. The evolution in this microstructure does not require diffusion to mediate the overall growth. Hence the evolution is purely governed by the interface adjustment. In contrast, when the microstructure is mixed, long-range diffusion will also play a role, which thus results in a slower coarsening rate. From the inset of Fig.10.3 (a), one can see that the growth rates do not follow a monotonic pattern, with respect to the volume fraction. A naive argument of this phenomenon, namely that the volume fraction of the $\beta$ phase should increase and the growth rate should decrease, is, however, partly contradictory to the observed behavior: From Fig.10.3 (a), one can see that the growth coefficient lies close to $m \approx 3.95$ for both mixed volume fraction cases. Nevertheless, it could be seen that the rate constant of $0.33\alpha$-$0.33\beta$-$0.33\gamma$ is lower than the $0.5\alpha$-$0.5\gamma$ system. When the microstructure is mixed with more than two phases, the number of regions, in which the mutual retardation of such phases occurs, is higher, and the evolution in these regions requires a complex diffusional path. Therefore, the lowest growth kinetics is observed for the $0.33\alpha$-$0.33\beta$-$0.33\gamma$ system.

The statistical accuracy has been attributed from the number of grains in the underlying microstructures. Therefore, the final microstructure should have a sufficient number of grains to investigate. The total number of grains in the microstructure is computed at each time step and is plotted in Fig.10.3 (b). The pure $\gamma$ system rapidly looses the grains where the microstructure evolution is quite faster than the rest. While the $0.5\alpha$-$0.5\gamma$ and $0.33\alpha$-$0.33\beta$-$0.33\gamma$ systems follow the similar power law kinetics ($m \approx 4$), their microstructure differs.

To compare the individual growth kinetics of the $\alpha$, $\beta$, and $\gamma$ phases, the results of the $0.33\alpha$-$0.33\beta$-$0.33\gamma$ simulation are analyzed further. In Fig.10.3 (c), the individual phase evolutions also follow the same power law trend as that of the overall microstructure. As the relative amounts of the phases are similar, the mean intergrain distance should be roughly the same. However, if there is a randomness in the initial distribution of the

grains, then even a small additional clustering bias near the similar phased grains will have a large impact on phase coarsening rate. It is noticed that the evolution of the grains of the $\gamma$ phase slightly varies from the $\alpha$ and $\beta$ phases, due to their re-arrangement behavior during the evolution.

The individual phase volume consistency is readily evident from the Fig.10.3 (d) ($0.33\alpha$-$0.33\beta$-$0.33\gamma$ case), where the $\alpha$, $\beta$, and $\gamma$ volume fractions are plotted as a function of time. The obtained results always lie close to the initial $f \approx 0.33$ value; however, the volume fraction of $\gamma$ is slightly higher than the other phases. The effect of this small initial volume variation can be seen in their growth kinetics, shown in Fig. 10.3 (c).

### 10.3.3.2    Case 2: $f_\alpha = f_\beta \neq f_\gamma$; and $\gamma \propto matrix\, phase$

In the following simulations, the $\gamma$-rich matrix phase with the minor phase addition of $\alpha$ and $\beta$ is chosen. The mean grain size evolution of the $0.11\alpha$-$0.11\beta$-$0.78\gamma$, $0.08\alpha$-$0.08\beta$-$0.84\gamma$ and $0.05\alpha$-$0.05\beta$-$0.90\gamma$ simulation is shown in Fig. 10.4 (a). It can be seen that the relative growth rate decreases when increasing the minor phase additions. In order to investigate the individual phase contribution, the $0.05\alpha$-$0.05\beta$-$0.90\gamma$ system has been selected (Fig. 10.4 (b)). The growth rate of the $\gamma$ phase is higher than the minor phase constituents ($\alpha$ and $\beta$). When we choose $0.9\gamma$, there is a higher probability of $\gamma$-$\gamma$ grain contacts over the rest in the matrix. For this reason, the long-range diffusion does not play a role, while the interfacial energy minimization mainly derives the overall $\gamma$ phase evolution. On the contrary, the intergrain distances of the minor phase constituents are very large. Therefore, the cooperative diffusion of the underlying components has to diffuse an extended distance to satisfy the equilibrium concentration of the minor phase grains. The observed overall growth kinetics lies between the growth regimes of the major and minor phase. The individual phase coarsening results suggest that the rate-controlling step is the long-range diffusion for these mixed microstructures.

### 10.3.3.3    Case 3: $f_\alpha = f_\gamma \neq f_\beta$; and $\beta \propto minor\, phase$

The equal volume fraction ($> 0.33$) of $\alpha$ and $\gamma$ phase grains, with the minor addition of $\beta$ phase systems, is selected. In Fig. 10.5 (a), the $0.45\alpha$-$0.10\beta$-$0.45\gamma$ system shows a relatively faster growth rate than the other systems. From the microstructural observation, it is noticed that the $\alpha$ phase grains lie next to the $\gamma$ phase grains. Thus, the mutual growth retardation is expected to be approximately equal for both phases. The neighboring arrangement of the $\alpha$ and $\beta$ phase grains also contributes to the growth. The initial filling of these major phases is random in nature; however, the rearrangement of similar phase grains aid the local growth kinetics via interface-mediated growth. The coarsening of minor $\beta$ phase grains requires long-range diffusion. Fig. 10.5 (b) presents the relative growth kinetics of the contributing phases. As expected, the overall kinetics lies between
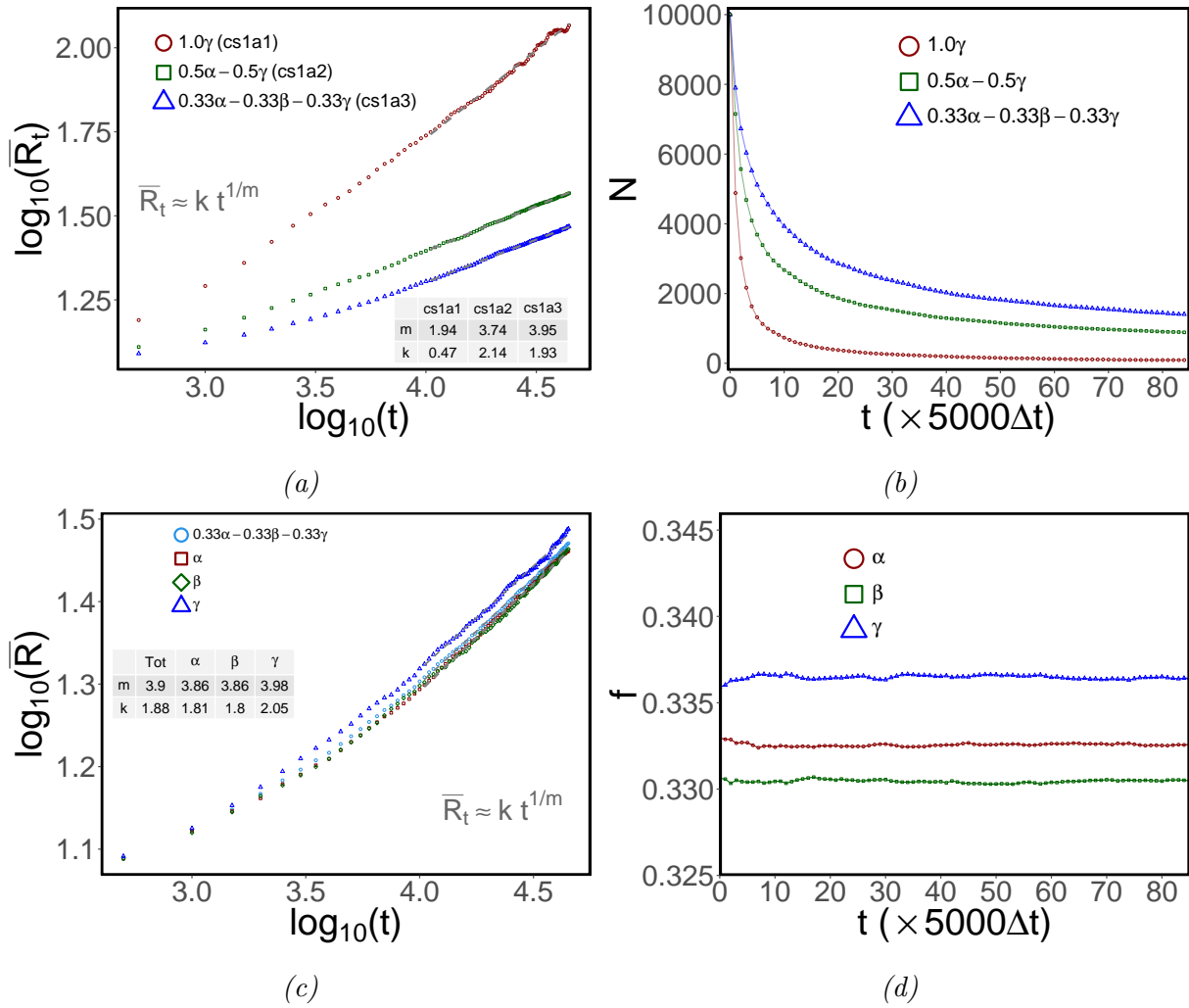
*Figure 10.3: Temporal evolution of the simulations of case 1. (a) The mean grain size evolutions of the three volume fraction cases are displayed over time. The growth of the pure -γ system is faster than the growth of the mixed microstructures. (b) The chosen systems show a diminished number of grains, compared to the initial time step, indicating a loss of grains during growth. (c) Growth distinctions between the individual phases for the 0.33α-0.33β-0.33γ system. (d) Corresponding volume fractions as a function of time, showing the volume conservation for each phase.*
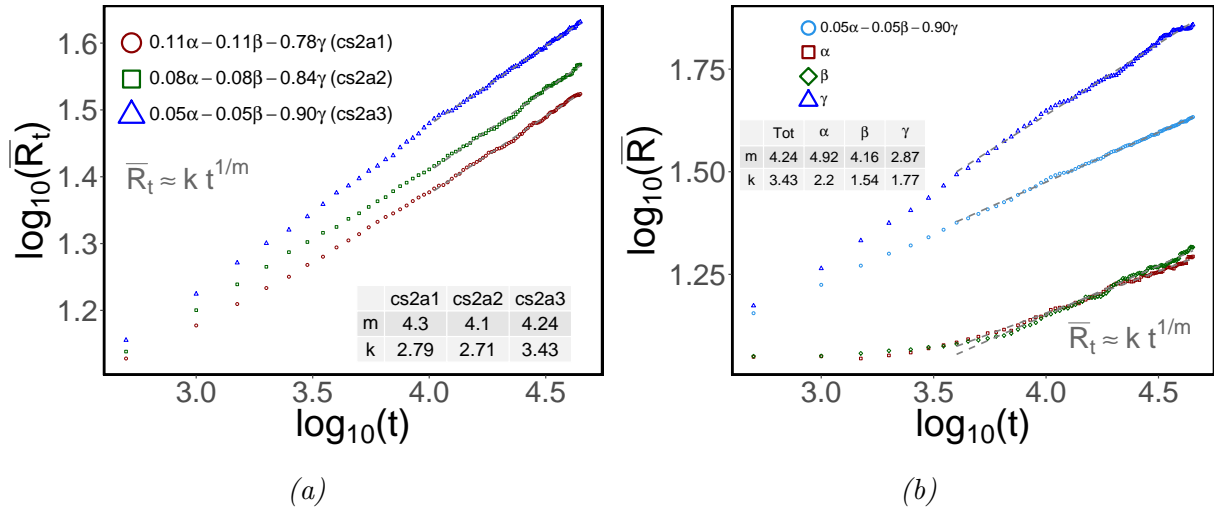
*Figure 10.4: Temporal evolution of the simulations of case 2 (a) Mean grain size evolution in log scale. (b) The growth of an individual phase at two different time steps, superimposed on each other, for the 0.05α-0.05β-0.90γ system. Since the intergrain distance of the α and β phase grains is very large, the long-range diffusion takes place at an extended length, which suppresses their growth rate.*

the growth rates of major ($\alpha$ and $\gamma$) and minor ($\beta$) phases. It is interesting to note that the equal volume fraction of $\alpha$ and $\gamma$ phase grains did not provide a similar growth rate. This indicates the importance of the arrangement of the grains of the individual phases in the microstructure. The $\beta$ phase yields the slowest coarsening rate, where the intergrain distance is a dominant factor.

### 10.3.3.4  Case 4: $f_\alpha \neq f_\beta \neq f_\gamma$; and $f_\gamma > f_\alpha > f_\beta$

The $\alpha \neq \beta \neq \gamma$ case is investigated using three different initial volume fraction conditions. The corresponding evolutions of the mean grain size are shown in Fig. 10.6 (a). The calculated evolutions of the mean grain size agree well with the existing fitting of the power growth law. The growth rates of 0.38$\alpha$-0.11$\beta$-0.51$\gamma$ and 0.33$\alpha$-0.11$\beta$-0.56$\gamma$ are almost similar in nature. On the other hand, the growth rate of 0.22$\alpha$-0.11$\beta$-0.67$\gamma$ is slightly faster than the other growth rate, where the matrix $\gamma$ holds the highest fraction of the $\gamma$-$\gamma$ grain boundary area. Fig. 10.6 (b) presents the individual phase evolution of the 0.22$\alpha$-0.11$\beta$-0.67$\gamma$ system. The maximum growth rate is observed for the $\gamma$ phase, followed by the $\alpha$ and $\beta$ phase. Moreover, the evolution of the mean grain size of the system lies between the $\gamma$ and $\alpha$ grain sizes. This suggests that the strong growth competition between the $\alpha$, $\beta$, and $\gamma$ phases leads to an overall microstructural evolution, which needs to be optimized for the stability of the system.
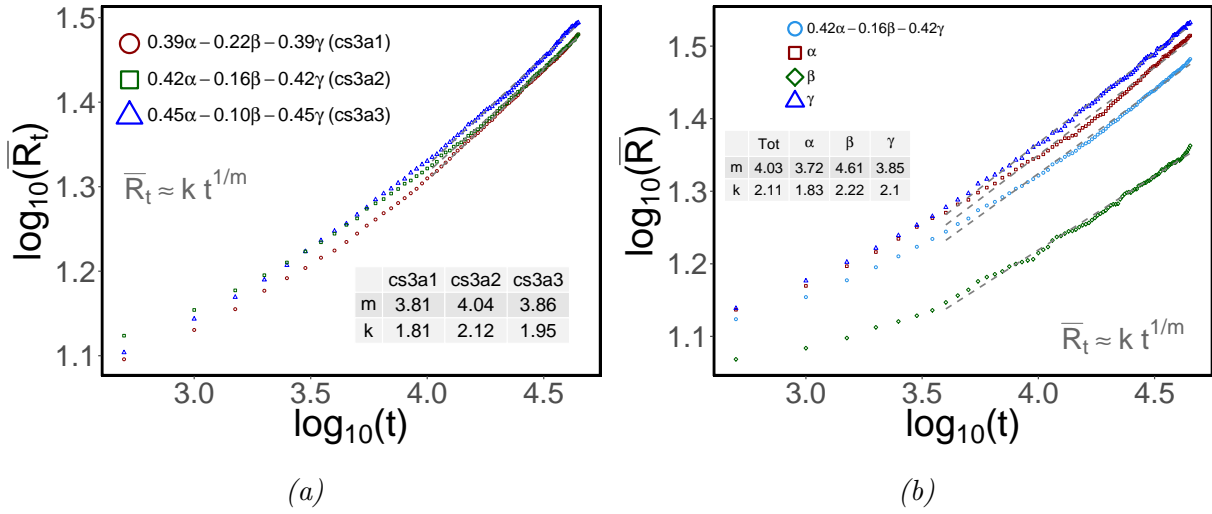
*Figure 10.5: Temporal evolution of the simulations of case 3 (a) Mean grain size evolution in the log scale. The intermediate fractions show a similar growth behavior. (b) Growth rate of individual phases in the 0.42α-0.16β-0.42γ system. Volume fraction-dependent growth, mediated by long-range diffusion, is observed.*
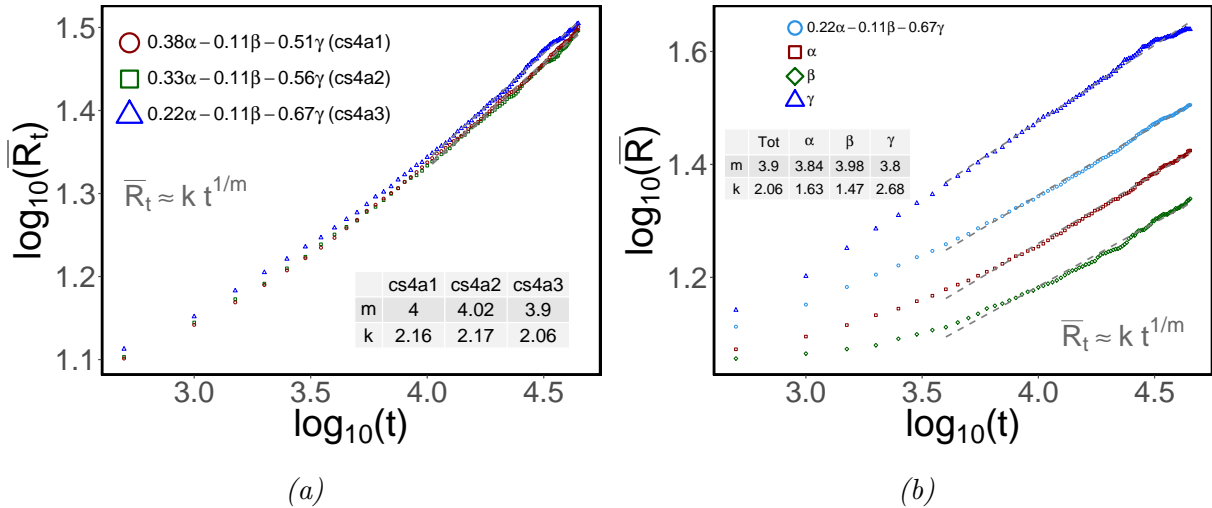


*Figure 10.6: Temporal evolution of the simulations of case 4. (a) The mean grain size evolutions of the three volume fraction cases are displayed over time. The overlapping data points in the figure approximately resembled case 3. (b) Individual growth rate of the phase for the 0.22α-0.11β-0.67γ system, corresponding to different mechanisms of grain growth.*
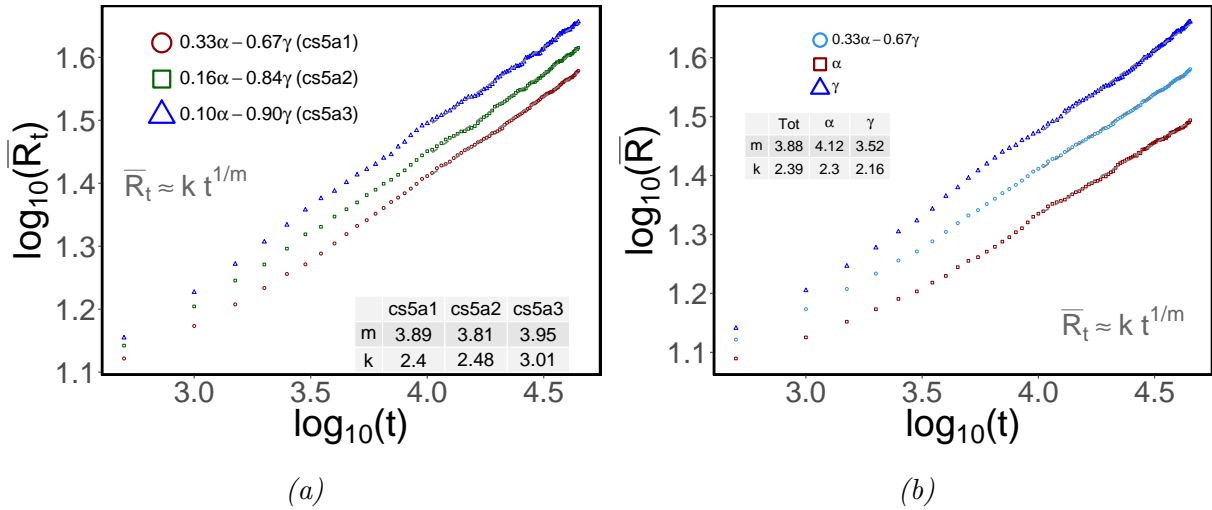
*Figure 10.7: Temporal evolution of the simulations of case 5. (a) Evolution of the mean grain size, with simulation time for two-phase systems. (b) Growth rate for the individual phase in 0.33α-0.67γ.*

**10.3.3.5  Case 5: $f_\beta = 0$; and $f_\gamma > f_\alpha$**

Finally, some of the nonequivolume, two-phase systems are investigated. The mean grain sizes of 0.33α-0.67γ, 0.16α-0.84γ, and 0.10α-0.90γ are summarized in Fig. 10.7 (a), as a function of time. As the volume fraction of α is increased, the obtained grain growth is sluggish. When the α grain starts growing, its movements are locally blocked by the neighbor γ grain. However, the magnitude of the mutual retardation effect strongly depends on the initial volume fraction of the system. Although we have initialized with a similar concentration profile, the time taken to reach a similar growth state has been reduced for three-phase and two-phase counterparts. Thus, the incorporation of an additional phase into the microstructure has a significant influence on the growth kinetics. In simple words, the concurrent effect of multi-principal component diffusion and multiphase grain growth retardation is more dominant in three-phase than in two-phase systems. In the case with 0.33α-0.67γ, the α phase has the least growth rate and the γ phase is relatively faster than the overall evolution (Fig. 10.7 (b)). The individual growth rate of α and γ exhibits the diffusion-controlled coarsening processes.

### 10.3.4  Grain size distribution

The self-similarity behavior of the microstructural evolution can be determined from the geometrical and topological characteristics, such as normalized mean grain size distribution (GSD), grain topological distribution (GTD), and correlation functions [23]. However, in this preliminary study, the geometrical characteristics are only considered. Thus, the GSD's are calculated for all selected simulation cases and are compared with the available classical models. In the earlier investigations, several analytical and empirical

functions were proposed to approximate the GSD's obtained from the experimental and simulation microstructures [20, 33, 34]. The chosen classical Hillert and Weibull functions are denoted in solid and dashed lines, respectively. An invariant behavior of the microstructure can be ascertained by matching the GSD's of several time frames. In case 1, the $0.33\alpha$-$0.33\beta$-$0.33\gamma$ system supports the close approximation for the Weibull function, by means of the value $\tilde{\beta} = 2.7$. To sustain consistency in our Weibull fit, the free parameter of $\tilde{\beta} = 2.7$ is used for all the simulation cases. The corresponding phases in each microstructure are also examined separately. The concerned GSD's of the individual phase are presented in the subplot of Fig. 10.8 (a). The equivolume fractions of the $\alpha$, $\beta$, and $\gamma$ phases also match well with the fit of the Weibull functional. In contrast, the simulations of case 2 return bimodal-type distributions in Fig. 10.8 (b). The $\gamma$ grains of the matrix phase, which are controlled by the interface, coarsen reasonably quicker than the constituents of the minor phase ($\alpha$, $\beta$). During this evolution, the grains of the minor phase are nearly trapped at the triple junctions of the relatively larger grains of the $\gamma$ phase. The higher peak at 0.5 symbolizes the large-sized grains of the $\gamma$ phase in the microstructure. On the other hand, the grains of the minor phase accommodate close to the peak at 2.1. Furthermore, the simulation set-up of $0.39\alpha$-$0.22\beta$-$0.39\gamma$, of case 3, is also presented. A time-invariant behavior is ascertained for the selected GSD's. The Weibull function adopts well for this dataset. Furthermore, the GSD's of the appropriate phase also agree with the Weibull fit. Subsequently, the GSD of the simulation of case 5 ($0.33\alpha$-$0.67\gamma$) shows a slight deviation from the Weibull fit. The perceived GSD results of the phase in the subplot validate the Weibull approximation. It is noted that the $\alpha$ phase is moderately sharper than the $\gamma$ phase distribution. Interestingly, the classic Hillert-type distribution is not supported by our 2-D simulation results. In all cases, the observed GSD curves are broader than the assumption of the Hillert model. Comparable results are reported in the earlier 2-D MC and other simulations [227].

### 10.3.5  Quasi-steady-state microstructures

In order to understand the coarsening behavior of the triplex system, a comprehensive volume fractional study is demanded. However, one cannot vary each phase randomly to compose the initial volume fraction, since the available computational power determines the number of possible simulations. Thus, selecting the optimum initial volume fractions in three-parametric space is a challenging task. The phase diagram in Fig. 10.9, showing a phase at ternary equilibrium, is constructed for $\alpha$, $\beta$, and $\gamma$ phases. For a detailed investigation, the lower triangle portion close to the $\gamma$ phase is taken. This picked triangle regime is the nearly symmetric one and can be shifted to other phase states. Approximately, the 20 initial volume fractions are considered to logically cover the chosen triangle area (green circles in red lines). The outcomes will be discussed in the next sections.

The extended morphological features at their quasi-steady-state ($90dt$) microstructure
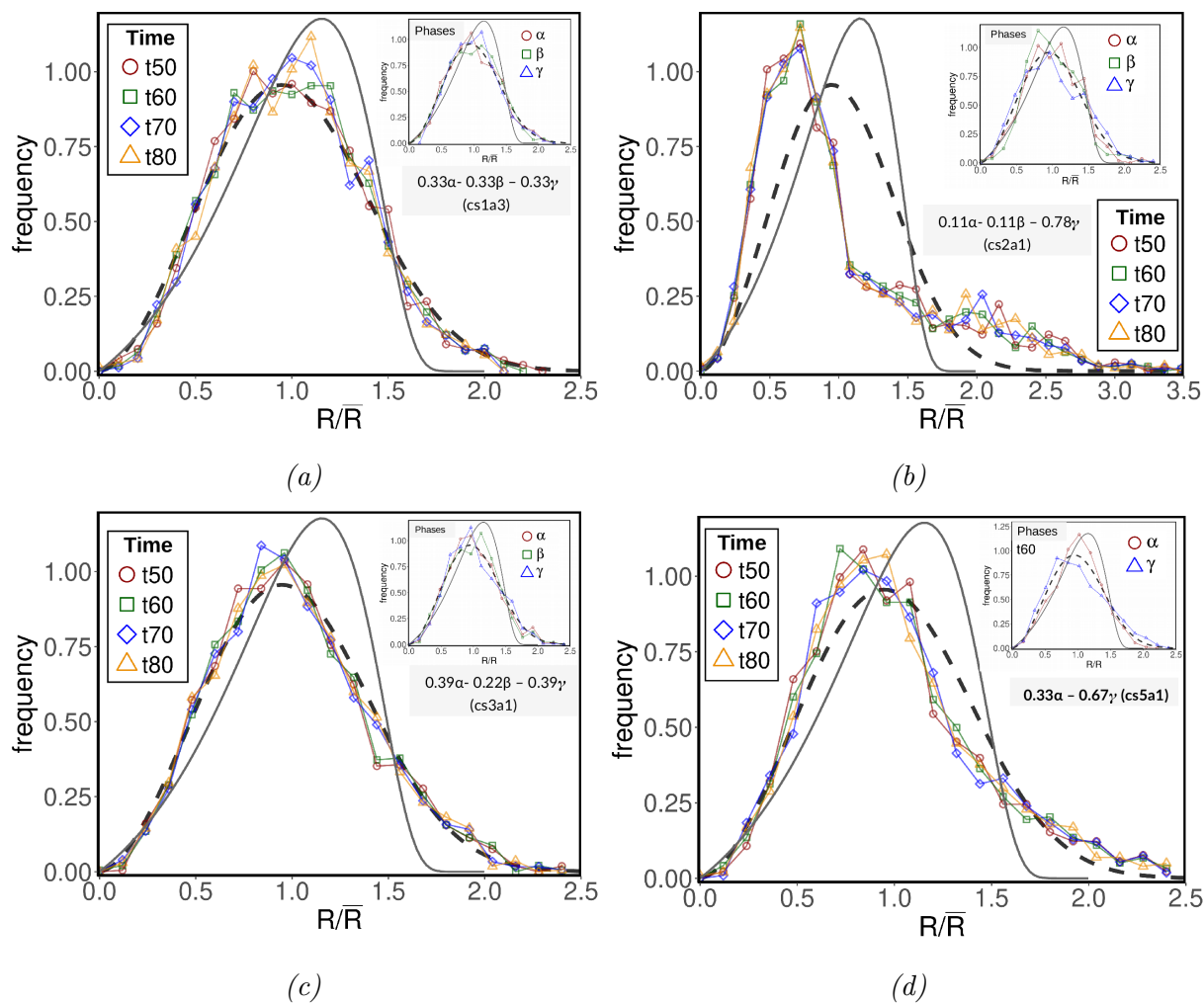
*Figure 10.8: Evolution of the normalized mean grain size for different simulation cases. Comparison to the theoretical models (solid line: Hillert function and dashed line: Weibull function) for the grain-size-related aspects. The inset shows the corresponding GSD's of the individual phase, along with the theoretical fit functions. (a) $0.33\alpha$-$0.33\beta$-$0.33\gamma$ (b) $0.11\alpha$-$0.11\beta$-$0.78\gamma$ (c) $0.39\alpha$-$0.22\beta$-$0.39\gamma$ (d) $0.33\alpha$-$0.67\gamma$*
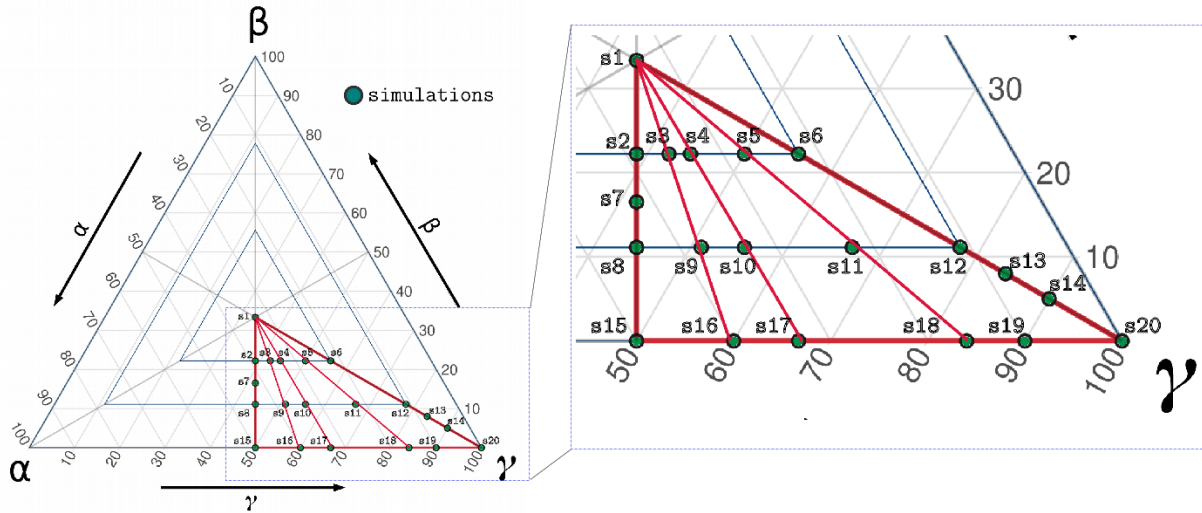
*Figure 10.9: Ternary diagram of α-β-γ, for the microstructural coarsening studies. The plot also displays the volume fractions investigated in this work.*

are manifested in Fig. 10.10. The principal volume fraction diversifies the geometrical and topological aspect of each contributing phase in the microstructure. The abnormal type of grains is not noticeable, concerning the preserved phases. In some cases ($f_{minor} < 0.20$), however, overall bimodal-type microstructures are apparent within major and minor phase constituents.

## 10.3.6   Growth kinetics: Total system

To establish the relative growth kinetics among all simulation cases, we first fix the growth coefficient ($m = 4$) and then calculate the growth rate constant ($k$). Fig. 10.11 compiles the relative growth rate in terms of their volume fraction. The $0.33\alpha$-$0.33\beta$-$0.33\gamma$ system delivers the lowest growth rate, compared to the rest. For a multiphase consideration, on the other hand, the maximum relative growth rate is noted for the $0.10\alpha$-$0.90\gamma$ system. The color scheme as well as the size variation (in the legend) for the dataset can be used to distinguish the values effectively. It is also seen that the triplex microstructures are generally slower than the two-phase structures. When the microstructure is mixed with an approximately equal volume fraction of multiple phases, the mutual grain growth retardation behavior predominates the Zener drag effect, which results in limited growth kinetics. In particular, the number of phases in the microstructure is also important to define the overall kinetics. For the two-phase case, the kinetics of the $0.50\alpha$-$0.50\gamma$ system is faster than the kinetics of the $0.33\alpha$-$0.33\beta$-$0.33\gamma$ system. On the other hand, the $0.50\alpha$-$0.50\gamma$ system is slower than the $0.10\alpha$-$0.90\gamma$ system. In other words, the coarsening of the $0.50\alpha$-$0.50\gamma$ system is notably sluggish in the $\alpha$-$\beta$ two-phase parametric space. Here, the $0.50\alpha$-$0.50\gamma$ system holds the high occurrence of the communications between the neighbor grains of the $\alpha$-$\gamma$ interface. Therefore, the expected long-range diffusional
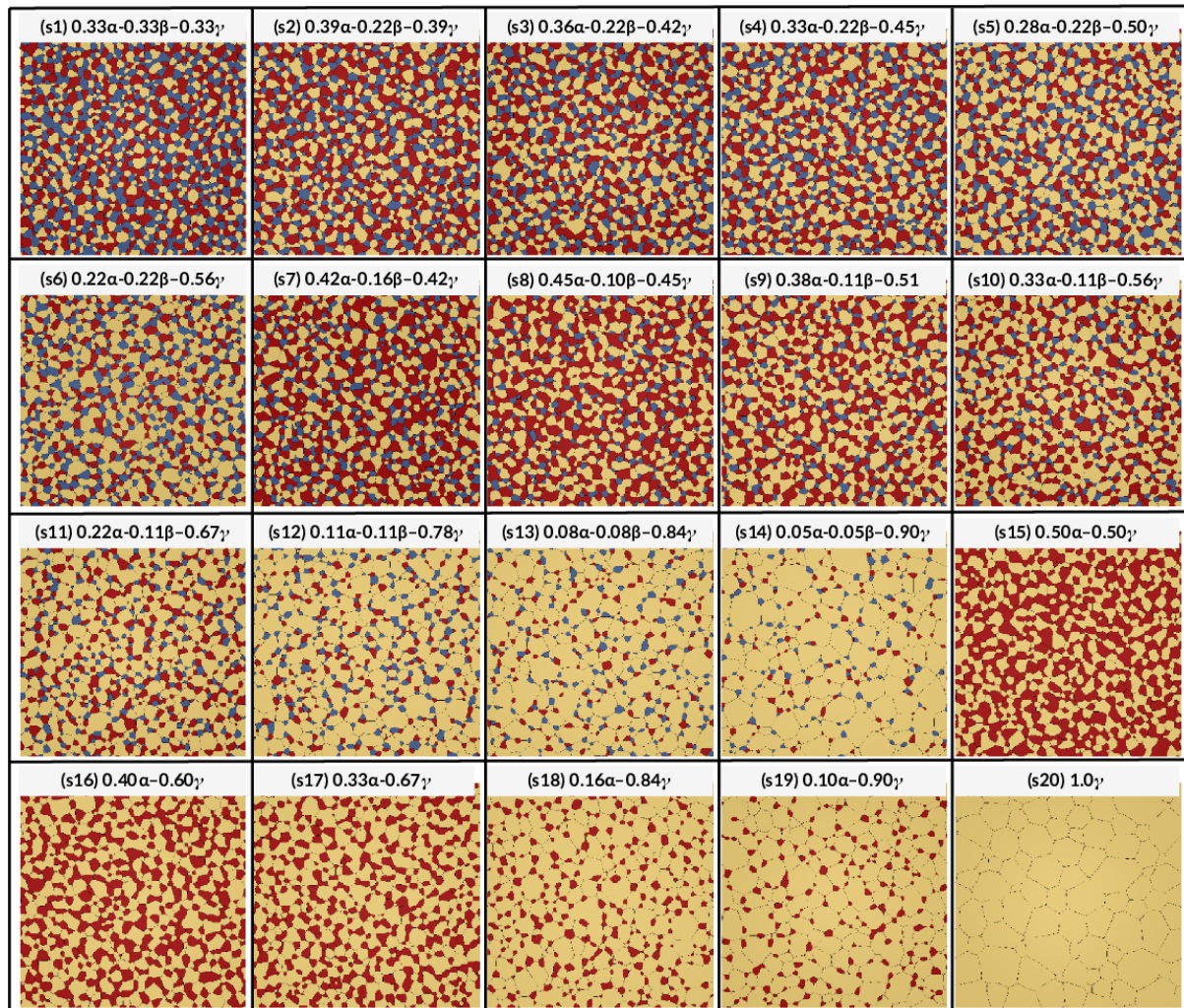
Figure 10.10: *Dependence of microstructures, simulated at a quasi-steady state, on the initial volume fraction condition.*
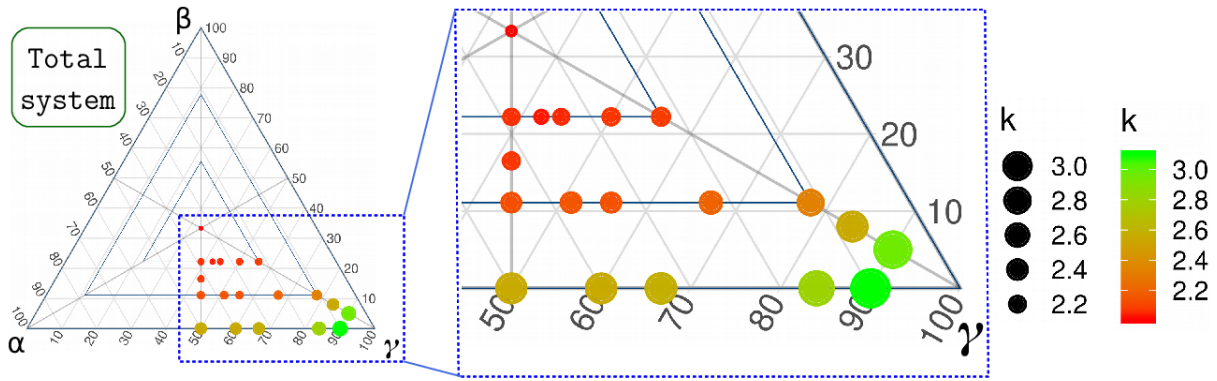
*Figure 10.11: Ternary plot for the relative growth rate constants from the simulation data, while fixing the growth coefficient (m ≈ 4).*

path is complex in nature. Similarly, for the triplex microstructures, the $0.33\alpha$-$0.33\beta$-$0.33\gamma$ system accommodates the highest probability of $\alpha$-$\beta$, $\alpha$-$\gamma$, $\beta$-$\gamma$ contacts, and ultimately, the weakest grain coarsening behavior is detected.

## 10.3.7   Growth kinetics: Phases

A similar procedure is followed to compute the relative growth rates of the individual phases on the triplex microstructure. Fig. 10.12 (a) shows the relative growth kinetics of the $\alpha$ phase, involving all simulation cases. The lowest value of $k = 1.37$ is obtained for the $\alpha$ phase in the $0.05\alpha$-$0.05\beta$-$0.90\gamma$ system. On the contrary, the highest coarsening kinetics of the $\alpha$ phase ($k = 2.53$) is perceived for $0.5\alpha$-$0.5\gamma$ systems. The intergrain distance of the $\alpha$ phase diminishes when progressing the volume fraction. Since the $0.05\alpha$ system accommodates the extended intergrain distances, the equilibrium concentration should diffuse to the prolonged distances. Therefore, the profound effect on coarsening can be observed. In order to verify the above hypothesis, the $0.33\alpha$-$0.22\beta$-$0.45\gamma$ and $0.33\alpha$-$0.11\beta$-$0.56\gamma$ systems are analyzed. Here, the $\alpha$ volume fraction is fixed, while the remaining phases vary. The growth rate of the $\alpha$ phase, $k = 2.01$, is for the $0.33\alpha$-$0.22\beta$-$0.45\gamma$ system and $k = 2.04$ is for the $0.33\alpha$-$0.11\beta$-$0.56\gamma$ system. These observed growth rate values are roughly the same, while the distribution of $\alpha$ phase grains in the matrix is not identical for both cases. Thus, the local neighbor interaction of $\alpha$ phase grains might contribute to the slight deviation in the dataset. Since we impose a random initial filling of individual phases in the microstructure, little discrepancies are anticipated for the similar volume fraction cases, in the growth kinetics. Nonrandom distribution may cause clustering bias and distinctly complicate the overall kinetics. However, in this present work, we did not focus on this clustering aspect of the similar phase grains.

The growth kinetics of the $\beta$ phase is presented in Fig. 10.12 (b). The used volume fraction of $\beta$ is in the range of 0 to 0.33. The highest $\beta$ coarsening rate ($k = 1.97$) is observed for the $0.33\alpha$-$0.33\beta$-$0.33\gamma$ system and the minimum coarsening rate ($k = 1.40$)

is seen for the $0.05\alpha$-$0.05\beta$-$0.90\gamma$ system. The higher volume fraction provides the faster coarsening rate of the specific phase and the corresponding Fig. 10.12 (b) describes the same. The second fastest coarsening rate is noted for $0.22\beta$, and is followed by systems holding $0.11\beta$. $0.22\alpha$-$0.11\beta$-$0.67\gamma$ and $0.38\alpha$-$0.11\beta$-$0.51\gamma$ yield $k = 1.48$ for the growth of $\beta$ phase grains. The other fixed volume fraction cases, for example $\beta = 0.22$, also exhibit roughly the same coarsening rate.

Fig. 10.12 (c) depicts the relative coarsening effect of the $\gamma$ phase. The maximum relative growth rate ($k = 4.76$) represents the $0.05\alpha$-$0.05\beta$-$0.90\gamma$ system and the lowest growth rate ($k = 2.07$) is for the $0.33\alpha$-$0.33\beta$-$0.33\gamma$ system. With the favor of a higher volume fraction ($\gamma$), $0.05\alpha$-$0.05\beta$-$0.90\gamma$ operates the substantial possibility of $\gamma$-$\gamma$ grain boundaries over the $\alpha$-$\gamma$ and $\beta$-$\gamma$ antiphase boundaries in the system. Hence the grain growth in the $\gamma$ phase region is essentially governed by the short-range interfacial energy minimization method.

Moreover, for the low volume fraction phases, for example, $\alpha$ and $\beta$ grains have to diffuse longer distances and the evolution is delayed. The large-sized grain boundaries ($\gamma$) are enclosed by small-sized $\alpha$ and $\beta$ grains, which yield the bimodal-type microstructure. By picking the similar volume fraction of $\gamma$ ($0.10\alpha$-$0.90\gamma$ ), which is analogous to the prior statement, the perceived value of the growth rate is $k = 4.60$, which is somewhat closer to $0.05\alpha$-$0.05\beta$-$0.90\gamma$. The volume-dependent growth kinetics of the phase is also verified for the $\gamma$ phase regimes.

## 10.3.8   Normal growth behavior

Abnormal grain growth is often regarded as a deleterious process which decreases the mechanical properties of the material. The anisotropic behavior of the microstructure, such as grain boundary energy and mobility advantages, initiates the abnormal grains ($R^{max} > 3\bar{R}$). However, the true characteristics of abnormal grain growth are not yet thoroughly understood. In this study, the chosen simulation parameters are isotropic in nature. Hence one should expect the normal grain growth behavior from the resultant microstructures. However, with some lower volume fraction cases ($f_{minor} < 0.2$), the overall microstructure yields a bimodal structure, where the small-sized constituents of the minor phase ($\alpha$, $\beta$) are embedded in the larger matrix of the $\gamma$ phase. Of course, the abnormal grain growth behavior in a multiphase, polycrystalline structure is again a complex process, where the volume fraction and other process parameters plays a significant part. The specific motivation here is to check the normal grain growth behavior of the individual phases during evolution.

Fig. 10.13 suggests the correspondence within the maximum grain size ($R^{max}$) and the mean grain size ($\bar{R}$) of the individual phases ($\alpha$, $\beta$ and $\gamma$ grains). The quasi-steady-state microstructure at $80dt$ is used. Furthermore, the color schemes of the legend are
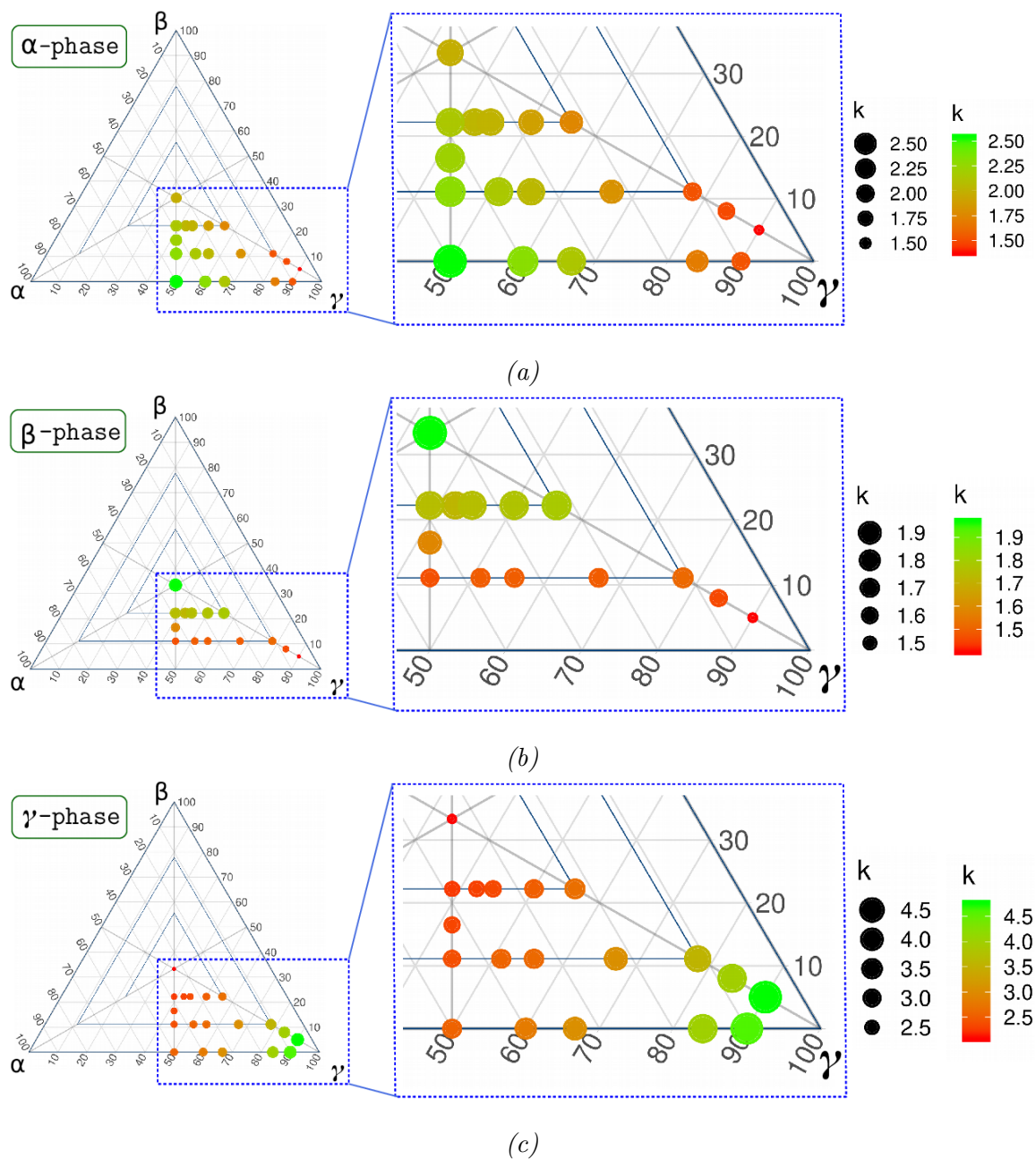
Figure 10.12: Ternary plots showing the relative growth kinetics of the individual phase. Each diagram shows the results from three phases (labeled), computed by $m \approx 4$ consideration. The relative growth rate constants for the (a) $\alpha$, (b) $\beta$, and (c)$\gamma$ phase.

represented as a function of the volume fraction of each phase. The positive correlation behavior is obtained from the figure. $(R_\alpha^{max}/\bar{R}_\alpha) \approx 2.36$ means that the growth of $\alpha$ does not promote any abnormality in its distribution. $(R_\beta^{max}/\bar{R}_\beta) \approx 2.64$ and $(R_\gamma^{max}/\bar{R}_\gamma) \approx 2.33$ are also established in the normal grain growth hypothesis.

### 10.3.9    Zener relation

In addition to the mutual grain growth retardation of each phase, the Zener drag is also associated with some special cases ($f_{major} > 0.8$). Since the classic Zener relation holds the spherical inert minor phase particle assumption, the influence of irregularly shaped coarsening particles is coupled in our earlier study [3]. Zener suggested that the mean grain size of the major phase, in a completely pinned microstructure, can be correlated with the volume fraction and the mean size of the particles of the second phase.

Moreover, there are multiple variations of the Zener equation, reported in the experimental and numerical investigations [51]. We accept that the original Zener hypothesis does not perfectly match the present simulation circumstances. With this in mind, the grain boundary dragging of concurrently coarsening minor phase constituents can be investigated by employing the general Zener equation. In the same way, the Zener formulation can also be adopted for three-phase microstructural growth.

Fig. 10.14 (a) portrays the classical Zener relationship for the temporal evolution result of the $0.16\alpha$-$0.84\gamma$ and $0.10\alpha$-$0.90\gamma$ simulations. The linear mean fit is used to determine the best fitting parameters of $k1 = 0.897$ and $q1 = 0.527$, for the dataset. The previous 2-D simulation results also admit that the Zener coefficient ($q1$) is close to 0.5.

$$\bar{R}_\gamma = k1\,(\bar{R}_\alpha/f_\alpha^{q1}) \tag{10.1}$$

For a three-phase study, on the other hand, we choose a comparable volume fraction of minor phase constituents. Here, $0.08\alpha$-$0.08\beta$-$0.84\gamma$ and $0.05\alpha$-$0.05\beta$-$0.90\gamma$ are tested. In this attempt, we propose the empirical equation among the primary $\gamma$ grain size and the grain sizes of the minor phase ($\alpha$, $\beta$) as a function of the volume fraction. Although there is a large possibility of the interaction terms in the equation, we simplify it by extending the multiplication of two minor phase contributions ($\alpha$, $\beta$):

$$\bar{R}_\gamma = k2\,(\bar{R}_\alpha/f_\alpha^{q2})(\bar{R}_\beta/f_\beta^{q2}) \tag{10.2}$$

Fig. 10.14 (b) explicates the extended Zener formulation for the three-phase microstructure. The similar linear mean fit method is adopted to compute $k2 = 0.032$ and $q2 = 0.302$. Nevertheless, both Zener-type formulations are actually nonlinear in nature, so that a direct comparison of the growth rate of the matrix phase is not as simple as that. For example, the overall growth rate constant ($k = 2.80$) of the $0.16\alpha$-$0.84\gamma$ system is higher than the growth rate constant ($k = 2.54$) of the $0.08\alpha$-$0.08\beta$-$0.84\gamma$ system, while

*(a)*

*(b)*

*(c)*
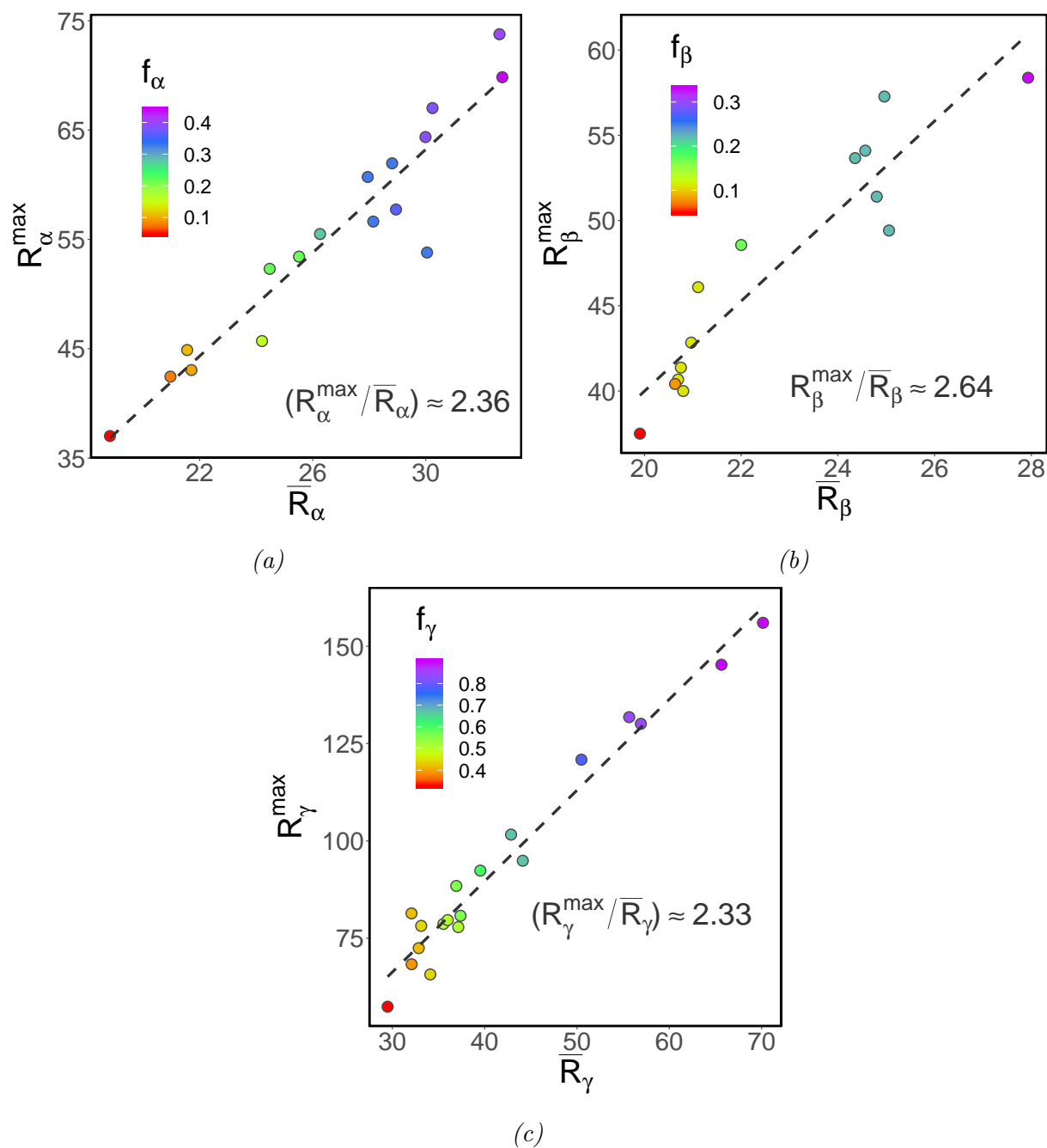
*Figure 10.13: The maximum attainable grain size to mean size ratio for the (a) α, (b) β, and (c)γ phase. The data points are displayed as a function of the volume fraction, for the quasi-steady-state condition. The obtained size ratio indicates the isotropic growth behavior.*
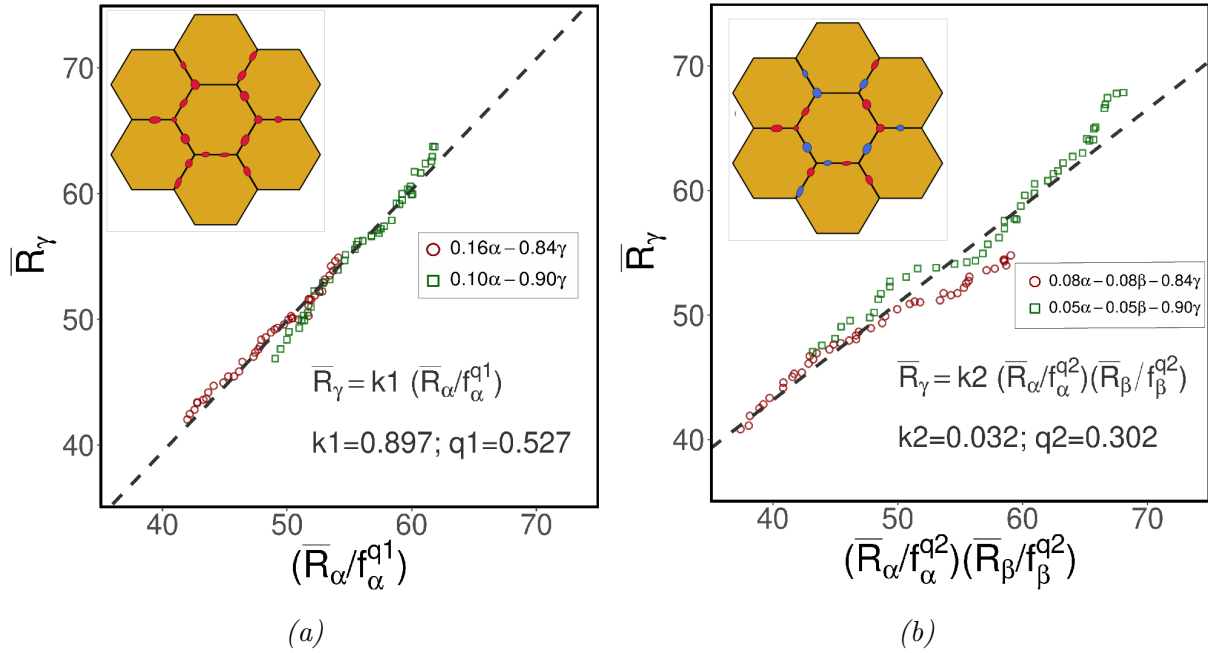
Figure 10.14: Variation of the matrix $(\gamma)$ grain size, as a function of the minor constituents $(\alpha$ and $\beta)$, at different conditions; (a) two-phase system $(\alpha$-$\gamma)$, (b) three-phase system $(\alpha$-$\beta$-$\gamma)$.

fixing the growth coefficient $(m = 4)$. Subsequently, the coarsening rate of the $\gamma$ phase in the previous two-phase system $(k = 3.99)$ is slightly greater than the three-phase system $(k = 3.96)$.

## 10.3.10   Local growth behavior

The local morphological features of the selected simulation cases are discussed in this section. Fig. 10.15 showcases the small region of the $0.05\alpha$-$0.05\beta$-$0.90\gamma$ system as a function of time. The highlighted $\gamma_1$ grain accommodates six neighbors of $\gamma$ grains, where von Neumann's law proposed that the grains with six neighbors can have a zero growth rate in an isotropic 2-D system [119, 152]. While this may be true for a single-phase material, the chosen three-phase microstructure extends the complexity of the evolution process. The first neighbors of the $\gamma_1$ grain include the grain interactions of the $\alpha$ and $\beta$ phase. In particular, the $\alpha_1$, $\beta_1$, and $\beta_2$ grains can behave as an obstacle to the growth of $\gamma_1$. The contact angle along the grain boundaries of $\gamma_1$ endures close to $120°$ in the microstructure.

To illustrate the topological influence, the grain edges of $\gamma_1$ are expressed as $e^n$, where $n$ is the edge number $(e)$. Other than the edge $e^6$, at least one corner of the remaining edges $(e^1$-$e^5)$ can have the antiphase grain contacts. In other words, the edge $e^6$ can free to move without the influence of minor phase constituents. The neighbor grain of $\gamma_3$ accommodates the five edges of $(\gamma)$ grains, in which the interfacial energy minimization mainly induces the growth. The grain $\gamma_3$, which is of a lower edge class, shrinks as a result
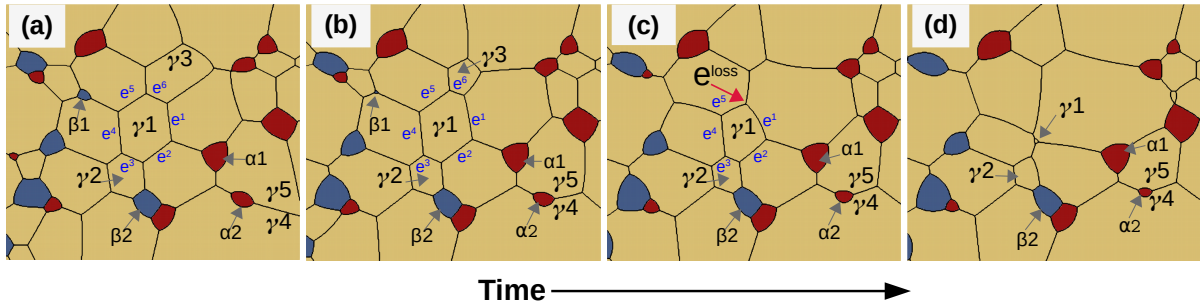
*Figure 10.15: The morphological evolution of* $0.05\alpha$-$0.05\beta$-$0.90\gamma$ *(magnified view of a selected region of the domain) leads to topological changes in the microstructure. The normal developmental pathways of some selected grains are highlighted.*

of neighbor growth. Above all, the edge length of $e^6$ contracts, while progressing time.

Figs. 10.15 (b) and (c) demonstrate the above hypothesis. Eventually, $\gamma_3$ disappears in 10.15 (d), in which the edge loss is indicated. In the same way, the neighbor grain $\gamma_2$ is studied further. $\gamma_2$ is surrounded by five $\gamma$ grains and one $\beta$ grain. For the evolution of $\gamma_2$, it therefore not only depends on the interfacial energy minimization but also on the long-range diffusional process. In other words, the neighbor $\beta_2$ has to shrink/grow for the morphological changes of $\gamma_2$, which can be observed in Fig. 10.15.

Another interesting morphological transition of the $\alpha_2$ grain is explained here. The lens-shaped $\alpha_2$ grain is found at the grain boundaries of $\gamma_4$ and $\gamma_5$. During the evolution, the $\alpha_2$ grain induces a Zener drag on the grain movement of $\gamma_5$. As a result, the shrinkage rate of $\gamma_5$ is diminished. Simultaneously, the $\alpha_2$ grain also undergoes Ostwald ripening via long-range diffusion.

Fig. 10.16 depicts the picked region of the $0.22\alpha$-$0.11\beta$-$0.67\gamma$ evolution. The six-sided $\beta_1$ grain holds one $\alpha$ and five $\gamma$ neighbors. As a result of energy minimization, the small-sized $\gamma$ neighbors consolidate mutually to form a single $\gamma$ grain. On the contrary, the neighbor $\alpha$ demands more time to shrink, due to long-range diffusion. From Fig. 10.16 (b) onwards, the $\beta_2$ grain develops a bulged semi-concave structure. This distinct grain shape persists, while the grain size varies with time.

In addition, the well-known, arrow-shaped, morphological evolution of $\alpha_1$ is noticed in Fig. 10.16 (b). The dashed green line designates the direction of the movement of the $\alpha_1$ grain. As the evolution proceeds, the $\alpha_1$ grain drops one edge and develops a lens-shaped structure. Figs. 10.16 (c) and (d) highlight the sandwich-type structure into which the $\alpha_2$ grain is embedded with the $\beta_2$ and $\beta_3$ grains. The phase variant of a similar sandwich structure can also be observed in other locations of the microstructure.
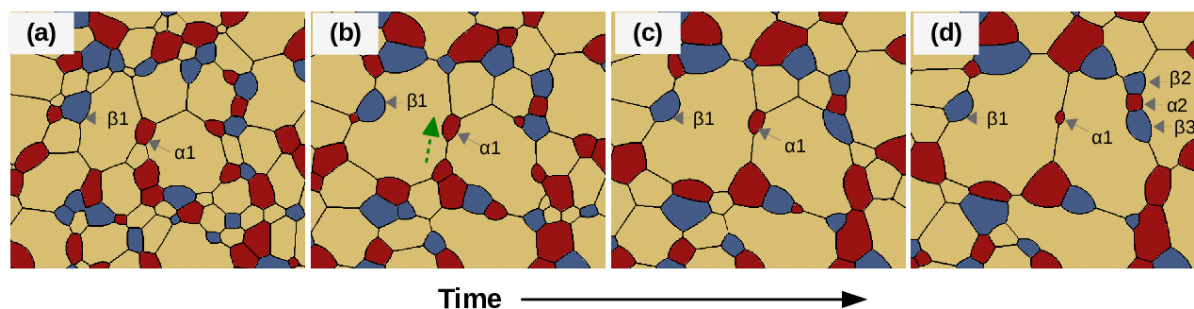
*Figure 10.16: The morphological evolution of 0.22α-0.11β-0.67γ (magnified view of a selected region of the domain). Formation of S-shaped interfaces and arrow-shaped grain and sandwich structures, due to the phase evolution, with the assistance of diffusion.*

## 10.3.11 Microstructural coarsening: 3-D analysis

The multiphase-field model formulated in the previous section is adopted to analyze the evolution of representative three-dimensional microstructures. In order to render a comparative analysis across various microstructures, the present investigation is confined to volume-diffusion governed transformation. More-over, all the diffusivities are considered equal to exclusively recognize the influence of the number of phases on the kinetics of the concurrent grain growth and coarsening. The concurrent grain growth and Ostwald ripening exhibited by binary two-phase (C2P2), ternary two-phase (C3P2) and ternary three-phase (C3P3) 3-dimensional systems are respectively shown in Figs. 10.17 (a), (b) and (c). In Figs. 10.17, it is evident that, despite the complex microstructural transformation, the overall volume fractions of the phases remain unchanged.

The kinetics of the microstructural evolution is quantitatively analyzed by examining the average grain-size. In Fig. 10.18, the increase in the average grain-size during the transformation of the different polycrystalline structures, considered in the present work, is plotted. The fitting values included in the illustration indicates consistency of the current numerical technique in recovering the power laws. The regular grain growth is primarily governed by the migration of the grain boundaries. In NGG, the bulk phases possess negligible significance and the evolution is entirely governed by the interface contribution. Unlike regular grain growth, the bulk contribution of the individual grains plays a significant role in this complex microstructural coarsening.

However, it is apparent that the grains evolve at a faster rate during a normal grain-growth, when compared to the complex grain-growth resulting in the multiphase microstructures. Moreover, with an increase in the number of phases, the transformation kinetics noticeably decreases, which can be termed as suppressed grain growth. Although the almost overlapping kinetics exhibited by the binary and ternary two-phase systems, slightly weaker coarsening rate of the ternary system can be noticed from the power-law fit parameters. It is realized that the influence of the components on the transformation
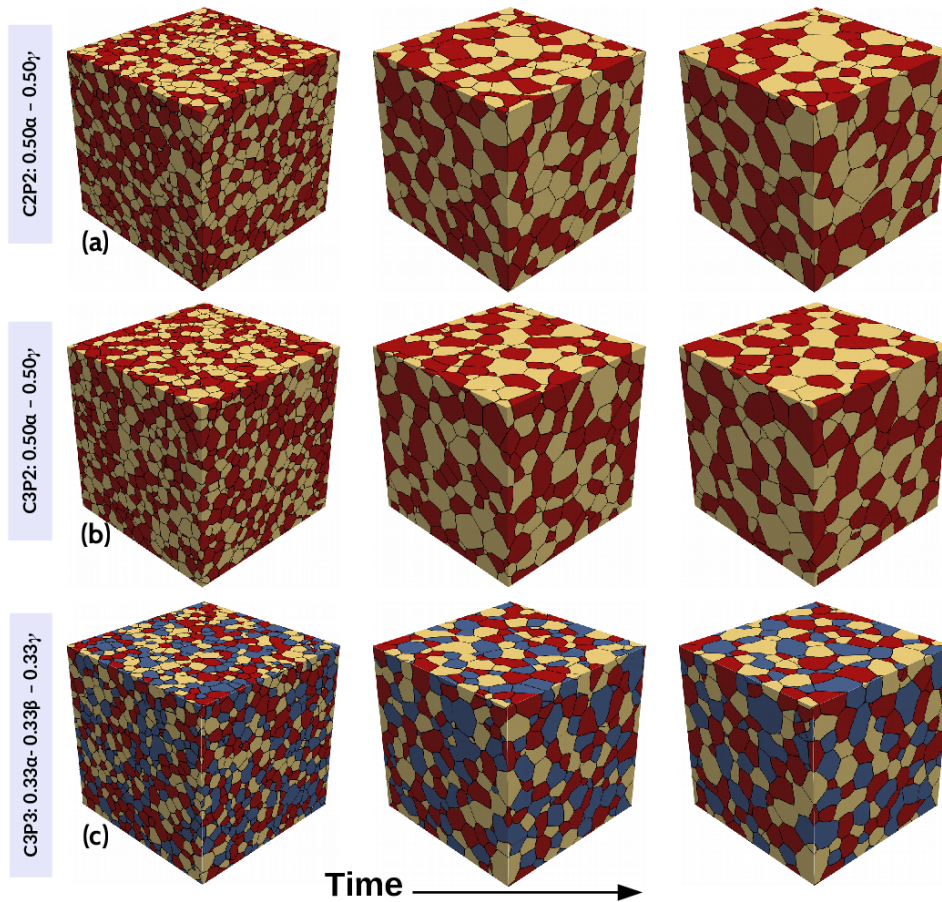
*Figure 10.17: 3-dimensional microstructural evolution of (a) $C2P2 : 0.5\alpha$-$0.5\gamma$, (b) $C3P2 : 0.5\alpha$-$0.5\gamma$, and (c) $C3P3 : 0.33\alpha$-$0.33\beta$-$0.33\gamma$. Effect of components and phases on grain coarsening kinetics can be seen.*

rate primarily depends on the kinetic coefficients of flux, diffusivity ($D$).

## 10.4   Summary

Binary and ternary multiphase polycrystalline systems have been simulated, with a wide range of volume fraction and bulk diffusivity conditions. The obtained results are as follows:

1. The kinetics of the grain growth power law can be adopted, $R = kt^{(1/m)}$, the growth coefficient is $3 < m < 4$; It depends on the bulk diffusivity values.

2. The slowest coarsening rate is observed for the $0.33\alpha$-$0.33\beta$-$0.33\gamma$ system compared to the rest.

3. Phases with a low volume fraction should take longer to coarsen, since their intergrain distance delays the long-range diffusion.
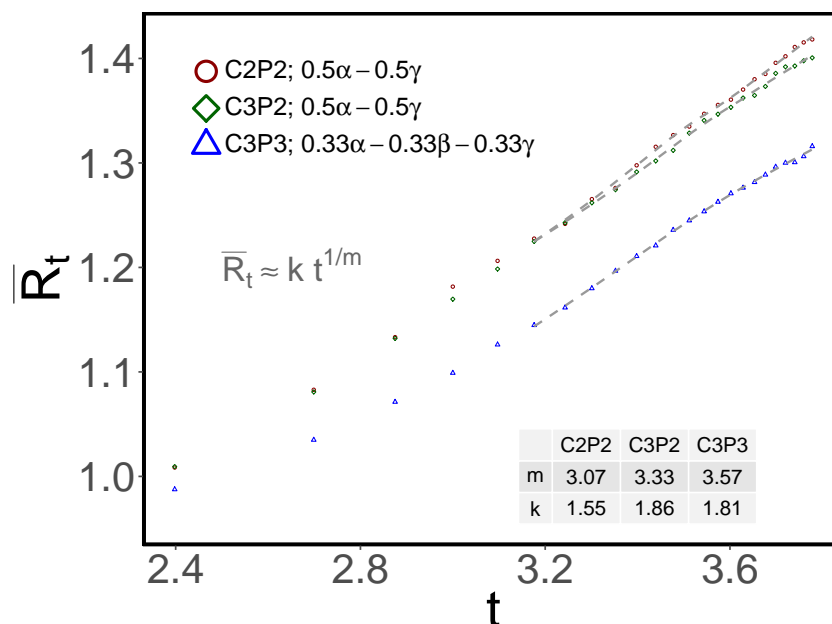
*Figure 10.18: Mean grain size evolution for a 3-D simulation cases.*

4. The close approximation of GSD works well with the form of the Weibull functional ($\tilde{\beta} = 2.7$). While this may be true for some specific volume fraction combinations, systems with low volume fractions ($f_{minor} < 0.2$) yield a bimodal microstructure.

5. The normal grain growth behavior of the individual phases is verified.

6. The extended Zener drag equation ($\bar{R}_\gamma = k2\,(\bar{R}_\alpha/f_\alpha^{q2})(\bar{R}_\beta/f_\beta^{q2})$) is proposed for three-phase systems.

7. The localized morphological features, such as Zener drag, arrow-shaped grains, and sandwich structures, are captured.

The concurrent effect of the cooperative diffusion of multi-principal elements, the mutual retardation of each phase, and the Zener drag effect are responsible for the sluggish microstructural evolution in these materials.

# Part V
# Conclusions and Future Directions

# Chapter 11

# Conclusions and outlook

## 11.1  General conclusions

A thermodynamically consistent multiphase-field approach was adopted to gain deeper insight into the microstructural evolution of multicomponent multiphase polycrystalline materials. Although being in a diverse process parametric space, the careful simulation studies discovered a lot of exciting results. The findings, highlights and the objectives fulfilled in the present dissertation can be summarized as follows :

1. **Grain growth phenomena in single-phase materials**

   In chapter 5, the topological evolution of the grains along with its first-neighbors was quantitatively analyzed using a Heat-map representation. Analysis of face-switching events in terms of face-gain, face-loss, and no-change events were performed. The relative dominance of face-loss events over gain events was in exact agreement with the existing results in the literature. Switching affinity of the face-loss event, monotonously decreases with an increase in face-class. The life expectancy of the grains with the topological evolution around and below face-class 14 was considerably short. Although there have been previous attempts to represent first-neighbor interactions, this is the first report of such Heat-maps depicting the number-density based contribution of the different face-classes to first neighbors during evolution were discussed. The deviations in topological arrangements predominantly occur in the initial stages of the transformation and shows time-invariant behavior eventually.

   In chapter 6, this work characterizes microstructures with precise short- and long-range geometrical and topological correlation functions. Normal grain growth invariably includes a transient and Quasi-steady-state growth regime. While in 2-D, the GSD is approximated by a Weibull function, the Hillert approximation is quickly reached in 3-D, which slightly contradicts the GSD developing at a later time. In

other words, the longtime annealing ensures that neither the Hillert nor the Weibull function corresponds to the exact 3-D GSD. The classical grain growth laws were adopted for our simulation dataset. Additionally, the empirical growth laws, based on the first neighbor correlations, have been suggested. The geometrical and topological evolution of the first neighbor grains, which shows the strong correlation, predominantly weakens for the long-range interactions. The influence of the initial arrangements of the grains, on reaching the self-similar state, was examined. With an increase in the initial heterogeneities of the microstructure, the duration of the transition period increases, as perceived from the simulation.

In chapter 7, presence of pre-existing abnormal grains ($2R_c$), prolongs the early growth regime by introducing a transition period. The temporal evolution of the volume fraction of the abnormal grains $F_o$, reveals two stages in complete agreement with the existing observation [178]. Over a hundred simulations with different $F_o$ and marginal degree of abnormality, $U_{max}$ were analyzed to quantify the change in the span of the transient phenomena. With an increase in the initial volume fraction of the abnormal grains, the duration of the transition period decreases. The microstructures with $U_{max}$ slightly greater than 2, and $F_o < 0.01$, the transient phenomena was not distinctly perceivable. The size-advantage of abnormal grains does not warrant increased growth kinetics.

2. **Microstructural coarsening in multiphase materials**

Chapter 8 deals with the study of the binary two-phase microstructural evolution by grain coarsening, with a wide variety of volume fractions and varying bulk diffusivity conditions. The kinetics of grain coarsening does not strictly follow the diffusion-controlled or interface-controlled mechanism when the volume fraction of the minority phase varies. For a critical volume fraction, the rate-limiting step is bulk diffusion, and the observed growth exponent is $m \approx 3$. The ratio between the mean grain size of the $\alpha$ and $\beta$ phase decreased with an increasing volume fraction of the $\beta$ phase. Grain growth of the $\alpha$ phase was adequately controlled by $\beta$ phase grains and vice versa.

In chapter 9, understanding of a complex microstructural evolution in equivolume $\alpha$-$\beta$ material in terms of interfacial energy ratios was presented. The maximum grain coarsening was observed for the isotropic case, as compared to the anisotropic interfacial energy systems. Varying the interfacial energy ratios, increasing fraction of quadruple to the triple junctions in the system was observed. The ratio between the mean grain size of the $\alpha$ and $\beta$ phase is roughly one which is independent of the interfacial energy ratio. The parallel-coordinate plot was introduced for qualitative assessment of multi-dimensional process parameters and duplex alloy microstructural features.

In chapter 10, the microstructural evolution of ternary multiphase polycrystalline

systems was studied. It was identified that, with an increase in the number of phases, the transformation kinetics significantly decreases and the grain growth is suppressed. However, the influence of the number of independent components is not as straightforward as the phases. The components predominantly affect the growth rate through their characteristic kinetic coefficients of flux. The slowest coarsening rate was observed for the $0.33\alpha$-$0.33\beta$-$0.33\gamma$ system compared to the rest. Phases with a low volume fraction required a longer time to coarsen since their inter-grain distance delays the long-range diffusion. The normal grain growth behavior of the individual phases was established. The extended Zener drag equation was proposed for low volume fraction three-phase systems.

In multicomponent multiphase studies, topological evolution of the grains, which have been largely overlooked in the present work, are to be addressed in the following studies. Furthermore, since the simulations are confined to 2-dimension in this study, a 3-dimensional extension of the present analysis will be the objectives of the future investigations. Although the works presented in the thesis is complete in its own right, several interesting extensions are possible. The straightforward continuation of the present work is discussed first.

## 11.2 Future directions

### 11.2.1 Development of bamboo microstructures

Grain growth in the bulk materials generally does not account for the influence of their free surfaces. In contrast, free surfaces play the most significant role in the grain growth of thin films, wires, and foams. Bamboo-like microstructures, where the grains span the whole cross-section, and where grain boundaries are perpendicular to the thickness direction, are commonly observed in these materials. The thickness is typically much smaller than the width of the film. For example, in electronic chips, thin metallic films, known as interconnects, develop bamboo grains during operation. The lifetime of an interconnect is predominantly affected by combined diffusivities and electro-migration rates, along with their complex grain boundary networks [228]. Thus, an understanding of the bamboo microstructures and their evolution has practical application prospects. However, it remains unclear how the bamboo grains begins and impacts the grain coarsening kinetics in these surface-dominated systems.

In the past few decades, considerable experimental and simulation attempts have been made to understand the bamboo formation kinetics in different systems [229, 230, 231, 232]. An empirical linear relationship has been proposed within the average length of the final bamboo grains, $\bar{L}$ and the tube diameter ($D$). The previously reported values were

$\bar{L} = 0.97D$, obtained from 3-D foam experiments [229], $\bar{L} = 2.3D$, achieved through 2-D thin film simulation studies [231], $\bar{L} = 1.43D$, acquired by mono-layer bubble coarsening experiments [230], $\bar{L} = 0.88D$, found in aqueous foams with variations of the liquid filling fractions [233], and recently $\bar{L} = 2.0D$, attained by means of 2-D MC simulations [232]. However, to our knowledge, no consolidated study has been performed to investigate the bamboo microstructures in two dimensional (2-D) and three dimensional (3-D) systems with identical processing conditions. The present simulation domain is analogous to a 3-D foam coarsening experiment in a tube [229]. The primary focus of this work is to perceive how the development of bamboo grains varies in a 2-D and 3-D polycrystalline setup.

The schematic illustration of the simulation domain is depicted in Fig.11.1(a). For all simulations involved in the present study, both a fixed boundary condition (Dirichlet BC) at the Y- and Z-domain surfaces and a periodic boundary condition at the X-domain are used. In the present work, the top and bottom layers can be treated as free surfaces where the phase field equation is not solved for the all the points in these layers. The 2-D domains with a size of $1600 \times D$ grid points are used ($X \times Y$). For 2-D simulations, the values of the film thickness $D$ are as follows: 32, 40, 48, 56, and 64 grid points. For a 3-D polycrystalline tube setup, $1200 \times D$ is selected, where the tube diameter $D$ is in the range of 32, 48, 64, and 80 grid points.

The microstructural evolution of the 2-D and 3-D simulations is presented in Fig. 11.1(b) and (c). The initial polycrystalline structure comprises grains which exhibit different sizes and topological properties. In our study, the mean grain size of the system was found to be increasing with time and the grain growth stagnation was also reached for a complete bamboo microstructure. Upon the formation of bamboo grains, flat interfaces could be observed at the horizontal planes, and their respective contact angles were roughly held to be $\approx 90°$. Furthermore, the grain coarsening rate is particularly dependent on the presence of local neighboring non-bamboo grain clusters. A localized stagnation appears at the interface of two bamboo grains. Fig. 11.1 (b) reveals the evolution of bamboo grains with the local clustering tendency of normal grains in the 2-D network. Throughout the evolution, bamboo grains were found to consume the neighboring non-edged grains. After a certain period of time, the microstructure only consisted of bamboo type grains and growth stagnation is observed. The grain coarsening stages observed in the 3-D tube setup, were similar to the 2-D results. The magnified local region is rendered for a better representation, showing transient neighbor grain rearranging features (Fig. 11.1(c)).

The average bamboo grain length ($\bar{L}$), computed for all simulations, and the best-fitted line are overlaid in Fig. 11.2. Although linear tendencies are observed, substantial disparities can be seen in the $\bar{L}/D$ slopes. For the 2-D and 3-D cases, $\bar{L} = 2.08D$ and $\bar{L} = 1.05D$ were obtained from our simulations. For the 2-D case, a varied initial Voronoi
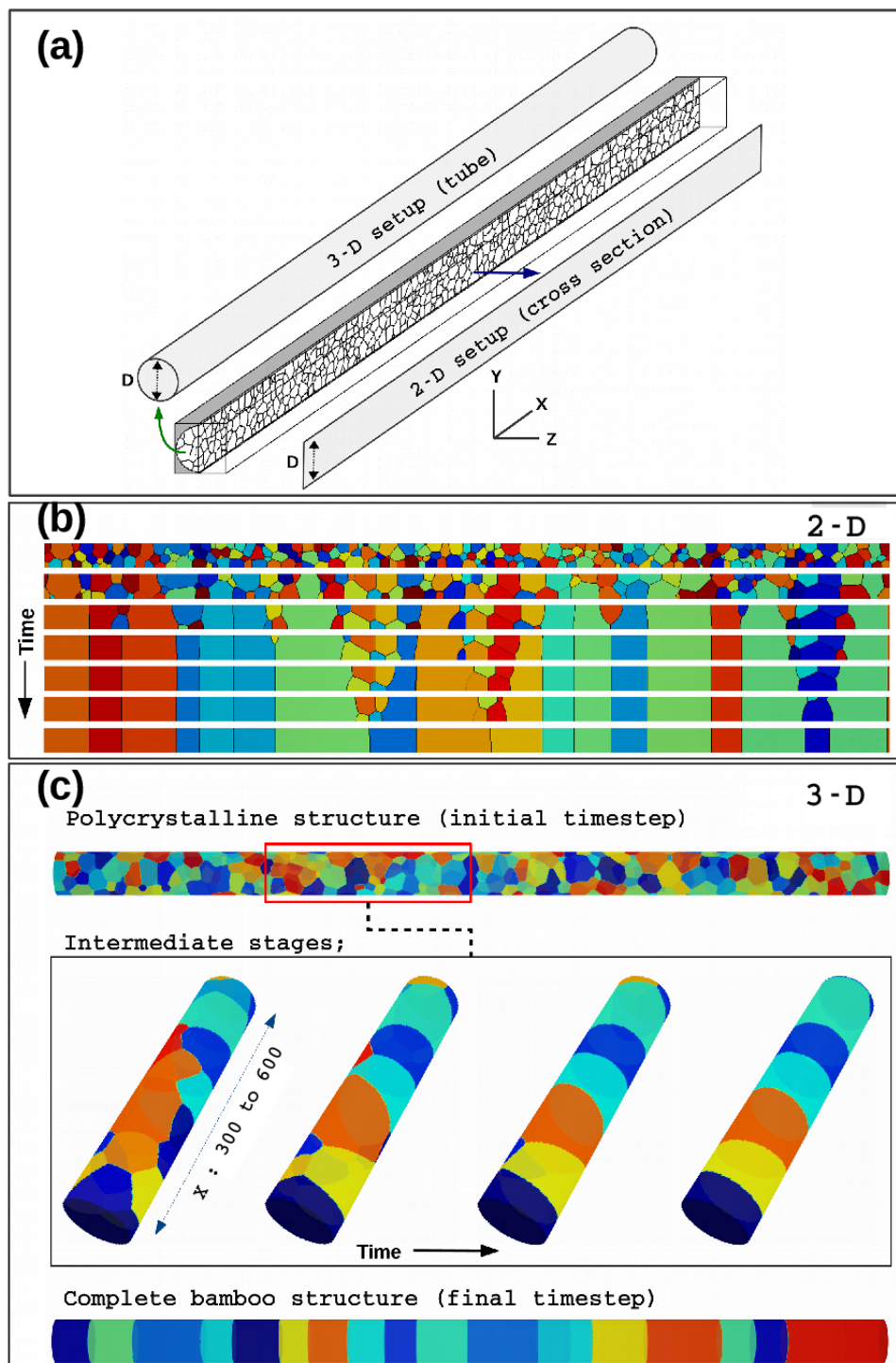
Figure 11.1: *Microstructural evolution in a (a) 2-D and (b) 3-D system. The inset shows the kinetics of the bamboo grain formation on an enlarged scale.*

filling shows some variations in the final bamboo characteristics. These 2-D results are consistent with the recent Dana Zöllner MC simulation [232]. Furthermore, the 3-D observations are in agreement with the 3-D foam experiments [229].

Since a wide range of $\bar{L}/D$ ratios has been reported in earlier studies, the true reason still has to be identified. The bamboo grains were obtained under identical thermodynamic driving forces, irrespective of their dimensions. However, the variation in the $\bar{L}/D$ ratio mitigates the fact that the dimensionality effect plays a substantial role in these systems. By a theoretical perspective, the topologically mediated grain growth kinetics marginally differs from the 2-D to the 3-D case [118, 120]. In this work, the comprehensive topological investigation is overlooked. The above results claim that similar curvature-driven simulations could produce varying $\bar{L}/D$ ratios. This also indicates that coarsening results from the 2-D case cannot be directly transferred to the 3-D use cases. Thus the need for a 3-D simulation setup is inevitable for quantitative thin film or foam coarsening studies.

## 11.2.2   The transient grain growth regimes in thin films

Polycrystalline thin films have wide application prospects; for example in coatings and semiconductor industries. Their physical, chemical and mechanical properties associated with the constituting microstructures in which the arrangements of internal grain boundary network are linked. Therefore, controlling their properties affiliated with the thickness and grain size of the film [234]. The formation of suitable film microstructure can be achieved by the optimized deposition processes and subsequent thermal treatments. Generally, the high temperature annealing conceive the grain growth and recrystallization phenomena.

Generally, grain growth in thin films appears slower than bulk materials, where their free surfaces contribute grooving and other rate-limiting mechanisms [235, 236, 237]. In bulk materials, the elemental grains relatively less exposed to the free surfaces compared to the thin film counterpart [238]. Hence the grains in bulk systems which hold similar geometrical and topological features yield roughly the same growth rate. On the contrary, in thin films, where internal grain arrangements incorporate bamboo type grains, may lead to transient growth behavior.

In the past few decades, numerous attempts have been made to explain the microstructural evolution in thin films [239, 240]. Grain growth phenomena in single- and multi-phase thin films have been reported in number of articles [241]. Much of the thin film studies have been concentrated on two-dimensional(2-D) representation of the actual three-dimensional (3-D) systems. The 3-D numerical studies were limited in the literature due to its high computational requirement and time. In the present work, grain growth in thin films is investigated using 3-D multi-phase-field simulations and the resultant
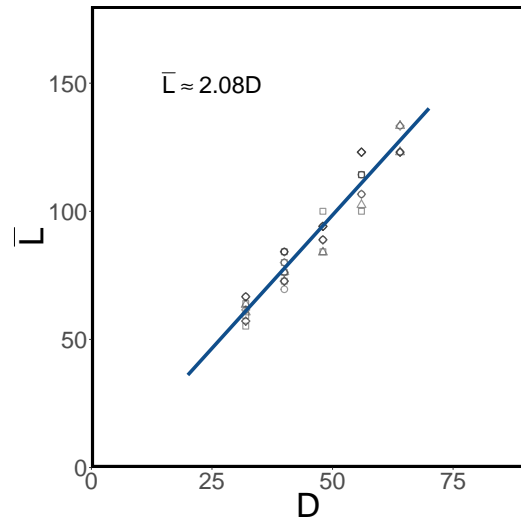
(a)
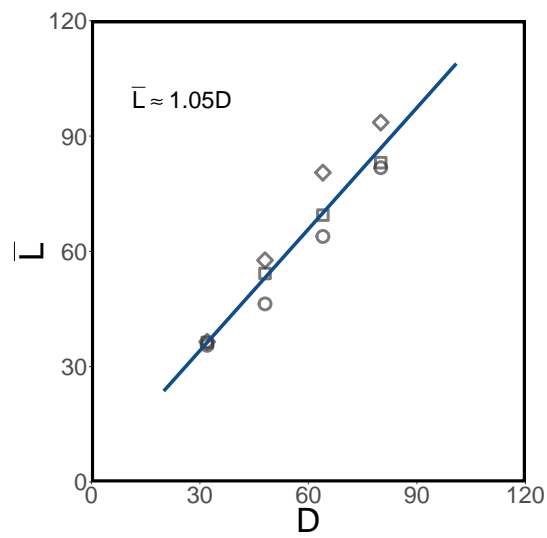


(b)

*Figure 11.2: Best-fitted curves showing the linear relationship between the average bamboo edge length and the tube diameter, within the various simulation setups. $\bar{L}$ as a function of $D$ (a) for a 2-D setup (b) for a 3-D setup*

microstructures are quantitatively analyzed.

Three-dimensional domains of size $512 \times 512 \times h$ grid-points with free boundaries at top and bottom and periodic boundary conditions for the remaining sides employed for all the simulations. Thin film thickness $h$ was chosen in the set of $\{20, 24, 32, 40, 48, 56\}$ grid points. For a fixed initial grain diameter ($\bar{D}_0 \approx 15$), the required number of grains were randomly distributed over the domain through a Voronoi tessellation.

Fig. 11.3(a) represent three types of grains: those at no contact with top and bottom free surfaces (IG), those at touch with at least one free surface (EG) and those at contact with both free surfaces (BG). When an individual grain grows, the local neighbor cluster may accommodate a mixed fraction of IG, EG and BG grains. The conversion from IG-EG-BG has an implicit constituent, which corresponds to their complex topological and geometrical characteristics during evolution. The growth kinetics of grains contacting at free surfaces are more complicated than for an inner grains. Hence, one may expect that the growth evolution does not simply follow the power law kinetics.

The microstructural evolution of $h = 40$ setup shown in Fig. 11.3(b). The initial polycrystalline network comprises of grains which exhibit a different fraction of IG, EG and BG grains. Besides isotropic thermodynamical driving condition, the free boundaries might influence the growth kinetics of grains at the top and bottom surfaces. Throughout the evolution, the number of grains of each group (IG, EG, BG) decreases. At large enough time, a substantial number of columnar grains ($CG \approx EG + BG$) appear to have consumed inner grains. Eventually, all the grains transformed into a BG at the end. There was no stagnation observed even for longer simulation times. Thus, there were always some topologically dominated grains could consume neighboring grains and growth proceed.

The rate at which IG-EG-BG conversion determines the global kinetics of grain coarsening in thin films. To understand the evolution, the magnified region from the simulation domain examined in detail. When the contact between the local neighboring grains exaggerated for better visualization, the individual grain morphologies clearly distinguished in Fig. 11.3(c). However, the above examination did not distinguish growth regimes. Further quantitative investigation of the relationship between the (IG, EG, BG) fraction and the nature of growth regimes demanded.

Mean grain size progressively increased with time for all the simulations. For example, the results of ($h = 40$) discussed in this section. There were three different transient growth regimes observed in Fig. 11.4(a). The initial grain growth regime ($I$) begun within the first few time steps and followed by the regime ($II$ & $III$). The corresponding relative fractions of EG, BG, and CG grains were also plotted as a function of time in Fig. 11.4(b). These results imply that grain diameter progressed with increasing time, but the differing rate for different regimes. The computed growth rate values found to vary approximately one order of magnitude from 0.002914 for regime $I$, 0.0022973 for
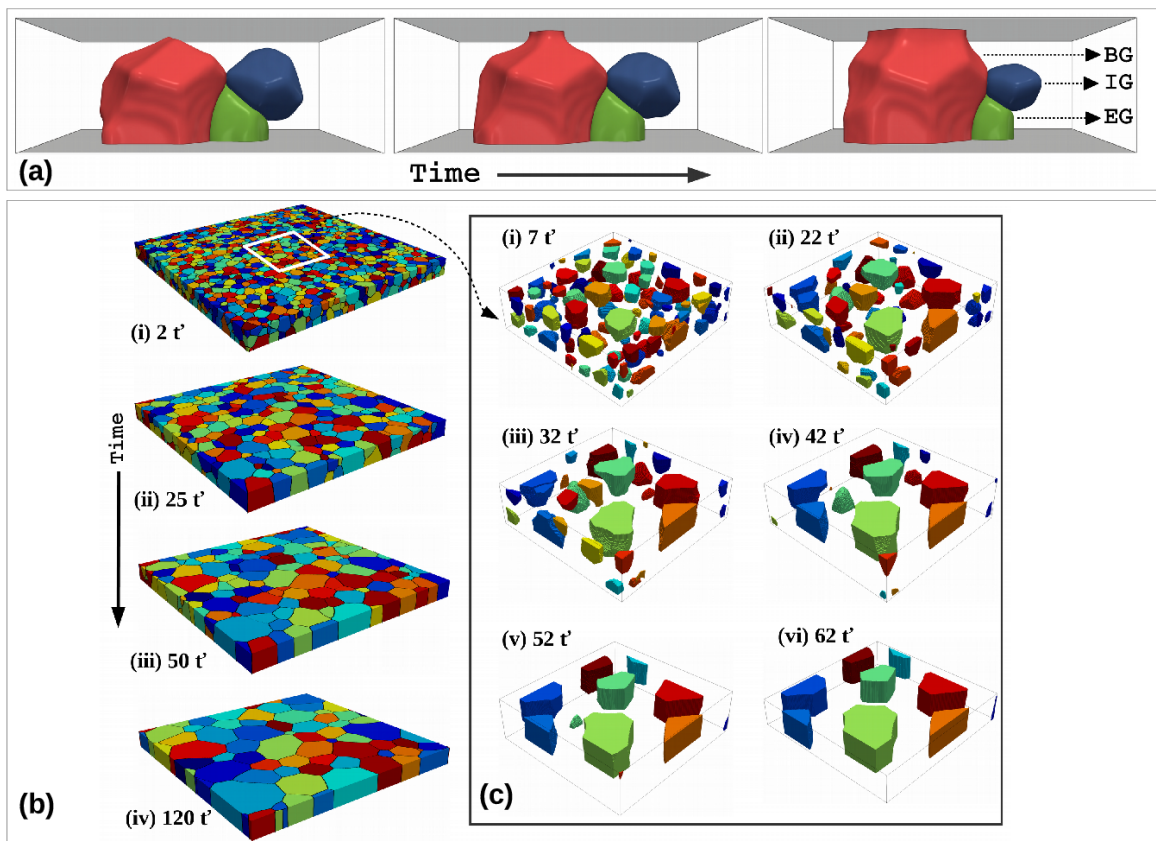
Figure 11.3: Microstructural evolution in 3-D system. (a) Representation of BG = Bamboo grains, IG = Inner grains and EG = Edge grains (b) temporal evolution of $h = 40$ where $\acute{t} = t \times 1000\Delta t$ (c) The kinetics of bamboo grain formation on an enlarged scale.
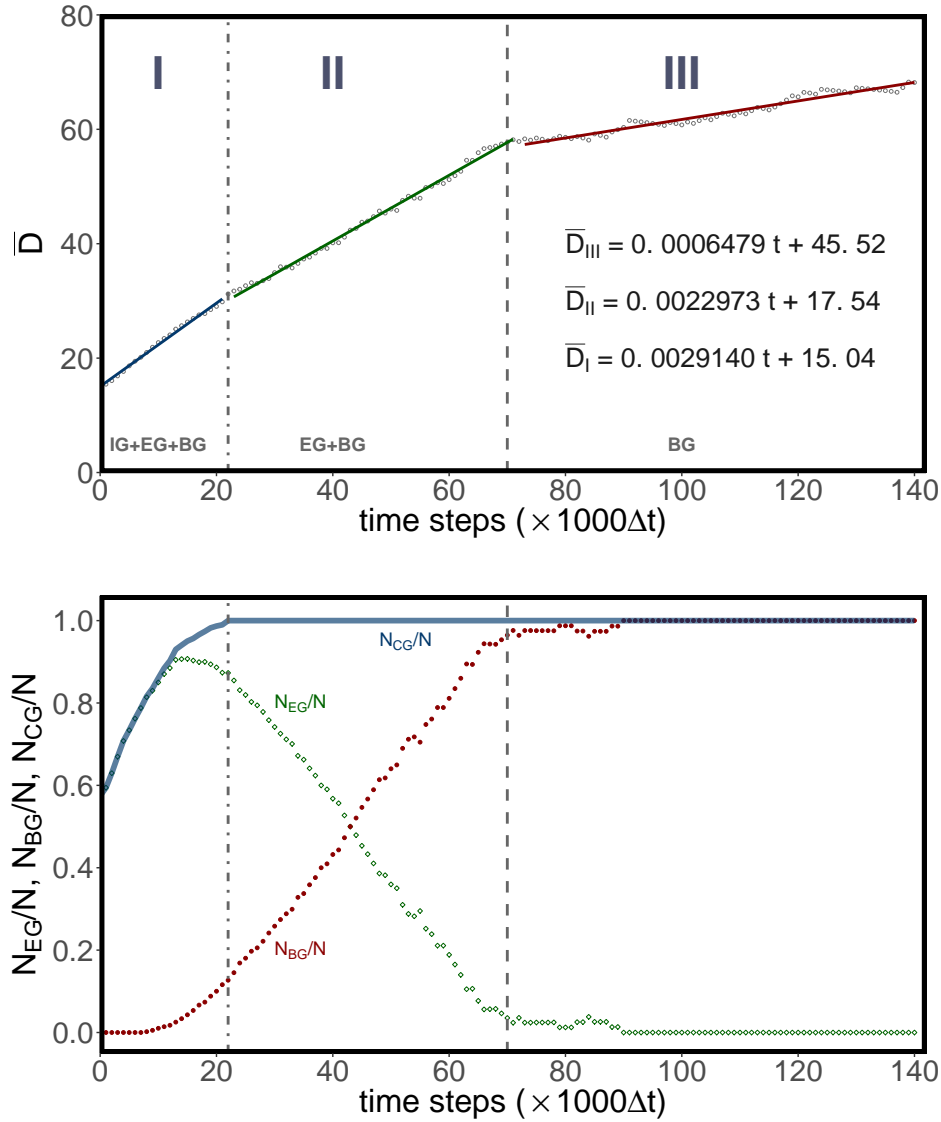
*Figure 11.4: (a) Mean grain size evolution (b) Relative fraction of IG, EG and BG grains.*

regime $II$ and 0.0006579 for regime $III$.

This suggests that the initial growth regime typically controlled by the inner grains transformation kinetics. However, at later times, the columnar grains ($CG$) are largely present, since the grain growth slows down. This may also indicate that free surfaces act as a drag on attached moving boundaries at later times. Similar grain growth regimes also reported in recent 3-D thin-film MC study [232]. Zöllner et al. proposed that the sluggish bamboo grain structure would be reached when the drag forces substantially induced by free surfaces. Our results also developed comparable explanation based on a consideration of a clear distinction between IG, EG, and BG grains. Since the topological transformation of these grains is expected to behave differently, their influence on growth regimes is currently not understood and needs further investigation.
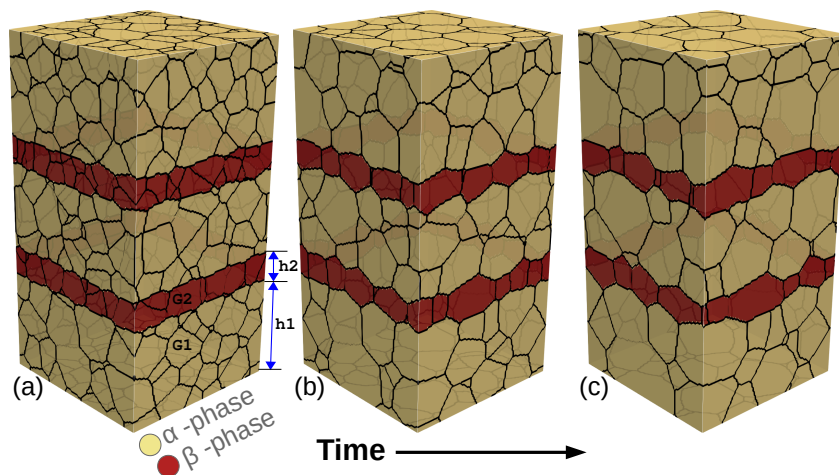
*Figure 11.5: Temporal evolution of the 3-D polycrystalline multilayer microstructures. h1: α layer thickness, h2: β layer thickness, G1: α grain size and G2: β grain size. Columnar grain structures and zig-zag morphology can be seen during evolution.*

Thermal stability of polycrystalline thin films have wide practical significance, yet underlying grain growth mechanism is not fully understood. Multi-phase-field model is adopted to simulate this complex 3-D microstructural evolutions.

## 11.2.3    Thermal stability of multilayers

Thin film metallic multilayers have been used in various applications, such as electronics, and magnetic storage media as hard protective coatings. This system should resist grain coarsening and break-down (pinch-off) at high temperature operating conditions. Multilayer film stability has been broadly investigated both experimentally and by using numerical models. However, little is known regarding the specific process parameters that optimize the complex microstructural features in systems. Most of the previous simulation studies have been concentrated on the 2-D representation of real 3-D systems. However, to fundamentally understand the physical mechanism, the large scale 3-D simulations are required. In addition, we need to explore factors such as grain boundary energy, interface free energy, grain size, and layer thickness, that control the stability of these films. Therefore, our future work addresses the issue of the thermal response of a multilayer system via detailed 3-D microstructural studies.

Preliminary 3-dimensional simulation of domain size $400 \times 200 \times 200$ grid-points with the binary two-phase system and yet, similar parameters are used in chapter 8 is shown in 11.5. A detailed polycrystalline multilayer study considering both geometrical and topological evolution of the grains and their mutual interactions of each layer will proceed in the prospective work. We believe that our model is more general and can be directly applied to the thin film, multilayer, wire, and foam coarsening studies.

# Bibliography

[1] R. Perumal, P. K. Amos, M. Selzer, and B. Nestler. Phase-field study on the formation of first-neighbour topological clusters during the isotropic grain growth. *Comput. Mater. Sci*, 140:209–223, 2017.

[2] R. Perumal, P. K. Amos, M. Selzer, and B. Nestler. Phase-field study of the transient phenomena induced by 'abnormally' large grains during 2-dimensional isotropic grain growth. *Comput. Mater. Sci*, 147:227–237, 2018.

[3] R. Perumal, M. Selzer, and B. Nestler. Concurrent grain growth and coarsening of two-phase microstructures; large scale phase-field study. *Comput. Mater. Sci*, 159:160–176, 2019.

[4] T. Takayama, M. Y. Wey, and T. Nishizawa. Grain growth in dual-phase steel. *Tetsu-to-Hagané*, 68(8):1016–1023, 1982.

[5] M. Abe, A. Hiura, K. Ishida, and T. Nishizawa. Grain growth in duplex stainless steels. *Tetsu-to-Hagané*, 70(15):2025–2032, 1984.

[6] R. DeHoff. Engineering of microstructures. *Mater. Res.*, 2(3):111–126, 1999.

[7] M. Knyazeva and M. Pohl. Duplex steels: Part I: genesis, formation, structure. *Metallography, Microstructure, and Analysis*, 2(2):113–121, 2013.

[8] J. Zhao and Z. Jiang. Thermomechanical processing of advanced high strength steels. *Prog. Mater Sci.*, 94:174–242, 2018.

[9] F. Humphreys. A unified theory of recovery, recrystallization and grain growth, based on the stability and growth of cellular microstructuresi. the basic model. *Acta Mater.*, 45(10):4231–4240, 1997.

[10] T. Hayashi, P. Sarosi, J. H. Schneibel, and M. J. Mills. Creep response and deformation processes in nanocluster-strengthened ferritic steels. *Acta Mater.*, 56(7):1407–1416, 2008.

[11] P. W. Voorhees. Ostwald ripening of two-phase mixtures. *Annu. Rev. Mater. Sci.*, 22(1):197–215, 1992.

[12] C. Zener. Private communication to CS Smith. *Trans. AIME*, 175(15):ll, 1949.

[13] N. Haroun and D. Budworth. Modifications to the Zener formula for limitation of grain size. *J. Mater. Sci.*, 3(3):326–328, 1968.

[14] G. Meetham. High-temperature materials – a general review. *J. Mater. Sci.*, 26(4):853–860, 1991.

[15] A. Ullah, G. Liu, J. Luan, W. Li, M. ur Rahman, and M. Ali. Three-dimensional visualization and quantitative characterization of grains in polycrystalline iron. *Mater. Charact.*, 91:65–75, 2014.

[16] J. Sun, A. Lyckegaard, Y. Zhang, S. Catherine, B. Patterson, F. Bachmann, N. Gueninchault, H. Bale, C. Holzner, E. Lauridsen, et al. 4D study of grain growth in armco iron using laboratory X-ray diffraction contrast tomography. In *IOP Conf. Ser.: Mater. Sci. Eng.*, volume 219, page 012039. IOP Publishing, 2017.

[17] C. Zhang, M. Enomoto, A. Suzuki, and T. Ishimaru. Characterization of three-dimensional grain structure in polycrystalline iron by serial sectioning. *Metall. Mater. Trans. A*, 35(7):1927–1933, 2004.

[18] J. Zhang, Y. Zhang, W. Ludwig, D. Rowenhorst, P. W. Voorhees, and H. F. Poulsen. Three-dimensional grain growth in pure iron. Part I. statistics on the grain level. *Acta Mater.*, 156:76–85, 2018.

[19] A. Bhattacharya, Y.-F. Shen, C. M. Hefferan, S. F. Li, J. Lind, R. M. Suter, and G. S. Rohrer. Three-dimensional observations of grain volume changes during annealing of polycrystalline Ni. *Acta Mater.*, 167:40–50, 2019.

[20] M. Hillert. On the theory of normal and abnormal grain growth. *Acta Metall.*, 13(3):227–238, 1965.

[21] W. Mullins. On idealized two dimensional grain growth. *Scr. Metall.*, 22(9):1441–1444, 1988.

[22] N. Louat. On the theory of normal grain growth. *Acta Metall.*, 22(6):721–724, 1974.

[23] P. Rios and D. Zöllner. Critical assessment 30: Grain growth–unresolved issues. *Mater. Sci. Technol.*, 34(6):629–638, 2018.

[24] C. Thompson, H. Frost, and F. Spaepen. The relative rates of secondary and normal grain growth. *Acta Metall.*, 35(4):887–890, 1987.

[25] K. Lücke, R. Brandt, and G. Abbruzzese. Normal and abnormal grain growth as transient phenomena. *Interface Sci.*, 6(1):67–76, 1998.

[26] M. Anderson, G. Grest, and D. Srolovitz. Computer simulation of normal grain growth in three dimensions. *Philos. Mag. B*, 59(3):293–329, 1989.

[27] D. Srolovitz, G. Grest, and M. Anderson. Computer simulation of grain growth-V. Abnormal grain growth. *Acta Metall.*, 33(12):2233–2247, 1985.

[28] N. M. Hwang. Simulation of the effect of anisotropic grain boundary mobility and energy on abnormal grain growth. *J. Mater. Sci.*, 33(23):5625–5629, 1998.

[29] H. Atkinson. Overview no. 65: Theories of normal grain growth in pure single phase systems. *Acta Metall.*, 36(3):469–491, 1988.

[30] E. A. Holm and S. M. Foiles. How grain growth stops: A mechanism for grain-growth stagnation in pure materials. *Science*, 328(5982):1138–1141, 2010.

[31] V. Yadav and N. Moelans. Analysis of grain topology and volumetric growth rate relation in three-dimensional normal grain growth. *Acta Mater.*, 156:275–286, 2018.

[32] S. Okita, E. Miyoshi, S. Sakane, T. Takaki, M. Ohno, and Y. Shibuta. Grain growth kinetics in submicrometer-scale molecular dynamics simulation. *Acta Mater.*, 153:108–116, 2018.

[33] Y. Sun, G. Liu, and C. Wang. On the grain size distributions obtained from different grain growth simulation techniques. *J. Mater. Sci.*, 39(7):2553–2556, 2004.

[34] M. F. Vaz and M. Fortes. Grain size distribution: The lognormal and the gamma distribution functions. *Scr. Metall.*, 22(1):35–40, 1988.

[35] R. B. Bergmann, F. G. Shi, H. J. Queisser, and J. Krinke. Formation of polycrystalline silicon with log-normal grain size distribution. *Appl. Surf. Sci.*, 123:376–380, 1998.

[36] C. Pande and G. McFadden. Self-similar grain size distribution in three dimensions: A stochastic treatment. *Acta Mater.*, 58(3):1037–1044, 2010.

[37] D. Zöllner and P. Streitenberger. Three-dimensional normal grain growth: Monte carlo potts model simulation and analytical mean field theory. *Scr. Mater.*, 54(9):1697–1702, 2006.

[38] J. Burke and D. Turnbull. Recrystallization and grain growth. *Prog. Met. Phys.*, 3:220–292, 1952.

[39] N. A. Haroun. Theory of inclusion controlled grain growth. *J. Mater. Sci.*, 15(11):2816–2822, 1980.

[40] D.-K. Kim and W. M. Kriven. Processing and characterization of multiphase ceramic composites Part II: Triplex composites with a wide sintering temperature range. *J. Am. Ceram. Soc.*, 91(3):793–798, 2008.

[41] E. Levine, I. Greenhut, and H. Margolin. Grain size and grain growth in an equiaxed alpha-beta titanium alloy. *Metall. Trans.*, 4(11):2519–2525, 1973.

[42] P. W. Voorhees. The theory of Ostwald ripening. *J. Stat. Phys.*, 38(1-2):231–252, 1985.

[43] I. M. Lifshitz and V. V. Slyozov. The kinetics of precipitation from supersaturated solid solutions. *J. Phys. Chem. Solids*, 19(1-2):35–50, 1961.

[44] C. Wagner. Theorie der alterung von niederschlägen durch umlösen (Ostwald-reifung). *Z. Elektrochem.*, 65(7-8):581–591, 1961.

[45] A. Ardell. The effect of volume fraction on particle coarsening: theoretical considerations. *Acta Metall.*, 20(1):61–71, 1972.

[46] C. Davies, P. Nash, and R. N. Stevens. The effect of volume fraction of precipitate on Ostwald ripening. *Acta Metall.*, 28(2):179–189, 1980.

[47] H. Calderon, P. Voorhees, J. Murray, and G. Kostorz. Ostwald ripening in concentrated alloys. *Acta Metall. Mater.*, 42(3):991–1000, 1994.

[48] S. Semiatin, B. Kirby, and G. Salishchev. Coarsening behavior of an alpha-beta titanium alloy. *Metall. Mater. Trans. A*, 35(9):2809–2819, 2004.

[49] C. S. Smith. Grains, phases, and interfaces: An introduction of microstructure. *Trans. Metall. Soc. AIME*, 175:15–51, 1948.

[50] R. Doherty, D. Srolovitz, A. Rollett, and M. Anderson. On the volume fraction dependence of particle limited grain growth. *Scr. Metall.*, 21(5), 1987.

[51] M. PA, M. Ferry, and T. Chandra. Five decades of the Zener equation. *ISIJ Int.*, 38(9):913–924, 1998.

[52] N. Moelans, B. Blanpain, and P. Wollants. A phase field model for the simulation of grain growth in materials containing finely dispersed incoherent second-phase particles. *Acta Mater.*, 53(6):1771–1781, 2005.

[53] Y. Liu and B. Patterson. Stereological analysis of Zener pinning. *Acta Mater.*, 44(11):4327–4335, 1996.

[54] D. Srolovitz, M. P. Anderson, P. S. Sahni, and G. S. Grest. Computer simulation of grain growthII. grain size distribution, topology, and local dynamics. *Acta Metall.*, 32(5):793–802, 1984.

[55] G. N. Hassold, E. A. Holm, and D. J. Srolovitz. Effects of particle size on inhibited grain growth. *Scr. Metall. Mater.*, (24):101, 1990.

[56] I.-W. Chen and L. A. Xue. Development of superplastic structural ceramics. *J. Am. Ceram. Soc.*, 73(9):2585–2609, 1990.

[57] Y. Suwa, Y. Saito, and H. Onodera. Phase field simulation of grain growth in three dimensional system containing finely dispersed second-phase particles. *Scr. Mater.*, 55(4):407–410, 2006.

[58] L. Vanherpe, N. Moelans, B. Blanpain, and S. Vandewalle. Bounding box algorithm for three-dimensional phase-field simulations of microstructural evolution in polycrystalline materials. *Phys. Rev. E*, 76(5):056702, 2007.

[59] G. Grewal and S. Ankem. Modeling matrix grain growth in the presence of growing second phase particles in two phase alloys. *Acta Metall. Mater.*, 38(9):1607–1617, 1990.

[60] T. Zhou, A. Gheribi, and H. Zurob. Austenite particle coarsening and delta-ferrite grain growth in model Fe–Al alloy. *Can. Metall. Q.*, 52(1):90–97, 2013.

[61] D. Fan and L.-Q. Chen. Computer simulation of grain growth using a continuum field model. *Acta Mater.*, 45(2):611–622, 1997.

[62] R. J. El-Khozondar and H. J. El-Khozondar. Numerical modeling of microstructural evolution in three-phase polycrystalline materials. *Arab. J. Sci. Eng.*, 34(1A), 2009.

[63] H. Ravash, J. Vleugels, and N. Moelans. Three-dimensional phase-field simulation of microstructural evolution in three-phase materials with different diffusivities. *J. Mater. Sci.*, 49(20):7066–7072, 2014.

[64] P. Palmero, V. Naglieri, G. Spina, and M. Lombardi. Microstructural design and elaboration of multiphase ultra-fine ceramics. *Ceram. Int.*, 37(1):139–144, 2011.

[65] R. P. Dillon, D.-K. Kim, J. E. Trujillo, W. M. Kriven, and M. L. Mecartney. Creep characteristics of alumina, nickel aluminate spinel, zirconia composites. *J. Mater. Res.*, 23(2):556–564, 2008.

[66] C. Oelgardt, J. Anderson, J. Heinrich, and G. Messing. Sintering, microstructure and mechanical properties of Al2O3–Y2O3–ZrO2 (AYZ) eutectic composition ceramic microcomposites. *J. Eur. Ceram. Soc.*, 30(3):649–656, 2010.

[67] B.-N. Kim, K. Hiraga, K. Morita, and Y. Sakka. A high-strain-rate superplastic ceramic. *Nature*, 413(6853):288, 2001.

[68] C. M. Hoo, D. Men, L. Taherabadi, and M. L. Mecartney. Grain-boundary sliding in a superplastic three-phase alumina–zirconia–mullite ceramic composite. *J. Am. Ceram. Soc.*, 94(7):2171–2180, 2011.

[69] Y. Zhang, T. T. Zuo, Z. Tang, M. C. Gao, K. A. Dahmen, P. K. Liaw, and Z. P. Lu. Microstructures and properties of high-entropy alloys. *Prog. Mater Sci.*, 61:1–93, 2014.

[70] F. Otto, Y. Yang, H. Bei, and E. P. George. Relative effects of enthalpy and entropy on the phase stability of equiatomic high-entropy alloys. *Acta Mater.*, 61(7):2628–2638, 2013.

[71] F. Otto, A. Dlouhỳ, K. G. Pradeep, M. Kuběnová, D. Raabe, G. Eggeler, and E. P. George. Decomposition of the single-phase high-entropy alloy CrMnFeCoNi after prolonged anneals at intermediate temperatures. *Acta Mater.*, 112:40–52, 2016.

[72] T. Chookajorn, H. A. Murdoch, and C. A. Schuh. Design of stable nanocrystalline alloys. *Science*, 337(6097):951–954, 2012.

[73] S. Praveen, J. Basu, S. Kashyap, and R. S. Kottada. Exceptional resistance to grain growth in nanocrystalline CoCrFeNi high entropy alloy at high homologous temperatures. *J. Alloys Compd.*, 662:361–367, 2016.

[74] P. Feltham. Grain growth in metals. *Acta Metall.*, 5(2):97–105, 1957.

[75] M. Hillert. Comments on grain growth. *Scr. Metall.*, 22(7):1035–1036, 1988.

[76] A. Rollett, F. Humphreys, G. Rohrer, and M. Hatherly. *Recrystallization and Related Annealing Phenomena*. Elsevier, Oxford, 2004.

[77] M. Anderson, D. Srolovitz, G. Grest, and P. Sahni. Computer simulation of grain growth -I. Kinetics. *Acta Metall.*, 32(5):783–791, 1984.

[78] F. Wakai, N. Enomoto, and H. Ogawa. Three-dimensional microstructural evolution in ideal grain growthgeneral statistics. *Acta Mater.*, 48(6):1297–1311, 2000.

[79] D. Weygand, Y. Brechet, and J. Lepinoux. A vertex simulation of grain growth in 2D and 3D. *Adv. Eng. Mater.*, 3(1-2):67–71, 2001.

[80] C. Krill Iii and L.-Q. Chen. Computer simulation of 3-D grain growth using a phase-field model. *Acta Mater.*, 50(12):3059–3075, 2002.

[81] S. Raghavan and S. S. Sahay. Modeling the grain growth kinetics by cellular automaton. *Mater. Sci. Eng., A*, 445:203–209, 2007.

[82] W. Fayad, C. Thompson, and H. Frost. Steady-state grain-size distributions resulting from grain growth in two dimensions. *Scr. Mater.*, 40(10):1199–1204, 1999.

[83] M. Elsey, S. Esedoglu, and P. Smereka. Large-scale simulation of normal grain growth via diffusion-generated motion. *Proc. Roy. Soc., A*, 467(2126):381–401, 2011.

[84] I. McKenna, S. Poulsen, E. M. Lauridsen, W. Ludwig, and P. Voorhees. Grain growth in four dimensions: A comparison between simulation and experiment. *Acta Mater.*, 78:125–134, 2014.

[85] J. K. Mason, E. A. Lazar, R. D. MacPherson, and D. J. Srolovitz. Geometric and topological properties of the canonical grain-growth microstructure. *Phys. Rev. E*, 92(6):063308, 2015.

[86] L. B. Mora. 2D vertex modeling for the simulation of grain growth and related phenomena. *Math. Comput. Simul.*, 80(7):1411–1427, 2010.

[87] J. Mason, E. Lazar, R. MacPherson, and D. J. Srolovitz. Statistical topology of cellular networks in two and three dimensions. *Phys. Rev. E*, 86(5):051128, 2012.

[88] K. Janssens. An introductory review of cellular automata modeling of moving grain boundaries in polycrystalline materials. *Math. Comput. Simul.*, 80(7):1361–1381, 2010.

[89] D. Fan and L.-Q. Chen. Diffusion-controlled grain growth in two-phase solids. *Acta Mater.*, 45(8):3297–3310, 1997.

[90] N. Moelans, F. Wendler, and B. Nestler. Comparative study of two phase-field models for grain growth. *Comput. Mater. Sci*, 46(2):479–490, 2009.

[91] A. Vondrous, M. Reichardt, and B. Nestler. Growth rate distributions for regular two-dimensional grains with Read–Shockley grain boundary energy. *Modell. Simul. Mater. Sci. Eng.*, 22(2):025014, 2014.

[92] H. Garcke, B. Nestler, and B. Stoth. A multiphase field concept: numerical simulations of moving phase boundaries and multiple junctions. *SIAM J. Appl. Math.*, 60(1):295–315, 1999.

[93] H. Emmerich. *The diffuse interface approach in materials science: thermodynamic concepts and applications of phase-field models.* Lecture Notes in Physics, Springer, Heidelberg, 2003.

[94] A. Kazaryan, Y. Wang, S. Dregia, and B. R. Patton. Generalized phase-field model for computer simulation of grain growth in anisotropic systems. *Phys. Rev. B*, 61(21):14275, 2000.

[95] A. Kazaryan, Y. Wang, S. Dregia, and B. Patton. Grain growth in anisotropic systems: comparison of effects of energy and mobility. *Acta Mater.*, 50(10):2491–2502, 2002.

[96] N. Provatas and K. Elder. *Phase-field methods in materials science and engineering.* Wiley, Weinheim, 2010.

[97] G. Caginalp. An analysis of a phase field model of a free boundary. *Arch. Ration. Mech. Anal.*, 92(3):205–245, 1986.

[98] Y. Suwa and Y. Saito. Computer simulation of grain growth in three dimensions by the phase field model and the Monte Carlo method. *Mater. Trans.*, 46(6):1214–1220, 2005.

[99] B. Nestler, H. Garcke, and B. Stinner. Multicomponent alloy solidification: phase-field modeling and simulations. *Phys. Rev. E*, 71(4):041609, 2005.

[100] H. Garcke, B. Stoth, and B. Nestler. Anisotropy in multi-phase systems: a phase field approach. *Interface Free Bound.*, 1(2):175–198, 1999.

[101] Y. Oono and S. Puri. Study of phase-separation dynamics by use of cell dynamical systems. I. Modeling. *Phys. Rev. A*, 38(1):434, 1988.

[102] I. Steinbach, B. Böttger, J. Eiken, N. Warnken, and S. Fries. CALPHAD and phase-field modeling: a successful liaison. *J. Phase. Equilib. Diff.*, 28(1):101–106, 2007.

[103] N. Moelans, B. Blanpain, and P. Wollants. An introduction to phase-field modeling of microstructure evolution. *Calphad*, 32(2):268–294, 2008.

[104] A. Choudhury and B. Nestler. Grand-potential formulation for multicomponent phase transformations combined with thin-interface asymptotics of the double-obstacle potential. *Phys. Rev. E*, 85(2):021602, 2012.

[105] D. Molnar, R. Mukherjee, A. Choudhury, A. Mora, P. Binkele, M. Selzer, B. Nestler, and S. Schmauder. Multiscale simulations on the coarsening of Cu-rich precipitates in $\alpha$-Fe using kinetic Monte Carlo, molecular dynamics and phase-field simulations. *Acta Mater.*, 60(20):6961–6971, 2012.

[106] R. Mukherjee, A. Choudhury, and B. Nestler. Composition pathway in Fe–Cu–Ni alloy during coarsening. *Modell. Simul. Mater. Sci. Eng.*, 21(7):075012, 2013.

[107] J. Hötzer, A. Reiter, H. Hierl, P. Steinmetz, M. Selzer, and B. Nestler. The parallel multi-physics phase-field framework Pace3D. *J. Comput. Sci.*, 26:1–12, 2018.

[108] P. R. Rios and M. E. Glicksman. Topological and metrical aspects of normal and abnormal grain growth. *Mater. Res.*, 10(4):371–375, 2007.

[109] P. Rios and M. Glicksman. Polyhedral model for self-similar grain growth. *Acta Mater.*, 56(5):1165–1171, 2008.

[110] S. Hilgenfeldt, A. Kraynik, D. Reinelt, and J. Sullivan. The structure of foam cells: Isotropic plateau polyhedra. *Europhys. Lett.*, 67(3):484, 2004.

[111] M. Glicksman. Analysis of 3-D network structures. *Philos. Mag.*, 85(1):3–31, 2005.

[112] E. A. Lazar, J. K. Mason, R. D. MacPherson, and D. J. Srolovitz. Complete topology of cells, grains, and bubbles in three-dimensional microstructures. *Phys. Rev. Lett.*, 109(9):095505, 2012.

[113] H. Wang, G. Liu, A. Ullah, and J. Luan. Topological correlations of three-dimensional grains. *Appl. Phys. Lett.*, 101(4):041910, 2012.

[114] J. Luan, G. Liu, H. Wang, and A. Ullah. A note on grain topology-size relationship of three-dimensional polycrystalline microstructures. *Europhys. Lett.*, 99(2):28001, 2012.

[115] W. Li, G. Liu, H. Wang, H. Zhang, J. Luan, and A. Ullah. Topological correlations of grain faces in polycrystal with experimental verification. *Europhys. Lett.*, 104(5):56006, 2014.

[116] D. Aboav. The arrangement of grains in a polycrystal. *Metallography*, 3(4):383–390, 1970.

[117] D. Weaire. Some remarks on the arrangement of grains in a polycrystal. *Metallography*, 7(2):157–160, 1974.

[118] J. Von Neumann. Metal interfaces. *American Society for Metals, Cleveland*, 108, 1952.

[119] W. W. Mullins. Two-dimensional motion of idealized grain boundaries. *J. Appl. Phys.*, 27(8):900–904, 1956.

[120] R. D. MacPherson and D. J. Srolovitz. The von neumann relation generalized to coarsening of three-dimensional microstructures. *Nature*, 446(7139):1053–1055, 2007.

[121] H. Wang, G. Liu, X. Song, and J. Luan. Topology-dependent description of grain growth. *Europhys. Lett.*, 96(3):38003, 2011.

[122] F. Wakai, Y. Shinoda, S. Ishihara, and A. Domínguez-Rodríguez. Topological transformation of grains in three-dimensional normal grain growth. *J. Mater. Res.*, 16(07):2136–2142, 2001.

[123] R. D. Kamachali and I. Steinbach. 3-D phase-field simulation of grain growth: topological analysis versus mean-field approximations. *Acta Mater.*, 60(6):2719–2728, 2012.

[124] R Core Team. *R: A Language and Environment for Statistical Computing.* R Foundation for Statistical Computing, Vienna, Austria, 2017.

[125] Z. Sun, V. Tikare, B. R. Patterson, and A. P. Sprague. Topological characterization of microstructures from 3D digitized voxel data. *Comput. Mater. Sci*, 55:329–336, 2012.

[126] B. R. Patterson, D. J. Rowenhorst, V. Tikare, R. DeHoff, and T. M. Kaub. Affinities for topological arrangements in grain structures. *Acta Mater.*, 79:411–420, 2014.

[127] C. Wang, G. Liu, G. Wang, and W. Xue. Three-dimensional grain size distribution: Comparison of an analytical form under a topology-related rate equation with computer simulations and experimental data. *Mater. Sci. Eng., A*, 454:547–551, 2007.

[128] D. Rowenhorst, A. Lewis, and G. Spanos. Three-dimensional analysis of grain topology and interface curvature in a $\beta$-titanium alloy. *Acta Mater.*, 58(16):5511–5519, 2010.

[129] M. Elsey, S. Esedoglu, and P. Smereka. Large-scale simulation of normal grain growth via diffusion-generated motion. *Proc. Roy. Soc., A*, 467(2126):381–401, 2011.

[130] S. Edwards and K. Pithia. A note on the Aboav-Weaire law. *Physica A*, 205(4):577–584, 1994.

[131] F. Wakai, Y. Shinoda, S. Ishihara, and A. Domínguez-rodríguez. Statistics of grain disappearance in three-dimensional normal grain growth. *Philos. Mag. B*, 81(5):517–524, 2001.

[132] H. Wang and G. Liu. Evaluation of growth rate equations of three-dimensional grains using large-scale monte carlo simulation. *Appl. Phys. Lett.*, 93(13):131902, 2008.

[133] G. Liu, H. Yu, X. Song, and X. Qin. A new model of three-dimensional grain growth: theory and computer simulation of topology-dependency of individual grain growth rate. *Mater. Des.*, 22(1):33–38, 2001.

[134] J. A. Glazier. Grain growth in three dimensions depends on grain topology. *Phys. Rev. Lett.*, 70(14):2170, 1993.

[135] D. Kinderlehrer. Mathematical physics: Added dimensions to grain growth. *Nature*, 446(7139):995–996, 2007.

[136] W. Mullins. Estimation of the geometrical rate constant in idealized three dimensional grain growth. *Acta Metall.*, 37(11):2979–2984, 1989.

[137] J. A. Glazier, S. P. Gross, and J. Stavans. Dynamics of two-dimensional soap froths. *Phys. Rev. A*, 36(1):306, 1987.

[138] L. B. Mora, G. Gottstein, and L. Shvindlerman. Three-dimensional grain growth: Analytical approaches and computer simulations. *Acta Mater.*, 56(20):5915–5926, 2008.

[139] A. P. Sprague, B. R. Patterson, and S. Grandhi. Topological characteristics of two-dimensional grain growth-simulation and analysis. *Metall. Mater. Trans. A*, 41(3):592–602, 2010.

[140] D. Aboav. The topology of a polycrystal in three dimensions. In *Mater. Sci. Forum*, volume 94, pages 275–280. Trans Tech Publ, 1992.

[141] N. Rivier. On the structure of random tissues or froths, and their evolution. *Philos. Mag. B*, 47(5):L45–L49, 1983.

[142] L. Meng, H. Wang, G. Liu, and Y. Chen. Study on topological properties in two-dimensional grain networks via large-scale Monte Carlo simulation. *Comput. Mater. Sci*, 103:165–169, 2015.

[143] P. Rios, T. Dalpian, V. Brandao, J. Castro, and A. Oliveira. Comparison of analytical grain size distributions with three-dimensional computer simulations and experimental data. *Scr. Mater.*, 54(9):1633–1637, 2006.

[144] J. Gao, M. Wei, L. Zhang, Y. Du, Z. Liu, and B. Huang. Effect of different initial structures on the simulation of microstructure evolution during normal grain growth via phase-field modeling. *Metall. Mater. Trans. A*, 49(12):6442–6456, 2018.

[145] C. Wang, G. Liu, and X. Qin. Effect of the initial grain size distribution on the process of grain growth. *J. Mater. Sci. Lett.*, 22(6):473–475, 2003.

[146] V. Yadav and N. Moelans. Investigation on the existence of a Hillert regime in normal grain growth. *Scr. Mater.*, 142:148–152, 2018.

[147] M. Nordbakke, N. Ryum, and O. Hunderi. The correlation theory of 2D normal grain growth. In *Mater. Sci. Forum*, volume 467, pages 1081–1086. Trans Tech Publ, 2004.

[148] O. Hunderi and N. Ryum. The influence of spatial grain size correlation on normal grain growth in one dimension. *Acta Mater.*, 44(4):1673–1680, 1996.

[149] K. Marthinsen, O. Hunderi, and N. Ryum. The influence of spatial grain size correlation and topology on normal grain growth in two dimensions. *Acta Mater.*, 44(4):1681–1689, 1996.

[150] D. Aboav. The arrangement of cells in a net. *Metallography*, 13(1):43–58, 1980.

[151] D. Wealire and J. Kermode. Computer simulation of a two-dimensional soap froth II. Analysis of results. *Philos. Mag. B*, 50(3):379–395, 1984.

[152] J. Von Neumann. Discussion: Shape of metal grains. *Metal Interfaces*, page 108, 1952.

[153] S. Hilgenfeldt, A. M. Kraynik, S. A. Koehler, and H. A. Stone. An accurate von Neumann's law for three-dimensional foams. *Phys. Rev. Lett.*, 86(12):2685, 2001.

[154] B. Nestler, F. Wendler, M. Selzer, B. Stinner, and H. Garcke. Phase-field model for multiphase systems with preserved volume fractions. *Phys. Rev. E*, 78(1):011604, 2008.

[155] M. Selzer. *Mechanische und strömungsmechanische topologieoptimierung mit der phasenfeldmethode*. PhD thesis, KIT, Karlsruhe, 2014.

[156] S. Vedantam and B. Patnaik. Efficient numerical algorithm for multiphase field simulations. *Phys. Rev. E*, 73(1):016703, 2006.

[157] A. Vondrous, P. Bienger, S. Schreijäg, M. Selzer, D. Schneider, B. Nestler, D. Helm, and R. Mönig. Combined crystal plasticity and phase-field method for recrystallization in a process chain of sheet metal production. *Comput. Mech.*, 55(2):439–452, 2015.

[158] W. Mullins and J. Vinals. Self-similarity and growth kinetics driven by surface free energy reduction. *Acta Metall.*, 37(4):991–997, 1989.

[159] P. Rios. Irreversible thermodynamics, parabolic law and self-similar state in grain growth. *Acta Mater.*, 52(1):249–256, 2004.

[160] M. Nordbakke, N. Ryum, and O. Hunderi. Invariant distributions and stationary correlation functions of simulated grain growth processes. *Acta Mater.*, 50(14):3661–3670, 2002.

[161] M. Nordbakke, N. Ryum, and O. Hunderi. Curvilinear polygons, finite circle packings, and normal grain growth. *Mater. Sci. Eng., A*, 385(1-2):229–234, 2004.

[162] D. Weygand. *Simulation numérique de la croissance de grains*. PhD thesis, Grenoble INPG, 1998.

[163] J. Stavans. The evolution of cellular structures. *Rep. Prog. Phys.*, 56(6):733, 1993.

[164] W. Mullins. Grain growth of uniform boundaries with scaling. *Acta Mater.*, 46(17):6219–6226, 1998.

[165] E. Schüle. A justification of the Hillert distribution by spatial grain growth simulation performed by modifications of Laguerre tessellations. *Comput. Mater. Sci*, 5(4):277–285, 1996.

[166] S. Kurtz and F. Carpay. Microstructure and normal grain growth in metals and ceramics. Part I. Theory. *J. Appl. Phys.*, 51(11):5725–5744, 1980.

[167] E. Miyoshi, T. Takaki, M. Ohno, Y. Shibuta, S. Sakane, T. Shimokawabe, and T. Aoki. Ultra-large-scale phase-field simulation study of ideal grain growth. *npj Comput. Mater.*, 3(1):25, 2017.

[168] C. Pande. On a stochastic theory of grain growth. *Acta Metall.*, 35(11):2671–2678, 1987.

[169] S. Chiu. Aboav-Weaire's and Lewis' laws–A review. *Mater. Charact.*, 34(2):149–165, 1995.

[170] H. Wang, G.-q. Liu, and X.-g. Qin. Grain size distribution and topology in 3D grain growth simulation with large-scale monte carlo method. *Int. J. Min. Met. Mater.*, 16(1):37–42, 2009.

[171] H. Wang, G. Liu, Y. Chen, and W. Li. Verification of a generalized Aboav-Weaire law via experiment and large-scale simulation. *Europhys. Lett.*, 105(6):68001, 2014.

[172] D. Zöllner, P. Streitenberger, and P. Rios. Shedding some light on the early grain growth regime: About the effect of the initial microstructure on normal grain growth. *Comput. Mater. Sci*, 113:11–20, 2016.

[173] J. Burke. Some factors affecting the rate of grain growth in metals. *Trans. Am. Inst. Min. Engrs*, pages 73–91, 1949.

[174] W. Mullins. The statistical self-similarity hypothesis in grain growth and particle coarsening. *J. Appl. Phys.*, 59(4):1341–1349, 1986.

[175] M. Ames, J. Markmann, R. Karos, A. Michels, A. Tschöpe, and R. Birringer. Unraveling the nature of room temperature grain growth in nanocrystalline materials. *Acta Mater.*, 56(16):4255–4266, 2008.

[176] V. Snyder, J. Alkemper, and P. Voorhees. Transient Ostwald ripening and the disagreement between steady-state coarsening theory and experiment. *Acta Mater.*, 49(4):699–709, 2001.

[177] R. Brandt, W. Graupner, and K. Luecke. Normal and abnormal grain growth and particularly the behaviour of large and small grains as predicted by simulations on the basis of the statistical model. In *Mater. Sci. Forum*, volume 204, pages 295–302. Trans Tech Publ, 1996.

[178] W. Benson and J. Wert. The effect of initial grain size distribution on abnormal grain growth in single-phase materials. *Acta Mater.*, 46(15):5323–5333, 1998.

[179] N. Chen, S. Zaefferer, L. Lahn, K. Günther, and D. Raabe. Effects of topology on abnormal grain growth in silicon steel. *Acta Mater.*, 51(6):1755–1765, 2003.

[180] J. Cabrera, A. Al Omar, and J. Prado. Abnormal grain growth in a medium-carbon microalloyed steel. *J. Mater. Sci.*, 31(5):1303–1309, 1996.

[181] S. Lee, D. Yoon, and M. Henry. Abnormal grain growth and grain boundary faceting in a model Ni-base superalloy. *Acta Mater.*, 48(12):3071–3080, 2000.

[182] V. Oliveira, H. Sandim, and D. Raabe. Abnormal grain growth in Eurofer-97 steel in the ferrite phase field. *J. Nucl. Mater.*, 485:23–38, 2017.

[183] J. Gruber, N. Ma, Y. Wang, A. D. Rollett, and G. S. Rohrer. Sparse data structure and algorithm for the phase field method. *Modell. Simul. Mater. Sci. Eng.*, 14(7):1189, 2006.

[184] F. Aurenhammer. Voronoi diagramsa survey of a fundamental geometric data structure. *ACM Comput. Surv.*, 23(3):345–405, 1991.

[185] I. Andersen, Ø. Grong, and N. Ryum. Analytical modelling of grain growth in metals and alloys in the presence of growing and dissolving precipitatesii. abnormal grain growth. *Acta Metall. Mater.*, 43(7):2689–2700, 1995.

[186] R. Messina, M. Soucail, and L. Kubin. Monte carlo simulation of abnormal grain growth in two dimensions. *Mater. Sci. Eng., A*, 308(1):258–267, 2001.

[187] V. Y. Novikov. Origin of microstructure instability in nanocrystalline materials. *Mater. Lett.*, 116:268–270, 2014.

[188] P. Rios. Abnormal grain growth in pure materials. *Acta Metall. Mater.*, 40(10):2765–2768, 1992.

[189] P. Rios. Abnormal growth and abnormal coarsening with a quasi-stationary distribution. *Mater. Sci. Eng., A*, 165(1):L5–L8, 1993.

[190] S. Ankem and H. Margolin. Grain growth relationships in two-phase titanium alloys. *Proc. 5th Int. Conf. on Titanium, Vol. 3, Deutsche Gesellsschaft*, page 1705, 1984.

[191] G. Grewal and S. Ikem. Particle coarsening behavior of $\alpha$-$\beta$ titanium alloys. *Metall. Trans. A*, 21(6):1645–1654, 1990.

[192] H. Ravash, J. Vleugels, and N. Moelans. Three-dimensional phase-field simulation of microstructural evolution in three-phase materials with different interfacial energies and different diffusivities. *J. Mater. Sci.*, 52(24):13852–13867, 2017.

[193] K. Chang, L.-Q. Chen, C. E. Krill, and N. Moelans. Effect of strong nonuniformity in grain boundary energy on 3-D grain growth behavior: A phase-field simulation study. *Comput. Mater. Sci*, 127:67–77, 2017.

[194] V. Yadav, L. Vanherpe, and N. Moelans. Effect of volume fractions on microstructure evolution in isotropic volume-conserved two-phase alloys: A phase-field study. *Comput. Mater. Sci*, 125:297–308, 2016.

[195] C. Hsueh, A. Evans, and R. Coble. Microstructure development during final/intermediate stage sintering −I. Pore/grain boundary separation. *Acta Metall.*, 30(7):1269–1279, 1982.

[196] D. R. Clarke. Interpenetrating phase composites. *J. Am. Ceram. Soc.*, 75(4):739–758, 1992.

[197] E. Holm, D. J. Srolovitz, and J. Cahn. Microstructural evolution in two-dimensional two-phase polycrystals. *Acta Metall. Mater.*, 41(4):1119–1136, 1993.

[198] K. B. Alexander, P. F. Becher, S. B. Waters, and A. Bleier. Grain growth kinetics in alumina–zirconia (CeZTA) composites. *J. Am. Ceram. Soc.*, 77(4):939–946, 1994.

[199] S. O. Poulsen, P. Voorhees, and E. M. Lauridsen. Three-dimensional simulations of microstructural evolution in polycrystalline dual-phase materials with constant volume fractions. *Acta Mater.*, 61(4):1220–1228, 2013.

[200] K. Okada, Y.-i. Yoshizawa, and T. Sakuma. Grain-Size Distribution in Al2O3 ZrO2 Generated by High-Temperature Annealing. *J. Am. Ceram. Soc.*, 74(11):2820–2823, 1991.

[201] K. Okada and T. Sakuma. The role of Zener's pinning effect on the grain growth in Al2O3-ZrO2. *J. Ceram. Soc. Jpn.*, 100(1160):382–386, 1992.

[202] B. K. Kad and P. M. Hazzledine. Monte carlo simulations of grain growth and Zener pinning. *Mater. Sci. Eng., A*, 238(1):70–77, 1997.

[203] V. Fradkov, M. Glicksman, M. Palmer, J. Nordberg, and K. Rajan. Topological rearrangements during 2D normal grain growth. *Physica D*, 66(1-2):50–60, 1993.

[204] F. Lange and M. M. Hirlinger. Hindrance of Grain Growth in Al2O3 by ZrO2 Inclusions. *J. Am. Ceram. Soc.*, 67(3):164–168, 1984.

[205] I. Ohnuma, K. Ishida, and T. Nishizawa. Computer simulation of grain growth in dual-phase structures. *Philos. Mag. A*, 79(5):1131–1144, 1999.

[206] J. Wilde and A. Greer. A new thermally stable structural duplex Ni–TaC nanocomposite. *Mater. Sci. Eng., A*, 304:932–936, 2001.

[207] J. Cahn. Stability, microstructural evolution, grain growth, and coarsening in a two-dimensional two-phase microstructure. *Acta Metall. Mater.*, 39(10):2189–2199, 1991.

[208] M. Fortes. Stability and dissociation of quadruple junctions in polycrystals. *Interface Sci.*, 1(2):147–155, 1993.

[209] K. Tsumuraya and Y. Miyata. Coarsening models incorporating both diffusion geometry and volume fraction of particles. *Acta Metall.*, 31(3):437–452, 1983.

[210] K. Banerjee, M. Militzer, M. Perez, and X. Wang. Nonisothermal austenite grain growth kinetics in a microalloyed X80 linepipe steel. *Metall. Mater. Trans. A*, 41(12):3161–3172, 2010.

[211] D. Empl, L. Felberbaum, V. Laporte, D. Chatain, and A. Mortensen. Dihedral angles in Cu–1 wt.% Pb: Grain boundary energy and grain boundary triple line effects. *Acta Mater.*, 57(8):2527–2537, 2009.

[212] J. D. French, J. Zhao, M. P. Harmer, H. M. Chan, and G. A. Miller. Creep of duplex microstructures. *J. Am. Ceram. Soc.*, 77(11):2857–2865, 1994.

[213] M. P. Harmer, H. M. Chan, and G. A. Miller. Unique opportunities for microstructural engineering with duplex and laminar ceramic composites. *J. Am. Ceram. Soc.*, 75(7):1715–1728, 1992.

[214] F. Najafkhani, H. Mirzadeh, and M. Zamani. Effect of Intercritical Annealing Conditions on Grain Growth Kinetics of Dual Phase Steel. *Met. Mater. Int.*, 25:1039–46, 2019.

[215] J. M. Rickman. Data analytics and parallel-coordinate materials property charts. *npj Comput. Mater.*, 4(1):5, 2018.

[216] H. Hu and B. Rath. On the time exponent in isothermal grain growth. *Metall. Trans.*, 1(11):3181–3184, 1970.

[217] J. A. Wert, N. Paton, C. Hamilton, and M. Mahoney. Grain refinement in 7075 aluminum by thermomechanical processing. *Metall. Trans. A*, 12(7):1267–1276, 1981.

[218] I. Weiss and S. Semiatin. Thermomechanical processing of beta titanium alloys–an overview. *Mater. Sci. Eng., A*, 243(1-2):46–65, 1998.

[219] G. Wang, D. Xu, E. Payton, N. Ma, R. Yang, M. Mills, and Y. Wang. Mean-field statistical simulation of grain coarsening in the presence of stable and unstable pinning particles. *Acta Mater.*, 59(11):4587–4594, 2011.

[220] M. Calcagnotto, D. Ponge, and D. Raabe. Effect of grain refinement to 1 $\mu$m on strength and toughness of dual-phase steels. *Mater. Sci. Eng., A*, 527(29-30):7832–7840, 2010.

[221] R. W. Rice, C. C. Wu, and F. Boichelt. Hardness–grain-size relations in ceramics. *J. Am. Ceram. Soc.*, 77(10):2539–2553, 1994.

[222] B. S. Murty, J.-W. Yeh, S. Ranganathan, and P. Bhattacharjee. *High-entropy alloys*. Elsevier, Amsterdam, 2019.

[223] D. B. Miracle and O. N. Senkov. A critical review of high entropy alloys and related concepts. *Acta Mater.*, 122:448–511, 2017.

[224] N. Moelans, B. Blanpain, and P. Wollants. Quantitative analysis of grain boundary properties in a generalized phase field model for grain growth in anisotropic systems. *Phys. Rev. B*, 78(2):024113, 2008.

[225] R. D. Kamachali, S.-J. Kim, and I. Steinbach. Texture evolution in deformed AZ31 magnesium sheets: Experiments and phase-field study. *Comput. Mater. Sci*, 104:193–199, 2015.

[226] C. Kuehmann and P. W. Voorhees. Ostwald ripening in ternary alloys. *Metall. Mater. Trans. A*, 27(4):937–943, 1996.

[227] C. Wang and G. Liu. On the stability of grain structure with initial weibull grain size distribution. *Mater. Lett.*, 57(28):4424–4428, 2003.

[228] Y.-C. Joo and C. V. Thompson. Analytic model for the grain structures of near-bamboo interconnects. *J. Appl. Phys.*, 76(11):7339–7346, 1994.

[229] M. Fortest, M. Emlia Rosa, S. Findlay, and M. Guedes. Development of bamboo structure in a foam: the kinetics of foam coarsening. *Philos. Mag. A*, 77(1):257–265, 1998.

[230] M. Rosa and M. Fortes. Development of bamboo structure in a 2D liquid foam. *Europhys. Lett.*, 41(5):577, 1998.

[231] D. Walton, H. Frost, and C. Thompson. Development of near-bamboo and bamboo microstructures in thin-film strips. *Appl. Phys. Lett.*, 61(1):40–42, 1992.

[232] D. Zöllner. Treating grain growth in thin films in three dimensions: a simulation study. *Comput. Mater. Sci*, 125:51–60, 2016.

[233] V. Sebag, A. Roth, and D. Durian. Final bubble lengths for aqueous foam coarsened in a horizontal cylinder. *Philos. Mag.*, 91(34):4357–4366, 2011.

[234] C. V. Thompson. Grain growth in thin films. *Annu. Rev. Mater. Sci.*, 20(1):245–268, 1990.

[235] W. W. Mullins. Theory of thermal grooving. *J. Appl. Phys.*, 28(3):333–339, 1957.

[236] H. Frost, C. Thompson, and D. Walton. Simulation of thin film grain structuresi. grain growth stagnation. *Acta Metall. Mater.*, 38(8):1455–1462, 1990.

[237] V. Y. Novikov. Simulation of grain growth in thin films with columnar microstructure. *Acta Mater.*, 47(18):4507–4514, 1999.

[238] J. S. Lee, B.-J. Lee, Y. M. Koo, and S. G. Kim. 3D simulations of grain growth in polycrystalline sheets and rods: Effects of free surface and shape of specimen. *Scr. Mater.*, 110:113–116, 2016.

[239] Z. An, H. Ding, Q. Meng, and Y. Rong. Kinetic equation of the effect of thickness on grain growth in nanocrystalline films. *Scr. Mater.*, 61(11):1012–1015, 2009.

[240] V. Y. Novikov. Abnormal grain growth in thin films not caused by decreased energy of their free surface. *Mater. Lett.*, 65(17-18):2618–2620, 2011.

[241] R. Dannenberg, E. Stach, J. Groza, and B. Dresser. In-situ TEM observations of abnormal grain growth, coarsening, and substrate de-wetting in nanocrystalline Ag thin films. *Thin Solid Films*, 370(1-2):54–62, 2000.

[242] P. Rios. Abnormal grain growth development from uniform grain size distributions. *Acta Mater.*, 45(4):1785–1789, 1997.

# Part VI
# Appendices

# Appendix A

# Heatmap description

Statistical understanding of huge data sets are often enhanced by appropriate tools [124]. Owing to the magnitude of data, the present computational study employs the tool 'heat-map', is adopted through the open-source statistical programming language R to provide a unique and meaningful description of the resulting data. The efficiency of this tool relies largely on the organization of the data and thus, the data sets are organized in form of matrices before incorporating heat-maps. The selection of appropriate quantities for the rows and columns of the matrix adds definite characteristics to the heat-map depiction. For the objectives of this work, the face-class of the selected grain and its surrounding grains are considered along the rows and columns, respectively. For primary understanding, raw data set, without any re-ordering of the rows or columns, is represented as heat-maps by assigning colors to the matrices based on their magnitude. In R, this is achieved by the package *gplots* in which most prominent color palettes are pre-defined. In keeping with the similar statistical studies, *blue-red* color scheme is used all through the current study. This scheme assigns blue to the low values, white to the intermediate and red to the high values. Apart from providing a distinction between the values (matrices), *blue-red* scheme innately distinguishes three regimes.

Elementary maps of this study reveal an apparent pattern which in a conventional case requires the re-ordering of rows or columns. This unique behavior is attributed to the inherent distribution of grains. To further deepen our understanding on the temporal behavior of the first neighbors, the rows of the matrices are re-ordered leaving the columns intact. Numerous techniques potentially render this re-ordering or 'clustering ' and in this work, two of the most effective techniques are employed.

'k-mean clustering' based on the partitioning technique is exclusively involved for the initial assessment of the data. In this preliminary assessment, the feasibility of clustering is ensured by 'Hopkins statistical method' of calculating the spatial randomness, $H$ by

$$H = \frac{\sum_{i=1}^{n} y_i}{\sum_{i=1}^{n} x_i + \sum_{i=1}^{n} y_i}. \tag{A.1}$$

211
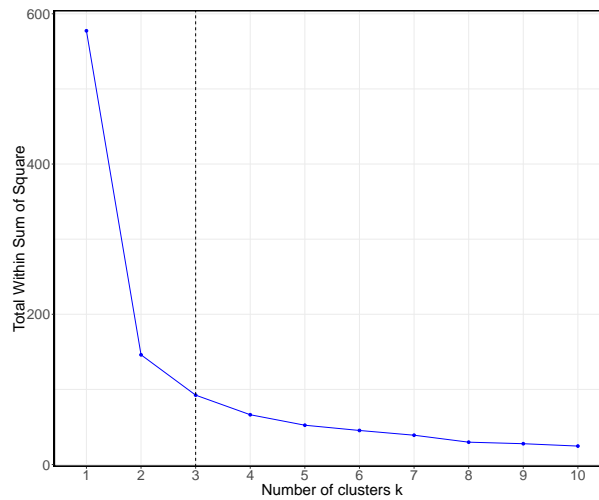
*Figure A.1: Degree of information lost due to the clustering with the change in the number of clusters considered. A significant bend is observed around 3, followed by an almost constant slope of the curve.*

Where, $x$ and $y$ are two vectors of length n. The spatial randomness, $H$ must be below 0.5 for efficient clustering, and $H \approx 0.2$ for the present data-set evidently favors re-ordering. This approach is instituted in R by applying *hopkins()* function in the *clustertend* package.

Furthermore, re-ordering in 'k-mean clustering' is achieved by emphasizing the differences within a cluster. Although, the clustering in the present study is not performed by this technique, an optimum number of clusters is ascertained by it. *within-cluster variation*, $W(C_k)$ for a given cluster $C_k$ is defined as

$$W(C_k) = \frac{1}{n_k} \sum_{x_i \in C_k} \sum_{x_j \in C_k} (x_i - x_j)^2 = \sum_{x_i \in C_k} (x_i - \mu_k)^2 \tag{A.2}$$

where $x_i$ and $\mu_k$ are the data-points and mean value of the points in cluster, $C_k$ respectively. Change in the *within-cluster variation*, $W(C_k)$ with increase in number of clusters is plotted in Fig.A.1. For the present data, an optimum number of clusters is chosen to be 3 by 'Elbow method' which ascertains the optimum number by considering the slope of the curve in Fig.A.1.

Owing to the size of the data, a 'hierarchical' approach is preferred for clustering. In this technique, data are clustered either by splitting the bigger cluster (*divisive clustering*) or grouping the smaller clusters, *agglomerative clustering*. Despite the identical efficiencies of both these approaches, 'bottom up', agglomerative clustering is adopted for this work. In a matrix of $n$ rows, this approach begins by considering each row as the cluster of 1. Now, the similarity between every pair of clusters (rows) is calculated in form of Euclidean distance. This distance, implying the similarity between two clusters ($\alpha$ and

$\beta$), is expressed as

$$d_{Euclidean}(x, y) = \sqrt{(x_1^\alpha - y_1^\beta)^2 + (x_2^\alpha - y_2^\beta)^2 + ... + (x_n^\alpha - y_n^\beta)^2} \qquad (A.3)$$

where $x_1^\alpha$ and $y_1^\beta$ are the first entries of cluster $\alpha$ and $\beta$, respectively, and $x_n^\alpha$ and $y_n^\beta$, the last entries of the clusters. While the distance 0 denotes the identical entries, the larger difference is captured by the greater distance. Pair of rows with least distance are re-order and placed together forming a cluster of 2, which reduces the total number of clusters to $m - 1$. Function $dist()$ facilitates this clustering approach in R.

Following the pair-wise clustering of rows, the resulting larger clusters are merged through the process of agglomeration. In order to achieve this agglomeration, the information is compromised to a certain extent. *Ward method*, a statistically substantial approach for agglomeration, re-orders the clusters by ensuring the least degree of information loss. In this approach, the information loss is calculated as the *Error Sum of Squares (ESS)*

$$minESS, ESS = \sum_{\alpha=1}^{n} \left( \sum_{i=1}^{n_\alpha} x_i^2 - \frac{1}{n_\alpha} \left( \sum_{i=1}^{n_\alpha} x \right)^2 \right) \qquad (A.4)$$

where $\alpha$ and $n_\alpha$ refer to the cluster considered and the number of entries in it, respectively. $i$ is the location of the entry and $x_i$ is its corresponding value. ESS can hence be defined as the squared difference between an entry and the mean of its group. In contrast to most commonly used statistical methods, only the rows are re-ordered and the columns remain undisturbed. Consequently, the ESS calculation and the corresponding agglomeration deal exclusively with re-ordering the face-classes of the neighboring grains in regards to their number density. Determining the ESS enables the comparison of the different clusters, both large and small, and further agglomeration.

# Appendix B

# Statistical distribution functions

The inhomogeneities on the grain size (GSD) and grain topological distributions (GTD) are examined using the statistical data processing approaches. The required statistical quantities have been calculated by the following equations from the 2-D and 3-D simulated microstructures.

$$\bar{x} = (1/N) \sum x_i \tag{B.1}$$

$$\mu_r(x) = (1/N) \sum (x_i - \bar{x})^r \tag{B.2}$$

$$\sigma(x) = [\mu_2(x)]^{1/2} \tag{B.3}$$

$$CV_N(x) = \sigma(x)/\bar{x} \tag{B.4}$$

$$CS_N(x) = \mu_3(x)/\sigma^3 x \tag{B.5}$$

$$CE_N(x) = [\mu_4(x)/\sigma^4 x] - 3 \tag{B.6}$$

where, $x$ and $x_i$ can be considered as grain size $R$, or the face class parameter $f$ of selected individual grain. N is the total number of grains in the simulation domain at that particular time step. $\bar{x}$ is the arithmetic mean of $x$ and $\mu_r(x)$ is the $r^{th}$ central moment. $\sigma(x)$, $CV_N(x)$, $CS_N(x)$ and $CE_N(x)$ are standard deviation, the coefficient of variation, the skewness and the kurtosis of given distribution of x respectively.

# Appendix C

# Single pre-existing abnormal (PEA) grain in a matrix of fine grains

In order to interpret the differences in the growth rate of PEA and normal grains, in terms of change in mean grain size is exercised. Generally, the PEA grains in the selected microstructure are geometrically and topologically favorable for growth. Therefore, it is presumed that the absolute growth rate of the PEA grains is greater than the neighbor normal grains. In literature, it is found that the relative growth rate of the large grains is always negative for the isotropic single-phase systems [24, 27, 242]. However, in some special cases, the relative growth of the abnormal grains advances with the process parameters such as grain boundary energy and mobility.

The subsequent investigations are carried out with the single PEA grain in a matrix of fine grains. The study is accompanied over a range of initial PEA grain size ratios ($U_A = R_{ab}/R_c = \{2.5, 5, 10, 15\}$) in a domain of $1200 \times 1200$ with approximately 9000 grains. Although the PEA grain may grow faster than the normal grains due to their size bias, the isotropic grain boundary energies will lead to NGG. Fig. C.1 shows the visual inspection of $U_A = 5.0$ simulation at various time steps. The resultant microstructures indicate that the presence of PEA grain does not provoke an abnormal growth. During evolution, the PEA grain decreases in relative size and incorporated in the distribution of the normal grain. To support our hypothesis, the quantitative investigation of PEA and normal grains are carried out and validated with the available AGG analytical formulations. For all the relative size $U_A$ cases, the temporal evolution yield negative slope in Fig. C.2. This predicts that the PEA grain size will eventually reach the size of the normal grains for a prolonged annealing time.

Thompson et. al, studied the evolution of abnormal grains in a fine grain matrix and proposed complementary arguments that are valid for both 2-D and 3-D setups [24]. The
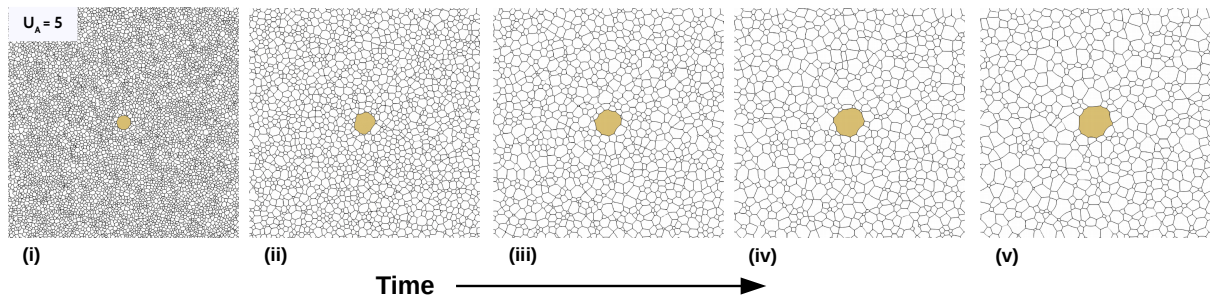
*Figure C.1: Temporal evolution of a microstructure in a presence of PEA grain with $U_A = 5$. Grain highlighted in yellow in microstructure indicates PEA grain.*
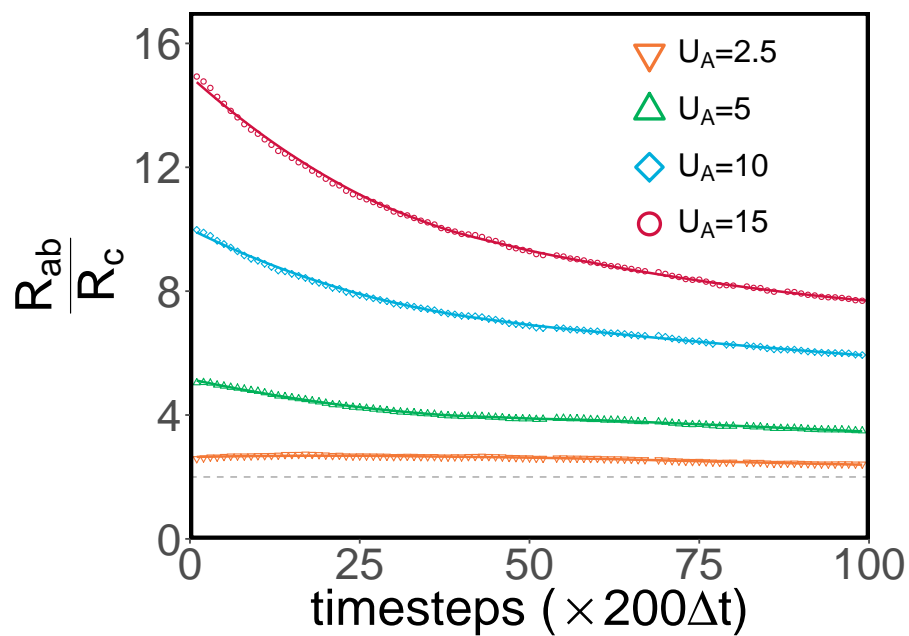


*Figure C.2: The time evolution of the different initial $U_A$ simulations. The decreasing slope indicates that size advantage of the PEA grain do not lead to AGG.*
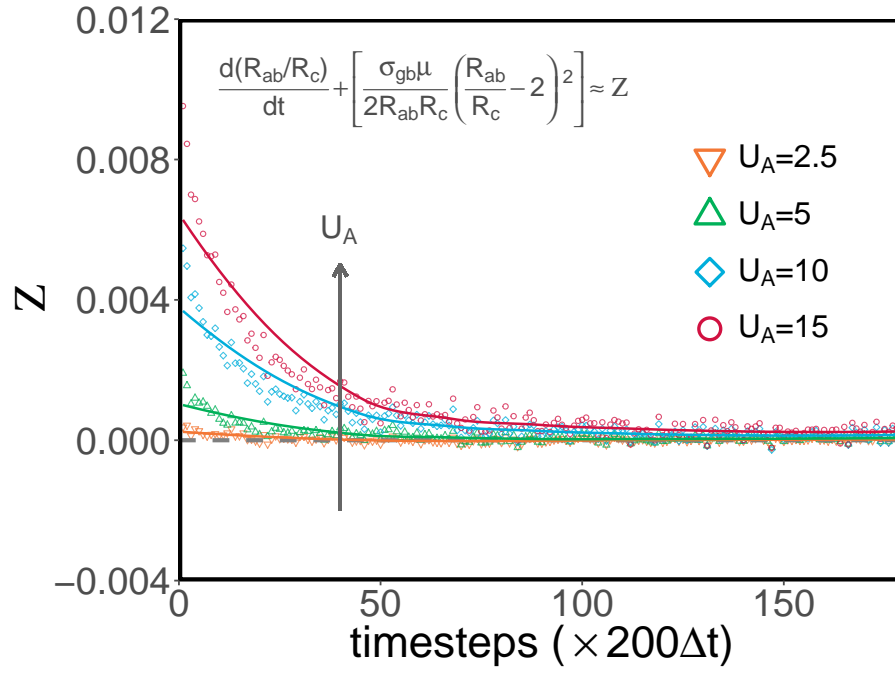
*Figure C.3:   The difference (Z) in analytical growth rate and the observed dataset as a function of $U_A$.   Simulation results indicate that the growth changes from abnormal to normal during evolution.*

analytical formulation for the relative growth rate of the PEA grains can be written as:

$$\frac{d}{dt}\left(\frac{\bar{R}_{ab}}{R_c}\right) = -\frac{\sigma_{gb}\mu}{2\bar{R}_{ab}R_c}\left(\frac{\bar{R}_{ab}}{R_c} - 2\right)^2, \tag{C.1}$$

where $\sigma_{gb}$ is the grain boundary energy and $\mu$ is the grain boundary mobility. This analysis establishes that the relative growth rate of abnormal grains does not outstrip the critical grain size. Our results are compared with the well-known growth equation of Eqn. C.1. Fig. C.3 represents the difference in the right and left-hand side of the equation as $Z$. The overall trend is that the faster drop during the initial period to reach the quasi-steady state in the microstructure, followed by a slower drop towards zero.

Although Thompson equation is based on classical Hillert' quasi-stationary grain size distribution conditions, the experimental grain size distributions generally demonstrate different functional form. Therefore, the relative growth rate of the PEA grain of relative size $U_A = R_{ab}/R_c$, can be generalized as [188]:

$$\frac{dU_A}{d\tau} = -(1/U_A)\Big[(U_A - U_1)(U_A - U_2)\Big], \tag{C.2}$$

$$U_1 = \frac{1 - (1 - 4\beta)^{1/2}}{2\beta}, \tag{C.3}$$

$$U_2 = \frac{1 - (1 + 4\beta)^{1/2}}{2\beta}, \tag{C.4}$$
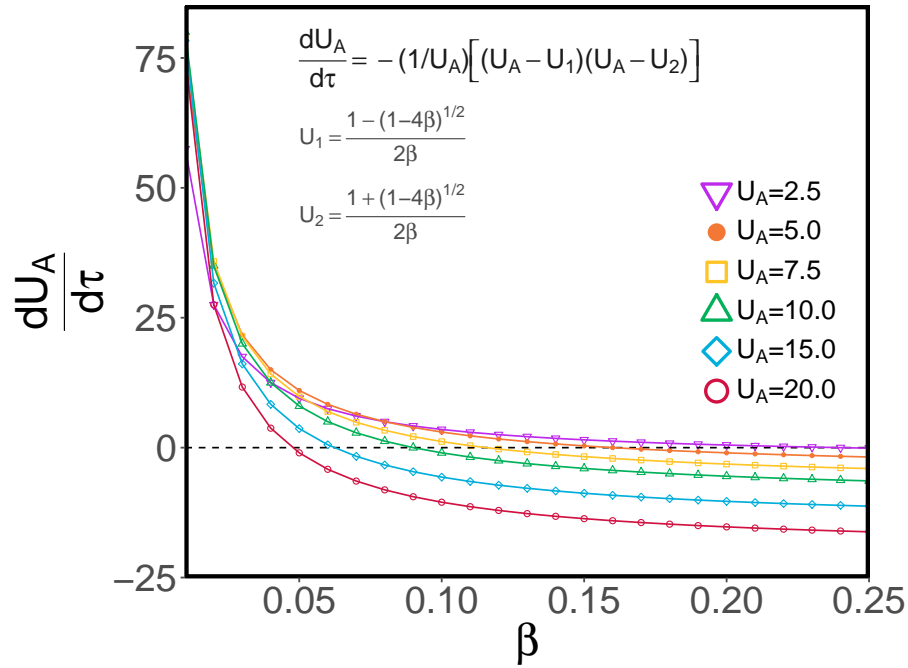
Figure C.4:  Effect of relative size ratio on the abnormal to normal transition.

where $\tau = ln(R_c)$, $Rc$ is equal to $\bar{R}$ for 2-D and $(9/8)\bar{R}$ for 3-D distributions. $\beta$ is a factor that depends on the grain size distribution.

$$\beta = \frac{1}{2\alpha\sigma\mu}\left(\frac{dR_c^2}{dt}\right), \tag{C.5}$$

The influence of $\beta$ in Eqn. C.2 is computed for different $U_A$ values and the Fig. C.4 displays the relative growth plot. It is interesting to note that our computed simulation data points are consistent with the theoretical models. Fig. C.5 proposes that the initial $U_A$ ratio hold a dominant role in the growth and the relative rate drop with time.

Fig. C.6 (a) shows the growth evolution of 3-dimensional PEA ($U_A = 3$) grain with roughly 5200 normal grains in a domain of $(200 \times 200 \times 200)$ size. The 2-dimensional cross-cut representation of 3-D domain is shown in Fig. C.6 (b) and the corresponding evolution microstructures are displayed. Similarly, the 2-D simulations are carried out with the starting microstructure of Fig. C.6 (b) (i) to understand the dimensionality effect during abnormal grain evolution. The grain structures were similar to those shown in Fig. C.6 (b) (i) and (c) (i). In the 3-D simulations, on the other hand, faster growth is occurred due to the curvature effect, although the decreasing relative growth rate appeared at the later period. The temporal evolution of the relative size ratio of both 3-D and 2-D simulations are shown in C.7.

The negative slope is perceived in Fig. C.7, which is consistent with what we observed in Fig. C.2. On the contrary, a higher volume fraction of PEA grain and the lesser number
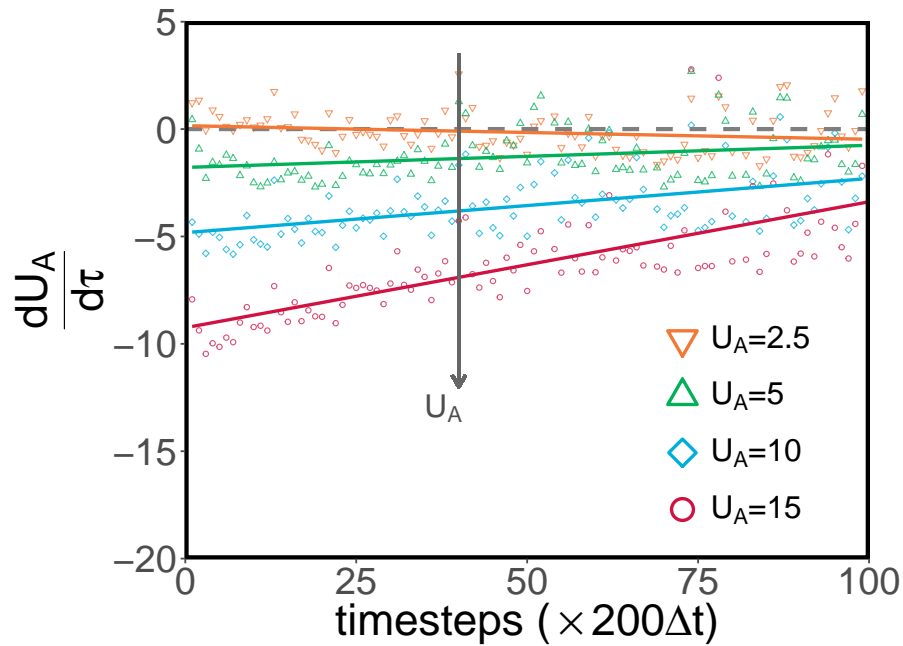
*Figure C.5:   Relative growth rate of PEA grains plot with respect to time. The observed results are consistent with the Eqn.C.2 growth behavior.*

of normal grains in a matrix causes the formation of abnormal grains and the occurrence of AGG in some systems. In addition, the dimensionality of the simulation domain plays a major role in the development of PEA grains in the microstructure. Nevertheless, if we assume that the domain is very big, the PEA grain does not substantially change the matrix microstructure and generally exhibit normal growth behavior.
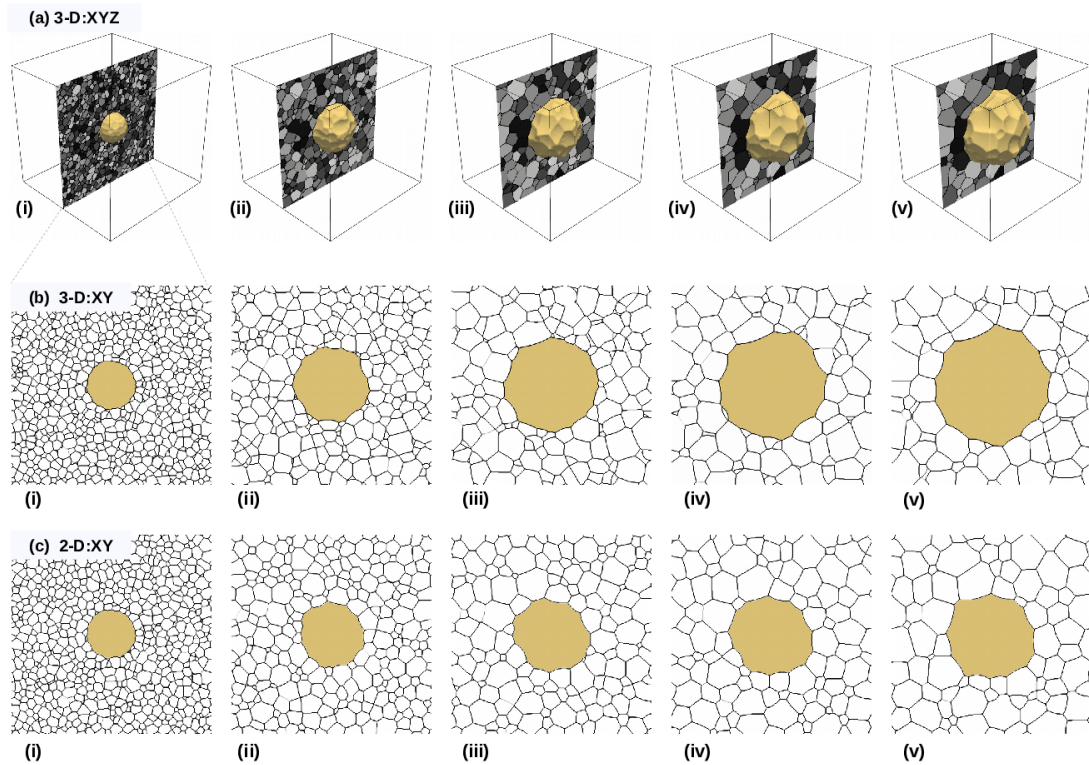
Figure C.6:   Temporal evolution of the single PEA grain $U_A \approx 5$ (a) 3-D simulation domain (XYZ) (b) 2-D representation of XY plane and (c) 2-D simulations of 3-D XY cut. Grain highlighted in yellow in microstructure indicates PEA grain.
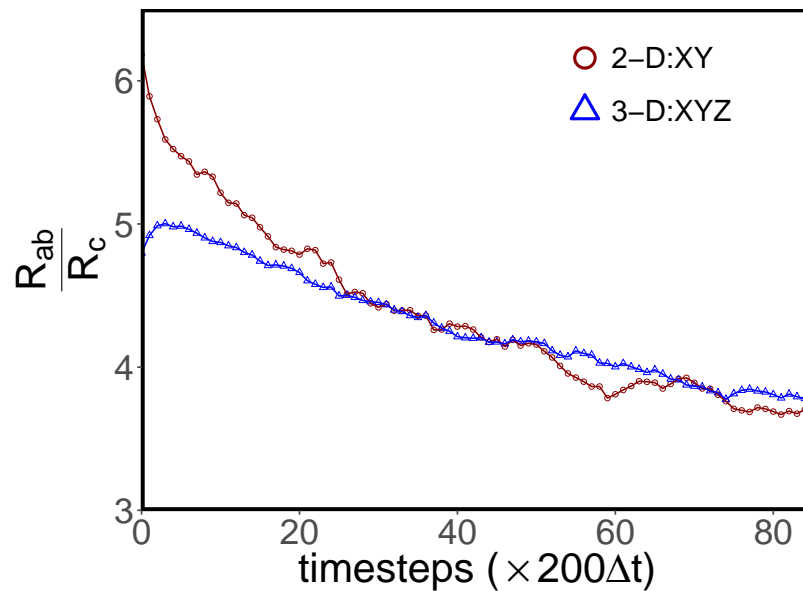


Figure C.7:   The relative growth rate of normal and abnormal grains in 2-D and 3-D setups. For the initial 2-D:XY setup, the PEA and normal grain size data is taken from the domain cut of 3-D:XYZ setup. Therefore, the initial $R_{ab}/R_c$ value do not match the initial ratio for the corresponding runs.

# Appendix D

# Abnormal grain growth simulation

## D.1    Pre-existing abnormal grains statistics

|    | $F_0$ | $\bar{U}_{max}$ | $R_c$ | $t_{F_{tp}}$ | $R_0$ | $d_{min}$ | $R_{str}$ | $PEA_{grains}$ | $Total_{grains}$ |
|----|--------|--------|--------|-----|-----|-----|-----|-----|--------|
| 1  | 0.0294 | 3.0641 | 8.2512 | 182 | 22 | 140 | 4  | 80  | 22723 |
| 2  | 0.0337 | 3.0871 | 8.2517 | 169 | 22 | 120 | 4  | 90  | 22709 |
| 3  | 0.0385 | 3.2429 | 7.3267 | 185 | 20 | 120 | 10 | 89  | 22665 |
| 4  | 0.0453 | 3.2663 | 7.3304 | 170 | 20 | 110 | 10 | 103 | 22568 |
| 5  | 0.0470 | 3.0701 | 7.3282 | 173 | 22 | 100 | 4  | 122 | 22579 |
| 6  | 0.0470 | 3.6776 | 7.3324 | 177 | 27 | 118 | 3  | 85  | 22476 |
| 7  | 0.0486 | 3.3003 | 7.3217 | 175 | 18 | 105 | 15 | 107 | 22542 |
| 8  | 0.0487 | 3.6566 | 8.2554 | 197 | 20 | 120 | 20 | 88  | 22339 |
| 9  | 0.0505 | 3.3813 | 7.3251 | 184 | 20 | 110 | 15 | 104 | 22479 |
| 10 | 0.0526 | 3.7368 | 7.3264 | 173 | 28 | 120 | 5  | 90  | 22360 |
| 11 | 0.0538 | 3.4360 | 8.2397 | 115 | 20 | 100 | 15 | 113 | 22392 |
| 12 | 0.0558 | 3.8805 | 7.3295 | 186 | 20 | 110 | 20 | 88  | 22341 |
| 13 | 0.0569 | 3.9202 | 7.3370 | 156 | 27 | 110 | 8  | 89  | 22256 |
| 14 | 0.0611 | 2.7081 | 8.2149 | 57  | 20 | 60  | 1  | 215 | 22591 |
| 15 | 0.0635 | 3.8632 | 8.2299 | 128 | 20 | 100 | 20 | 103 | 22264 |
| 16 | 0.0645 | 3.8886 | 7.3303 | 153 | 20 | 100 | 20 | 101 | 22218 |
| 17 | 0.0664 | 2.9336 | 8.2167 | 65  | 15 | 60  | 15 | 201 | 22425 |
| 18 | 0.0665 | 4.1090 | 8.2376 | 130 | 25 | 100 | 15 | 96  | 22172 |
| 19 | 0.0693 | 3.8442 | 8.2372 | 120 | 25 | 90  | 10 | 116 | 22152 |
| 20 | 0.0710 | 4.6452 | 8.2430 | 142 | 30 | 120 | 15 | 79  | 21991 |
| 21 | 0.0723 | 2.6120 | 8.1961 | 49  | 15 | 40  | 10 | 306 | 22452 |
| 22 | 0.0724 | 3.5990 | 8.2397 | 92  | 20 | 80  | 15 | 137 | 22136 |
| 23 | 0.0753 | 4.1462 | 8.2368 | 106 | 25 | 90  | 15 | 107 | 22015 |
| 24 | 0.0776 | 4.4446 | 7.3269 | 135 | 35 | 100 | 1  | 94  | 21938 |

| 25 | 0.0776 | 5.0755 | 7.3293 | 176 | 40 | 120 | 1 | 72 | 21871 |
| 26 | 0.0788 | 4.9937 | 7.3291 | 177 | 35 | 120 | 10 | 75 | 21863 |
| 27 | 0.0791 | 4.5586 | 7.3286 | 154 | 25 | 110 | 25 | 87 | 21881 |
| 28 | 0.0798 | 3.2348 | 8.2105 | 71 | 20 | 60 | 10 | 192 | 22247 |
| 29 | 0.0811 | 3.8253 | 8.2251 | 103 | 20 | 80 | 20 | 134 | 21989 |
| 30 | 0.0815 | 4.7668 | 8.2399 | 120 | 30 | 100 | 15 | 87 | 21839 |
| 31 | 0.0850 | 5.0957 | 7.3225 | 143 | 35 | 100 | 10 | 79 | 21786 |
| 32 | 0.0861 | 2.7396 | 8.1888 | 47 | 20 | 40 | 1 | 293 | 22457 |
| 33 | 0.0865 | 4.4216 | 8.2281 | 98 | 30 | 90 | 10 | 108 | 21856 |
| 34 | 0.0874 | 5.2026 | 7.3347 | 183 | 40 | 120 | 10 | 73 | 21642 |
| 35 | 0.0879 | 3.8462 | 8.2178 | 77 | 25 | 70 | 10 | 148 | 21965 |
| 36 | 0.0903 | 3.6153 | 8.2013 | 66 | 25 | 60 | 5 | 174 | 22084 |
| 37 | 0.0918 | 4.3043 | 8.2310 | 101 | 25 | 80 | 20 | 119 | 21712 |
| 38 | 0.0936 | 4.3317 | 8.2279 | 88 | 30 | 80 | 10 | 122 | 21714 |
| 39 | 0.0943 | 4.5668 | 7.3156 | 109 | 35 | 80 | 1 | 110 | 21714 |
| 40 | 0.0957 | 3.3534 | 8.2048 | 59 | 25 | 50 | 1 | 216 | 22068 |
| 41 | 0.1002 | 3.9469 | 7.3032 | 89 | 25 | 60 | 10 | 158 | 21808 |
| 42 | 0.1002 | 4.8703 | 8.2376 | 100 | 30 | 80 | 15 | 103 | 21557 |
| 43 | 0.1014 | 4.2743 | 7.3914 | 120 | 20 | 80 | 30 | 125 | 21174 |
| 44 | 0.1028 | 3.8889 | 7.3148 | 93 | 20 | 60 | 20 | 162 | 21721 |
| 45 | 0.1042 | 5.7736 | 7.3221 | 134 | 45 | 100 | 1 | 75 | 21359 |
| 46 | 0.1043 | 5.5852 | 7.3144 | 146 | 40 | 100 | 10 | 79 | 21390 |
| 47 | 0.1051 | 2.7372 | 7.2681 | 49 | 20 | 30 | 1 | 354 | 22321 |
| 48 | 0.1063 | 3.2906 | 8.1902 | 51 | 20 | 40 | 10 | 245 | 21989 |
| 49 | 0.1067 | 3.6035 | 8.1950 | 56 | 25 | 50 | 5 | 207 | 21886 |
| 50 | 0.1103 | 4.4740 | 7.3042 | 90 | 30 | 70 | 10 | 133 | 21551 |
| 51 | 0.1132 | 5.7564 | 7.3258 | 157 | 40 | 100 | 15 | 79 | 21181 |
| 52 | 0.1134 | 5.0210 | 7.3117 | 112 | 35 | 80 | 10 | 107 | 21364 |
| 53 | 0.1163 | 5.8029 | 7.3370 | 153 | 40 | 100 | 20 | 78 | 21056 |
| 54 | 0.1180 | 4.9980 | 7.3095 | 102 | 40 | 80 | 1 | 112 | 21289 |
| 55 | 0.1192 | 4.5602 | 8.2268 | 75 | 30 | 60 | 10 | 141 | 21337 |
| 56 | 0.1197 | 6.5388 | 7.3256 | 143 | 50 | 100 | 1 | 68 | 21011 |
| 57 | 0.1213 | 4.6570 | 7.3007 | 83 | 35 | 60 | 1 | 138 | 21401 |
| 58 | 0.1217 | 4.5037 | 8.2230 | 74 | 25 | 60 | 20 | 145 | 21306 |
| 59 | 0.1218 | 3.0594 | 7.2801 | 52 | 17 | 30 | 13 | 319 | 21877 |
| 60 | 0.1222 | 5.8060 | 7.3198 | 119 | 40 | 80 | 10 | 88 | 21102 |
| 61 | 0.1224 | 5.5640 | 7.3132 | 122 | 35 | 80 | 20 | 93 | 21095 |
| 62 | 0.1242 | 2.7536 | 7.2469 | 38 | 20 | 20 | 1 | 416 | 22198 |
| 63 | 0.1256 | 5.6096 | 7.3305 | 113 | 45 | 80 | 1 | 94 | 20959 |
| 64 | 0.1271 | 2.8878 | 7.2446 | 51 | 18 | 24 | 8 | 382 | 22084 |

| | | | | | | | | | |
|---|---|---|---|---|---|---|---|---|---|
| 65 | 0.1368 | 2.7484 | 7.2432 | 36 | 20 | 15 | 1 | 460 | 22097 |
| 66 | 0.1387 | 2.9913 | 7.2518 | 44 | 20 | 20 | 5 | 391 | 21885 |
| 67 | 0.1388 | 4.6440 | 7.3149 | 68 | 35 | 50 | 1 | 158 | 21052 |
| 68 | 0.1419 | 3.8470 | 7.2780 | 57 | 27 | 32 | 4 | 240 | 21379 |
| 69 | 0.1423 | 3.9634 | 7.2797 | 55 | 28 | 38 | 5 | 224 | 21333 |
| 70 | 0.1464 | 3.2900 | 7.2586 | 44 | 20 | 24 | 10 | 337 | 21600 |
| 71 | 0.1469 | 2.0809 | 7.2490 | 37 | 15 | 5 | 1 | 862 | 22397 |
| 72 | 0.1476 | 4.0140 | 7.2814 | 51 | 30 | 35 | 1 | 228 | 21222 |
| 73 | 0.1528 | 3.3207 | 7.2499 | 40 | 23 | 22 | 3 | 350 | 21579 |
| 74 | 0.1561 | 3.7940 | 7.2769 | 45 | 28 | 28 | 1 | 272 | 21187 |
| 75 | 0.1566 | 5.3753 | 7.2843 | 74 | 40 | 50 | 1 | 135 | 20782 |
| 76 | 0.1577 | 4.0315 | 7.2993 | 48 | 30 | 30 | 1 | 241 | 20982 |
| 77 | 0.1583 | 3.0626 | 7.2326 | 35 | 20 | 14 | 6 | 427 | 21709 |
| 78 | 0.1591 | 3.8549 | 7.2902 | 64 | 20 | 30 | 20 | 257 | 20992 |
| 79 | 0.1593 | 3.1752 | 7.2442 | 39 | 21 | 17 | 6 | 398 | 21576 |
| 80 | 0.1594 | 3.2720 | 7.2495 | 39 | 24 | 18 | 1 | 377 | 21510 |
| 81 | 0.1597 | 4.6611 | 7.3136 | 58 | 35 | 40 | 1 | 181 | 20713 |
| 82 | 0.1600 | 4.5846 | 7.2798 | 58 | 30 | 40 | 10 | 188 | 20878 |
| 83 | 0.1637 | 4.4828 | 7.2883 | 73 | 20 | 40 | 30 | 190 | 20712 |
| 84 | 0.1701 | 4.8872 | 7.2980 | 57 | 35 | 40 | 5 | 175 | 20581 |
| 85 | 0.1742 | 4.0418 | 7.2693 | 43 | 30 | 25 | 1 | 267 | 20880 |
| 86 | 0.1750 | 4.7195 | 7.2823 | 51 | 35 | 35 | 1 | 196 | 20649 |
| 87 | 0.1805 | 2.7439 | 7.2681 | 31 | 20 | 10 | 1 | 605 | 21405 |
| 88 | 0.1873 | 5.9514 | 7.3005 | 67 | 45 | 45 | 1 | 130 | 20057 |
| 89 | 0.1879 | 6.6693 | 7.3233 | 87 | 50 | 50 | 1 | 104 | 19827 |
| 90 | 0.1906 | 7.0424 | 7.3149 | 92 | 55 | 55 | 1 | 92 | 19744 |
| 91 | 0.1932 | 4.0720 | 7.2472 | 40 | 30 | 20 | 1 | 294 | 20706 |
| 92 | 0.1937 | 7.6510 | 7.3136 | 103 | 60 | 60 | 1 | 79 | 19615 |
| 93 | 0.2035 | 8.8995 | 7.3053 | 127 | 70 | 70 | 1 | 61 | 19337 |
| 94 | 0.2100 | 8.0866 | 7.3154 | 102 | 65 | 65 | 1 | 75 | 19233 |
| 95 | 0.2123 | 4.6054 | 7.2653 | 42 | 30 | 20 | 10 | 249 | 20156 |
| 96 | 0.2267 | 4.1091 | 7.2278 | 33 | 28 | 12 | 6 | 339 | 20296 |
| 97 | 0.2467 | 4.8175 | 7.2576 | 40 | 40 | 40 | 1 | 261 | 19536 |

| | $(F_0)_G$ | $(\bar{U}_{max})_G$ | Count | $(t_{F_{tp}})_{mean}$ | $(t_{F_{tp}})_{min}$ | $(t_{F_{tp}})_{max}$ | $(R_c)_{mean}$ | $(R_c)_{min}$ | $(R_c)_{max}$ |
|---|---|---|---|---|---|---|---|---|---|
| 1 | 0.03 | 3 | 2 | 175.50 | 169 | 182 | 8.2515 | 8.2512 | 8.2517 |
| 2 | 0.04 | 3 | 1 | 185.00 | 185 | 185 | 7.3267 | 7.3267 | 7.3267 |
| 3 | 0.05 | 3 | 5 | 163.40 | 115 | 184 | 7.5090 | 7.3217 | 8.2397 |
| 4 | 0.05 | 4 | 3 | 182.33 | 173 | 197 | 7.6381 | 7.3264 | 8.2554 |
| 5 | 0.06 | 3 | 1 | 57.00 | 57 | 57 | 8.2149 | 8.2149 | 8.2149 |

| 6 | 0.06 | 4 | 4 | 155.75 | 128 | 186 | 7.5567 | 7.3295 | 8.2299 |
|---|---|---|---|---|---|---|---|---|---|
| 7 | 0.07 | 3 | 2 | 57.00 | 49 | 65 | 8.2064 | 8.1961 | 8.2167 |
| 8 | 0.07 | 4 | 3 | 114.00 | 92 | 130 | 8.2382 | 8.2372 | 8.2397 |
| 9 | 0.07 | 5 | 1 | 142.00 | 142 | 142 | 8.2430 | 8.2430 | 8.2430 |
| 10 | 0.08 | 3 | 1 | 71.00 | 71 | 71 | 8.2105 | 8.2105 | 8.2105 |
| 11 | 0.08 | 4 | 3 | 114.67 | 103 | 135 | 7.9296 | 7.3269 | 8.2368 |
| 12 | 0.08 | 5 | 4 | 156.75 | 120 | 177 | 7.5567 | 7.3286 | 8.2399 |
| 13 | 0.09 | 3 | 1 | 47.00 | 47 | 47 | 8.1888 | 8.1888 | 8.1888 |
| 14 | 0.09 | 4 | 5 | 86.00 | 66 | 101 | 8.2212 | 8.2013 | 8.2310 |
| 15 | 0.09 | 5 | 3 | 145.00 | 109 | 183 | 7.3243 | 7.3156 | 7.3347 |
| 16 | 0.1 | 3 | 1 | 59.00 | 59 | 59 | 8.2048 | 8.2048 | 8.2048 |
| 17 | 0.1 | 4 | 3 | 100.67 | 89 | 120 | 7.3365 | 7.3032 | 7.3914 |
| 18 | 0.1 | 5 | 1 | 100.00 | 100 | 100 | 8.2376 | 8.2376 | 8.2376 |
| 19 | 0.1 | 6 | 2 | 140.00 | 134 | 146 | 7.3182 | 7.3144 | 7.3221 |
| 20 | 0.11 | 3 | 2 | 50.00 | 49 | 51 | 7.7292 | 7.2681 | 8.1902 |
| 21 | 0.11 | 4 | 2 | 73.00 | 56 | 90 | 7.7496 | 7.3042 | 8.1950 |
| 22 | 0.11 | 5 | 1 | 112.00 | 112 | 112 | 7.3117 | 7.3117 | 7.3117 |
| 23 | 0.11 | 6 | 1 | 157.00 | 157 | 157 | 7.3258 | 7.3258 | 7.3258 |
| 24 | 0.12 | 3 | 2 | 45.00 | 38 | 52 | 7.2635 | 7.2469 | 7.2801 |
| 25 | 0.12 | 5 | 4 | 83.50 | 74 | 102 | 7.7650 | 7.3007 | 8.2268 |
| 26 | 0.12 | 6 | 3 | 131.33 | 119 | 153 | 7.3233 | 7.3132 | 7.3370 |
| 27 | 0.13 | 3 | 1 | 51.00 | 51 | 51 | 7.2446 | 7.2446 | 7.2446 |
| 28 | 0.13 | 6 | 1 | 113.00 | 113 | 113 | 7.3305 | 7.3305 | 7.3305 |
| 29 | 0.14 | 3 | 2 | 40.00 | 36 | 44 | 7.2475 | 7.2432 | 7.2518 |
| 30 | 0.14 | 4 | 2 | 56.00 | 55 | 57 | 7.2789 | 7.2780 | 7.2797 |
| 31 | 0.14 | 5 | 1 | 68.00 | 68 | 68 | 7.3149 | 7.3149 | 7.3149 |
| 32 | 0.15 | 3 | 2 | 42.00 | 40 | 44 | 7.2543 | 7.2499 | 7.2586 |
| 33 | 0.15 | 4 | 1 | 51.00 | 51 | 51 | 7.2814 | 7.2814 | 7.2814 |
| 34 | 0.16 | 3 | 3 | 37.67 | 35 | 39 | 7.2421 | 7.2326 | 7.2495 |
| 35 | 0.16 | 4 | 4 | 57.50 | 45 | 73 | 7.2887 | 7.2769 | 7.2993 |
| 36 | 0.16 | 5 | 3 | 63.33 | 58 | 74 | 7.2926 | 7.2798 | 7.3136 |
| 37 | 0.17 | 4 | 1 | 43.00 | 43 | 43 | 7.2693 | 7.2693 | 7.2693 |
| 38 | 0.17 | 5 | 2 | 54.00 | 51 | 57 | 7.2902 | 7.2823 | 7.2980 |
| 39 | 0.18 | 3 | 1 | 31.00 | 31 | 31 | 7.2681 | 7.2681 | 7.2681 |
| 40 | 0.19 | 4 | 1 | 40.00 | 40 | 40 | 7.2472 | 7.2472 | 7.2472 |
| 41 | 0.19 | 6 | 1 | 67.00 | 67 | 67 | 7.3005 | 7.3005 | 7.3005 |
| 42 | 0.21 | 5 | 1 | 42.00 | 42 | 42 | 7.2653 | 7.2653 | 7.2653 |
| 43 | 0.23 | 4 | 1 | 33.00 | 33 | 33 | 7.2278 | 7.2278 | 7.2278 |
| 44 | 0.25 | 5 | 1 | 40.00 | 40 | 40 | 7.2576 | 7.2576 | 7.2576 |

# List of Figures

# List of Tables

239